Investigating the Warburg effect and the role of pyruvate kinase M2 in retinal Müller glial cells

Thaksaon Kittipassorn

M.D., B. Sc. (Hons)

A thesis submitted in fulfillment of the requirements of
the degree of Doctor of Philosophy (Sciences)

Department of Molecular & Biomedical Science (Biochemistry)
School of Biological Sciences
University of Adelaide, Australia
October 2019

Table of contents

Abstract

Surprisingly, similar to various cancer cells, Müller glial cells and light-sensing photoreceptors of the mammalian retina display the Warburg effect (aerobic glycolysis), an unusual metabolism whereby the cells tend to convert glucose into lactate via glycolysis regardless of oxygen availability. In cancer, the glycolytic enzyme pyruvate kinase M2 (PKM2) promotes lactate production and acts as a coactivator for the transcription factor hypoxia-inducible factor-1 (HIF-1), stimulating glycolysis; thus, PKM2 is implicated in driving the Warburg effect. PKM2 has also been shown to be expressed in the retina and cultured Müller cells (MCs).

This thesis elucidates MC glucose metabolism and tests the hypothesis that PKM2 drives the Warburg effect in cultured MCs.

Primary rat MCs, the SV40-immortalised rMC-1 MC line and a novel spontaneously immortalised rat SIRMu-1 MC line were used as experimental models. The SIRMu-1 is a novel spontaneously immortalised cell line that was derived from primary MCs during the course of this thesis. It retains similar cellular morphology to cultured primary rat MCs. Immunofluorescence, western blotting and RNA sequencing show that the SIRMu-1 cells closely resemble primary MCs in regard to overall transcriptome and expression of the MC markers cellular retinaldehyde-binding protein, glutamine synthetase, S100, vimentin and glial fibrillary acidic protein at both the mRNA and the protein levels. SIRMu-1 cells, however, proliferate rapidly, do not senesce and have a high transfection efficiency. RNA sequencing also shows that the SIRMu-1 cells were derived from a male rat. The cell line is a valuable experimental tool to study MCs.

Glucose metabolism of primary MCs, rMC-1 and SIRMu-1 cells was investigated using lactate assays and a Seahorse XFe96 Analyser system. Primary MCs and rMC-1 cells display the Warburg effect, while SIRMu-1 cells depend predominantly on oxidative phosphorylation. This shows that the Warburg effect does not always exist in highly-proliferative cells as commonly postulated.

As the rMC-1 cells retain the Warburg effect observed in primary MCs, they were used to investigate the role of PKM2. Short hairpin RNA-mediated PKM2 knockdown and CRISPR/Cas9-mediated PKM2 knockout did not significantly alter the high glycolytic activity of rMC-1 cells, indicating that PKM2 is not a main driver of the Warburg effect in cultured MCs. This demonstrates that the role of PKM2 in the Warburg effect is cell type-dependent. This project improves our understanding of MC metabolism and may contribute to research on retinal diseases associated with MC abnormality.

Candidate's declaration

I certify that this work contains no material which has been accepted for the award of any other degree or diploma in my name in any university or other tertiary institution and, to the best of my knowledge and belief, contains no material previously published or written by another person, except where due reference has been made in the text. In addition, I certify that no part of this work will, in the future, be used in a submission in my name for any other degree or diploma in any university or other tertiary institution without the prior approval of the University of Adelaide and where applicable, any partner institution responsible for the joint award of this degree.

The author acknowledges that copyright of published works contained within this thesis resides with the copyright holder(s) of those works.

I give permission for the digital version of my thesis to be made available on the web, via the University's digital research repository, the Library Search and also through web search engines, unless permission has been granted by the University to restrict access for a period of time.

23/10/2019

Thaksaon Kittipassorn Date

Acknowledgements

(H)IF life was a theme park, doing a PhD would probably be a roller coaster. Here's a thank you to all those who have kept me on track.

First of all, I would like to thank my principal supervisor, Dan Peet, for your endless patience, understanding, enthusiasm, guidance, support and great puns. Thank you for accepting me as an Honours student in Biochemistry in 2013 despite not knowing much about me and despite my different academic background being a medical doctor with no research experience. From not even knowing what a plasmid was, with your help I completed the Honours course and got accepted to do a PhD. You have not only supported me academically but also in my living in a foreign country away from home. Thank you for putting up with my strange working hours, my finishing assignments at the last minute and my worrying, and for your tremendous help with this thesis.

Thank you to my co-supervisor, Murray Whitelaw, your valuable advice and support (and occasional great jokes) have been so great. Thank you also to my other co-supervisor, Bob Casson, for your unwavering enthusiasm and advice and for your great help with my thesis.

Thank you to all the past and present members of the Peet Lab. Rachel, you have helped and supported me more than I can say and I couldn't have survived my Honours and PhD without you. Nat and Jay, you were the first student members of the Lab that I met! Thank you for welcoming me into the lab and for your help with my experiments and advice over the years. I will always remember our 'Breezeblocks' days. Tracey, thanks for making the lab that much more cheerful. Cameron, thank you for reading my thesis front to back in five days and giving great comments (OCRs?) and for helping with my experiments and students when I needed. I enjoyed our working on related projects and our arguments on the Warburg effect, among other things. Josh, you're awesome and I would really buy stocks of your bio product company if you ever founded one. Thanks for all your help when I asked and also when I didn't but really needed it. You notice things that others usually don't and that is much appreciated. Simon, thanks for all the fun times in the lab. Marie, Navdeep, Yagnesh, Yinan, Josiah and Erin, it was great working with you. Luke, your puns are one of a kind and always make me laugh, and thank you for appreciating my advice. Nick S, teaching and helping you this year has been great and a good learning experience for me, and our bantering is always fun. Lorenzo, thanks for being such a cool lab mate and for your good work. Carla, welcome to the lab. I hope you have a great time in this lab as much as I have had.

Thank you to all the past and present members of the Whitelaw Lab. Dave, thank you for all your help and advice (and plasmids) over the years. I don’t know if you know but we know that you know everything and we are in awe of you. Thank you also for the idea to do RNA sequencing with our new cell line and for your funny unexpected jokes although sometimes (most of the times?) it takes me a little while to get them. Adrienne, thank you for your kind advice and patience. Veronica, thanks for talking me through your western blotting protocol that I and others in the lab still use to this day and thank you for your great comments on my presentations. Emily, we started out together in Honours and then PhD, and having you with me all through the years has been such a great support, without which I wouldn’t have been able to get through my PhD. I love our conversations both in person and online and thank you for always being there for me. Alexis, thanks for sticking together, for all the ice cream, for all your help and support and for the MEFs. I can’t imagine my PhD life without you. Joe, thank you for your understanding of my obsessiveness and worries, for all your help, and for all the talks we’ve had. Tim, you are both mean and nice to me, and that is a rare and difficult to achieve combination. Thanks for the laughs and the help. Lachlan and Victoria, it was nice working with you. Yesha, welcome! You’re in good hands!

Thank you to other members of our MLS family. Keith, our Postgraduate coordinator, thank you for replying to my email about applying for Honours and all the other emails after that and for your great support. Yulee, thank you for being away from home together and for all your advice and help with experiments. Adi and Chan, thank you for your advice regarding CRISPR and plasmids and for your friendship. Byron, your friendship and your organising things are much appreciated. Emily K, you’re such a joy! Thanks for listening to me and for always smiling. Louise, thank you for our nice chats and for commenting on the CRISPR method section of my thesis. Paul, John B, Grant, Michael, Nick E, Dale, Dan Pederick, thank you for your help, advice, mouse tissues (Dan Pederick), and 293FT cells (Michael’s lab). Mel, Ruby, Ella, Rosa, Blagojce, Chuan and Kylie, it has been great working and hanging out with you. Lynn, thank you for your support. I love our hellos and chats.

Thank you to members of the Casson Lab. John Wood and Teresa Mammone, thank you for all your help and advice, for providing the primary retinal cultures and rat tissues, and for showing me how to do IF, among other things. John, thank you also for your great help with my thesis – much appreciated.

I would also like to thank the team from In Vitro Technology and Agilent Technologies for a Seahorse analyser training session and for technical support. Thank you also to Rebecca Robker, Yasmyn Gordon, Nicholas Hatzirodos, Darryl Russell and the Faculty of Health and Medical Sciences of the University for the support with the Seahorse usage and access. Thank you to Jane Sibbons and the Adelaide Microscopy (Adelaide, SA, Australia) for the help with the ArrayScan. Thank you to Kate Pilkington and the CCB Cytometry Facility (UniSA Cancer Research Institute, Adelaide, SA, Australia) for providing cell sorting assistance. Thank you to Joel Geoghegan, Andreas Schreiber, Wendy Parker and Ming Lin (ACRF Cancer Genomics Facility, Adelaide, SA, Australia) for their assistance with RNA sequencing. Thank you to the Australian Genomics Research Facility (AGRF, Adelaide, SA, Australia) for Sanger sequencing service. Thank you to Dr Vijay Sarthy (Northwestern University, Chicago, IL, USA) and Dr Binoy Appukuttan (Flinders University, Adelaide, SA, Australia) for providing the rMC-1 cell line.

Thank you to the University of Adelaide and the Graduate Centre for providing me with research facilities, assistance and the Adelaide Postgraduate Research Scholarship. Thank you to the School of Biological Sciences and our Department (with a number of name changes over the years but awesome just the same).

Thank you to the Department of Physiology, Faculty of Medicine Siriraj Hospital (Bangkok, Thailand) for providing me with scholarships and an opportunity to come and do a PhD in Adelaide and also to the people in the Department and the Faculty, including Dr Supatra Lohsiriwat, Dr Wattana

Watanapa, Dr Sorachai Srisuma and Ms Pensri Phongchaikul, for their great support and advice both before and after the start of my PhD.

Thank you to my brother, family and friends in Thailand. I've missed you. See you soon!

Finally, thank you to my mum and dad for being everything to me and always being there for me: My dad, Sukitti Kittipassorn, who takes care of everything at home and is my one-man support team and the most amazing dad in the world, and my mum, Kanchana Kittipassorn, who has travelled 5000+ km to Adelaide to take care of me countless of times and done more things for me than words can express. Mama and Papa, this thesis is for you.

Yours in wontons,

Ice Thaksaon Kittipassorn

Publications arising from this thesis

Paper 1

Ng, S.K., Wood, J.P., Chidlow, G., Han, G., Kittipassorn, T., Peet, D.J., and Casson, R.J. (2015). Cancer-like metabolism of the mammalian retina. Clinical & Experimental Ophthalmology 43, 367-376. http://dx.doi.org/10.1111/ceo.12462 (Appendix 7.1)

Paper 2

Casson, R.J., Wood, J.P., Han, G., Kittipassorn, T., Peet, D.J., and Chidlow, G. (2016). M-Type Pyruvate Kinase Isoforms and Lactate Dehydrogenase A in the Mammalian Retina: Metabolic Implications. Investigative Ophthalmology & Visual Science 57, 66-80. http://dx.doi.org/10.1167/iovs.15-17962 (Appendix 7.2)

Paper 3

Peet, D.J., Kittipassorn, T., Wood, J.P., Chidlow, G., and Casson, R.J. (2017). HIF signalling: The eyes have it. Experimental Cell Research 356, 136-140. http://dx.doi.org/10.1016/j.yexcr.2017.03.030 (Appendix 7.3)

Paper 4

Kittipassorn, T., Haydinger, C.D., Wood, J.P.M., Mammone, T., Casson, R.J., and Peet, D.J. (2019a). Characterization of the novel spontaneously immortalized rat Muller cell line SIRMu-1. Experimental Eye Research 181, 127-135. https://doi.org/10.1016/j.exer.2019.01.013 (Chapter 3)

Paper 5

Kittipassorn, T., Haydinger, C.D., Wood, J.P.M., Mammone, T., Casson, R.J., and Peet, D.J. (2019b). RNA sequencing data of cultured primary rat Müller cells, the spontaneously immortalized rat Müller cell line, SIRMu-1, and the SV40-transformed rat Müller cell line, rMC-1. Data in Brief 23, 103721. https://doi.org/10.1016/j.dib.2019.103721 (Chapter 3)

Presentations and communications arising from this thesis

2015

- Hypoxia-inducible factor-1 & pyruvate kinase M2: roles in the Warburg effect in mammalian retina (poster presentation)

  The School of Biological Sciences Postgraduate Symposium 2015, Australia

2016

- Cancer-like metabolism in mammalian retina: the expected and the unexpected (oral presentation)

  The 3rd Annual EMBL (European Molecular Biology Laboratory) Australia Postgraduate Symposium, Australia
- Behind cancer-like metabolism of mammalian retina: the expected and the unexpected (poster and 3-minute poster teaser oral presentations)

  The 6th Australia and New Zealand Society for Cell and Developmental Biology (ANZSCDB) Adelaide meeting, Australia
- Mulling over Müller cells: cancer-like metabolism in mammalian retina (oral presentation)

  The ComBio2016 conference, Australia
- The eyes have it: the commonality between retina and cancer (oral presentation)

  The School of Biological Sciences Postgraduate Symposium 2016, Australia

2017

- More than meets the eye: does the glycolytic enzyme PKM2 drive cancer-like metabolism of mammalian retina? (poster presentation)

  The 7th Australia and New Zealand Society for Cell and Developmental Biology (ANZSCDB) Adelaide meeting, Australia
- Cancer-like metabolism of mammalian retina: does the glycolytic enzyme PKM2 play a role? (poster and 2-minute poster teaser oral presentations)

  The ComBio2017 conference, Australia
- More than meets the eye: insights into diseases of the retina (oral presentation)

  The School of Biological Sciences Postgraduate Symposium 2017, Australia

- Mulling over retinal Müller cells: behind cancer-like metabolism of mammalian retina (poster presentation)

  The Annual Scientific Meeting 2017 of the Australian Society for Medical Research (ASMR) SA Division, Australia
- Mulling over retinal Müller Cells: what drives cancer-like metabolism of mammalian retina? (poster presentation)

  The international Keystone Symposia Conference "Tumor Metabolism: Mechanisms and Targets", Canada

2018

- And they proliferate rapidly ever after: an immortalised Müller cell story (oral presentation)

  The 8th Australia and New Zealand Society for Cell and Developmental Biology (ANZSCDB) Adelaide meeting, Australia
- More than meets the eye: does the HIF-1/PKM2 axis drive cancer-like metabolism of mammalian retina? (oral presentation)

  The Oxygen meeting, Flinders University, Australia
- Disruption of the glycolytic enzyme PKM2 decreases retinal Müller glial cell number via glucose metabolism-independent mechanism (poster presentation)

  The Adelaide Protein Group Student Awards 2018 meeting, Australia
- Metabolic and transcriptomic analyses of Müller glial cells of the retina (poster presentation)

  The 39th Annual Lorne Genome Conference 2018, Australia

2019

- More than meets the eye: does the glycolytic enzyme PKM2 drive cancer-like metabolism of mammalian retina? (poster presentation)

  The Nature Conference on Cellular Metabolism, Xiamen, China

Awards

2013	Scholarship from the Faculty of Medicine Siriraj Hospital, Mahidol University, Thailand, as financial support for an Honours Degree of Bachelor of Science
2014	Adelaide Graduate Research Scholarship (AGRS) from the University of Adelaide as financial support for a PhD
2017	Seahorse travel bursary award from Agilent Technologies
2017	Scholarship from the Faculty of Medicine Siriraj Hospital, Mahidol University, Thailand, as financial support for a PhD

List of symbols and abbreviations

µL	microlitre
µm	micrometre
µM	micromolar
µs	microsecond
acetyl CoA	acetyl Coenzyme A
AK1	adenylate kinase 1
AMD	age-related macular degeneration
ATP	adenosine triphosphate
ATPR	ATP production rate
$\mathrm{ATPR_{glyco}}$	ATPR derived from glycolysis
$\mathrm{ATPR_{res}}$	ATPR derived from respiration
$\mathrm{ATPR_{total}}$	total ATPR
bp	base pair
BSA	bovine serum albumin
Cas9	CRISPR associated protein 9
chr	chromosome
CO_2	carbon dioxide
COX IV	cytochrome c oxidase subunit IV
CRISPR	clustered regularly interspaced short palindromic repeats
CS	Cell Signaling Technology
DMEM	Dulbecco's Modified Eagle Medium
DMSO	dimethyl sulfoxide
DTT	dithiothreitol
ECAR	extracellular acidification rate
$\mathrm{ECAR_{basal}}$	basal ECAR

$ECAR_{oligo}$	oligomycin-induced ECAR
ECL	enhanced chemiluminescence
EDTA	ethylenediaminetetraacetic acid
ERG	electroretinography
ETC	electron transport chain
EV	empty vector
FACS	fluorescence activated cell sorting
FAD	flavin adenine dinucleotide
FBP	fructose 1,6-bisphosphate
FBS	fetal bovine serum
FCCP	carbonyl cyanide-4-(trifluoromethoxy) phenylhydrazone
FGFR1	fibroblast growth factor receptor type 1
FIH	factor inhibiting HIF
GAPDH	glyceraldehyde 3-phosphate dehydrogenase
GCL	ganglion cell layer
GCR	glucose consumption rate
GCR_{glyco}	GCR that is due to glycolysis
GCR_{res}	GCR that is due to respiration
GCR_{total}	total GCR
gDNA	genomic DNA
GFP	green fluorescence protein
GLUT	glucose transporter
gRNA	guide RNA
GTS	glycine/tris/SDS buffer
H^+	hydrogen ion/protons
H_2O	water

HBSS	Hank's Balanced Salt Solution
HCl	hydrochloric acid
HCO_3^-	bicarbonate Ion
HEK	human embryonic kidney
HEPES	hydroxyethyl piperazineethanesulfonic acid
HIF-1	hypoxia-inducible factor-1
HK	hexokinase
HK2	hexokinase 2
hnRNPs	heterogeneous nuclear ribonucleoproteins
IDT	Integrated DNA Technologies
INL	inner nuclear layer
IPL	inner plexiform layer
KD	knockdown
KO	Knockout
LB	luria broth
LDH	lactate dehydrogenase
LDHA	lactate dehydrogenase A
LDHB	lactate dehydrogenase B
M	molar
mA	milliampere
MC	Müller cell
MCT4	monocarboxylate transporter 4
MEF	mouse embryonic fibroblast
MEM	minimal essential medium
$MgCl_2$	magnesium chloride
miR30	microRNA-30

mL	millilitre
mM	millimolar
N	Novus Biologicals
NaCl	Sodium chloride
NAD	nicotinamide adenine dinucleotide
NaOH	sodium hydroxide
NDPK	nucleoside-diphosphate kinase
NEB	New England Biolabs
nm	nanometre
^{o}C	degree Celsius
O_2	oxygen
OCR	oxygen consumption rate
OCR_{basal}	basal OCR
$OCR_{coupled}$	OCR coupled to ATP production
OCR_{FCCP}	FCCP-induced OCR
OCR_{mito}	OCR due to mitochondrial respiration
$OCR_{non\text{-}mito}$	OCR due to non-mitochondrial respiration
OCR_{oligo}	oligomycin-induced OCR
OGDH	oxoglutarate/alpha-ketoglutarate dehydrogenase
ONL	outer nuclear layer
OPL	outer plexiform layer
OXPHOS	oxidative phosphorylation
P/O ratio	ratio of ATP formed to oxygen atom consumed
PAM	protospacer adjacent motif
PBS	phosphate-buffered saline
PCR	polymerase chain reaction

PDH	pyruvate dehydrogenase
PDK-1	pyruvate dehydrogenase kinase-1
PEI	Polyethylenimine
PEP	phosphoenolpyruvate
PER	proton efflux rate
PER_{basal}	basal PER
PER_{glyco}	PER due to the conversion of glucose to lactate via glycolysis
PER_{res}	PER due to mitochondrial respiration
PFK1	phosphofructokinase 1
PGI	phosphoglucose isomerase
PGK	phosphoglycerate kinase
PGM	phosphoglycerate mutase
PHD	prolyl hydroxylase
PI3K	phosphoinositide 3-kinase
PK	pyruvate kinase
PKM	pyruvate kinase M
PMSF	phenylmethanesulfonyl fluoride
PPP	pentose phosphate pathway
PT	Proteintech
qRT-PCR	quantitative real-time PCR
rMC-1	SV40-immortalised rat Müller cell line
Rlbp1	retinaldehyde binding protein 1
RNA-seq	RNA sequencing
RO	reverse osmosis
ROS	reactive oxygen species
Rot/AA	rotenone/antimycin A

RPE	retinal pigment epithelium
rpm	revolutions per minute
SAICAR	succinylaminoimidazolecarboxamide ribose-5′-phosphate
SDS-PAGE	sodium dodecyl sulfate–polyacrylamide gel electrophoresis
shRNA	short hairpin RNA
SIRMu-1	spontaneously immortalised rat Müller cell line
siRNA	small interfering RNA
SOC	Super Optimal broth with Catabolite repression
STK	succinate thiokinase
TCA	tricarboxylic acid
TPI	triose phosphate isomerase
V	volt
VMD2	vitelliform macular dystrophy-2
WT	wildtype

Chapter 1

Introduction

CHAPTER 1: Introduction

1.1 Overview

The retina serves as the primary organ for the generation of vision. This ocular tissue contains photoreceptor cells that convert light to electrical signals which are processed by specialised neurons and transmitted via retinal ganglion cells along the optic nerve to the brain for higher processing. One of the major cell types of the retina is the Müller cell (MC), a type of resident glial cell that provides structural and functional support to retinal neurons. (Barrett et al., 2012; Bringmann et al., 2006; Mescher, 2010; Vecino et al., 2016). Interestingly, unlike most other physiological cells in the body, and in particular the brain, the mammalian retina displays an unusual glucose metabolism, termed the Warburg effect, also known as aerobic glycolysis (reviewed in Paper 1 (Ng et al., 2015)) (Cohen and Noell, 1960; Poitry-Yamate et al., 1995; Tornquist and Alm, 1979; Warburg, 1925; Warburg et al., 1924; Warburg et al., 1930; Winkler, 1981, 1995; Winkler et al., 2000; Winkler et al., 2003). This describes the phenomenon where cells preferentially convert glucose into lactate via glycolysis, despite the presence of abundant oxygen, which should theoretically drive mitochondrial oxidative phosphorylation (OXPHOS) (Koppenol et al., 2011; Warburg et al., 1927). The Warburg effect is a common feature of most cancer cells (Koppenol et al., 2011; Vander Heiden et al., 2009) and is also displayed in other highly proliferative cells, such as stimulated lymphocytes (Abdel-Haleem et al., 2017). Although Warburg's team noted the presence of aerobic metabolism in the retina in the 1920s (Warburg, 1925; Warburg et al., 1924; Warburg et al., 1930), this phenomenon received relatively little attention until recently. Given the large energy requirements of the retina and the potentially important role that impaired energy metabolism plays in a number of common blinding conditions (Bringmann et al., 2006; Hartong et al., 2008), it is clearly pertinent to investigate the mechanisms and control of aerobic glycolysis in this tissue. The work presented in this thesis, therefore, aimed to elucidate the existence of the Warburg effect in the retina and more specifically in MCs which provide support to most of the cells in this tissue. Furthermore, this thesis sought to investigate whether the glycolytic enzyme pyruvate kinase M2 (PKM2), which has been shown to drive the Warburg effect in various cancer cells (Christofk et al., 2008a; Clower et al., 2010; Goldberg and Sharp, 2012; Siddiqui et al., 2018), plays a similar role in MCs.

1.2 Glucose metabolism: glycolysis and oxidative phosphorylation

Energy is essential to cellular survival and function. Cells use adenosine triphosphate (ATP) to transfer energy. In order to produce ATP, most quiescent, differentiated cells utilise cytoplasmic glycolysis and mitochondrial OXPHOS (Fig. 1.1 and 1.2). In the glycolytic pathway (Fig. 1.1), which comprises a series of sequential cytoplasmic enzymatic reactions, a single glucose molecule is converted via several intermediates to two molecules of pyruvate, producing two ATP molecules. In the last step of glycolysis, pyruvate is generated from phosphoenolpyruvate (PEP), a reaction catalysed by pyruvate kinase (PK) (Fig. 1.1).

When levels of oxygen are sufficient, pyruvate is predominantly converted into acetyl Coenzyme A (acetyl CoA) by the pyruvate dehydrogenase complex consisting of three enzymes, including pyruvate dehydrogenase (PDH) (Fig. 1.1 and 1.2A). Acetyl CoA then enters the tricarboxylic acid (TCA) cycle in the mitochondrion, ultimately resulting in the production of ATP by OXPHOS. More specifically, the TCA cycle generates NADH (reduced nicotinamide adenine dinucleotide (NAD)) and $FADH_2$ (reduced flavin adenine dinucleotide) which are energy-rich molecules that act as electron donors in the subsequent electron transport chain (ETC) (Fig. 1.1). The ETC consists of four protein complexes (complexes I, II, III and IV) that transfer electrons from a series of electron donors to electron acceptors via redox reactions, with oxygen as the final electron acceptor (Fig. 1.1). The transfer of electrons releases energy which pumps protons (hydrogen ions, H^+) from the mitochondrial matrix across the inner membrane to the intermembrane space (Fig. 1.1). This creates a proton gradient causing H^+ to re-enter the matrix, a process which powers the generation of ATP by ATP synthase (also referred to as complex V) (Fig. 1.1). This process of electron transfer from NADH and $FADH_2$ to oxygen to produce ATP is OXPHOS, and the oxidation of glucose by oxygen ultimately produces water (H_2O) and carbon dioxide (CO_2). Overall, under aerobic conditions ~30-33 ATP molecules are produced by the complete oxidation of one glucose molecule (Brand, 2005; Mookerjee et al., 2017; Mookerjee et al., 2015).

Under hypoxic conditions, the majority of pyruvate is converted to lactate by lactate dehydrogenase A (LDHA) via anaerobic glycolysis (Fig. 1.2B), which yields only two ATP molecules per one glucose molecule (Vander Heiden et al., 2009). Lactate is then exported out of the cells. The conversion of pyruvate to lactate by LDHA regenerates NAD+ (an oxidised form of NAD) to continuously feed the glycolytic pathway (Goda and Kanai, 2012).

Under aerobic or anaerobic conditions, metabolic intermediates from the glycolytic pathway can be directed to biosynthesis, including lipid, nucleic acid and amino acid production (Fig. 1.1). These products are subsequently used as substrates for the production of biomass needed for cellular proliferation (Mucaj et al., 2012; Vander Heiden et al., 2009). Anabolic synthesis of amino acids and lipids are also carried out by mitochondria (Ahn and Metallo, 2015). Furthermore, the pentose phosphate pathway (PPP), which runs parallel to glycolysis and is also fed by metabolites of glucose, plays a significant role in cellular protection against oxidative stress (Stincone et al., 2015). Thus, whether aerobic or anaerobic pathways are used, glucose metabolism is central to cellular energy production, and essential for survival, normal function and proliferation.

1.3 The Warburg effect/aerobic glycolysis

Proliferating cells, including cancer cells, commonly metabolise glucose by a different process from that of quiescent cells described above; they tend to convert glucose to lactate via glycolysis even in the presence of abundant levels of oxygen (Fig. 1.2C); this is a much less efficient way to produce ATP (Hsu and Sabatini, 2008; Koppenol et al., 2011; Vander Heiden et al., 2009; Warburg, 1956; Warburg et al., 1927). The upregulated conversion of glucose into lactate results in higher glucose consumption and lactate production (Hsu and Sabatini, 2008; Koppenol et al., 2011; Vander Heiden et al., 2009; Warburg, 1956; Warburg et al., 1927). This process is known as aerobic glycolysis and eponymously as the Warburg effect, after Otto Warburg who first described the phenomenon in cancer cells in the 1920s. Warburg and colleagues found that under aerobic conditions cancer cells produced a larger amount of lactate compared to normal tissues and converted the majority of glucose into lactate, rather than use it for respiration (Warburg, 1956; Warburg et al., 1924; Warburg et al., 1927; Warburg et al., 1930). In addition to cancer cells, several non-cancerous highly proliferative cells have been shown to display the Warburg effect, including activated macrophages and T-lymphocytes of the immune system, endothelial cells and pluripotent embryonic stem cells (Abdel-Haleem et al., 2017; Palsson-McDermott and O'Neill, 2013; Rodriguez-Prados et al., 2010).

Figure 1.1

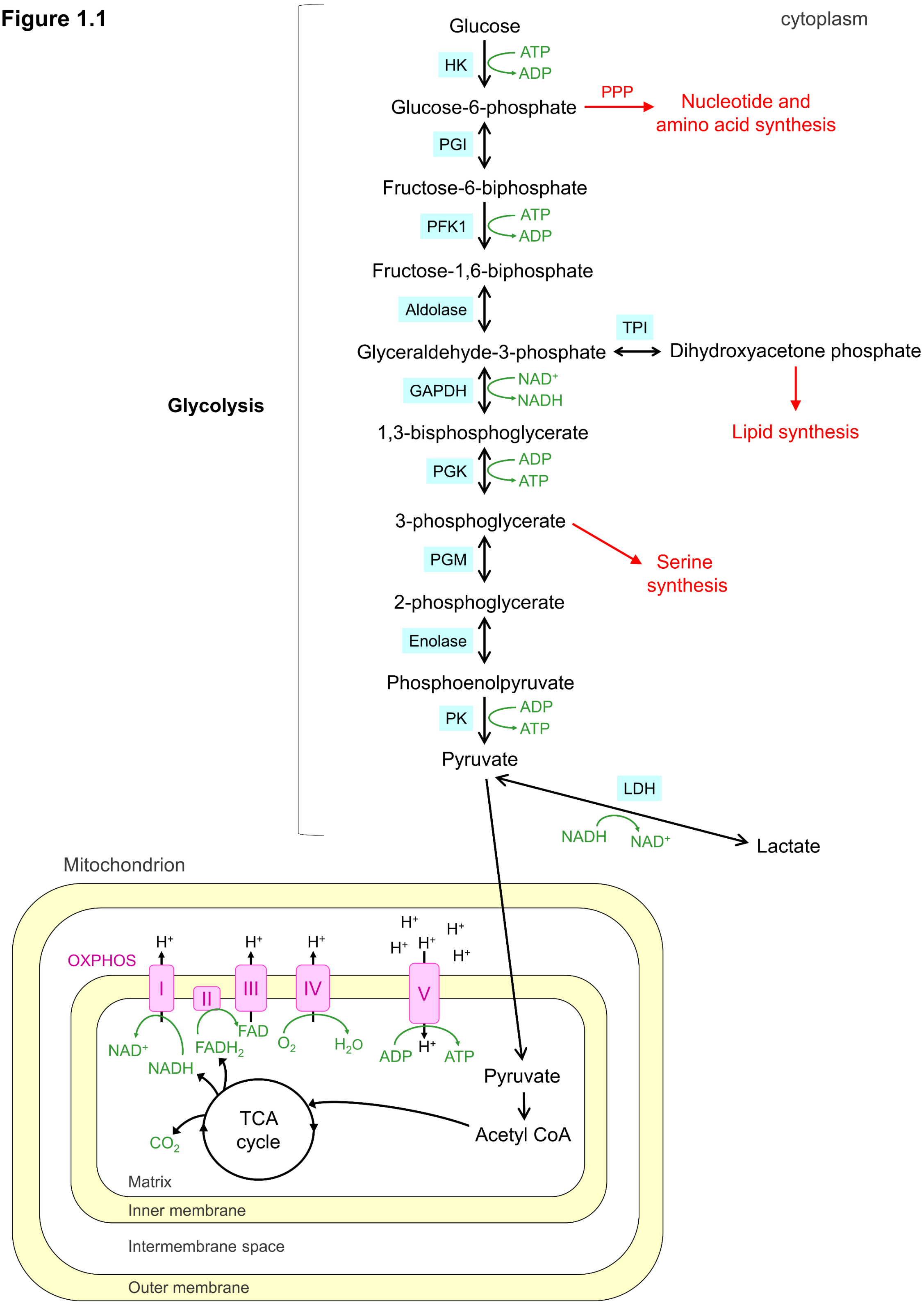
Glycolysis
cytoplasm
Glucose
HK
ATP
ADP
Glucose-6-phosphate
PPP
Nucleotide and amino acid synthesis
PGI
Fructose-6-biphosphate
PFK1
ATP
ADP
Fructose-1,6-biphosphate
Aldolase
TPI
Glyceraldehyde-3-phosphate
Dihydroxyacetone phosphate
Lipid synthesis
GAPDH
NAD^+
NADH
1,3-bisphosphoglycerate
PGK
ADP
ATP
3-phosphoglycerate
Serine synthesis
PGM
2-phosphoglycerate
Enolase
Phosphoenolpyruvate
PK
ADP
ATP
Pyruvate
LDH
NADH
NAD^+
Lactate
Mitochondrion
OXPHOS
H^+
I
II
III
IV
V
NAD^+
NADH
$FADH_2$
FAD
O_2
H_2O
ADP
ATP
Pyruvate
Acetyl CoA
TCA cycle
CO_2
Matrix
Inner membrane
Intermembrane space
Outer membrane

Figure 1.1. Cellular glucose metabolism. To produce energy, cells metabolise glucose to pyruvate via the glycolytic pathway which is a series of multiple enzymatic reactions. Pyruvate can either be converted into acetyl CoA or lactate. In the former case, acetyl CoA enters the tricarboxylic acid (TCA) cycle which ultimately produces NADH (reduced nicotinamide adenine dinucleotide) and $FADH_2$ (reduced flavin adenine dinucleotide), high energy molecules that act as electron donors in the electron transport chain (ETC). The ETC is composed of four protein complexes (complexes I, II, III and IV). The transfer of electrons through these protein complexes to oxygen, the final electron acceptor, creates a proton gradient by pumping protons (hydrogen ions, H^+) from the mitochondrial matrix across the inner membrane to the intermembrane space. The proton gradient causes H^+ to re-enter the matrix, powering the generation of ATP by ATP synthase (complex V). These processes make up oxidative phosphorylation (OXPHOS). Glycolytic intermediates can also be shunted to biosynthetic pathways (indicated in red). Two-way arrows indicate reversible reactions and one-way arrows irreversible reactions. Enzymes that catalyse each step are shown in blue boxes. GAPDH, glyceraldehyde 3-phosphate dehydrogenase; HK, hexokinase; LDH, lactate dehydrogenase; PPP, pentose phosphate pathway; PFK1, phosphofructokinase 1; PGI, phosphoglucose isomerase; PGK, phosphoglycerate kinase; PGM, phosphoglycerate mutase; PK, pyruvate kinase; TPI, triose phosphate isomerase.

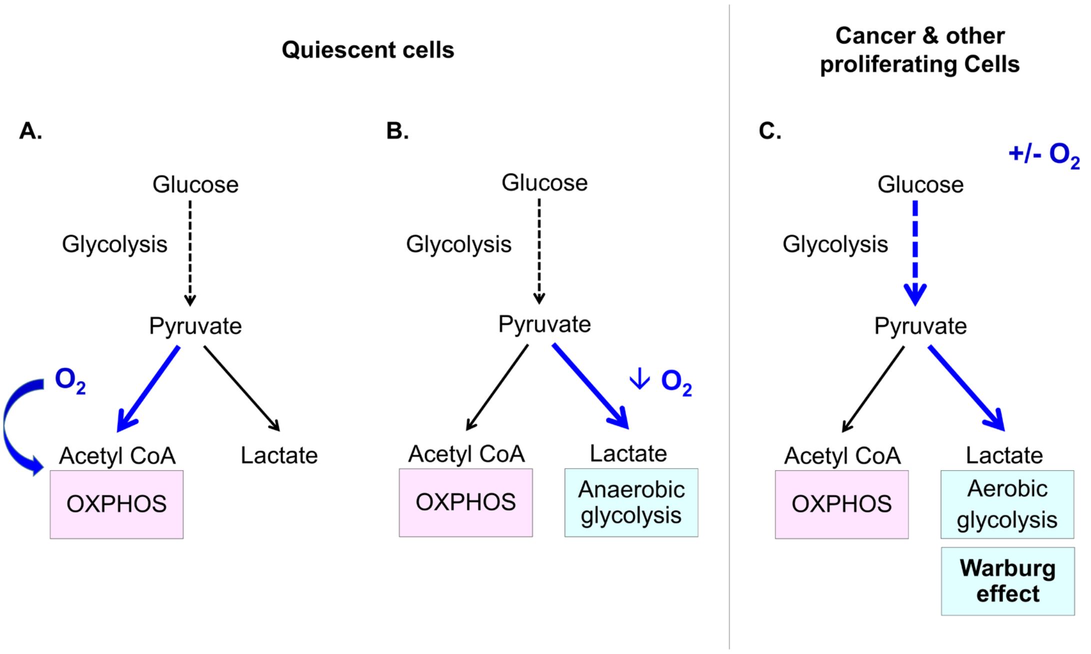

Figure 1.2. Glucose metabolism in quiescent cells and in cancer and other proliferating cells under aerobic and anaerobic conditions. Cells convert glucose into pyruvate via the glycolytic pathway. **(A)** In quiescent/differentiated cells, when there is abundant oxygen most pyruvate is converted into acetyl CoA, leading to oxidative phosphorylation (OXPHOS), a process which requires oxygen. **(B)** In hypoxia, quiescent/differentiated cells turn most pyruvate into lactate and this is anaerobic glycolysis. **(C)** Cancer and other proliferating cells tend to preferentially convert pyruvate into lactate regardless of oxygen availability, a phenomenon known as aerobic glycolysis or the Warburg effect.

Originally, Warburg postulated that aerobic glycolysis was involved in carcinogenesis and occurred as a result of defective mitochondria (Warburg, 1956). However, more recent studies have indicated that mitochondria are functional in most cancer cells, suggesting that limited oxidative capacity is not the reason behind the Warburg effect in cancer (reviewed in (Moreno-Sanchez et al., 2007; Vander Heiden et al., 2009)). A number of explanations for the existence of the Warburg effect in proliferating cells have been proposed. One widely purported explanation is that the Warburg effect fulfils metabolic requirements of proliferating cells because it leads to a greater amount of glycolytic intermediates and thereby provides a mechanism to divert such intermediates to biosynthesis required for cell growth and proliferation (Vander Heiden et al., 2009). However, the stoichiometry of this explanation is arguably flawed because if the vast majority of carbon atoms from glucose are converted to lactate despite the presence of oxygen (by definition, the Warburg effect), then there are inadequate carbon atoms for biosynthesis (Liberti and Locasale, 2016; Mookerjee et al., 2017). Furthermore, there is evidence that only a small proportion of carbon atoms from glucose in highly glycolytic cancer cells, such as non-small cell lung cancer cell lines H1299 and A549, is converted to biosynthetic precursors such as amino acids or nucleotides (Hosios et al., 2016). Hence, there are theoretical and empirical reasons to doubt this “biosynthesis hypothesis”. An arguably more likely explanation for the presence of the Warburg effect is that cells with high energy demands metabolise glucose to lactate via glycolysis for much more immediate ATP production and regeneration of NAD+. This process is therefore self-reinforcing, continuously supplying the correct cellular environment for maintenance of the glycolytic pathway (Liberti and Locasale, 2016; Mookerjee et al., 2017). Although the conversion of glucose to lactate via glycolysis is considered a less efficient way to produce ATP per glucose molecule than OXPHOS, glycolysis can occur more rapidly leading to rapid ATP synthesis with higher glucose consumption (Liberti and Locasale, 2016). Among other explanations is that cells use glycolysis rather than OXPHOS for energy generation to free up mitochondria for other processes such as biosynthesis of amino acids and lipids (Liberti and Locasale, 2016).

Although reasons behind the existence of the Warburg effect and how it benefits cancer cells remain largely uncertain and require further investigations, several mechanisms and agents implicated in driving the Warburg effect have been characterised. Key drivers of the Warburg effect in cancer include the phosphoinositide 3-kinase (PI3K) pathway (Ward and Thompson, 2012), the transcription factor and proto-oncogene Myc (Dejure and Eilers, 2017), the transcription factor hypoxia-inducible factor-1 (HIF-1) (Semenza, 2012) and the glycolytic enzyme PKM2 (Chaneton and Gottlieb, 2012; Dayton et al., 2016b), the latter of which forms the focus of this thesis. Among other effects, these factors upregulate glucose uptake, increase glycolytic flux and/or inhibit OXPHOS through various downstream signalling pathways and hence, drive the Warburg effect.

1.4 PKM2 and its roles in the Warburg effect in proliferative cells

1.4.1 PKM2: an isoform of pyruvate kinase

PKM2 has been shown to promote the Warburg effect in cancer and proliferating cells (Christofk et al., 2008a; Clower et al., 2010; Goldberg and Sharp, 2012; Palsson-McDermott et al., 2015). It is one of four currently known isoforms of PK, a cytoplasmic enzyme that catalyses the final step of glycolysis: the conversion of PEP into pyruvate. The other three isoforms are pyruvate kinase M1 (PKM1), L (PKL) and R (PKR). The *PKLR* gene encodes PKL and PKR under the control of different promoters (Noguchi et al., 1987). PKL is expressed in liver and kidney and PKR in erythrocytes (Imamura and Tanaka, 1972; Imamura et al., 1973). PKM1 is a closely-related alternatively-spliced isoform of PKM2; both are encoded by the *PKM* gene (Noguchi et al., 1986). PKM1 is primarily expressed in muscle tissue, brain, fibroblasts and bladder, while PKM2 is expressed in most cells with the exception of muscle cells (Bluemlein et al., 2011; Imamura and Tanaka, 1972; Tsutsumi et al., 1988) (reviewed in (Luo and Semenza, 2012)).

The *PKM* gene contains 12 exons, with *PKM1* mRNA and *PKM2* mRNA each having 10 common exons (exons 1-8, 11 and 12) and a single mutually-exclusive exon due to alternative splicing: exon 9 for *PKM1* and exon 10 for *PKM2* (Fig. 1.3) (Chaneton and Gottlieb, 2012; Noguchi et al., 1986). Both PKM1 and PKM2 proteins are comprised of 531 amino acids. The mutually-exclusive exons 9 and 10 each encodes 56 amino acids (residues 381-436) with only 22 being variant between the human PKM1 (NCBI Reference Sequence: NP_872270.1) and PKM2 (NCBI Reference Sequence: NP_002645.3) (Noguchi et al., 1986); this results in very similar predicted molecular weights between PKM1 (58.06 kDa) and PKM2 (57.94 kDa) (molecular weights calculated based on reference sequences using an online tool, https://web.expasy.org/protparam/; (Gasteiger et al., 2005)). Similarly, the mouse PKM1 (NCBI Reference Sequence: NP_001240812.1) and PKM2 (NCBI Reference Sequence: NP_035229.2) differ by only 22 amino acids with predicted molecular weights of 57.99 kDa and 57.84 kDa, respectively, and the rat PKM1 (GenBank: AAB93666.1) and PKM2 (GenBank: AAB93667.1) differ by just 21 amino acids with predicted molecular weights of 57.82 kDa and 57.78 kDa, respectively (Gasteiger et al., 2005).

A number of factors have been found to influence the alternative splicing of the *PKM* gene primary RNA transcript. At high concentrations, three heterogeneous nuclear ribonucleoproteins (hnRNPs), hnRNPI, hnRNPA1 and hnRNPA2, commonly upregulated in cancer cells, promote the excision of exon 9 and processing to *PKM2* mRNA (Chen et al., 2012; Clower et al., 2010). At low concentrations, however, these factors inhibit exon 10 inclusion, thereby promoting processing to *PKM1* mRNA (Chen et al., 2012; Clower et al., 2010).

A common perception in the published literature is that in cancer there is a specific switch from PKM1 to PKM2 expression, leaving PKM2 as the predominant PKM isoform which can thus drive the metabolic changes in cancer cells (Chaneton and Gottlieb, 2012). However, this perception is based on studies using antibodies; one such study, for example, used western blotting and showed that several cancer cell lines exclusively expressed PKM2 (Christofk et al., 2008a). However, it should be noted that the antibodies used in these studies have not been well validated for specificity, calling into question some of these findings (reviewed in (Chaneton and Gottlieb, 2012)). Nevertheless, a proteomic study has recently reported that PKM2 predominates over PKM1 in both cancers and normal tissue-matched controls and that, in fact, expression of both PKM1 and PKM2 are increased in cancer (Bluemlein et al., 2011).

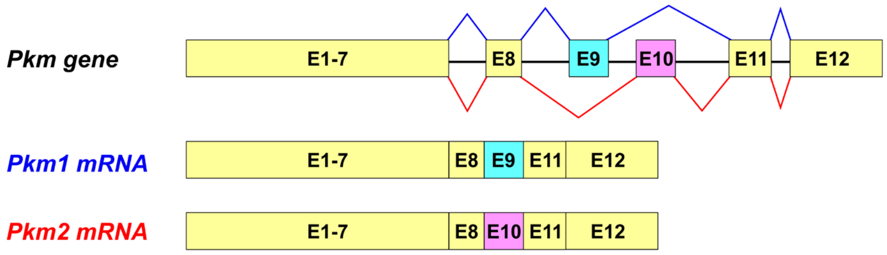

Figure 1.3. Alternative splicing of the *PKM* gene. Pyruvate kinase M1 (PKM1) and pyruvate kinase M2 (PKM2) are both encoded by the *PKM* gene. *PKM1* mRNA and *PKM2* mRNA have 10 common exons and a mutually-exclusive exon due to alternative splicing: exon 9 for PKM1 and exon 10 for PKM2. E, exon. Based on (Chaneton and Gottlieb, 2012).

1.4.2 PKM2 and the Warburg effect

A variety of studies support a specific role for PKM2 in the Warburg effect. Firstly, PKM2-specific knockdown (KD) by small interfering RNA (siRNA) decreased lactate production by approximately two-fold in the human colorectal carcinoma cell line HCT116, indicating that a decrease in PKM2 protein levels results in a decrease in the Warburg effect (Goldberg and Sharp, 2012). Secondly, shRNA-mediated PKM2 KD in human lung carcinoma H1299 cells led to a decrease in glucose consumption and lactate production (Siddiqui et al., 2018). Thirdly, in two human lung carcinoma lines, H1299 and A549, and a human renal cell carcinoma line, SN12C, PKM2 deficient cells rescued with mouse PKM2 exhibited a lower oxygen consumption and a higher lactate production (hence an increase in the Warburg effect) compared with cells rescued with mouse PKM1 (Christofk et al., 2008a). This adds support to the idea that PKM2, but not PKM1, is involved in the regulation of the Warburg effect. Fourthly, in the glioblastoma cell line A-172 KD of hnRNPI, or the combined KD of hnRNPA1 and hnRNPA2, which promote the alternative splicing to *PKM1* mRNA thereby decreasing PKM2 protein levels, also decreased lactate production (Clower et al., 2010). Finally, PKM2 isoform-specific deletion reduced aerobic glycolysis in macrophages activated by lipopolysaccharide (LPS) (Palsson-McDermott et al., 2015), demonstrating a specific role of PKM2 in the Warburg effect in a non-cancerous context.

PKM2 expression in cancer has also been implicated in cellular proliferation and tumourigenesis. However there are conflicting data; some studies have reported that PKM2 is important for cancer cell proliferation and viability (Christofk et al., 2008a; Goldberg and Sharp, 2012; Siddiqui et al., 2018), while others have shown that it is not essential (Dayton et al., 2016a; Israelsen et al., 2013). Nevertheless, unlike these conflicting roles of PKM2 in cellular proliferation, most data support the involvement of PKM2 in promoting the Warburg effect.

1.4.3 Allosteric regulation of PKM2 and glucose metabolism

Unlike PKM1, which only exists as a constitutively high-activity tetramer, PKM2 has been reported to exist as both a high-activity tetramer and a low-activity monomer or dimer (Fig. 1.4) (Ashizawa et al., 1991; Wang et al., 2014) (reviewed in (Chaneton and Gottlieb, 2012; Dayton et al., 2016b)).

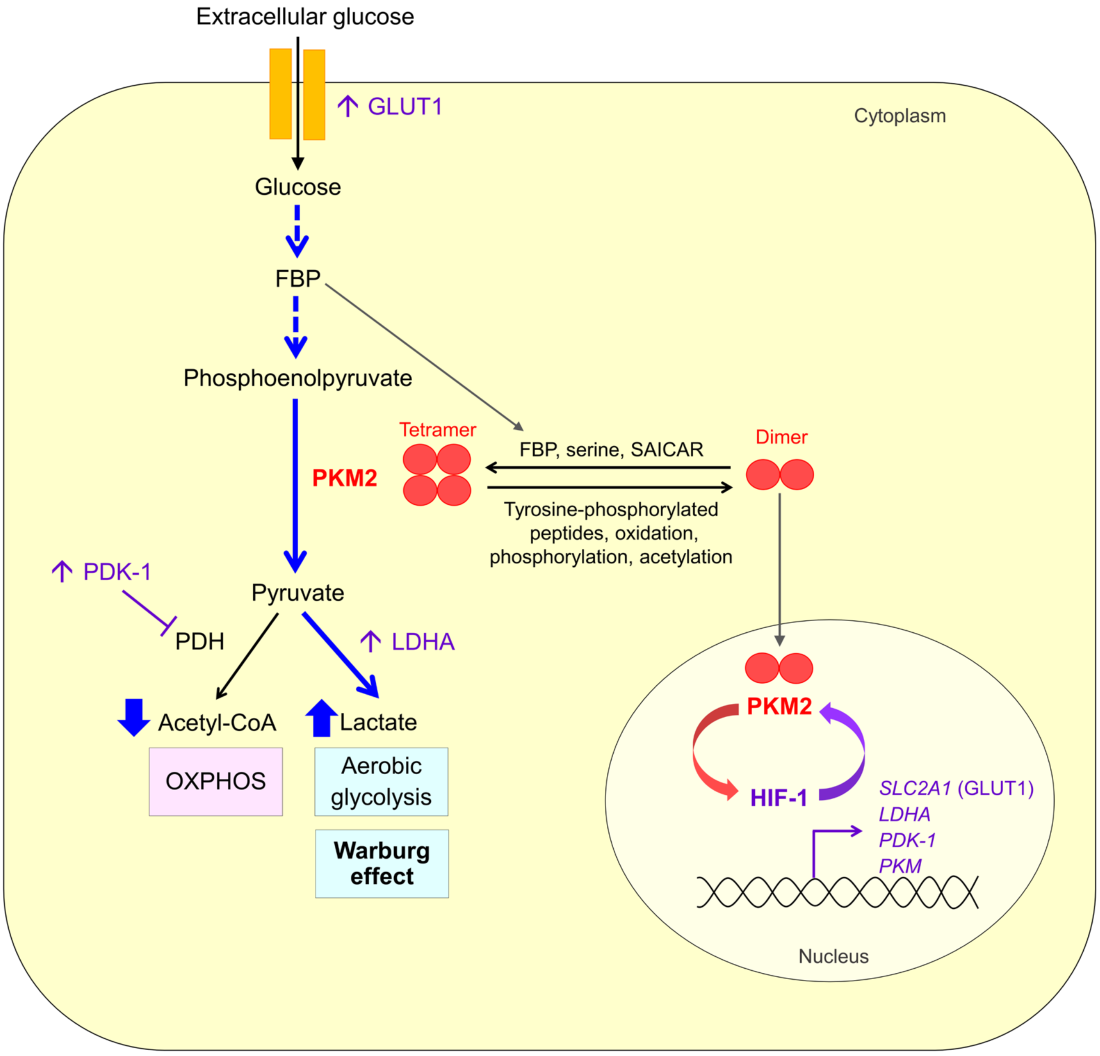

Figure 1.4. Role of PKM2 in the Warburg effect in cancer cells. PKM2 exists in two forms: an enzymatically active tetramer and a less active dimer. The upstream glycolytic intermediate fructose 1,6-bisphosphate (FBP), serine and succinylaminoimidazolecarboxamide ribose-5′-phosphate (SAICAR) promote formation of the active tetramer PKM2, whereas tyrosine-phosphorylated polypeptides and post-translational modifications of PKM2 (oxidation, phosphorylation and acetylation) favour the formation of the less active dimer. The dimeric form of PKM2 can act as a coactivator of the transcription factor hypoxia-inducible factor-1 (HIF-1) in the nucleus, leading to an increased expression of HIF-1 target genes, many of which are involved in promoting glycolytic metabolism including *SLC2A1* (the gene encoding glucose transporter 1, GLUT1), *LDHA* (lactate dehydrogenase A) and *PDK-1* (pyruvate dehydrogenase kinase-1). *PKM*, which encodes PKM2, is also a target gene of HIF-1.

The tetrameric form is more enzymatically active as it has a higher affinity for its substrate, PEP. Thus, the tetrameric form favours the conversion of PEP into pyruvate. The monomeric or dimeric form has a lower affinity for PEP and is less active, leading to the accumulation of upstream glycolytic intermediates. Hence the low-activity form of PKM2 has been proposed to promote diversion of such intermediates to biosynthetic pathways, leading to the production of biomolecules for cellular proliferation (Chaneton and Gottlieb, 2012; Dayton et al., 2016b; Luo and Semenza, 2012). Thus it has been hypothesised that, being able to alternate between the high-activity tetrameric and the low-activity monomeric/dimeric forms, PKM2 regulates whether the cells convert glucose into pyruvate for energy production or use glucose for biosynthesis (Mazurek, 2011).

The switch between the active tetrameric and the less active monomeric or dimeric forms of PKM2 is controlled by several factors. The upstream glycolytic intermediate fructose 1,6-bisphosphate (FBP) (Fig. 1.4) can bind to PKM2 and this promotes tetramer formation, thereby increasing PKM2 enzymatic activity (Bailey et al., 1968). This event is unique to PKM2 and not PKM1, as the 22 amino acid residues in PKM2 that are different from PKM1 form a binding pocket for FBP (Dombrauckas et al., 2005; Noguchi et al., 1986), enabling PKM2 allosteric regulation. Serine and succinyl-aminoimidazolecarboxamide ribose-5′-phosphate (SAICAR), an intermediate of the *de novo* purine nucleotide synthetic pathway, also increase PKM2 enzymatic activity (Fig. 1.4) (Chaneton et al., 2012; Keller et al., 2012; Morgan et al., 2013). On the other hand, a number of mechanisms have been shown to decrease PKM2 activity. Tyrosine-phosphorylated polypeptides associated with receptor tyrosine kinase signalling, when bound to PKM2 release FBP, promote dimeric formation and inhibit PKM2 enzymatic activity (Fig. 1.4) (Christofk et al., 2008b). In addition, PKM2 activity is controlled by post-translational modifications; phosphorylation of tyrosine residue 105 of PKM2 by fibroblast growth factor receptor type 1 (FGFR1), oxidation of cysteine residue 358 induced by intracellular reactive oxygen species (ROS), and acetylation of lysine residue 305 under high glucose concentration reduce PKM2 enzymatic activity (Fig. 1.4) (Anastasiou et al., 2011; Hitosugi et al., 2009; Lv et al., 2011). These mechanisms implicate PKM2 in regulating cellular metabolic responses to growth factor signalling, oxidative stress and nutrient conditions. The ability of PKM2 to be differentially regulated to switch between quaternary structures, with different enzymatic activities, and thereby influence the fate of glucose within cells implicates it in control of cellular metabolism.

However, it is not clear how the enzymatic function of PKM2 can favour the conversion of pyruvate to lactate and promote the Warburg effect.

1.4.4 Non-enzymatic functions of PKM2

In addition to its enzymatic role in the glycolytic pathway in the cytosol, the dimeric form of PKM2 has been found in the nucleus where it has been shown to have additional functions (Gao et al., 2012). PKM2 can act as a protein kinase leading to histone and other protein modifications, events which can also influence cancer proliferation (Yang et al., 2012). More importantly in terms of metabolic regulation, dimeric PKM2 can also enhance activities of transcription factors including β-catenin (Yang et al., 2011) and HIF-1 (Fig. 1.4) (Luo et al., 2011).

HIF-1 is a heterodimeric transcription factor that is vital for regulating various cellular responses to hypoxia; it consists of an oxygen-regulated HIF-1α subunit and a constitutive HIF-1β subunit, also known as ARNT (Semenza and Wang, 1992; Wang et al., 1995). Under conditions of physiological oxygen levels (normoxia), HIF-1α is efficiently hydroxylated by prolyl hydroxylases (PHDs), which have three isoforms (PHD 1-3), and also by an asparaginyl hydroxylase known as factor inhibiting HIF or FIH, leading to inactivation of HIF-1 (Epstein et al., 2001; Lando et al., 2002a; Lando et al., 2002b). This occurs because when hydroxylated by PHDs, HIF-1α is targeted for ubiquitination by the von Hippel-Lindau protein (pVHL) and subsequently for rapid proteosomal degradation. Furthermore, hydroxylation of HIF-1α by FIH prevents the interaction of the HIF-1α C-terminal transactivation domain with the coactivators CBP and p300 and therefore inhibits its transcriptional activity. When oxygen is below physiological levels (hypoxia), the activities of the PHDs and FIH are reduced as they are oxygen-dependent; thus HIF-1α avoids hydroxylation and becomes stabilised and active. It translocates to the nucleus and dimerises with HIF-1β, forming the HIF-1 complex which can bind to hypoxia response elements (HREs) in the regulatory regions of target genes to induce gene expression (Chilov et al., 1999).

HIF-1 has also been implicated in driving the Warburg effect in cancer (Semenza, 2012). Among the large set of HIF-1 target genes (approximately 200), many are involved in energy metabolism, including the genes encoding glucose transporter 1 (GLUT1), LDHA and pyruvate dehydrogenase kinase-1 (PDK-1), as well as key enzymes in the glycolytic pathway (Goda and Kanai, 2012; Hu et al., 2003). The upregulation of GLUT1, LDHA and PDK-1 by HIF-1 results in the increased cellular uptake of glucose, the increased production of lactate and the inactivation of PDH leading to a decrease in acetyl CoA formation, respectively. Ultimately, the induction of these and other HIF-1 target genes promotes the upregulation of glycolysis and the inhibition of OXPHOS. This, and the observation that HIF-1α is active in many cancer cells, due to hypoxic conditions in tumours or genetic abnormalities independent of oxygen availability (Ke and Costa, 2006; Zhong et al., 1999), implicates HIF-1 activity in cancer metabolism and, importantly, the Warburg effect.

There are a number of functional connections between PKM2 and HIF-1, with important implications for regulating the Warburg effect. Firstly, studies have shown that the *PKM* gene, which encodes PKM1 and PKM2, is a direct target gene of HIF-1 (Fig. 1.4) (Luo et al., 2011; Semenza et al., 1994). More relevantly, it has been shown that PKM2 can act as a coactivator of HIF-1α to increase target gene induction in the HeLa cervical cancer cell line and the Hep3B hepatoblastoma cell line. Specifically, PKM2 enhances HIF-1 binding and p300 recruitment to HREs of HIF-1 target genes, resulting in increased transactivation of target genes, including those that upregulate glycolysis (Fig. 1.4) (Luo et al., 2011). In HeLa cells, PKM2 KD mediated by short hairpin RNA (shRNA) reduced expression of the HIF-1 target genes *SLC2A1* (the gene encoding GLUT1), *LDHA* and *PDK1* (Luo et al., 2011). This regulation is specific for PKM2, as the PKM1 isoform cannot regulate HIF-1 activity (Luo et al., 2011).

In addition, PKM2 can interact directly with PHD3, one of the HIF prolyl hydroxylases. The interaction between PKM2 and PHD3 results in both increased PKM2 binding to HIF-1α and PKM2 coactivator activity (Luo et al., 2011). In RCC4 cells, a VHL-deficient renal cell carcinoma line in which HIF-1 is constitutively expressed and active (Maxwell et al., 1999), PHD3 KD decreased glucose uptake, glycolytic flux and lactate production whilst increasing oxygen consumption in normoxia (Luo et al., 2011), which further supports a stabilisation-independent role for PHD3 in regulating HIF-1, mediated by PKM2. The interaction of HIF-1 and PKM2 has also been reported in macrophages activated by

LPS, and cells with PKM2 deletion exhibited a decreased expression of HIF-1α target genes (Palsson-McDermott et al., 2015).

Hence the interaction of PKM2 with HIF-1 may explain a putative mechanism by which PKM2 can drive the Warburg effect in cancer, where PKM2 not only controls the production of pyruvate by its enzymatic function, but also the fate of pyruvate through regulation of lactate production and OXPHOS mediated by HIF-1 (Fig. 1.4).

1.5 Retina

Although it is not a proliferating tissue, the mammalian retina also displays the Warburg effect (reviewed in Paper 1 (Ng et al., 2015) (Appendix 7.1)) (Lindsay et al., 2014; Tornquist and Alm, 1979; Winkler, 1995; Winkler et al., 2000).

The eye is generally considered to be comprised of three distinct layers: the outer protective layer consisting of sclera and cornea, the middle vascular layer containing choroid, ciliary body and iris, and the innermost layer, the retina (Barrett et al., 2012; Kolb, 1995b; Mescher, 2010) (Fig. 1.5A). The retina is a complex tissue containing a number of prominent cell types: retinal neurons, including the light-sensing photoreceptors, bipolar cells, ganglion cells, amacrine cells and horizontal cells, and glial cells such as MCs (Barrett et al., 2012) (Fig. 1.5B). There are two types of photoreceptors, rods and cones (Fig.1.5B and C). Rod cells, being highly sensitive, are used for vision under low light conditions, while cones are responsible for colour perception (Kolb, 1995a). A photoreceptor consists of the synaptic terminal zone, the cell body containing the nucleus, the inner segment containing mitochondria, and the constantly-renewed outer segment which contains visual pigments and is connected to the inner segment by the cilium (Barrett et al., 2012; Bibliowicz et al., 2011) (Fig. 1.5C). Photoreceptors, bipolar cells, ganglion cells, amacrine cells and horizontal cells form distinct and specialised classes of retinal neurons. MCs comprise the major type of glial cell in the retina and are generally thought to provide functional and structural support for all retinal neurons (reviewed in Paper 4 (Kittipassorn et al., 2019a) in Chapter 3, (Bringmann et al., 2006; Vecino et al., 2016)).

The retinal cells are organised into three distinct cellular layers, the outer nuclear layer (ONL), the inner nuclear layer (INL) and the ganglion cell layer (GCL), which are separated by two layers of synapses, the outer plexiform layer (OPL) and the inner plexiform layer (IPL) (Kolb, 1995b) (Fig. 1.5B). Among the three cellular layers, the ONL is the nearest to the choroid (the farthest from the vitreous cavity) and the GCL is the closest to the vitreous humour (Fig. 1.5B). The ONL contains rod and cone photoreceptor cell bodies, the INL contains perikarya of bipolar cells, horizontal cells, amacrine cells and MCs, and the GCL contains ganglion cells and some displaced amacrine cells (Barrett et al., 2012; Kolb, 1995b) (Fig. 1.5B). Separating these cellular layers are the two layers of synapses, the OPL and the IPL (Barrett et al., 2012). In the OPL, the layer of synapses between the ONL and the INL, horizontal cells form lateral connections among photoreceptors (Barrett et al., 2012) (Fig. 1.5B). In the INL, the layer of synapses between the INL and the GCL, amacrine cells make connections among ganglion cells and bipolar cells (Barrett et al., 2012) (Fig. 1.5B). Of note, while MC bodies are in the INL, their processes span the entire retina (Fig. 1.5B), providing the retinal neurons with a supporting framework (Mescher, 2010). Moreover, the end feet of MCs form the inner limiting membrane, the boundary between the retina and the vitreous (Fig. 1.5B) (Barrett et al., 2012). The outer limiting membrane separates the inner segment of photoreceptors from their cell bodies, and the retinal pigment epithelium (RPE), the layer adjacent to the choroid, comprises cells which surround and support the outer segments of retinal photoreceptors (Fig. 1.5B).

Rod and cone photoreceptors detect light and convert it into electrical signals, via an elaborate intracellular signalling cascade (Kolb, 1995a). These electrical signals are sent via bipolar cells to ganglion cells, whose axons form the nerve fibre layer and the optic nerve, transporting the signals to the brain (Barrett et al., 2012).

Figure 1.5

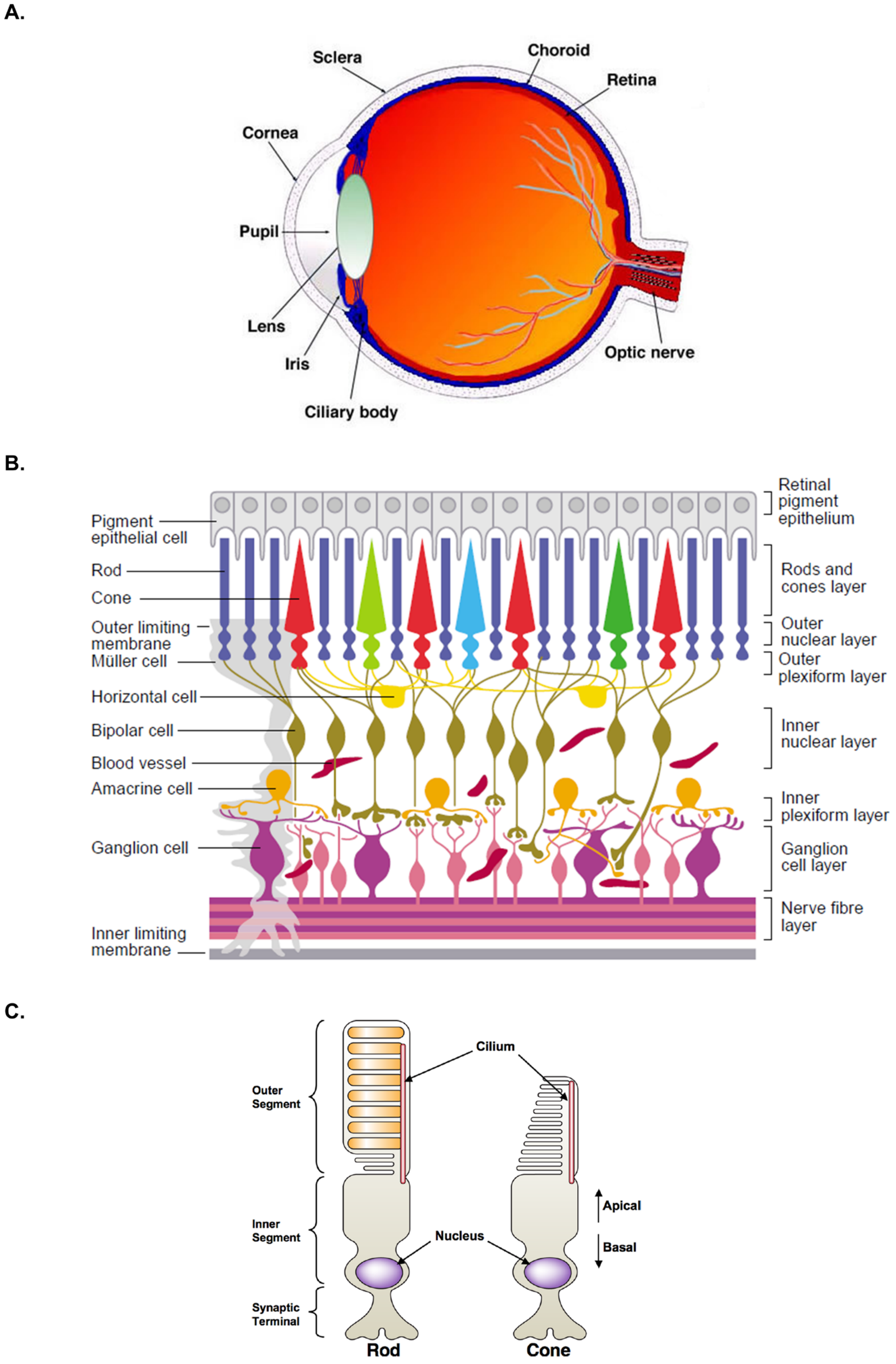
A.
Sclera
Choroid
Retina
Cornea
Pupil
Lens
Iris
Ciliary body
Optic nerve
B.
Pigment epithelial cell
Rod
Cone
Outer limiting membrane
Müller cell
Horizontal cell
Bipolar cell
Blood vessel
Amacrine cell
Ganglion cell
Inner limiting membrane
Retinal pigment epithelium
Rods and cones layer
Outer nuclear layer
Outer plexiform layer
Inner nuclear layer
Inner plexiform layer
Ganglion cell layer
Nerve fibre layer
C.
Outer Segment
Inner Segment
Synaptic Terminal
Cilium
Nucleus
Apical
Basal
Rod
Cone

Figure 1.5. The eye and the retina. (A) A diagram of the mammalian eye. Modified (This is a part of the original figure; the original also contains a schematic enlargement of the retina, which is omitted here.) from (Kolb, 1995b) (http://webvision.med.utah.edu/) for academic purposes under an Attribution, Noncommercial 4.0 International (CC BY-NC) Creative Commons license (https://creativecommons.org/licenses/by-nc/4.0/legalcode). **(B)** The organisation of the retina. Note that light enters through the inner limiting membrane. Reproduced with permission from Wilkinson-Berka, J.L (2004), Diabetes and retinal vascular disorders: role of the renin-angiotensin system, Expert reviews in molecular medicine, Volume 6, Issue 15, Pages 1-18. (Wilkinson-Berka, 2004). **(C)** Rod and cone photoreceptor structure, with light entering basally. Reprinted from Progress in Molecular Biology and Translational Science, Volume 100, Bibliowicz, J., Tittle, R.K., and Gross, J.M., Toward a better understanding of human eye disease insights from the zebrafish, Danio rerio, Pages No. 287-330, Copyright (2011), with permission from Elsevier. (Bibliowicz et al., 2011).

1.6 Retinal metabolism

Unlike most other tissues, which primarily rely on OXPHOS to meet their energy demands, the non-proliferative mammalian retina, specifically the photoreceptors and MCs, display the Warburg effect (reviewed in Paper 1 (Ng et al., 2015)) (Cohen and Noell, 1960; Poitry-Yamate et al., 1995; Tornquist and Alm, 1979; Warburg, 1925; Warburg et al., 1924; Warburg et al., 1930; Winkler, 1981, 1995; Winkler et al., 2000; Winkler et al., 2003). This distinct metabolism of the retina is surprisingly similar to cancer and other proliferating cells, and renders the retina one of the very few non-proliferative cells and tissues that exhibit the Warburg effect, others of which include Sertoli cells in the testis (Oliveira et al., 2015).

It is not certain why the Warburg effect exists in the retina (Paper 1 (Ng et al., 2015) (Appendix 7.1)). It has been postulated that retinal tissue, specifically the photoreceptors, has similar metabolic requirements to those of proliferating cells (Casson et al., 2012) possibly because of a high turnover rate of photoreceptor outer segments (Young, 1967). However, this “biosynthesis hypothesis” suffers the same stoichiometric flaw as it does in cancer. Alternatively, photoreceptors are highly energy demanding (Okawa et al., 2008) and may rely on the Warburg effect for rapid ATP production. Regarding MCs, it has been postulated that they may rely on aerobic glycolysis to produce lactate to supply to neurons (Bringmann et al., 2006; Poitry-Yamate et al., 1995). On the other hand, Winkler and colleagues reported that retinal neurons mainly utilise glucose and not lactate (Winkler et al., 2004), and Lindsay et al. proposed that MCs use photoreceptor-derived lactate as a substrate to produce energy (Lindsay et al., 2014). With these conflicting data, this matter requires further investigation.

Furthermore, and importantly, in contrast to cancer and other proliferating cells, little was known about the molecular drivers of the Warburg effect in the retina, which led to the work presented in this thesis.

1.7 Background summary and project rationale

In summary, cancer cells (Hsu and Sabatini, 2008; Koppenol et al., 2011; Vander Heiden et al., 2009; Warburg, 1956; Warburg et al., 1927) and the mammalian retina (reviewed in Paper 1 (Ng et al., 2015)) (Cohen and Noell, 1960; Poitry-Yamate et al., 1995; Tornquist and Alm, 1979; Warburg, 1925; Winkler, 1981, 1995; Winkler et al., 2000; Winkler et al., 2003) both display the Warburg effect. The reason for this unusual type of metabolism in the retina is unclear but may emulate the same teleology as cancer. (Casson et al., 2012; Ng et al., 2015). Various factors driving the Warburg effect in cancer cells have been characterised but not much is known about such factors in the retina.

We hypothesised that the mechanisms that drive the Warburg effect in the retina and proliferating cells such as cancer cells are conserved. More specifically, a number of studies support PKM2 as a driver of the Warburg effect in cancer cells (Christofk et al., 2008a; Clower et al., 2010; Goldberg and Sharp, 2012; Siddiqui et al., 2018), and PKM2 is known to be expressed in the mammalian retina (Morohoshi et al., 2012). The findings led to the central hypothesis of this thesis, that PKM2 drives the Warburg effect in MCs. The studies herein were undertaken to investigate whether PKM2 played a role in establishing and maintaining the Warburg effect in the mammalian retina in a similar manner to cancer cells.

The retina is critical for vision, and retinal diseases commonly cause blindness. In addition, the retina has large energy requirements, and impaired energy metabolism plays a potential pathogenic role in a number of diseases (Bringmann et al., 2006; Hartong et al., 2008). It is, therefore, crucial to characterise the molecular factors and mechanisms by which retinal energy metabolism, specifically the Warburg effect, is driven. Understanding this phenomenon could potentially lead to new therapeutic strategies for retinal diseases. Furthermore, if the mechanisms driving the Warburg effect in cancer cells and the retina are conserved, novel drugs that target regulators of the Warburg effect in cancer (Tennant et al., 2010; Vander Heiden et al., 2010a; Yu et al., 2016) could adversely affect the retina (Ng et al., 2015).

It has been well established that cultured MCs from mammalian retinas display a strong Warburg effect as shown in freshly-isolated guinea pig MCs (Poitry-Yamate et al., 1995), primary human MCs (Winkler et al., 2000) and the immortalised rMC-1 rat MC line (Winkler et al., 2003). Moreover, MCs can be easily cultured and used to determine aspects of retinal function and metabolism (Limb et al., 2002; Sarthy, 1985; Sarthy et al., 1998; Savage et al., 1988). In practical terms, the laboratory of the candidate's co-supervisor, Robert Casson (Department of Ophthalmology and Visual Sciences, Adelaide Medical School, University of Adelaide, Adelaide, SA, Australia), routinely utilise rat retinas for the generation and maintenance of primary retinal cultures, containing both neurons and glial cells (Wood et al., 2005; Wood et al., 2003). In contrast to photoreceptor cells, cultured primary rat MCs can easily be generated from these primary retinal cultures (Sarthy, 1985; Wood et al., 2005), which we have also demonstrated and utilised previously (Honours thesis (Kittipassorn, 2013)). Furthermore, cultured primary rat MCs were shown to express PKM2, by using a well-characterised antibody (Paper 2 (Casson et al., 2016) in Appendix 7.2), in the candidate's Honours thesis (Kittipassorn, 2013). Thus, cultured primary rat MCs were chosen as a model to study the Warburg effect in the mammalian retina in this PhD project.

A well-established SV40-transformed rat MC line rMC-1 (Sarthy et al., 1998) and a novel spontaneously immortalised rat MC line SIRMu-1 (Paper 4 (Kittipassorn et al., 2019a) in Chapter 3), which was generated during the course of this thesis, were also used to complement the experiments on primary MCs.

1.8 Hypotheses and aims

Hypotheses

1. The SIRMu-1 cell line originated from primary MCs
2. Cultured rat MCs display the Warburg effect
3. PKM2 drives the Warburg effect in cultured MCs.

Aims

1. To establish and characterise a novel spontaneously immortalised rat MC line SIRMu-1 (Chapter 3)
2. To determine whether cultured rat MCs display the Warburg effect (Chapter 4)
    2.1. To develop and optimise techniques for metabolic analysis
    2.2. To characterise metabolism of glucose in cultured primary rat MCs
    2.3. To characterise metabolism of glucose in the SV40-transformed rat MC line rMC-1 and the spontaneously immortalised rat MC line SIRMu-1 compared to primary MCs
3. To investigate whether PKM2 drives the Warburg effect in MCs (Chapter 5)
    3.1. To study the effect of PKM2 KD on the metabolism of glucose in MCs
    3.2. To study the effect of PKM2 KO on the metabolism of glucose in MCs

1.9 Experimental approach

Experiments were performed on cultured rat primary MCs, the SV40-immortalised rat MC line rMC-1 (Sarthy et al., 1998) and a novel spontaneously immortalised rat MC line SIRMu-1, derived by the candidate (Paper 4 (Kittipassorn et al., 2019a)).

Aim 1: To establish and characterise a novel spontaneously immortalised rat MC line SIRMu-1

During the course of studying retinal metabolism using primary MCs, a population of immortalised rat MCs spontaneously arose. A monoclonal line of these novel cells was isolated by single cell isolation by serial dilution and named SIRMu-1 (spontaneously immortalized rat Muller cell line). To determine if the SIRMu-1 cells retained the properties of primary MCs, expression of MC marker proteins was characterised by immunofluorescence and western blotting, and expression of MC marker mRNA by RNA sequencing (RNA-seq). RNA-seq data were also used to study the overall transcriptome of SIRMu-1 cells. In addition, transfection efficiency was determined by transfecting the cells with a fluorescence protein-encoding plasmid using various commercially-available transfection reagents. All experiments were also performed on primary MCs and/or the rMC-1 cell line for comparisons.

Aim 2: To characterise MC glucose metabolism

Aim 2.1. To develop and optimise metabolic analysis techniques

Experimental techniques to investigate cellular metabolism had never been performed in the candidate's laboratories before. Therefore, assays performed using a Seahorse extracellular flux analyser (Agilent Technologies) were developed and optimised in order to measure cellular oxygen consumption and extracellular acidification, which are a common indicator of OXPHOS and glycolysis, respectively.

Aim 2.2. To characterise metabolism of glucose in cultured primary rat MCs

Primary rat MCs grown in culture medium with glucose as a sole substrate for energy production were subjected to metabolic analysis by lactate assays and a Seahorse extracellular flux analyser. These analyses were carried out to characterise glucose metabolism of these cells and to determine whether they displayed the Warburg effect. Lactate assays measured the levels of lactate released in culture medium, and the Seahorse analyser measured oxygen consumption (representing OXPHOS) and extracellular acidification (commonly representing glycolysis); this allowed us to determine whether the cells investigated were primarily oxidative or glycolytic, the latter of which would be cells that were exhibiting the Warburg effect.

Aim 2.3. To characterise metabolism of glucose in the SV40-transformed rat MC line rMC-1 and the spontaneously immortalised rat MC line SIRMu-1 compared to primary MCs

rMC-1 and SIRMu-1 cells were subjected to the same metabolic analysis as primary MCs described in Aim 2.2 and the results compared.

Aim 3: To investigate whether PKM2 drives the Warburg effect in MCs

In order to study the role of PKM2 in MC metabolism, these cells were modified to have a partial or a complete loss of PKM2 protein before cellular glucose metabolism was analysed. If PKM2 served as an important driver of the Warburg effect in MCs, a decreased PKM2 level and/or the absence of PKM2 should result in a significantly reduced glycolytic activity of the cells, indicative of a decrease in the Warburg effect.

Aim 3.1. To study the effect of PKM2 knockdown on the metabolism of glucose in MCs

PKM2 was knocked down in MCs using shRNAs that specifically targeted this protein and not the closely-related isoform PKM1. The shRNAs were introduced into the cells by a lentiviral-based system. KD was verified by determining the changes in PKM2 protein level. MCs in which PKM2 had been knocked down were then subjected to metabolic analyses in the presence of glucose.

Aim 3.2. To study the effect of PKM2 knockout on the metabolism of glucose in MCs

MCs with a complete loss of PKM2 were generated by using clustered regularly interspaced short palindromic repeats (CRISPR)/CRISPR associated protein 9 (Cas9) genome editing technology to remove exon 10 from the *PKM* gene, thereby knocking out PKM2 without knocking out PKM1. The KO cells were verified by PCR, DNA sequencing and western blotting. MCs where PKM2 had been knocked out were then subjected to metabolic analyses in the presence of glucose in a similar manner to the cells where PKM2 had been knocked down.

Chapter 2

Materials and methods

CHAPTER 2: Materials and methods

This chapter covers materials and methods for Aim 2 (to determine whether cultured rat MCs display the Warburg effect; Chapter 4) and Aim 3 (to investigate whether PKM2 drives the Warburg effect in MCs; Chapter 5) of the thesis. Materials and methods for Aim 1 (to establish and characterise a novel spontaneously immortalised rat MC line SIRMu-1) are described in Paper 4 (Kittipassorn et al., 2019a) and Paper 5 (Kittipassorn et al., 2019b) in Chapter 3.

2.1 Mammalian cell cultures and techniques

2.1.1 Primary cultures and cell lines

Cells used in this thesis and their sources are described in table 2.1

Table 2.1. Primary cultures and immortalised cell lines used in this thesis

Primary (1°) culture/cell line	Source
1° rat mixed retinal cultures	Gifts from Dr John Wood and Teresa Mammone, Laboratory of Professor Robert Casson*
1° rat Müller cell (MC) cultures	Derived from 1° rat mixed retinal culture by the candidate
rMC-1 rat MC line	A gift of Dr Vijay Sarthy#, obtained from Dr Binoy Appukuttan†
SIRMu-1 rat MC line	Generated during the course of this thesis
1° mouse embryonic fibroblasts (MEFs)	A gift from Alexis Gerassimou, Laboratory of Professor Murray Whitelaw*
HeLa human cervical cancer cell line	A gift from Dr Jane Sibbons, Laboratory of Dr Kirk Jensen* Originally obtained from ATCC (CCL-2)
HEK 293FT human embryonic kidney cell line	A gift from Laboratory of Associate Professor Michael Beard*. Originally obtained from ThermoFisher Scientific (#R70007).

* University of Adelaide, Adelaide, SA, Australia;

Northwestern University, Chicago, IL, USA

† Flinders University, Adelaide, SA, Australia

ATCC, American Type Culture Collection

As an immortalised human cell line used in metabolic experiments in this thesis, HeLa cells were submitted to CellBank Australia (Westmead, NSW, Australia) for human cell line authentication testing. The results were consistent with the cells having correct identity with 96% of alleles identical to HeLa cells from the American Type Culture Collection (ATCC) catalogue (CCL-2) (Appendix 7.4). Primary MCs, rMC-1 cells and SIRMu-1 cells were characterised and authenticated in Paper 4 (Kittipassorn et al., 2019a) in Chapter 3. Primary MEFs and rat mixed retinal cultures were generated directly from animals in the laboratories of the candidate's co-supervisors, Professor Murray Whitelaw and Professor Robert Casson, respectively (University of Adelaide, Adelaide, SA, Australia). HEK 293FT cells were used for lentiviral production.

2.1.2 Generation of primary cultures

Sprague-Dawley rats were used for the generation of primary mixed retinal and MC cultures. Animal handling complied with the Australian Code of Practice for the Care and Use of Animals for Scientific Purposes 2004, and the ARVO Statement for the Use of Animals in Ophthalmic and Vision Research. Primary mixed retinal cultures were generated by Dr John Wood and Teresa Mammone (Laboratory of Professor Robert Casson) as described previously (Wood et al., 2005; Wood et al., 2003) and in Paper 4 (Kittipassorn et al., 2019a) in Chapter 3. Primary MC cultures were derived from primary mixed retinal cultured by the candidate as described previously (Osborne, 1990; Wood et al., 2005) and in Paper 4 (Kittipassorn et al., 2019a) in Chapter 3.

Primary mouse embryonic fibroblasts (MEFs) were isolated from C57BL/6J mice by Alexis Gerassimou (Laboratory of Professor Murray Whitelaw). Embryos were first dissected out from a pregnant mouse at embryonic day 11.5, head and internal organs removed, washed with 1x phosphate-buffered saline (PBS) and incubated in 1 mL of 0.05% trypsin/EDTA/PBS at 37^{o}C for 5 minutes. Next, 3 mL of Dulbecco's Modified Eagle Medium (DMEM, +HEPES, #12430062, Life Technologies Australia, Scoresby, VIC, Australia) containing 10% fetal bovine serum (FBS), 1% penicillin/streptomycin and 2 mM L-glutamine was added, and the embryos in trypsin/medium were centrifuged at 500 rpm for a minute. Trypsin/medium was then removed, and the embryos resuspended in 4 mL fresh medium and dissociated with pipetting. Cells were counted and plated at 2 x 10^6 cells per a 15-cm dish in 25 mL fresh medium.

2.1.3 Culture maintenance

All cells were maintained in growth medium described in table 2.2 (unless otherwise stated) at 37°C and 5% CO_2. Primary mixed retinal cultures were used to generate primary MC cultures as described above and were not passaged. All other cell types were passaged when they reached 80-90% confluency, using trypsinisation with passage ratios and frequencies as described in table 2.2. Firstly, spent medium was aspirated from a culture vessel and cells were washed with 1x PBS and incubated in 0.05% trypsin/EDTA/PBS at 37°C for two to ten minutes before fresh growth medium was added. Cells were then resuspended in trypsin/medium and a proportion of cells according to the passage ratio transferred to a new culture vessel containing appropriate amount of fresh growth medium. Note that DMEM was used in the isolation of MEF as per the protocol described in section 2.1.2, but MEM was used in the maintenance of MEF for metabolic experiments so that it was consistent with primary MCs.

2.1.4 Cryopreservation of cells

Culture medium was aspirated and cells were washed with 1x PBS and incubated in 0.05% trypsin/EDTA/PBS at 37°C for two to ten minutes before fresh growth medium was added. Cells were then resuspended in trypsin/medium and centrifuged at 1400 rpm for 3 minutes before trypsin/medium was aspirated and the cell pellet resuspended in 10% dimethyl sulfoxide (DMSO) in FBS. Next, cell suspension was aliquoted into cryogenic vials. The vials were placed in an isopropanol freezing container which was then placed in a -80°C freezer. The isopropanol freezing container was used to enable a gradual decrease in temperature (approximately -1°C per minute), which is important for cell preservation. Once frozen, the vials were moved to liquid nitrogen storage for long term preservation.

2.1.5 Thawing of cryopreserved cells

A frozen cell vial from a -80°C freezer or liquid nitrogen storage was placed in a 37°C water bath. As soon as the vial was just thawed, cell suspension was transferred to a tube already containing fresh medium which was then centrifuged at 1400 rpm for three minutes. Next, the supernatant was aspirated and the cell pellet resuspended in fresh medium and transferred to a culture vessel.

Table 2.2. Growth medium and passage ratio and frequency

1° culture/cell line	Growth medium	Passage ratio and frequency
1° mixed retinal cultures	MEM, 10-20% FBS, 87 mg/L gentamicin sulfate, 2.2 mg/L amphotericin B, 25 mM glucose, 2 mM L-glutamine	-
1° MCs	MEM, 10-20% FBS, 87 mg/L gentamicin sulfate, 2.2 mg/L amphotericin B, 25 mM glucose, 2 mM L-glutamine	1:2 every 7 days
rMC-1	MEM, 10% FBS, 25 mM glucose, 2 mM L-glutamine	1:10 every 2-3 days
SIRMu-1	MEM, 10-20% FBS, 25 mM glucose, 2 mM L-glutamine	1:3 to 1:5 every 2-4 days
1° MEFs	MEM, 10-20% FBS, 25 mM glucose, 2 mM L-glutamine	1:2 to 1:3 every 7-10 days
HeLa	MEM, 10% FBS, 25 mM glucose, 2 mM L-glutamine	1:10 every 2-3 days
HEK 293FT	DMEM, 25 mM glucose, 10% FBS	1:10 every 2-3 days

1° MEFs, primary mouse embryonic fibroblasts; 1° mixed retinal cultures, primary rat mixed retinal cultures; 1° MCs, primary rat Müller cells; HEK 293FT, human embryonic kidney cell line; HeLa, human cervical cancer cell line; rMC-1, SV40-transformed rat Müller cell line; SIRMu-1, spontaneously immortalised rat Müller cell line; DMEM, Dulbecco's Modified Eagle Medium (DMEM, #12430062, Life Technologies Australia); FBS, fetal bovine serum (heat inactivated); MEM, minimal essential medium, +Earle's Salts, -L-glutamine, #11090, Life Technologies)

2.2 Lactate assay

L-lactate concentration in culture medium was determined using a Lactate Colorimetric Assay Kit II (#K627-100, BioVision, Milpitas, CA, USA) according to the manufacturer’s instructions. Media from wells without cells collected at the same time were used as blank controls. Samples for lactate assays were collected from cell culture plates during the preparation process for Seahorse assays (see section 2.3.1).

2.3 Seahorse extracellular flux assay

2.3.1 Seahorse XF Cell Mito Stress Test protocol

Seahorse XF Cell Mito Stress Tests (#103015-100, Agilent Technologies, Santa Clara, CA, USA) were employed to analyse cellular metabolism. In these tests, oxygen consumption rates (OCRs) and extracellular acidification rates (ECARs) of cells were measured at a basal state and in response to three compounds that were serially injected into wells at specific time points by a Seahorse XFe96 extracellular flux analyser (Agilent Technologies), under the control of the Wave software. The three compounds, in the order of injection, were oligomycin, carbonyl cyanide-4-(trifluoromethoxy) phenylhydrazone (FCCP) and a mix of rotenone and antimycin A (Rot/AA). Assays were performed as per the manufacturer's instructions with modifications described below.

At least 24 hours before cell seeding for Seahorse assays, culture media for all cell types were changed from the usual growth media (Table 2.2) to MEM containing 10% FBS, 5.5 mM glucose and 2 mM L-glutamine. The day before the assay (approximately 16-20 hours before the assay), unless otherwise stated, primary MC (15,000 cells/well), rMC-1 (15,000 cells/well), SIRMu-1 (10,000 cells/well), primary MEF (15,000 cells/well), or HeLa (10,000 cells/well) cells were seeded in MEM containing 10% FBS, 5.5 mM glucose and 2 mM L-glutamine (80 µL per well) in a Seahorse 96-well cell culture plate (pre-coated with 0.2% gelatin in PBS). Wells A1, A12, H1 and H12 were left without cells as blank controls in the Seahorse assay. The cell plate was allowed to rest at room temperature for 45-60 minutes to promote even cell distribution (Lundholt et al., 2003) before it was kept in a humidified, 37^{o}C incubator with 5% CO_2. Sensor probes of a sensor cartridge (#102601-100, Agilent Technologies) were hydrated by submerging and incubating in XF calibrant solution (#100840-000, Agilent Technologies) in a utility plate (200 µL per well) overnight in a humidified, 37^{o}C incubator without CO_2.

On the assay day, unless otherwise specified, assay medium was made up from XF base medium (#102353-100, Agilent Technologies) and glucose (final concentration 10 mM), warmed to 37°C, pH adjusted to 7.35 ± 0.05 with NaOH and sterile filtered. Next, cells were checked under a light microscope, washed one time with assay medium, and incubated in fresh assay medium (100 µL per well) for an hour in a humidified, 37°C incubator with 5% CO_2. The medium of each well was then collected and stored at -80°C for later use in lactate assays (see also section 2.2). Cells were washed again and fresh assay medium added (175 µL per well). Cells were immediately inspected under a light microscope before incubating for approximately 90 minutes in a humidified, 37°C incubator without CO_2.

While the cells were incubating, the three Cell Mito Stress Test compounds were added to designated drug ports of all wells of the sensor cartridge: ports A, oligomycin; ports B, FCCP; ports C, Rot/AA. The final concentrations of each compound, unless otherwise stated, were 2 µM for oligomycin, 0.5 µM for FCCP and 0.5 µM each for Rot/AA. Compound preparation and addition are described in table 2.3. The sensor cartridge was then placed in the Seahorse XFe96 analyser for calibration. Once calibration of the sensors and the required cell incubation had completed, the cell plate was placed in the Seahorse analyser for simultaneous measurements of OCRs and ECARs at basal state and after the addition of oligomycin, FCCP and Rot/AA. Three measurement cycles of mix (three minutes)-wait (none)-measure (three minutes) were carried out during each of the four conditions. Oligomycin, FCCP and Rot/AA were injected at 16, 36 and 56 minutes after the start of the assay, respectively. After the end of each assay, cells were inspected under a light microscope and the number of cells per well determined, using the methods described in section 2.3.2, for normalisation of OCR and ECAR data.

In a number of assays, additional wells were set up to determine buffer factors. A buffer factor (mM/pH) is the amount of H^+ that changes the pH level in the medium by one pH unit as measured in a Seahorse analysis system and can be determined by adding known amounts of H^+ into a well over the course of an assay (instead of the three Cell Mito Stress Test compounds) and measuring changes in ECARs. Buffer factors of the assay medium (XF base medium containing 10 mM glucose) used with the Seahorse XFe96 system in this thesis were determined according to the manufacturer's instructions (Agilent Technologies user guide "Agilent Seahorse XF Buffer Factor Protocol", 2017). Three serial injections of 25 µL of 5 mM HCl were injected into wells containing assay medium without cells instead of oligomycin, FCCP and Rot/AA at the same time points and ECARs measured as above. In the control wells, assay medium was serially injected instead of HCl. Buffer factors were used in the calculation of proton efflux rates (PERs) (see section 2.3.3.3).

Table 2.3. Preparation and addition of Cell Mito Stress Test compounds to drug ports of the sensor cartridge

Injection order and compound	Stock conc. (µM)	Volume (µL) to add to ports	Total volume (µL) per well before and after the addition of compound		Final conc. (µM)
			before	after	
1st - oligo	16	25	175	200	2
2nd - FCCP	4.5	25	200	225	0.5
3rd - Rot/AA	5	25	225	250	0.5

conc., concentration; FCCP, carbonyl cyanide-4-(trifluoromethoxy) phenylhydrazone; oligo, oligomycin; Rot/AA, rotenone and antimycin A.

2.3.2 Cell number determination

The number of cells per well at the end of each Seahorse assay was determined by one of the following three methods. The method used for each assay is specified in figure legends.

Trypsinisation method

Cells in all wells were trypsinised and counted using a hemocytometer or an automated cell counter (TC20™ automated cell counter, Bio-Rad Laboratories, Gladesville, NSW, Australia).

Fluorescence microscopy method

Cells in representative wells (three wells per experimental group) were stained with Hoechst 33342 nuclear stain (NucBlue Live ReadyProbes Reagent, #R37605, Life Technologies Australia) and fluorescence images were taken (one image per well) by a fluorescence microscope (Nikon Eclipse Ti microscope, Nikon Australia). Fiji (a distribution of ImageJ) software (Schindelin et al., 2012) was used to count the number of cells per image and determine the size of the area covered by each image, from which the number of cells per well was derived. Every well was observed under a light microscope to ensure that the cell confluency of all wells in a group was similar and that wells used for cell counting were representative of that group. The average of the number of cells from the three representative wells of each group was used to normalise OCR and ECAR data for all wells of that group.

ArrayScan method

Cells in every well were stained with Hoechst 33342 nuclear stain. Fluorescence images of every well (16 images per well, covering the whole well surface area) were taken automatically by an ArrayScan XTI Live High Content Platform (ThermoFisher Scientific) and the number of cells per well determined using the HCS Studio Cell Analysis software. This enabled the normalisation of OCR and ECAR data from each individual well with the actual cell number of that well. Access to the ArrayScan was gained in September 2018, after which the number of cells per well in all Seahorse assays was determined by this method.

2.3.3 Data analysis

In the Cell Mito Stress Test, OCRs (pmol O_2/min) and ECARs (mpH/min), in the basal state, and in response to the three compounds, are directly measured by the Seahorse analyser. Typical Seahorse Cell Mito Stress Test kinetic profiles for OCAR and ECARs are shown in figure 2.1. The three compounds added during the course of the Cell Mito Stress Test affect cellular metabolism, and consequently OCRs and ECARs.

2.3.3.1 Oxygen consumption rates

OCRs at the first three measurement points before the addition of the compounds are basal OCR (OCR_{basal}). Typically, the injection of the first compound oligomycin, which inhibits ATP synthase (complex V), results in a decrease in OCR (Fig. 2.1B). This decrease (the difference between the OCR_{basal} and the oligomycin-induced OCR (OCR_{oligo})) represents **oxygen consumption that is**

linked to ATP production (Fig. 2.1A, upper panel). The injection of the second compound FCCP, which uncouples oxygen consumption from ATP synthesis by transporting H^+ across mitochondrial inner membrane into the matrix (Fig. 2.1B), results in a maximal increase in OCR which represents maximal respiration rate. The difference between the FCCP-induced OCR (OCR_{FCCP}) and the OCR_{basal} is **spare or reserve respiratory capacity** (Fig. 2.1A, upper panel), and this describes the potential for the mitochondria in a particular cell to be brought to a theoretical maximum. Finally, the third injection comprising Rot/AA, which completely inhibit OXPHOS by inhibiting complexes I and III in the ETC respectively (Fig. 2.1B), leads to a drastic decrease in OCR. Remaining OCR are due to **non-mitochondrial respiration** ($OCR_{non\text{-}mito}$) (Fig. 2.1A, upper panel). The difference between the OCR_{basal} and the $OCR_{non\text{-}mito}$ indicates **basal mitochondrial respiration** (OCR_{mito}) (Fig. 2.1A, upper panel). The difference between the OCR_{FCCP} and the $OCR_{non\text{-}mito}$ indicates **maximal respiration** (Fig. 2.1A, upper panel). Lastly, the difference between the OCR_{oligo} and the $OCR_{non\text{-}mito}$ indicates **proton leak-linked respiration** (Fig. 2.1A, upper panel) which is resulted from ATP synthase-independent proton leakage across the inner mitochondrial membrane (Divakaruni et al., 2014).

2.3.3.2 Extracellular acidification rates

ECARs at the first three measurement points before the addition of the compounds are basal ECARs ($ECAR_{basal}$), representing extracellular acidification in the basal state. Oligomycin, which inhibits ATP synthase, leads to an increase in ECAR, indicating increased glycolytic activity to compensate for the loss of ATP production from the inhibition of OXPHOS. The difference between the $ECAR_{basal}$ and the oligomycin-induced ECAR ($ECAR_{oligo}$) is the **glycolytic reserve** of the cells (Fig. 2.1A, middle panel).

Figure 2.1

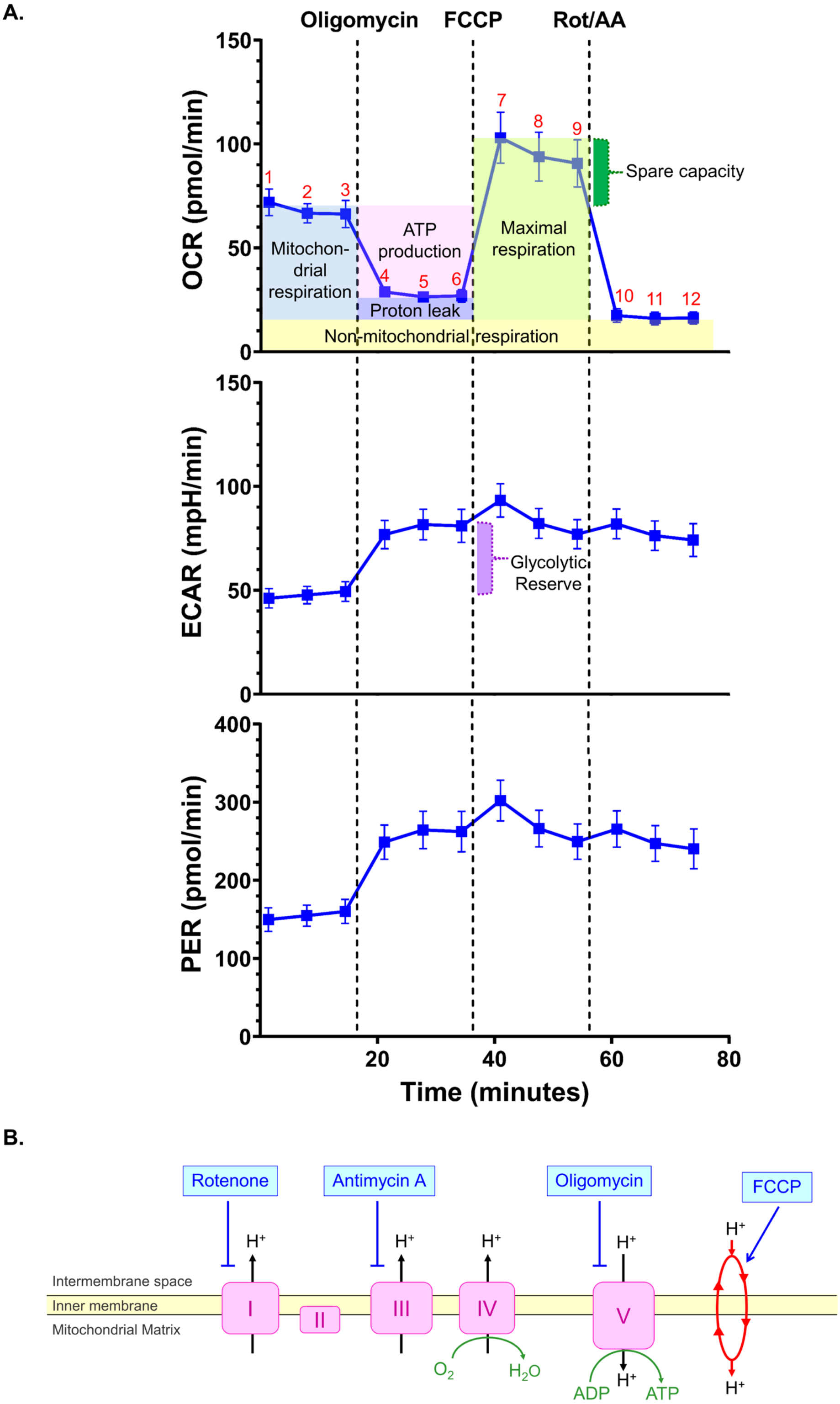
A.
Oligomycin
FCCP
Rot/AA
OCR (pmol/min)
150
100
50
0
1
2
3
4
5
6
7
8
9
10
11
12
Mitochon-drial respiration
ATP production
Proton leak
Maximal respiration
Spare capacity
Non-mitochondrial respiration
ECAR (mpH/min)
150
100
50
0
Glycolytic Reserve
PER (pmol/min)
400
300
200
100
0
20
40
60
80
Time (minutes)
B.
Rotenone
Antimycin A
Oligomycin
FCCP
H+
Intermembrane space
Inner membrane
Mitochondrial Matrix
I
II
III
IV
V
O2
H2O
ADP
ATP

Figure 2.1. Seahorse XF Cell Mito Stress Test. (A) A typical kinetic profile of oxygen consumption rates (OCRs), extracellular acidification rates (ECARs) and proton efflux rates (PERs) from a Cell Mito Stress Test, from which several metabolic parameters can be determined as illustrated. Numbers in red indicate measurement points. **(B)** A schematic diagram of inner mitochondrial membrane showing the targets in the electron transport chain (complexes I-V) of three compounds (oligomycin, carbonyl cyanide-4-(trifluoromethoxy) phenylhydrazone (FCCP) and a mixture of rotenone and antimycin A (Rot/AA)) used in a Cell Mito Stress Test. H^+, proton.

2.3.3.3 Proton efflux rates

ECARs (mpH/min) indicate changes in the pH level in the assay medium and can be converted to absolute changes in H^+, or PERs (pmol H^+/min), using the buffer factor (mM/pH) (see section 2.3.1). Changes in ECARs after the serial addition of 25 µL of 5 mM HCl or assay medium, performed as described above, were used to calculate the buffer factor, using the Seahorse XF Buffer Factor Calculator Excel Spreadsheet designed by the manufacturer. The calculated buffer factor was then input into the Wave software which automatically calculated and reported PER, based on the calculations as described by the manufacturer (Agilent Technologies user guide "Improving Quantification of Cellular Glycolytic Rate Using Agilent Seahorse XF Technology", 2017). An example kinetic profile of PERs is shown is figure 2.1. In this thesis, not including optimisation experiments, nine independent Seahorse assays were performed: three assays of MC, MEF and HeLa cell metabolic characterisation (Chapter 4), three assays on rMC-1 cells with PKM2 knocked down (Chapter 5), and three assays on rMC-1 cells with PKM2 knocked out (Chapter 5). Buffer factors were determined in the same assay trays as two of the nine Seahorse assays, the rMC-1 PKM2 KO Seahorse assay number 1 and the rMC-1 PKM2 KO Seahorse assay number 3, resulting in a buffer factor of 0.94 mM/pH and 0.84 mM/pH, respectively. Each value was used for data analysis of the corresponding Seahorse assays. The average of the two values (0.89) was used for data analysis of all other assays.

2.3.3.4 Generation of kinetic graphs and calculation of metabolic parameters

In Seahorse assays, each experimental group was performed in a number of technical replicate wells (numbers of replicate wells in each assay are indicated in figure legends). Due to occasional issues with incomplete drug injection by the analyser, loss of cells during washing, or bacterial contamination, individual wells that were outliers were excluded from analysis. Outliers were defined as individual wells that displayed an atypical profile in a group that displayed a uniform kinetic profile, wells that displayed OCRs or ECARs greater than five-fold different than the mean, wells with negative OCR or ECAR level at the basal state or after the oligomycin injection or after the FCCP injection, wells with obvious bacterial contamination, or wells that had major differences in cell confluency compared to the representative wells used for cell number determination (for the assays whose cell numbers were determined by the Fluorescence microscopy method).

In kinetic graphs of OCRs, ECARs and PERs shown in this thesis, data are presented as mean ± SD of each measurement point across replicate wells. Graphs were generated by GraphPad Prism Version 8.0.0, using OCR, ECAR and PER data exported from the Wave software result files.

In addition to kinetic graphs, a number of metabolic parameters can be derived from OCR, ECAR and PER data in the basal state and/or in response to oligomycin, FCCP, Rot/AA, measured by the Seahorse analyser. Calculations of parameters pertinent to this thesis are listed below. These were performed based on manufacturer's instructions for Seahorse Cell Mito Stress Tests as well as the work by Mookerjee and colleagues (Mookerjee et al., 2017, 2018). Parameter numbers 1-8 were calculated using RStudio and an R script written by Cameron Haydinger (Laboratory of Associate Professor Dan Peet, University of Adelaide, Adelaide, SA, Australia). Parameter numbers 9 and 10 were calculated using Microsoft Excel.

1. Basal OCR (OCR_{basal}) = the average of OCRs at measurement point 3 across all replicate wells

2. Oligomycin-induced OCR (OCR_{oligo}) = the lowest among the following three OCR values:
    - The average of OCRs at measurement point 4 across all replicate wells
    - The average of OCRs at measurement point 5 across all replicate wells
    - The average of OCRs at measurement point 6 across all replicate wells

3. FCCP-induced OCR (OCR_{FCCP}) = the highest among the following three OCR values:
    - The average of OCRs at measurement point 7 across all replicate wells
    - The average of OCRs at measurement point 8 across all replicate wells
    - The average of OCRs at measurement point 9 across all replicate wells

4. Non-mitochondrial respiration ($OCR_{non\text{-}mito}$) = the lowest among the following three OCR values:
    - The average of OCRs at measurement point 10 across all replicate wells
    - The average of OCRs at measurement point 11 across all replicate wells
    - The average of OCRs at measurement point 12 across all replicate wells

5. Basal ECAR ($ECAR_{basal}$) = the average of ECARs of all replicate wells at measurement point 3

6. Oligomycin-induced ECAR ($ECAR_{oligo}$) = the highest among the following three ECARs values:
   - The average of ECARs at measurement point 4 across all replicate wells
   - The average of ECARs at measurement point 5 across all replicate wells
   - The average of ECARs at measurement point 6 across all replicate wells

7. Glycolytic reserve = $ECAR_{oligo} – ECAR_{basal}$

8. Basal PER (PER_{basal}) = the average of PERs of all replicate wells at measurement point 3

9. ECAR/OCR ratios = $ECAR_{basal}/OCR_{basal}$

10. Mitochondrial respiration (OCR_{mito}) = $OCR_{basal} – OCR_{non\text{-}mito}$

11. OCR coupled to ATP production ($OCR_{coupled}$)
    = ($OCR_{basal} – OCR_{oligo}$)/hyperpolarization correction factor
    = ($OCR_{basal} – OCR_{oligo}$)/0.908

    Directly calculating $OCR_{coupled}$ from the difference between OCR_{basal} and OCR_{oligo} measured by the Seahorse analyser results in a slight underestimation of $OCR_{coupled}$ because the oligomycin-dependent hyperpolarization of the mitochondrial inner membrane induces a slight increase in OCR_{oligo} (Mookerjee et al., 2017, 2018). This has to be corrected for and can be performed as previously described, using the hyperpolarization correction factor of 0.908 (Affourtit and Brand, 2009; Mookerjee et al., 2017, 2018).

2.3.3.5 *Contribution of glycolysis and respiration to PER*

PER_{basal} is not only the result of PER that is due to the conversion of glucose to lactate via glycolysis (PER_{glyco}) but also PER that is due to mitochondrial respiration (PER_{res}). This is because CO_2 produced from OXPHOS can partially hydrate in the medium to produce H^+ and bicarbonate Ion (HCO_3^-) (Mookerjee et al., 2015).

PER_{res} can be calculated from OCR_{mito} calculated in section 2.3.3.4, using the equation and constant values shown below, as described previously (Mookerjee et al., 2015). PER_{glyco} can then be calculated by subtracting PER_{res} from PER_{basal} determined in section 2.3.3.4. All parameters described in this section were calculated using Microsoft Excel.

PER_{res} (pmol H^+/min) = OCR_{mito} x (Max H^+/O_2) x $(10^{pH-pK_1}/(1+(10^{pH-pK_1}))$

where max H^+/O_2 (the maximum amount of H^+ released per O_2 consumed by respiration) is 1 in the case of complete oxidation of glucose, pH of assay medium is presumed to be 7.4, K_1 is the combined equilibrium constant of CO_2 hydration and dissociation to HCO_3^- and H^+, and pK_1 at 37°C equals 6.093 (Garrett and Grisham, 2010; Mookerjee et al., 2015).

$PER_{glyco} = PER_{basal} - PER_{res}$

2.3.3.6 *Contribution of glycolysis and respiration to ATP production and glucose consumption rates*

Total ATP production rate ($ATPR_{total}$) comprises ATPR that is derived from glycolysis ($ATPR_{glyco}$) and from respiration ($ATPR_{res}$). These parameters can be calculated from the parameters in sections 2.3.3.4 and 2.3.3.5, as described extensively by Mookerjee and colleagues (Mookerjee et al., 2017, 2018). The equations and values used for calculation when glucose is the sole substrate (Mookerjee et al., 2017), as is the case in this thesis, are briefly explained below. All the parameters described in this section were calculated using Microsoft Excel.

$ATPR_{glyco}$ (pmol ATP/min)

= (ATPR due to glycolysis converting glucose to pyruvate and then to lactate) + (ATPR produced by glycolysis converting glucose to pyruvate that is subsequently converted to HCO_3^-)

= (PER_{glyco} x ATP/lactate) + (OCR_{mito} x $2P/O_{glyco}$)

= (PER_{glyco} x 1) + (OCR_{mito} x 2 x 0.167)

ATP/lactate is the number of ATP molecules produced per one lactate molecule produced. P/O_{glyco} is a P/O ratio (ratio of ATP formed to oxygen atom consumed) caused by glycolysis-produced pyruvate that is then fully oxidised and converted to HCO_3^- (Mookerjee et al., 2017; Mookerjee et al., 2015). When glucose is the substrate, ATP/lactate equals 1 and P/O_{glyco} equals 0.167 (Mookerjee et al., 2017). P/O_{glyco} is multiplied by 2 to account for the change from oxygen atom (O) in P/O to oxygen molecules (O_2) in OCR (Mookerjee et al., 2017, 2018) measured from the Seahorse analyser.

$ATPR_{res}$ (pmol ATP/min)

= (ATPR due to OXPHOS) + (ATPR due to substrate-level phosphorylation at succinyl-CoA synthetase in the TCA cycle)

= ($OCR_{coupled}$ x $2P/O_{oxphos}$) + (OCR_{mito} x $2P/O_{TCA}$)

= ($OCR_{coupled}$ x 2 x 2.486) + (OCR_{mito} x 2 x 0.121)

P/O_{oxphos} and P/O_{TCA} values used above are as previously described (Mookerjee et al., 2017). Both P/O ratios are multiplied by 2 to account for the change from O in P/O to O_2 in OCR as above.

$ATPR_{total}$ (pmol ATP/min) = $ATPR_{glyco}$ + $ATPR_{res}$

$ATPR_{glyc}$ (% of ATPRtotal) = ($ATPR_{glyc}$ x 100)/ATPRtotal

$ATPR_{res}$ (% of ATPRtotal) = ($ATPR_{res}$ x 100)/ATPRtotal

In a similar fashion to ATPR, total glucose consumption rate (GCR_{total}) is made up of GCR that is due to glycolysis (GCR_{glyco}) and GCR that is due to respiration (GCR_{res}). The conversion of one glucose molecule to two lactate anions indirectly releases $2H^+$, while the complete oxidation of one glucose molecule yields $6H^+$ (Divakaruni et al., 2014). Therefore, different GCR can be calculated as follows.

GCR_{glyco} (pmol/min) = the amount of glucose converted to lactate

= $PER_{glyc}/2$

GCR_{res} (pmol/min) = the amount of glucose oxidised to HCO_3^-

= PERres/6

GCR_{total} (pmol/min) = $GCR_{glyco} + GCR_{res}$

GCR_{glyco} (% of GCR_{total}) = $(GCR_{glyco} \text{ x } 100)/GCR_{total}$

GCR_{res} (% of GCR_{total}) = $(GCR_{res} \text{ x } 100)/GCR_{total}$

2.4 Protein techniques

2.4.1 Whole cell extraction

All cells used in this thesis were adherent cells from which proteins were extracted using the following protocol. Spent culture medium was aspirated from the culture vessel and cells washed with ice-cold 1x PBS. Next, sufficient ice-cold whole cell extract whole cell extract buffer (20 mM HEPES pH 7.8, 0.42 M NaCl, 0.5% Igepal, 25% glycerol, 0.2 mM EDTA, 1.5 mM MgCl2 with freshly added 1 mM DTT, 1 mM PMSF, 2 µg/mL aprotinin, 4 µg/mL bestatin, 5 µg/mL leupeptin, and 1 µg/ml pepstatin) to cover the culture vessel surface was added and the cells scraped and transferred into a 1.5 ml tube. Cells in whole cell extract buffer were incubated on a rotating shaker at 4°C for 30 minutes and centrifuged at 14,000 rpm for 30 minutes, after which the supernatant (protein lysate) was transferred into a new 1.5 mL tube without disturbing the cell pellet. The lysate was then used for a protein quantification assay and western blotting or kept at -20^{o}C until use.

2.4.2 Tissue protein extraction

Mouse liver and muscle tissues were gifts from Dr Daniel Pederick (Laboratory of Professor Paul Thomas, University of Adelaide and South Australian Health and Medical Research Institute, Adelaide, SA, Australia). Liver, muscle and retinal tissues from adult Sprague-Dawley rats were gifts from Teresa Mammone (Laboratory of Professor Robert Casson). Tissues were cut into small pieces and each piece weighed and placed in a 6 cm culture dish on ice. Ice-cold whole cell extract buffer was then added to the dish (approximately 1 mL of buffer per 100 mg of tissue). The tissue was minced with a surgical blade, transferred together with the buffer to a 1.5 mL tube, grinded with a tissue grinder, and incubated on a rotating shaker at 4^{o}C for 30 minutes and centrifuged at 14,000 rpm for 30 minutes, after which the supernatant (protein lysate) was transferred into a new 1.5 mL tube without disturbing the tissue pellet. The lysate was then used for a protein quantification assay and western blotting or kept at -20^{o}C until use.

2.4.3 Protein quantification

Protein lysates were quantified by Bio-Rad protein assay (#5000006, Bio-Rad) performed in a clear 96-well plate according to the manufacturer’s instructions with minor modifications. Protein standards of 1, 2, 3, 4 and 5 µg/well were created by adding 2, 4, 6, 8, and 10 µL of 0.5 µg/µL bovine serum albumin (BSA) in MQ water into wells, respectively. Next, samples were added to wells in duplicate. Volumes of samples added per well varied from 0.5 to 10 µL, depending on protein concentrations. 200 µL of 1x Dye reagent was added to each well containing standards or samples and thoroughly mixed. The same amount was also added to a blank well (0 µg/well control). The plate was then incubated at room temperature for at least five minutes and optical densities at 620 nm (OD620) assessed. The results were used to plot a standard curve between different protein amounts (0, 1, 2, 3, 4 and 5 µg/well) and their OD620 values. Protein amount (µg) per well of each sample was obtained by applying its OD620 to the standard curve. The protein amount (µg) and the sample volume added (µL) per well were then used to calculate the protein concentration (µg/µL) of each sample.

2.4.4 Denaturing SDS-PAGE for protein separation

For each gel, equivalent amounts (µg protein) of each sample were used. Three parts of protein lysates were mixed with one part of 4x SDS loading buffer (0.5 M Tris pH 6.8, β-Mercaptoethanol, 0.05 M Bromophenol blue, 10% SDS, 10% Glycerol). Lysate/buffer mixtures were incubated at 95°C for five minutes and centrifuged at 13,000 rpm at room temperature for five minutes. Sample mixtures and protein ladder for size determination (Precision Plus Protein Dual Colour Standards, #161-0374, Bio-Rad) were then loaded onto a mini 7.5% or 10% polyacrylamide gel and separated by electrophoresis at 120-160 V in 1x glycine/tris/SDS (GTS) buffer.

2.4.5 Western blotting

2.4.5.1 Protocol

Proteins were transferred to nitrocellulose membranes either by a wet/tank blotting system (Bio-Rad) or a Trans-Blot Turbo Transfer System (Bio-Rad).

The wet/tank transfer was performed in a tank filled with 1x wet transfer buffer at 250 mA for two hours at 4°C for one or two mini gels. 1x wet transfer buffer was made by mixing one part of 5x wet transfer buffer (58 g TRIS, 290 g glycine, 100 mL 10% SDS, make up to 2 L with MQ water), one part of methanol and three parts of RO water.

Trans-Blot Turbo Transfer was performed according to the manufacturer’s instruction, using the protocol for 1.5 mm gels (for one mini gel: 1.3 A constant, up to 25 V, ten minutes).

After the transfer, ponceau stain was applied onto the membranes, and the membranes were rinsed with RO water to remove excess stain and observe the proteins to determine whether the transfer was successful. Western blotting was then continued as described in Paper 4 (Kittipassorn et al., 2019a) in Chapter 3. Membranes were blocked with 10% (w/v) skimmed milk in PBS containing 0.1% nonionic detergent (TWEEN20, #P1379, Sigma-Aldrich, Castle Hill, NSW, Australia) for one hour on a shaker at room temperature and then incubated overnight at 4 °C on a nutator or a rotator with primary antibodies (Table 2.4, section 2.4.5.2) diluted in 2% skimmed milk in 0.1% TWEEN20/PBS. On the following day, membranes were washed with 0.1% TWEEN20/PBS, incubated in horseradish peroxidase-conjugated secondary antibodies for one hour on a shaker at room temperature, washed with 0.1% TWEEN20/PBS again, and protein bands visualised using enhanced chemiluminescence (ECL) reagents with a ChemiDoc Imaging system (Bio-Rad) and ImageLab software. ECL reagent used was either a home-made reagent (per membrane: 100 mM Tris pH 8.5 10 mL, 30% H_2O_2 3 μl, 250 mM luminal 50 μl, 90 mM p-coumaric acid 25 μl), Clarity ECL substrate (#170-5060, Bio-Rad) or SuperSignal™ West Femto Maximum Sensitivity Substrate (#34095, Life Technologies Australia). Band intensity of proteins of interest was quantified using the ImageLab software.

2.4.5.2 Antibodies and dilutions

Table 2.4. Primary antibodies used in Chapters 4 and 5 of this thesis.

Target protein	Species	Source*	Cat. No. /clone	Dilution
PKM1	Rabbit	CS	7067	1:500
PKM1	Rabbit	PT	15821-1-AP	1:500
PKM1	Rabbit	N	NBP2-14833	1:500
PKM2	Rabbit	CS	3198S	1:500-1:1000
Total PKM	Rabbit	CS	3190S	1:500-1:1000
β-Actin	Rabbit	Abcam	ab8227	1:2000
α-tubulin	rat	N	NB600-506	1:2000

*Source: Abcam (Melbourne, VIC, Australia); CS, Cell Signaling Technology (Danvers, MA, USA); N, Novus Biologicals (Littleton, CO, USA); PT, proteintech (Rosemont, IL, USA).

Secondary antibodies (1:5000 to 1:10,000 dilutions) were horseradish peroxidase conjugated goat anti-rabbit IgG (Pierce and Life Technologies Australia) and horseradish peroxidase conjugated goat anti-rat IgG (Abcam).

2.5 DNA techniques

2.5.1 Primers

All primer sequences are shown from 5’ to 3’.

microRNA-30 (miR30) isothermal forward primer for shRNA cloning

CTTGCTGGGATTACTTCTTCAGGTTAACCCAACAGAAGGCTCGAGAAGGTATATTGCTGTTGACAGTGAGCG

miR30 isothermal reverse primer for shRNA cloning

AACAAGATAATTGCTCCTAAAGTAGCCCCTTGAATTCGATTCCGAGGCAGTAGGCA

pENTR1a reverse sequencing primer

GTGTCTCAAAATCTCTGATGTTAC

gRNA U6 V1 sequencing primer

GGTTTCGCCACCTCTGACTTG

bgh PA F sequencing primer

TGCATCGCATTGTCTGAGTAGG

PKM2 KO screening forward primer

AGCCTCCAGTCAATCCACAGAC

PKM2 KO screening reverse primer

TCCATTGAGCTCCCTCCAAGTG

2.5.2 Plasmids

2.5.2.1 Plasmids obtained elsewhere

pENTR1a-dnucTomato-miR30

A Gateway Entry vector with the dimeric nuclear Tomato sequence, miR30-based shRNA cassettes and the kanamycin resistance gene (Bersten et al., 2015), a gift from Dr David Bersten (Laboratory of Professor Murray Whitelaw)

pENTR1a-dnucTomato-miR30-shGL3 1309

A pENTR1a-dnucTomato-miR30c with shRNA cassettes targeting luciferase (shGL3 1309) (Bersten et al., 2015), a gift from Veronica Bhakti (Laboratory of Professor Murray Whitelaw)

pLV410 (empty)

A lentiviral, mammalian expression, Gateway Destination vector with the ampicillin resistance gene (Bersten et al., 2015), a gift from Dr David Bersten (Laboratory of Professor Murray Whitelaw), originally obtained from Professor Simon Barry (Robinson Research Institute, Adelaide, SA, Australia).

Lentiviral plasmids

Lentiviral plasmids used in this thesis include pCMV-dR8.2 dvpr (a second-generation lentiviral packaging vector), pRSV-Rev (a third-generation lentiviral packaging vector) and pMD2.G (a Vesicular Stomatitis Virus glycoprotein (VSV-G)-expressing envelope plasmid). All were gifts from the Laboratory of Professor Murray Whitelaw, originally obtained from commercially sources.

pEF-IRES-Puro6

A mammalian expression vector with the ampicillin resistance gene and a puromycin selection cassette, a gift from the Laboratory of Professor Murray Whitelaw)

pDG458

A dual-guide RNA (gRNA) Cas9 nuclease plasmid with a green fluorescence protein (GFP) selection cassette and the ampicillin resistance gene (Adikusuma et al., 2017), a gift from Chandran Pfitzner (Laboratory of Professor Paul Thomas).

2.5.2.2 Plasmids cloned in this thesis

pENTR1a-dnucTomato-miR30-shPKM2 1572, 1452, 1499 or 1501

A pENTR1a-dnucTomato-miR30 (Bersten et al., 2015) with shRNA cassettes targeting mouse and rat *Pkm2* mRNA. Four different plasmids were generated, each with either shPKM2 1572, 1452, 1499 or 1501 (see section 2.6.1.1).

pLV410-dnucTomato-miR30-shPKM2 1572, 1452, 1499 or 1501

A pLV410 plasmid with miR30 based shRNA cassettes targeting mouse and rat *Pkm2* mRNA. Four different plasmids were generated, each with either shPKM2 1572, 1452, 1499 or 1501 (see section 2.6.1.2).

pLV410-dnucTomato-miR30-shGL3 1309

A pLV410 plasmid with miR30 based shRNA cassettes targeting luciferase (shGL3 1309) (see section 2.6.1.2).

pDG458-gRNAs [A1+B1] and pDG458-gRNAs [A2+B2]

A pDG458 dual-gRNA plasmid (Adikusuma et al., 2017) expressing a pair of gRNAs, one targeting the intron between exon 9 and exon 10 of the *Pkm* gene (gRNA A1 or B1) and the other the intron between exon 10 and exon 11 (gRNA A2 or B2). Two plasmids were generated, one expressing gRNAs A1 and B1 (pDG458-gRNAs [A1+B1]), the other gRNAs A2 and B2 (pDG458-gRNAs [A2+B2]). The generation of these plasmids is described in section 2.7.1.

2.5.3 Bacterial transformation

2.5.3.1 Bacterial strains

Two different *E. coli* bacterial strains were used: DH5α chemically competent cells for cloning experiments and preparation of most plasmids, and DB3.1 chemically competent cells, containing a DNA gyrase mutant, used specifically for preparation of empty Gateway cloning destination vectors expressing the *ccd*B gene. The *ccdB* gene encodes the CcdB protein which is toxic to and would inhibit the propagation of DH5α cells.

2.5.3.2 Transformation protocol

E.coli chemically competent cells were taken out of -80°C storage and thawed on ice. For general plasmid preparations, a short transformation protocol was employed. Plasmid DNA (30-100 ng) was added to 30-50 µL of competent cells and the mixture incubated on ice for 20 minutes. Next, the mixture was incubated (heat shocked) at 42°C for 30 seconds, incubated on ice for a further two minutes and plated on a luria broth (LB) agar plate containing appropriate selection antibiotic (100 µg/mL ampicillin or 50 µg/mL kanamycin).

For ligation, isothermal assembly or gateway reactions, long transformation was performed using the same protocol as the short transformation with additional steps before plating. After the two-minute incubation on ice, 250 µL Super Optimal broth with Catabolite repression (SOC) medium was added to the DNA/competent cells mixture. The mixture was then incubated at 37°C on a shaker for 1-2 hours and centrifuged at 2400 rpm for 2-3 minutes at room temperature. Next, 200 µL of the supernatant was aspirated without disturbing the cell pellet, and the cell pellet was gently resuspended in the rest of the supernatant and plated on a LB agar plate containing appropriate selection antibiotic. Plates were incubated at 37°C overnight and used to inoculate LB cultures for plasmid miniprep or midiprep (see the next section).

2.5.4 DNA plasmid preparation

2.5.4.1 Plasmid miniprep

Five millilitre LB cultures containing a suitable selection antibiotic (final concentrations of 100 µg/mL for ampicillin or 50 µg/mL for kanamycin) were inoculated with single colonies picked from transformation plates and grown on a shaker at 37°C overnight. Plasmid DNA was purified using a QIAprep Spin Miniprep Kit (#27106, Qiagen, Chadstone Centre, VIC, Australia) as per the manufacturer's instructions. Purified DNA concentration was determined by a Nanodrop spectrophotometer (Life Technologies) based on the absorbance at 260 nm (A260). Expected A260/280 ratio for pure DNA is ~ 1.8. DNA samples were stored at -20°C.

2.5.4.2 Plasmid midiprep

100-200 mL LB cultures containing a suitable selection antibiotic (final concentrations of 100 µg/mL for ampicillin or 50 µg/mL for kanamycin) were inoculated with single colonies picked from transformation plates and grown on a shaker at 37°C overnight. Plasmid DNA was purified using a NucleoBond Xtra Midi Plus Kit (#740412.50, Macherey Nagel, Düren, Germany) as per the manufacturer's instructions. DNA concentrations were determined by the same method as DNA purified from a miniprep kit in section 2.5.4.1.

2.5.5 Restriction digestion

Digestion reactions for desired restriction enzymes were set up as recommended by New England Biolabs (NEB; Ipswich, MA, USA), using 500-2000 µg DNA, 1x NEB buffer, 100 ng/µL BSA (optional for some reactions) and 0.2-0.5 µL enzyme per reaction. Reactions were incubated at 37°C and analysed on agarose gels. All enzymes used were obtained from NEB.

2.5.6 Gibson's isothermal assembly and PCR

Gibson's isothermal assembly (Gibson et al., 2009) was used to assemble inserts containing shRNA sequences and digested vectors with overlapping ends (see also section 2.6.1.1). Products to be used as inserts were amplified using Phusion DNA polymerase. PCR primer design was carried out as described previously (Gibson et al., 2009) to generate PCR-amplified inserts which contained 40 bp of overlapping sequence to the ends of digested vectors. Primers were designed by Dr David Bersten (Laboratory of Professor Murray Whitelaw, University of Adelaide, Adelaide, SA, Australia). Each PCR reaction was set up as follows: 0.5 µL Phusion DNA polymerase (NEB), 5 µL 5x Phusion GC buffer (NEB), 1 µL 10 mM dNTPs, 1 µL 50 mM $MgCl_2$, 1 µL 10 µM forward primer, 1 µL 10 µM reverse primer, 100 ng DNA template, and MQ water to a total volume of 25 µL. PCR reactions then underwent the following cycling parameters: 98°C for 30 seconds; 35 cycles of 98°C for 10 seconds, 60°C for 30 seconds, 72°C for 60 seconds; 72°C for 5 minutes; hold at 4°C.

Gibson's isothermal assembly was carried out as described previously (Gibson et al., 2009), using Gibson's isothermal assembly mix (NEB), containing ligase, polymerase and exonuclease.

2.5.7 Gateway recombination

Each reaction contained 2 µL LR clonase II enzyme mix (#P/N 56484, Life Technologies Australia), 1 µL of 300 ng/µL entry vector, 1 µL 150 ng/µL destination vector and 6 µL TE (Tris/EDTA) buffer. Reactions were incubated at room temperature for one hour, 2 µL of 2 µg/µL Proteinase K added per reaction, further incubated at 37°C for ten minutes, and used for long transformation.

2.5.8 Genomic DNA extraction and PCR

Genomic DNA (gDNA) and PCR were used to screen PKM2 KO cells (see section 2.7.3). Cells were trypsinised and cell suspension centrifuged. Cell pellet was washed with 1x PBS and gDNA extracted using a MyTaq Extract-PCR kit (#21126, Bioline Australia, Alexandria, NSW, Australia) according to the manufacturer's instructions. DNA concentration was determined by a Nanodrop spectrophotometer based on the absorbance at 260 nm (A260). gDNA was PCR amplified using Taq DNA polymerase. Each PCR reaction was set up as follows: 0.25 µL Taq DNA polymerase (NEB), 5 µL 10x standard Taq buffer (NEB), 1 µL 10 mM dNTPs, 1 µL 10 µM forward primer, 1 µL 10 µM reverse primer, 0.5-2 µL gDNA template, 2.5 µL 100% DMSO, and MQ water to a total volume of 50 µL. PCR reactions then underwent the following cycling parameters: 95°C for 30 seconds; 30 cycles of 95°C for 30 seconds, 61°C for 60 seconds, 68°C for 90 seconds; 68°C for 5 minutes; hold at 4°C.

2.5.9 DNA analysis on agarose gel

DNA samples (plasmids, restriction digests, PCR products) and ladder for size determination (1 Kb Plus DNA Ladder, #10787-026, Life Technologies Australia) were separated on 1-2% agarose gels (depending on expected DNA fragment sizes) by electrophoresis and visualised by in-gel ethidium bromide on a UV transilluminator (UVP). Gels were made by dissolving agarose powder in 1x Tris-Borate-EDTA (TBE) buffer and ethidium bromide added (1 µL per 20 mL 1x TBE buffer).

2.5.10 Gel extraction and purification of DNA fragments

DNA fragments of interest were excised from the gel using a scalpel blade and purified using a QIAquick Gel Extraction Kit (#28706, Qiagen) according to the manufacturer's protocol.

2.5.11 DNA clean up

DNA clean up was performed using a QIAquick PCR purification kit (#28106, Qiagen) as per the manufacturer's instruction.

2.5.12 DNA sequencing

DNA samples were sequenced by Sanger sequencing. Samples were prepared and submitted to the Australian Genomics Research Facility (AGRF, Adelaide, SA, Australia) for analysis, either as labelled DNA in dried down pellet form or purified DNA.

<u>Labelled DNA in dried down pellet form</u>

Each sequencing reaction was set up as follows: 1 µL Big Dye Terminator, 3 µl 5x sequencing buffer, 0.5 µL primer, 400 ng DNA (double stranded plasmids) and MQ water to a total volume of 15 µl. For sequencing of pENTR1a plasmids, 1 µL of 15 µM dGTP was also added per reaction. Samples underwent the following cycling parameters: 96°C for three minutes and 25 cycles of 96°C for 30 seconds, 50°C for 15 seconds and 60°C for four minutes. Samples were then cleaned of any free bases and precipitated by the following protocol. Each reaction was mixed with 80 µL 75% isopropanol and 1 µL glycogen, incubated at room temperature for 30 minutes and centrifuged at

13,000 rpm at room temperature for 20 minutes. The supernatant was then removed without disturbing the DNA pellet. The pellet was washed with 150 µL 75% isopropanol, air dried at 50 °C for approximately ten minutes and submitted to AGRF for analysis.

Purified DNA

Purified DNA samples were prepared as per AGRF Sample Preparation Guide. Each sample was mixed with 1 µL of 10 µM sequencing primer and MQ added to the total volume of 12 µL. Samples were submitted to AGRF for Sanger sequencing. Amounts of DNA samples used depended on sample type: 600-1500 ng for double stranded plasmids, 70-105 ng for PCR products longer than 800 bp, 30 ng for 400-600 bp PCR products, and 18 ng for 200-400 bp PCR products.

2.6 Generation and analysis of lentiviral-based shRNA-mediated PKM2 knockdown Müller cells

The miR30 based shRNA system as described previously (Bersten et al., 2015) was employed to knock down PKM2 in rat MCs. The system was adapted from that of Dow and colleagues (Dow et al., 2012). Firstly, four shRNAs targeting *Pkm2* mRNA (shPKM2s) were designed and each cloned into a pENTR1a-dnucTomato-miR30 plasmid (Bersten et al., 2015), using Gibson's isothermal assembly, to generate four pENTR1a-dnucTomato-miR30-shPKM2 plasmids. Secondly, the dnucTomato-miR30-shPKM2 DNA fragment from each of the four pENTR1a-dnucTomato-miR30-shPKM2 plasmids was transferred into an empty pLV410 vector (Bersten et al., 2015) by Gateway recombination to generate lentiviral mammalian expression pLV410-dnucTomato-miR30-shPKM2 plasmids, which were introduced into MCs via lentiviral transduction.

2.6.1 Generation of *Pkm2*-targeting short hairpin RNA constructs

2.6.1.1 Generation of pENTR1a-dnucTomato-miR30-shPKM2 plasmids

Four different 22 nucleotide shRNAs targeting *Pkm2* mRNA (shPKM2s) (Fig. 2.2A) were originally designed against the exclusive exon 10 of mouse *Pkm2* mRNA by Stephen Bent (University of Adelaide, Adelaide, SA, Australia) using an algorithm as described (Bersten et al., 2015). When aligning the mouse and the rat exon 10, there is only one mismatch (Fig. 2.2B) which is not among

A.

shRNA	Base*	Anti-sense sequence
PKM2	1572	TTGGTGAGCACGATAATGGCCC
PKM2	1452	TGCAAGTGGTAGATGGCAGCCT
PKM2	1499	TGGGGTCGCTGGTAATGGGCGC
PKM2	1501	TGTGGGGTCGCTGGTAATGGGC

B.

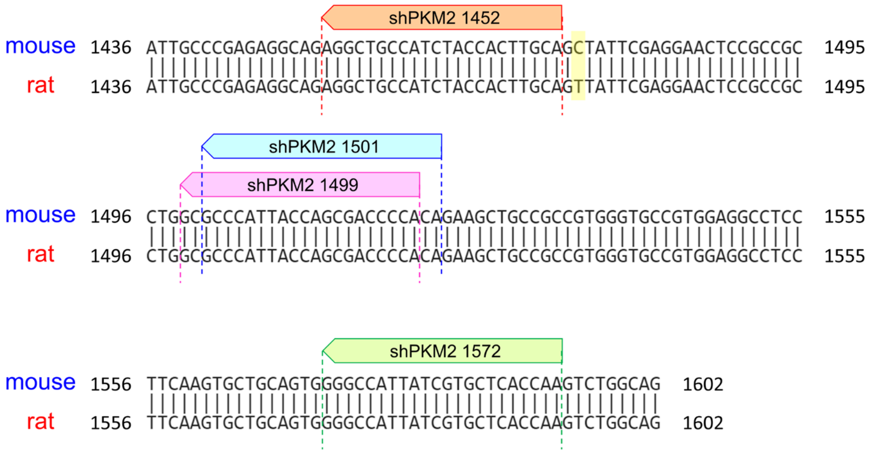

Figure 2.2. Short hairpin RNAs (shRNAs) targeting exon 10 of *Pkm2* mRNA (shPKM2s). (A) Sequences of four shPKM2s designed to target exon 10 of mouse *Pkm2* mRNA. *Base, the number of the base in the mouse *Pkm2* mRNA (NCBI Reference Sequence: NM_011099.3) to which the first base on the 3' end of each shPKM2 matches. **(B)** The nucleotide sequence (the sense strand) of the mouse *Pkm2* exon 10 (bases 1436 to 1602 of mouse *Pkm2* mRNA, NCBI Reference Sequence: NM_011099.3) is aligned with the rat *Pkm2* exon 10 (sequence taken from pyruvate kinase M1 and M2 subunit genes, complete coding sequence, GenBank: M24359.1), using the NCBI BLAST services. Exon 10 of both the mouse and the rat *Pkm2* is 167 bp long. A mismatch between the mouse and the rat exon 10 is highlighted in yellow. Positions on exon 10 to which shPKM2s from (A) targets are shown.

the nucleotides targeted by the four shPKM2s. In other words, all nucleotides to which the four shPKM2s target are conserved between the two species (Fig. 2.2B), enabling these shPKM2 to knock down rat PKM2.

Cloning of shPKM2 into the pENTR1a-dnucTomato-miR30 plasmids was performed as described previously (Bersten et al., 2015). The pENTR1a-dnucTomato-miR30 vectors were XhoI/EcoRV-digested and gel-purified (performed by Dr Jacqueline Fabrizio, Laboratory of Associate Professor Dan Peet). Single-stranded 97mer template shRNA oligonucleotides (Ultramer DNA Oligos from Integrated DNA Technologies (IDT), Coralville, IA, USA) (table 2.5), each consisting of miR30 context flanking each of the 22 nucleotide shPKM2 guide sequences, were amplified using miR30 isothermal forward and reverse primers (see section 2.5.1), to generate double-stranded ~190 bp PCR products with overlapping sequence to the XhoI/EcoRV-digested pENTR1a-dnucTomato-miR30 plasmids. PCR reactions were performed as described in section 2.5.6. Half of the reactions was analysed on a 2% agarose gel. If the expected bands were present, the remainder of the PCR reactions were cleaned up according to the standard protocol. The PCR products of all shPKM2s were digested by XhoI and EcoRV, gel-purified, pooled together (multiplex cloning), mixed with the XhoI/EcoRV-digested gel-purified pENTR1a-dnucTomato-miR30 vectors and underwent Gibson's isothermal assembly as previously described (Gibson et al., 2009). Assembly reactions were transformed into DH5α cells using the long transformation protocol and plates incubated overnight. Single colonies were picked, grown in LB overnight, DNA purified (minipreps) and checked with EcoRI restriction digestion. Different shPKM2 clones were confirmed by Sanger sequencing using the pENTR1a reverse sequencing primer.

Table 2.5. Single-stranded 97mer template shRNA oligonucleotides

shPKM2	Single stranded 97mer template shRNA oligonucleotides*
1572	TGCTGTTGACAGTGAGCGAGGCCATTATCGTGCTCACCAATAGTGAAGCCACAGATGTATTGGTGAGCACGATAATGGCCCTGCCTACTGCCTCGGA
1452	TGCTGTTGACAGTGAGCGCGGCTGCCATCTACCACTTGCATAGTGAAGCCACAGATGTATGCAAGTGGTAGATGGCAGCCTTGCCTACTGCCTCGGA
1499	TGCTGTTGACAGTGAGCGACGCCCATTACCAGCGACCCCATAGTGAAGCCACAGATGTATGGGGTCGCTGGTAATGGGCGCTGCCTACTGCCTCGGA
1501	TGCTGTTGACAGTGAGCGACCCATTACCAGCGACCCCACATAGTGAAGCCACAGATGTATGTGGGGTCGCTGGTAATGGGCTGCCTACTGCCTCGGA

* commercially sourced from Integrated DNA Technologies (IDT)

2.6.1.2 Generation of pLV410-dnucTomato-miR30-shRNA plasmids

pLV410-dnucTomato-miR30-shPKM2 plasmids were generated by Gateway recombination (see section 2.5.7) to transfer the dnucTomato-miR30-shPKM2 DNA fragment from each of the four pENTR1a-dnucTomato-miR30-shPKM2 plasmids into an empty pLV410 vector (Bersten et al., 2015). Similarly, a pLV410-dnucTomato-miR30-shGL3 plasmid, to be used as a non-targeting shRNA control, was generated by Gateway recombination to transfer the dnucTomato-miR30-shGL3 1309 DNA fragment from the pENTR1a-dnucTomato-miR30-shGL3 1309 plasmid into an empty pLV410 vector (Bersten et al., 2015). In the remainder of this thesis the shGL3 is referred to as the shControl. Gateway reactions were transformed into DH5α cells using the long transformation protocol and plates incubated overnight. Single colonies were picked and grown overnight in LB, and plasmids were purified (minipreps) and analysed by FspI restriction digestion.

2.6.2 Lentiviral production

Firstly, 3 x 10^6 HEK 293FT cells were seeded in a T75 flask. On the following day, cells were transfected with 12.5 µg of one of the five pLV410-dnucTomato-miR30-shRNA plasmids (shPKM2 1572, 1452, 1499, 1501 or shControl), 7.5 µg pCMV-dvpr 8.2, 6.25 µg pRSV-Rev and 3.75 µg pMD2.G using lipofectamine 2000 (#11668019, Life Technologies Australia). This was performed by combining the required plasmids and 70 µL of lipofectamine 2000 in 1 mL culture medium without FBS, incubating at room temperature for 20 minutes and adding to the cells. The cells were left for one day before the culture medium was removed, the cells washed and fresh medium added. Then the cells were left for a further two days and the medium containing lentivirus was harvested, centrifuged at 1000 rpm for ten minutes and filtered through a 0.45 µm filter. The lentivirus was used for transduction experiments or stored at -80°C until use.

2.6.3 Lentiviral transduction and determination of transduction efficiency

Primary MCs or rMC-1 cells were seeded into a culture vessel. Approximately 3-4 hours after seeding, lentivirus encoding either one of the five pLV410-dnucTomato-miR30-shRNA plasmids (shPKM2 1572, 1452, 1499, 1501 or shControl) was added to the cells with polybrene (8 µg/mL final concentration). Cell seeding density, type of culture vessel and amount of lentivirus used in each experiment are specified in figure legends. Approximately 24 hours later, the cells were washed and fresh medium added. Cells were left for approximately 24 or 48 hours (specified in figure legends) and then stained with Hoechst 33342 nuclear stain. Fluorescence images were taken with a fluorescence microscope (Nikon Eclipse Ti microscope, Nikon Australia), and transduction efficiency determined from proportions of transduced cells expressing nuclear Tomato fluorescence to total cell numbers indicated by nuclear staining. Cells in each image were counted using the Fiji software (Schindelin et al., 2012).

2.6.4 Fluorescence activated cell sorting (FACS)

Primary MCs were subjected to FACS to enrich for transduced cells. Cells were seeded in a 6-well tray (160,000 cells per well) and transduced with lentivirus encoding either one of three pLV410-dnucTomato-miR30-shRNA plasmids (shPKM2 1572, shPKM2 1452 or shControl). Approximately 24 hours after transduction, cells were washed and fresh growth medium added. Approximately 48 hours after transduction, cells were trypsinised, centrifuged and resuspended in sorting buffer (1x Hank's Balanced Salt Solution (HBSS), 1 mM EDTA, 25 mM HEPES pH 7.0, 2% FBS). Cells were then submitted to and FACS carried out at the Detmold facility (SA Pathology, Adelaide, SA, Australia.). FACS was performed using a Beckman Coulter MoFlo Astrios EQ High Speed Cell Sorter running Summit Software version 6.2.4.15830 (Beckman Coulter, Miami, FL, USA) to select cells based on Tomato fluorescence protein expression. The cytometer was enclosed within Baker SterilGuard BSL Class II Biosafety cabinet (The Baker Company, Sanford, Maine, USA). Sorted cells were collected in MEM containing 20% FBS, 25 mM glucose and 2 mM L-glutamine.

2.6.5 Lentiviral-based shRNA-mediated PKM2 knockdown

rMC-1 cells were seeded and transduced with lentivirus encoding either one of the five pLV410-dnucTomato-miR30-shRNA plasmids (shPKM2 1572, 1452, 1499, 1501 or shControl) as described in section 2.6.3. Cell seeding density, type of culture vessel and amount of lentivirus used in each experiment are specified in figure legends. Approximately 48-72 hours (specified in figure legends) after transduction, cells were washed and proteins extracted, quantified and analysed by western blotting to determine PKM2 and total PKM protein levels.

2.6.6 Metabolic analysis of PKM2 knockdown rMC-1 cells

rMC-1 cells (3759 cells per well) were seeded in MEM containing 10% FBS, 5.5 mM glucose and 2 mM L-glutamine (80 µL per well) in a Seahorse 96-well cell culture plate (pre-coated with 0.2% gelatin in PBS). The cell plate was allowed to rest at room temperature for 45-60 minutes to promote even cell distribution (Lundholt et al., 2003) before being moved to a humidified, 37^{o}C incubator with 5% CO_2. Approximately 3-4 hours after seeding, cells were transduced with lentivirus encoding either one of four pLV410-dnucTomato-miR30-shRNA plasmids (shPKM2 1572, 1452, 1499 or shControl) (generated as described in section 2.6.1.2). One day after transduction, cells were washed and fresh medium added. Three days after transduction, cells were subjected to lactate and Seahorse assays as described in sections 2.2 and 2.3. In each experiment, unless otherwise stated, after the Seahorse assay was performed and cell numbers determined, proteins were extracted and analysed by western blotting to determine PKM2 protein levels.

2.7 Generation and analysis of CRISPR/Cas9-mediated PKM2 knockout Müller cells

In order to knock out PKM2 but not PKM1 in MCs, the PKM2-exclusive exon 10 in the *Pkm* gene was targeted using CRISPR/Cas9 technology.

2.7.1 Generation of pDG458 Cas9 nuclease plasmids containing *Pkm*-targeting guide RNAs

The strategy to remove exon 10 was to use a pair of guide gRNAs, one targeting the intron between exon 9 and exon 10 of the *Pkm* gene (designated as gRNA [A]) and the other the intron between exon 10 and exon 11 (designated as gRNA [B]) (Fig. 2.3). Two different pairs of gRNAs (Table 2.6) were used to control for non-specific off-target effects and were designed to target NGG protospacer adjacent motif (PAM) sites using an online CRISPR design tool (http://crispr.mit.edu/) with the target rat *Pkm* sequence from the National Center for Biotechnology Information website (NCBI Reference Sequence: NC_005107.4). Forward and reverse oligonucleotides for each of the four gRNAs with appropriate overhanging ends were designed (Table 2.7), phosphorylated and annealed as described previously (Adikusuma et al., 2017). The annealed gRNA A1 oligonucleotides were paired with the annealed gRNA B1 oligonucleotides and both ligated into empty pDG458 Cas9 plasmids, which are capable of harbouring two gRNAs, using one step cloning as described previously (Adikusuma et al., 2017) to generate the pDG458-gRNAs [A1+B1] plasmids. Similarly, the annealed gRNA A2 oligonucleotides were paired with the annealed gRNA B2 oligonucleotides and both ligated into empty pDG458 Cas9 plasmids to generate the pDG458-gRNAs [A2+B2] plasmids. Ligation reactions were transformed into DH5α using the long transformation protocol and plates incubated overnight. Single colonies were picked and grown overnight in LB, and plasmids (minipreps) analysed by BbSI/EcoRI restriction digestion. Positive clones were verified by Sanger sequencing using the seq gRNA U6 V1 and the bgh PA F primers.

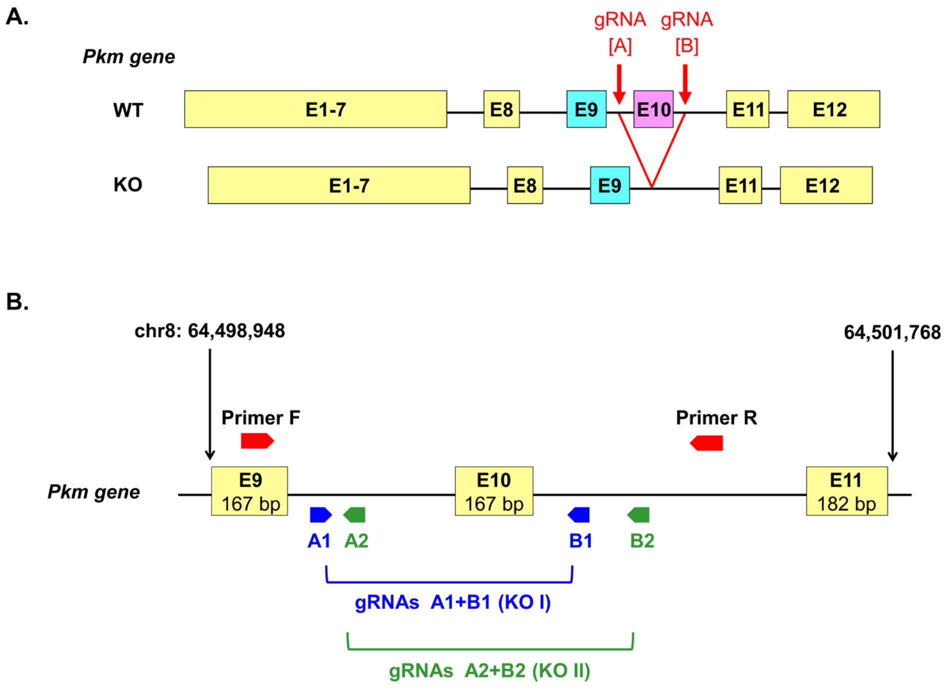

Figure 2.3. The strategy to generate and screen PKM2 knockout (KO) rMC-1 cell lines. (A) Schematic diagram illustrating the strategy used to generate PKM2 knockout cells by removing exon (E) 10 from the *Pkm* gene, using CRISPR/Cas9 technology. E10 was removed using a dual-guide RNA expressing Cas9 nuclease plasmid (Adikusuma et al., 2017) containing a pair of guide RNAs (gRNAs), one targeting the intron between E9 and E10 (gRNA [A]), the other targeting the intron between E10 and E11 (gRNA [B]). **(B)** Two gRNAs (gRNAs A1 and A2) were designed to target the intron between E9 and E10, and another two gRNAs (gRNAs B1 and B2) were designed to target the intron between E10 and E11. gRNA A1 was paired with B1 to generate a KO I cell population (indicated by blue arrows and text). gRNA A2 was paired with B2 to generate a KO II cell population (indicated by green arrows and text). Forward (F) and reverse (R) primers flanking the sites on the *Pkm* gene targeted by the gRNAs were designed to screen for a successful removal of E10. Positions of the start of E9 and the end of E11 on chromosome (chr) 8 and the length of each exon are illustrated. Black lines between exons indicate introns. The diagram is not to scale. WT, wildtype

Table 2.6. Guide RNA (gRNA) sequences targeting the flanking introns of exon 10 in the *Pkm* gene and NGG protospacer adjacent motif (PAM) sites

Target area	**gRNA**	**Target strand on the *Pkm* gene**	**Sequence (5' to 3')**	**PAM**
Intron between exons 9 and 10	A1	sense	CAGCCAAGGAGGTCACGATA	GGG
	A2	anti-sense	GTACCCACTAGGGAATCCTT	TGG
Intron between exons 10 and 11	B1	anti-sense	GCCACCTAATCTGGTGTACC	TGG
	B2	anti-sense	CACCTCTTCTGCCCGAATGC	TGG

Table 2.7. Forward and reverse oligonucleotides containing the guide RNA (gRNA) sequences targeting the *Pkm* gene with appropriate overhangs for cloning into pDG458 Cas9 plasmids

gRNA	**Oligo pair (5' to 3')**
A1	CACCGCAGCCAAGGAGGTCACGATA
	AAACTATCGTGACCTCCTTGGCTGC
A2	CACCGTACCCACTAGGGAATCCTT
	AAACAAGGATTCCCTAGTGGGTAC
B1	ACCGCCACCTAATCTGGTGTACCGT
	TAAAACGGTACACCAGATTAGGTGG
B2	ACCGCACCTCTTCTGCCCGAATGCGT
	TAAAACGCATTCGGGCAGAAGAGGTG

gRNA sequences are shown in red. Oligonucleotides were commercially sourced from Sigma-Aldrich.

2.7.2 Generation of rMC-1 Müller cells with PKM2 knocked out

rMC-1 cells in ~80% confluent T75 flasks were co-transfected with the following:

1) 15 µg of pEF-IRES-Puro6 plasmids (a mammalian expression vector that constitutively expresses a puromycin resistance gene)
2) 15 µg of either one of three Cas9 nuclease plasmids:
    - empty pDG458 without gRNAs targeting the rat *Pkm* gene, to generate wildtype (WT) control cells
    - pDG458-gRNAs [A1+B1]
      pDG458 containing the first pair of gRNAs (A1 and B1) to generate PKM2 KO (KO) I cells
    - pDG458-gRNAs [A2+B2]
      pDG458 containing the second pair of gRNAs (A2 and B2) to generate PKM2 KO II cells

These plasmids were mixed with 800 µL MEM without FBS and 90 µL Polyethylenimine (PEI) (#23966-1, Polysciences, Warrington, PA, USA), incubated at room temperature for 15 minutes and added to the flasks. Approximately 48 hours after transfection, culture medium was changed to medium containing 2 µg/mL puromycin to select for transfected cells. After a further 48 hours, puromycin was removed and cells left to recover.

2.7.3 Screening of rMC-1 Müller cells with PKM2 knocked out

After the cells recovered following puromycin selection, they were propagated and gDNA extracted (~10 days after transfection) for KO screening by PCR (see section 2.5.8) using PKM2 KO screening forward and reverse primers which flank the targeted sites on the *Pkm* gene (Fig. 2.3). PCR products were analysed on 1% agarose gels.

2.7.4 Monoclonal isolation and screening

Monoclonal isolation of the WT, the PKM2 KO I and the PKM2 KO II cells was performed by limiting dilution. Cells were seeded in 96-well trays at a final concentration of 0.5 cells per well. When the cells reached confluency (approximately 2 weeks), they were propagated, and gDNA extracted for

PCR screening as in section 2.7.3. PCR products were gel-purified and analysed by Sanger sequencing using the PKM2 KO screening reverse primer. Proteins were extracted for analysis by western blotting to determine PKM2 and total PKM levels.

2.7.5 Metabolic analysis of monoclonal PKM2 knockout rMC-1 cell lines

One monoclonal line was chosen, based on the screening results, for each of the WT, the PKM2 KO I and the PKM2 KO II cells, for lactate and Seahorse assays as described in sections 2.2 and 2.3. Cells were seeded at 15,000 cells per well the day before Seahorse assays.

2.8 Data presentation and statistical analysis

Graphs were generated and statistically significant differences between experimental groups were determined using GraphPad Prism Version 8.0.0 software by either unpaired two-tailed student's t-tests (comparing between two experimental groups) or one-way analysis of variance (ANOVA) followed by Dunnett's multiple comparison test (comparing between more than two experimental groups). $p<0.05$ is considered statistically significant.

Chapter 3

Characterisation of the novel spontaneously immortalised rat Müller cell line SIRMu-1

CHAPTER 3: Characterisation of the novel spontaneously immortalised rat Müller cell line SIRMu-1

3.1 Introduction

MCs are a crucial and major type of glial cell in the retina, where they provide structural and functional support for retinal neurons (reviewed in (Bringmann et al., 2006) (Fig. 1.5). During the course of the current study where primary MCs were being utilised for metabolic analyses, a population of spontaneously immortalised cells arose from a batch of rat mixed retinal cultures, from which primary MC cultures were usually derived. A monoclonal cell line was isolated from these spontaneously immortalised cells, named the SIRMu-1 (Spontaneously Immortalised Rat Muller) cell line and characterised using western blotting, immunofluorescence, RNA-seq and transfection experiments. It was hypothesised that the SIRMu-1 cell line originated from primary MCs and the results were consistent with the hypothesis (see Paper 4 (Kittipassorn et al., 2019a) in section 3.3.1). These novel SIRMu-1 cells were compared directly to the primary MCs and the SV40-transformed rMC-1 cell line (Sarthy et al., 1998).

The work has been published in two publications in peer-review journals. The establishment and characterisation of the SIRMu-1 cell line were published in Paper 4 (Kittipassorn et al., 2019a) and additional information on RNA-seq data and methodology was published in Paper 5 (Kittipassorn et al., 2019b). The SIRMu-1 cell line has been deposited to CellBank Australia and is now available for distribution to researchers worldwide (http://www.cellbankaustralia.com/sirmu-1.html). The entire RNA-seq dataset has been deposited into NCBI Gene Expression Omnibus (Edgar et al., 2002) and is accessible through GEO ID: GSE123161 (https://www.ncbi.nlm.nih.gov/geo/query/acc.cgi?acc=GSE123161).

3.2 Chapter aims

This chapter addresses Aim 1 of the thesis: to establish and characterise a novel spontaneously immortalised rat MC line SIRMu-1.

3.3 Publications

Detailed introduction, experimental approach, materials and methods, results and discussion are presented in the following publications.

3.3.1 Paper 4: Characterization of the novel spontaneously immortalized rat Müller cell line SIRMu-1

Kittipassorn, T., Haydinger, C.D., Wood, J.P.M., Mammone, T., Casson, R.J., and Peet, D.J. (2019a). Characterization of the novel spontaneously immortalized rat Muller cell line SIRMu-1. Experimental eye research 181, 127-135.

https://doi.org/10.1016/j.exer.2019.01.013

Statement of Authorship

Title of Paper	Characterization of the novel spontaneously immortalized rat Müller cell line SIRMu-1	
Publication Status	☑ Published ☐ Submitted for Publication	☐ Accepted for Publication ☐ Unpublished and Unsubmitted work written in manuscript style
Publication Details	Kittipassorn, T., Haydinger, C.D., Wood, J.P.M., Mammone, T., Casson, R.J., Peet, D.J., 2019. Characterization of the novel spontaneously immortalized rat Muller cell line SIRMu-1. Experimental eye research 181, 127-135.	

Principal Author

Name of Principal Author (Candidate)	Thaksaon Kittipassorn		
Contribution to the Paper	Conceived the project. Planned experiments. Established, isolated and maintained the SIRMu-1 cell line in culture. Conducted most of the experimental work. Interpreted the results. Generated Table 2, Figure 1, Figure 2, Figure 3 and Figure 4D. Contributed to Table 1, Figure 4 and Supplementary figure S1. Wrote most of the manuscript. Reviewed and edited the manuscript. Please note that all of the experiments in this paper were performed during the period of my PhD, with the only exception of determining primary MC transfection efficiency (mentioned in the text in the paper in section 3.5 on page 133) which was performed during the period of my Honours degree and presented in my Honours thesis.		
Overall percentage (%)	65%		
Certification:	This paper reports on original research I conducted during the period of my Higher Degree by Research candidature and is not subject to any obligations or contractual agreements with a third party that would constrain its inclusion in this thesis. I am the primary author of this paper.		
Signature		Date	14/02/2019

Co-Author Contributions

By signing the Statement of Authorship, each author certifies that:

i. the candidate's stated contribution to the publication is accurate (as detailed above);

ii. permission is granted for the candidate in include the publication in the thesis; and

iii. the sum of all co-author contributions is equal to 100% less the candidate's stated contribution.

Name of Co-Author	Cameron D Haydinger		
Contribution to the Paper	Planned experiments. Interpreted the results. Analysed data for and generated Figure 4 and Supplementary figure S1. Wrote parts of the manuscript: the methods for analysing mRNA sequencing data (subsection 2.7 in the Materials and Methods section), and together with author Thaksaon Kittipassorn the results of the mRNA sequencing (subsection 3.4 in the Results section). Reviewed and edited the manuscript.		
Signature		Date	18/02/2019

Name of Co-Author	John PM Wood		
Contribution to the Paper	Planned experiments. Provided primary cell cultures. Together with author Thaksaon Kittipassorn conducted experiments for Figure 3. Interpreted the results. Reviewed and edited the manuscript.		
Signature		Date	190219

Name of Co-Author	Teresa Mammone		
Contribution to the Paper	Provided primary cell cultures. Together with author Thaksaon Kittipassorn contributed to Table 1. Reviewed and edited the manuscript.		
Signature		Date	19.02.2019

Name of Co-Author	Robert J Casson		
Contribution to the Paper	Conceived and supervised the project. Planned experiments. Interpreted the results. Reviewed and edited the manuscript.		
Signature		Date	14/02/2019

Name of Co-Author	Daniel J Peet		
Contribution to the Paper	Conceived and supervised the project. Planned experiments. Interpreted the results. Reviewed and edited the manuscript.		
Signature		Date	14/2/2019

Graphical abstract

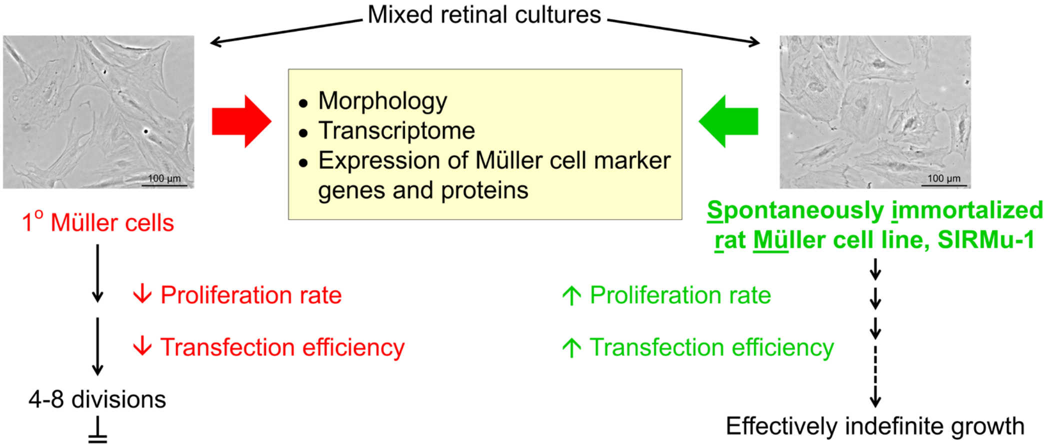

Mixed retinal cultures

1^{o} Müller cells

- Morphology
- Transcriptome
- Expression of Müller cell marker genes and proteins

Spontaneously immortalized rat Müller cell line, SIRMu-1

↓ Proliferation rate

↓ Transfection efficiency

4-8 divisions

↑ Proliferation rate

↑ Transfection efficiency

Effectively indefinite growth

Experimental Eye Research 181 (2019) 127–135

Contents lists available at ScienceDirect

Experimental Eye Research

journal homepage: www.elsevier.com/locate/yexer

Characterization of the novel spontaneously immortalized rat Müller cell line SIRMu-1

Thaksaon Kittipassorn[a,1], Cameron D. Haydinger[a], John P.M. Wood[b], Teresa Mammone[b], Robert J. Casson[b], Daniel J. Peet[a,*]

[a] *School of Biological Sciences, Molecular Life Sciences Building, University of Adelaide, Adelaide, SA, 5005, Australia*
[b] *Department of Ophthalmology and Visual Sciences, Adelaide Health and Medical Sciences Building, University of Adelaide, Adelaide, SA, 5000, Australia*

ARTICLE INFO

Keywords:
Müller cell
Spontaneously immortalized cell
SIRMu-1
Retina
Cell culture

ABSTRACT

Müller cells (MCs) play a crucial role in the retina, and cultured MC lines are an important tool with which to study MC function. Transformed MC lines have been widely used; however, the transformation process can also lead to unwanted changes compared to the primary cells from which they were derived. To provide an alternative experimental tool, a novel monoclonal spontaneously immortalized rat Müller cell line, SIRMu-1, was derived from primary rat MCs and characterized. Immunofluorescence, western blotting and RNA sequencing demonstrate that the SIRMu-1 cell line retains similar characteristics to cultured primary MCs in terms of expression of the MC markers cellular retinaldehyde-binding protein, glutamine synthetase, S100, vimentin and glial fibrillary acidic protein at both the mRNA and protein levels. Both the cellular morphology and overall transcriptome of the SIRMu-1 cells are more similar to primary rat MCs than the commonly used rMC-1 cells, a well-described, transformed rat MC line. Furthermore, SIRMu-1 cells proliferate rapidly, have an effectively indefinite life span and a high transfection efficiency. The expression of Y chromosome specific genes confirmed that the SIRMu-1 cells are derived from male MCs. Thus, the SIRMu-1 cell line represents a valuable experimental tool to study roles of MCs in both physiological and pathological states.

1. Introduction

Müller cells (MCs) are the major type of glial cell of the vertebrate retina. They have diverse functions, including mechanical support of the neural retina, removal of neurotransmitters from the extracellular space, spatial buffering of potassium cations, storage of glycogen, and possible transfer of substrates for cellular metabolic reactions to neighboring neurons (Bringmann et al., 2006; Vecino et al., 2016). Since they span the entire thickness of the retina, MCs have also been proposed to guide light through other retinal layers to photoreceptors in the outer nuclear layer, reducing light scattering and increasing visual acuity (Franze et al., 2007; Labin and Ribak, 2010). MCs undergo reactive gliosis in retinal diseases and injuries (Bringmann et al., 2006; Vecino et al., 2016). Stressed MCs have also been shown to dedifferentiate into multipotent progenitor cells which can subsequently differentiate into retinal neurons, including photoreceptors (Bringmann et al., 2006; Jadhav et al., 2009; Jayaram et al., 2014; Lawrence et al., 2007; Ramirez et al., 2012; Vecino et al., 2016). Experimental systems using cultured primary MCs enable detailed biochemical analysis of this important cell type, and allow chemical and genetic manipulation (Linser and Moscona, 1979; Sarthy, 1985; Savage et al., 1988). However, analysis of primary cells is restricted by difficulties in acquiring and maintaining the cells, slow proliferation rates, early senescence, and low transfection efficiency (Roque et al., 1997; Sarthy et al., 1998).

As an alternative to primary MCs, numerous studies use immortalized MCs, which proliferate rapidly, do not senesce and are relatively easy to maintain and manipulate. These immortalized MCs have been largely generated by transformation of primary cells with viral oncogenes. The rMC-1 and the RMC HPV-16 E6/E7 rat MC lines, for example, were immortalized by transfecting primary MCs with simian virus 40 (SV40) DNA and by transducing with human papillomavirus (HPV) type 16 E6 and E7 viral construct, respectively (Roque et al., 1997; Sarthy et al., 1998). However, the transformation process can alter other characteristics in addition to proliferation and life span

---

[*] Corresponding author.

E-mail addresses: thaksaon.kit@mahidol.ac.th (T. Kittipassorn), cameron.haydinger@adelaide.edu.au (C.D. Haydinger), john.wood2@sa.gov.au (J.P.M. Wood), teresa.mammone@adelaide.edu.au (T. Mammone), robert.casson@adelaide.edu.au (R.J. Casson), daniel.peet@adelaide.edu.au (D.J. Peet).

[1] Other affiliation/permanent address. Department of Physiology, Faculty of Medicine Siriraj Hospital, Mahidol University, 2 Wanglang Road, Bangkoknoi, Bangkok, 10700, Thailand.

https://doi.org/10.1016/j.exer.2019.01.013
Received 5 October 2018; Received in revised form 10 January 2019; Accepted 10 January 2019

List of abbreviations

CMF-HBSS	calcium- and magnesium-free Hank's balanced salt solution
cpm	count per million reads
CRALBP	cellular retinaldehyde-binding protein
DAPI	4′,6-diamidino-2-phenylindole dihydrochloride
DEGs	differentially expressed genes
FBS	fetal bovine serum
FDR	false discovery rate
GFAP	glial fibrillary acidic protein
GO	gene ontology
GS	glutamine synthetase
HBSS	Hank's balanced salt solution
HPV	human papillomavirus
MCs	Müller cells
MEM	minimal essential medium
mRNA-seq	mRNA sequencing
NG2	neuron glial antigen-2
PBS-HS	horse serum in phosphate-buffered saline
PEI	polyethylenimine
RPE	retinal pigmented epithelial
RPKM	reads per kilobase per million
SIRMu	spontaneously immortalized rat Müller cells
SIRMu-1	spontaneously immortalized rat Müller cell line
SV40	simian virus 40

compared to primary cells, such as cellular morphology (Sarthy et al., 1998) and metabolism (Bissell et al., 1972). Hence, spontaneously immortalized cell lines which have not been intentionally transformed by exogenous reagents often retain a greater similarity to primary cells than transformed cells, and therefore serve as more relevant experimental tools.

To provide an alternative and valuable model for MC research, we established and characterized a novel spontaneously immortalized rat Müller cell line, SIRMu-1. The MC-like characteristics of this monoclonal line are described in relation to primary rat MCs and the commonly-used transformed rat MC line rMC-1 (Sarthy et al., 1998), including cellular morphology, expression of MC and other retinal cell marker proteins, a comprehensive transcriptomic analysis and transfection efficiency.

2. Materials and methods

2.1. Primary rat mixed retinal, MC and retinal pigmented epithelial (RPE) cell cultures

Sprague-Dawley rats were used for the generation of primary MC cultures. Handling of these animals conformed to the Australian Code of Practice for the Care and Use of Animals for Scientific Purposes 2004, and the ARVO Statement for the Use of Animals in Ophthalmic and Vision Research. Mixed retinal cell cultures consisting of neurons, photoreceptors and glial cells were prepared from litters of 2–4 day post-natal pups using a trypsin-mechanical digest method as described previously (Wood et al., 2003, 2005). Briefly, freshly dissected rat pup retinas were incubated for 5 min in a shaking water bath in sterile incubation medium (5.4 mM KCl, 116 mM NaCl, 0.096 mM $NaH_2PO_4{\cdot}2H_2O$, 19.5 mM glucose, 0.15 mM $MgSO_4$, 23.8 mM $NaHCO_3$, 3 g/L bovine serum albumin, 10 mg/L phenol red) containing 0.1 mg/ml trypsin. After allowing tissue to settle for an additional 5 min, the trypsin/incubation medium was removed and replaced with incubation medium containing 1000 U DNAse (bovine pancreas, type II), soybean trypsin inhibitor (type I-S, 0.667 mg/ml) and 0.19 mM $MgSO_4$. After a further 5 min, trituration was carried out with a flame-rounded glass pipette until all tissue had been dissociated. After a brief centrifugation (180 g/5 min/4 °C) dissociated retinal cells were resuspended and then grown in minimal essential medium (MEM, + Earle's Salts, -L-glutamine, #11090, Life Technologies Australia, Scoresby, VIC, Australia) containing 10% fetal bovine serum (FBS), 87 mg/L gentamicin sulfate, 2.2 mg/L amphotericin B, 25 mM glucose and 2 mM L-glutamine. 25 mM glucose was used to facilitate attachment of primary cells in mixed retinal cell cultures. Cultures were maintained in a humidified incubator at 37 °C, 5% CO_2 without disruption for 7 days, and then continuously maintained with medium changed every 3 days for 28–42 days until almost all other cell types died and detached from the culture vessel surface, leaving predominantly MCs (Osborne, 1990; Wood et al., 2005). Once isolated, MC cultures were grown as above but with 20% FBS, and used at passage numbers 2–4 for experiments.

Production of primary RPE cell cultures was based on a method described previously (Mayerson et al., 1985). Litters of 10–12 day old Dark Agouti rat pups were used to generate cultures. Briefly, enucleated eyes from pups were washed in Hank's balanced salt solution (HBSS with 1.26 mM $CaCl_2$, 0.49 mM $MgCl_2.6H_2O$, 0.41 mM $MgSO_4.7H_2O$, #14025-092, Life Technologies Australia), containing 50 µg/ml gentamicin and 100 µg/ml kanamycin. Intact eyes were subsequently incubated in HBSS containing 100 U/ml collagenase and 50 U/ml hyaluronidase for 60 min followed by incubation in calcium- and magnesium-free HBSS (CMF-HBSS) containing 1 mg/ml trypsin for 60 min. Eyes were transferred to growth medium (MEM containing 2 mM L-glutamine, gentamicin/kanamycin as above, and 20% FBS), where they were opened via a circumferential incision immediately below the ora serrata and the anterior segment, and vitreous and retina were discarded. RPE sheets were brushed out of eye-cups in fresh growth medium, rinsed and incubated in CMF-HBSS containing 1 mg/ml trypsin for 5 min. RPE cells were mechanically dissociated, centrifuged (180 g/5 min/4 °C) and adjusted to 1000 cells/mm^3 in growth medium. Cultures were maintained in growth medium and were used at passage number 2 for experiments.

2.2. Establishment of a spontaneously immortalized rat MC line and monoclonal isolation

Rapidly-proliferating, spontaneously immortalized cells were derived from primary MCs in a mixed retinal cell culture and cultured in MEM containing 20% FBS (unless otherwise stated), 25 mM glucose and 2 mM glutamine at 37 °C with 5% CO_2. Cells were cultured in 25 mM glucose to keep the growth conditions consistent with the primary retinal cultures. A monoclonal line was isolated from these cells by 2 sequential rounds of single cell cloning by serial dilution. For each round, 4000 cells were added to well A1 of a 96-well plate. Serial ½ dilutions were performed vertically down the first column on the plate (wells A1-A8). Each of these wells were then serially diluted ½ horizontally across the plate. Culture medium was added to each well to give a final volume of 200 µl, and plates incubated for 14–20 days. Single clones were selected as a single colony of growth at the highest dilutions across the plate. After 2 sequential rounds of single cell isolation 8 monoclonal lines were generated, all of which retained a similar morphology to primary MCs and a rapid proliferation. One was expanded and named the spontaneously immortalized rat Müller cell line SIRMu-1. SIRMu-1 cells of passage numbers 6–22 were used for experiments.

2.3. Culture of the rMC-1 cell line

The rMC-1 cells were a kind gift of Dr Vijay Sarthy (Northwestern University, Chicago, IL, USA), obtained from Dr Binoy Appukuttan (Flinders University, Adelaide, SA, Australia), and maintained under the same conditions as the SIRMu-1 line but with 10% FBS. Cells of passage numbers 23–34 were used for experiments.

2.4. Immunocytochemical analysis

Immunofluorescence was performed as previously described (Wood et al., 2012) with minor modifications as outlined below. Cells seeded on coverslips, coated with 0.2% gelatin in phosphate-buffered saline (PBS), were fixed with 4% paraformaldehyde/PBS for 20 min, washed with PBS, permeabilized by incubating in 0.1% triton X-100/PBS for 15 min at room temperature, washed with PBS, and blocked with 3.3% (v/v) horse serum/PBS (PBS-HS) for 15 min at room temperature. Primary antibody incubation was performed overnight at room temperature using antibodies diluted in PBS-HS against vimentin, SV40 T-antigen, S100, glial fibrillary acidic protein (GFAP), rhodopsin, blue cone opsin, tau, CD11b, neuron glial antigen-2 (NG2), and RPE65 (Table 1). The following day, cells were incubated for 1 h at room temperature with secondary antibodies (1:250 to 1:500 dilutions; Life Technologies Australia): anti-mouse Alexa Fluor 594 (#A11005, #A21203), anti-rabbit Alexa Fluor 594 (#A21207), anti-rabbit Alexa Fluor 488 (#A21206), and anti-goat Alexa Fluor 594 (#A11058) antibodies. Nuclear counterstaining was performed with 500 ng/mL 4′,6-diamidino-2-phenylindole dihydrochloride (DAPI; #D8417, Sigma-Aldrich, Castle Hill, NSW, Australia). Cell coverslips were mounted onto glass slides with a fluorescence-protecting mounting medium (ProLong Gold Antifade Mountant, #P10144, Life Technologies Australia) and visualized using fluorescence microscopy (Nikon Eclipse Ti microscope, Nikon Australia, Rhodes, NSW, Australia).

2.5. Western blotting

Protein lysates were prepared in whole cell extract buffer (20 mM HEPES pH 7.8, 0.42 M NaCl, 0.5% Igepal, 25% glycerol, 0.2 mM EDTA, 1.5 mM $MgCl_2$ with freshly added 1 mM DTT, 1 mM PMSF, 2 μg/mL aprotinin, 4 μg/mL bestatin, 5 μg/mL leupeptin, and 1 μg/ml pepstatin), and quantified by Bio-rad protein assay (#5000006, Bio-Rad Laboratories, Gladesville, NSW, Australia). Equivalent amounts of total protein were separated on 10% SDS-PAGE and transferred to nitrocellulose membranes using a Trans-Blot Turbo Transfer System (Bio-Rad Laboratories). Membranes were blocked with 10% (w/v) skimmed milk in PBS containing 0.1% nonionic detergent (TWEEN20, #P1379, Sigma-Aldrich) for 1 h at room temperature, incubated overnight at 4 °C with primary antibodies for glutamine synthetase (GS), cellular retinaldehyde-binding protein (CRALBP), and α-tubulin (Table 1) diluted in 2% skimmed milk in 0.1%TWEEN20/PBS, and detected using horseradish peroxidase-conjugated secondary antibodies (goat anti-mouse IgG, #31430, Life Technologies Australia, and goat anti-rat IgG, #ab6845, Abcam, Melbourne, VIC, Australia; both at 1:5000 dilution) and visualized using chemiluminescence and a Bio-Rad ChemiDoc Imaging system (Bio-Rad Laboratories).

2.6. mRNA sequencing (mRNA-seq)

Primary MCs, SIRMu-1 and rMC-1 cells were trypsinised, pelleted and RNA extracted with a *mir*Vana miRNA Isolation Kit (#AM1561, Life Technologies Australia). RNA samples (4 biological replicates of primary MCs of passage numbers 3–4, 5 of SIRMu-1 cells of passage numbers 6–20, and 3 of rMC-1 cells of passage numbers 23–26 (Table 1 in Kittipassorn et al., 2019)) were submitted to the Australian Cancer Research Foundation (ACRF) Cancer Genomics Facility (Adelaide, SA, Australia), quality determined with an Agilent RNA 6000 Nano kit (#5067-1511, Agilent Technologies, Santa Clara, CA, USA) on an Agilent 2100 bioanalyzer and concentrations determined using a Qubit RNA HS assay kit (#Q32852, Life Technologies Australia). 5 ng of enriched polyA RNA was used for library preparation by a KAPA stranded RNAseq HyperPrep kit (#KK8544, KAPA, Cape Town, South Africa). Briefly, RNA was fragmented (approximate insert length: 200 base-pairs) and converted to cDNA, followed by end-repair and A-tailing. Adapters compatible with Illumina sequencing were ligated to the cDNA with an approximate adapter to molar insert ratio of 200:1, and a post-ligation clean-up to remove excess adapters performed. The libraries were amplified with 10 cycles of PCR and cleaned with 1 × ratio of beads. Library sizes and yields were confirmed using an Agilent High Sensitivity DNA kit (#5067-4626, Agilent Technologies) with an Agilent 2100 bioanalyzer and diluted to 4 nM stocks. Libraries were pooled in equimolar ratios and sequenced on an Illumina NextSeq 500 system using a 75 cycle high output kit (#FC-404-2005, Illumina, San Diego, CA, USA).

2.7. Analysis of mRNA-seq data

Sequencing reads were mapped to the reference rat genome (Rnor_6.0) using the STAR algorithm (Dobin et al., 2013). Raw count data were imported into R. Genes that were either not expressed or expressed at very low levels (not detected at greater than one count per million reads (cpm) for all samples of at least one group) were filtered out of the analysis. Counts for the remaining genes (10,236 genes) were normalized to library size and composition using the “TMM” method in Bioconductor's EdgeR package (McCarthy et al., 2012; Robinson et al., 2010). The TMM-normalized data were used for generation of the multidimensional scaling plot.

Differential expression was determined using Bioconductor's Limma package which employs a linear modelling approach (Ritchie et al., 2015). A fold-change threshold of 5 with a Benjamini-Hochberg corrected P-value of < 0.05 defined whether a gene was differentially expressed (Benjamini and Hochberg, 1995). Gene ontology (GO) analysis was also performed. Overrepresentation of GO-slim biological process terms (PANTHER annotation version 13.1, released 2018-02-03) among lists of differentially expressed genes, relative to the *Rattus norvegicus* reference list, was assessed using the PANTHER statistical overrepresentation test (released 2017-12-05) (Mi et al., 2017). Fisher's exact test with false discovery rate (FDR) correction was used, and terms with a FDR < 0.05 were considered overrepresented.

For generation of the heatmap showing expression of MC marker genes, TMM-normalized count data were further normalized to transcript length (downloaded from the Ensembl database, release 91 (Zerbino et al., 2018), Rnor_6.0, INSDC Assembly GCA_000001895.4) to obtain reads per kilobase per million (RPKM) for each gene, and log-transformed by taking $\log_2$ (RPKM + 1).

Table 1
Primary antibodies used in the present study.

Target protein	Species	Source[a]	Cat. No./clone	Dilution
vimentin	mouse	DAKO	V9	1:500^{IF}
SV40 T-antigen	mouse	Abcam	AB16879	1:50^{IF}
S100	rabbit	Sigma-Aldrich	S2644	1:50^{IF}
GFAP	rabbit	DAKO	Z033429	1:100^{IF}
GS	mouse	BD Bioscience	610517	1:250^{WB}
CRALBP	mouse	Life Technologies	MA1-813	1:250^{WB}
α-tubulin	rat	Novus Biologicals	NB600-506	1:2000^{WB}
rhodopsin	mouse	Abcam	AB3267	1:1000^{IF}
blue cone opsin	goat	Santa Cruz	SC-14363	1:2000^{IF}
Tau	rabbit	DAKO	A0024	1:5000^{IF}
CD11b	mouse	Ab D Serotec	MCA275R	1:500^{IF}
NG2	rabbit	Merk Millipore	AB5320	1:1000^{IF}
RPE65	mouse	Santa Cruz	SC-53489	1:1000^{IF}

[a] Source location: Abcam, Melbourne, VIC, Australia; Ab D Serotec, Kidlington, UK; BD Bioscience, Franklin Lakes, NJ, USA; DAKO, Sydney, NSW, Australia; Life Technologies Australia, Scoresby, Victoria, Australia; Merk Millipore, North Ryde, NSW, Australia; Novus Biologicals, Littleton, CO, USA; Santa Cruz Biotechnology, Paso Robles, CA, USA; Sigma-Aldrich, Castle Hill, NSW, Australia, ^{IF}dilution used for immunofluorescence; ^{WB}dilution used for western blotting.

2.8. Transfection efficiency

SIRMu-1 and rMC-1 cells were seeded into a 24-well plate (20,000 cells per well), and transfected 20–24 h later with a plasmid encoding nuclear Tomato fluorescence protein (500 ng per well) using either FuGENE HD (#E2311, Promega Australia, Alexandria, NSW, Australia), FuGENE 6 (#E2692, Promega Australia), Lipofectamine 2000 (#11668019, Life Technologies Australia) or Polyethylenimine (PEI) (#23966-1, Polysciences, Warrington, PA, USA) according to the manufacturers' instructions, at a transfection reagent:DNA ratio of 3:1. 24 h after transfection the cells were labelled with Hoechst 33342 nuclear stain (NucBlue Live ReadyProbes Reagent, #R37605, Life Technologies Australia) and imaged using fluorescence microscopy (Nikon Eclipse Ti microscope, Nikon Australia). Transfection efficiency was calculated from proportions of Tomato fluorescence-positive transfected cells to total cell numbers indicated by nuclear staining. Cell counts were performed on three different fields of vision for each sample using the Fiji (a distribution of ImageJ) software (Schindelin et al., 2012). Data are presented as mean ± SD of 3 independent experiments.

3. Results

3.1. Establishment and initial characterization of spontaneously immortalized rat Müller cells

Primary MC cultures were generated by continuous culturing for 28–42 days of mixed retinal cells derived from neonatal rat retinas, resulting in the loss of retinal neurons and other cell types to leave an almost homogeneous population of MCs (Osborne, 1990; Wood et al., 2005). The cultured primary MCs were typically large, flat and adherent with a unique “ghost-like” morphology, and a large nucleus (Fig. 1A) (Roque et al., 1997; Sarthy, 1985; Sarthy et al., 1998; Vecino et al., 2016; Wood et al., 2005). Primary rat MCs proliferate with a doubling time of approximately 7 days and typically senesce after 4 to 8 divisions.

After 28 days of culturing a batch of neonatal rat mixed retinal cells, a visible colony of rapidly-proliferating cells was observed. These large cells had a similar morphology to primary MCs (Fig. 1A). The proliferating cells were passaged and continued to rapidly proliferate beyond 12 weeks, well after the time which primary MCs would typically senesce (Sarthy, 1985). The doubling time of these cells was approximately 2–3 days, and they retained a MC-like morphology. As these cells had survived for more than 12 weeks *in vitro*, had been derived under the commonly-used conditions to generate primary MC cultures and had a characteristic morphology of MCs, it was hypothesized that they originated from primary MCs, and not another retinal cell type. These cells were maintained in culture, being passaged at 1:10 every 5–7 days. After 30 passages (approximately 7 months) these cells still proliferated rapidly and maintained a morphology similar to primary MCs (data not shown). Arising from primary cultures without having been transformed, they were named spontaneously immortalized rat Müller cells (SIRMu).

Initial characterization was performed on early passage number cells (passage number 6) to confirm that these SIRMu cells display common features of MCs. Analysis by immunocytochemistry clearly shows that the MC marker vimentin is expressed in the cytoplasm of every cell, similar to primary MCs and the transformed rMC-1 cell line (Fig. 1B). Since the SIRMu cells were established while the transformed rMC-1 cells were being cultured in the same facility, it was important to confirm that the SIRMu cells were unique, and not simply a potential contamination of primary MCs with rMC-1 cells, although the smaller, more elongated and spindle-like morphology of the rMC-1 cells (Fig. 1A) indicated that such a contamination was unlikely. Hence, the SIRMu cells were labelled for expression of the SV40 T-antigen used to generate the rMC-1 cells (Sarthy et al., 1998). Fig. 1C shows that as expected the rMC-1 cells label strongly for the nuclear SV40 T-antigen, while both the primary MCs and the SIRMu cells do not show any staining, demonstrating that the SIRMu cells are a unique line of spontaneously immortalized cells. These SIRMu cells have now been continuously cultured for more than 32 months and passaged over 140 times (greater than 400 population doublings), consistent with

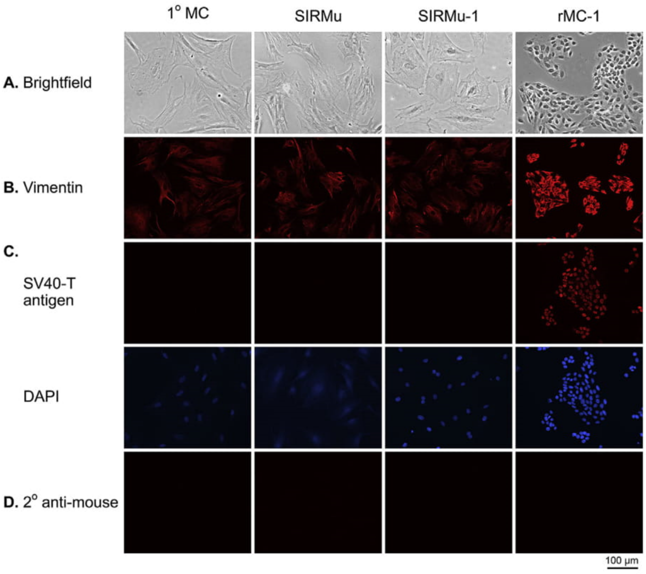

Fig. 1. Initial characterization of SIRMu and SIRMu-1 cells. Immunocytochemistry was performed on primary (1°) MCs, SIRMu, SIRMu-1 and rMC-1 cells. (**A**) Phase contrast images of cells fixed with 4% paraformaldehyde/PBS. Cells were labelled with primary antibodies targeting (**B**) vimentin and (**C**) SV40 T-antigen. (**D**) Anti-mouse Alexa Fluor 594 secondary (2°) antibody control, in the absence of primary antibody, for B and C. DAPI was used for nuclear staining. Scale bar = 100 μm and applies to all images.

effectively indefinite growth (Pirisi et al., 1987; Roque et al., 1997).

3.2. Monoclonal isolation of the SIRMu cells

To ensure purity of this spontaneously immortalized line, we generated a single monoclonal line by performing 2 sequential rounds of cell cloning by serial dilution on the SIRMu cells (from passage 9 of the original preparation). The first passage after the first serial dilution was defined as passage number 1 for the isolated monoclonal line. This monoclonal line had a similar proliferation rate and morphology to the original culture, and was named SIRMu-1. Immunocytochemistry demonstrated that the monoclonal SIRMu-1 cells do not express the SV40 T-antigen and hence were not derived from rMC-1 cells (Fig. 1C).

The SIRMu-1 cell line has been cultured in both 10% and 20% FBS, with estimated doubling times of 36 and 30 h, respectively. To date, it has been passaged over 40 times and has retained a similar morphology to primary MCs.

3.3. Marker protein expression of the SIRMu-1 cells

To validate that the SIRMu-1 cells were derived from MCs, immunocytochemistry was performed on primary MCs, SIRMu-1 and rMC-1 cells to detect expression of the commonly used MC markers vimentin and S100, in addition to the glial cell marker GFAP (Lewis et al., 1988; Limb et al., 2002; Roque et al., 1997; Sarthy et al., 1998) (Figs. 1B, 2A and 2B). The SIRMu-1 cells express all of these markers at similar levels to the primary MCs and the rMC-1 cells. Western blotting analysis of two other MC markers, which are associated with mature MCs, GS (Ji et al., 2017; Linser and Moscona, 1979; Sarthy, 1985) and CRALBP (Bunt-Milam and Saari, 1983; Sarthy et al., 1998) (Fig. 2D) show that both the SIRMu-1 and the rMC-1 cells express GS, but at a lower level compared to primary MCs, and that all 3 cell lines express a low level of CRALBP.

In addition to MCs, other retinal cell types can be present in mixed retinal cultures, including rod and cone photoreceptors, neurons, astrocytes, microglia, pericytes, and RPE cells (Wood et al., 2005, 2012). To confirm that the SIRMu-1 cells were not derived from other non-MC cell types, immunofluorescence was performed for expression of rhodopsin (a marker of rod photoreceptors), blue cone opsin (cone photoreceptors), tau (neurons), CD11b (microglia), NG2 (pericytes), and RPE65 (RPE cells) (Fig. 3). In contrast to mixed retinal cultures, in which distinct populations of cells positively label for rhodopsin, blue cone opsin, tau, CD11b and NG2, the SIRMu-1 cells do not show expression of any of these markers, with the exception of NG2 where low levels of staining slightly above background are visible (Fig. 3A–E). As expected, cultured primary rat RPE cells express RPE65, while the SIRMu-1 cells do not (Fig. 3I). Finally, although rat retinal astrocytes can also be immunoreactive to vimentin, S-100, GFAP and GS (Derouiche and Rauen, 1995; Mansour et al., 2008; Vecino et al., 2016), in culture they have a characteristic star shape with a smaller nucleus (Vecino et al., 2016) that is distinct from primary MCs and the SIRMu-1 cells, and they do not express the MC-specific marker CRALBP observed in the SIRMu-1 cells (Fig. 2D). Hence, it is clear that the SIRMu-1 were not derived from astrocytes. Taken together these data strongly support the hypothesis that the SIRMu-1 cells originated from primary MCs rather than any other retinal cell type, and that they retain MC-like characteristics, including their distinct morphology and the expression of MC marker proteins.

3.4. Transcriptomic analysis of the SIRMu-1, primary MCs, and the rMC-1

To further characterize the SIRMu-1 cell line, the transcriptomes of the SIRMu-1, primary MC and rMC-1 cells were analysed using mRNA-seq. RNA was isolated from 5 biological replicates of SIRMu-1 cells, 4 of primary MCs, and 3 of the rMC-1. To control for potential differences in gene expression between cell types being due to differences in culture media, 2 out of the 5 SIRMu-1 RNA samples were isolated from cells grown in the presence of the antibiotic gentamicin and the antifungal amphotericin B, to match the culture conditions of the primary MCs, whereas the other 3 samples were isolated from SIRMu-1 cells grown in the absence of these drugs, which is the usual culture condition of SIRMu-1 and rMC-1 cells. The total RNA was polyA enriched, barcoded and sequenced, with 44–84 million reads per sample (60 million average). Transcripts from 10,236 different genes were detected at significant levels in all cells.

Analysis of the sequences obtained showed that on average 98.25% of reads per sample (range of 97.91–98.47%) mapped successfully to the rat genome, confirming that all three lines are of rat origin. Based on overall gene expression, a multidimensional scaling plot shows clustering of the RNA-seq samples (Fig. 4A). Three distinct clusters of samples are evident, each representing one of the distinct cell types, indicating that the sequencing results were consistent among replicates within the same cell groups. Importantly, the multidimensional scaling plot demonstrates that the transcriptome of the SIRMu-1 cells is more similar to the transcriptome of the primary MCs than the rMC-1 transcriptome is to the primary MCs. These data also demonstrate that there are no large differences in gene expression profiles between all of the 5 SIRMu-1 samples, including the 2 samples derived from cells cultured in medium with gentamicin and amphotericin B, indicating that the two

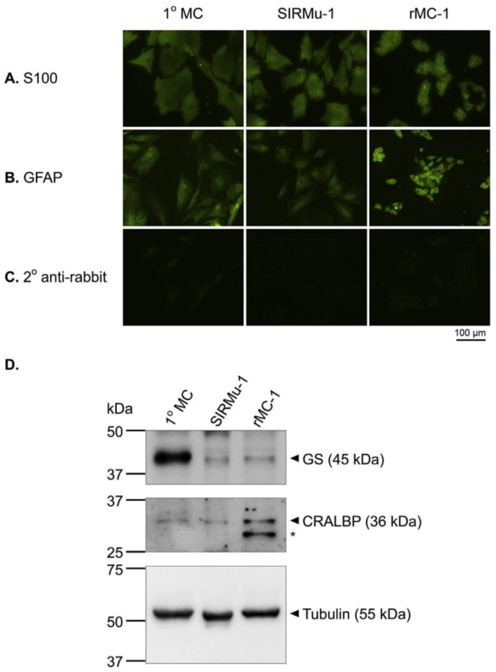

Fig. 2. Expression of MC markers in SIRMu-1 cells. Immunocytochemistry was performed on primary (1°) MCs, SIRMu-1 and rMC-1 cells, labelled for (**A**) S100 and (**B**) glial fibrillary acidic protein (GFAP). (**C**) Anti-rabbit Alexa Fluor 488 secondary (2°) antibody control, in the absence of primary antibody, for A and B. Scale bar = 100 µm and applies to all images. (**D**) Western blots of 1° MCs, SIRMu-1 and rMC-1 cells, probed for glutamine synthetase (GS) and cellular retinaldehyde-binding protein (CRALBP). Expected band size of each protein is shown in brackets. Arrows indicate target protein bands and asterisks indicate non-specific bands.

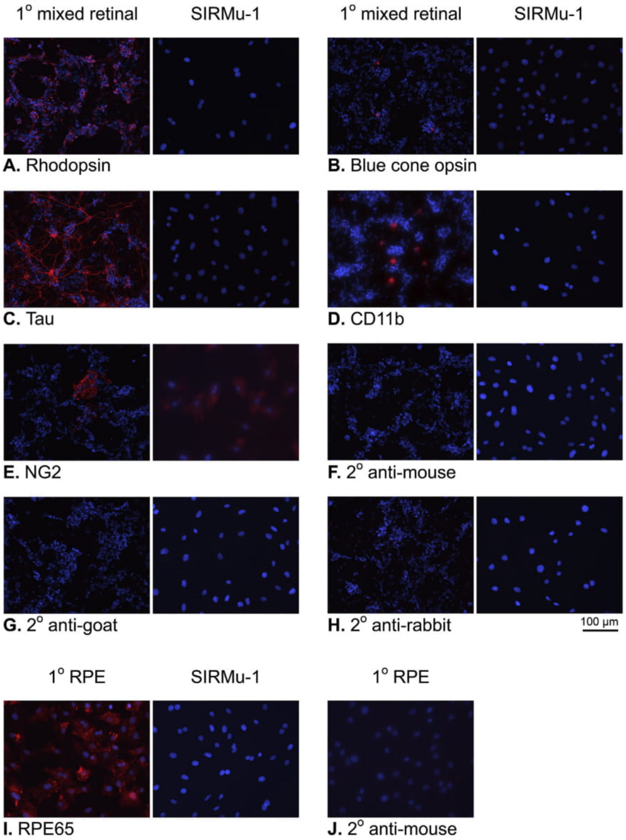

Fig. 3. Immunocytochemical analysis of retinal cell markers on SIRMu-1 cells. Primary (1°) mixed retinal cultures and SIRMu-1 cells were labelled for (**A**) rhodopsin, (**B**) blue cone opsin, (**C**) tau, (**D**) CD11b and (**E**) NG2. (**F**) Anti-mouse Alexa Fluor 594 secondary (2°) antibody control, in the absence of primary antibody, for A and D. (**G**) Anti-goat Alexa Fluor 594 secondary antibody control for B. (**H**) Anti-rabbit Alexa Fluor 594 secondary antibody control for C and E. (**I**) 1° retinal pigmented epithelial (RPE) cells and SIRMu-1 cells were stained for RPE65. (**J**) Anti-mouse Alexa Fluor 594 secondary antibody control for 1° RPE in I. See F for SIRMu-1 anti-mouse secondary antibody control. DAPI was used for nuclear staining. Scale bar = 100 μm and applies to all images.

drugs in the growth medium do not have a major effect on the transcriptome.

Transcriptomic differences between groups were further examined by comparing differentially expressed genes (DEGs) between each of the two immortalized cell lines and the primary MCs. Genes that were expressed at very low levels or not expressed in all groups were first filtered out of the analysis, leaving 10,236 genes that were tested for differential expression. Genes that were upregulated or downregulated greater than 5-fold compared to the primary MCs were considered differentially expressed. A total of 10,036 genes (98% of the 10,236 expressed genes) were not differentially expressed in the SIRMu-1 cell line compared to the primary MCs, with 200 genes differentially expressed. Among these 200 DEGs, 13 genes were upregulated and 187 were downregulated (Fig. 4B). In comparison, for the rMC-1 cells 9304 genes (91%) were not differentially expressed compared to the primary MCs, but 932 genes were, with 314 upregulated and 618 downregulated (Fig. 4B). These data indicate that both the SIRMu-1 and rMC-1 cell lines have a similar transcriptome to the primary MCs, but that the SIRMu-1 cells are more closely related to the primary MCs than are the rMC-1 cells.

Interestingly, among the 200 DEGs in the SIRMu-1 compared to primary MCs and the 932 DEGs in the rMC-1 compared to primary MCs, there were 126 genes in common (Supplementary Fig. S1A, Supplementary Table S1). For the remainder of the DEGs, 74 genes were differentially expressed uniquely in the SIRMu-1 cells, while 806 genes were differentially expressed uniquely in the rMC-1 cells (Supplementary Fig. S1A, Supplementary Table S1). To assess functional differences between each immortalized cell line and primary MCs, GO analyses were performed using the PANTHER classification system. The lists of genes differentially expressed in both cell lines with respect to primary MCs were classified by GO-Slim biological process terms, and statistically overrepresented terms were determined by comparison to their frequency in a reference rat genome. There were no statistically significantly (FDR < 0.05) overrepresented biological process terms among the 74 genes differentially expressed between SIRMu-1 cells and primary MCs, nor among the 126 genes differentially expressed in both cell lines compared to primary MCs, possibly due in part to the relatively low number of genes in these two groups. However, there was significant overrepresentation of terms among the 806 genes differentially expressed between rMC-1 cells and primary MCs. The top 10 such terms by fold-enrichment are shown in Supplementary Fig. S1B. Consistent with being a highly-proliferative transformed cell line, a large proportion of the DEGs in rMC-1 cells are involved in DNA replication and cell division-related processes.

Next, expression of the transcripts encoding the MC marker proteins were examined. The SIRMu-1 cells express similar levels of transcripts

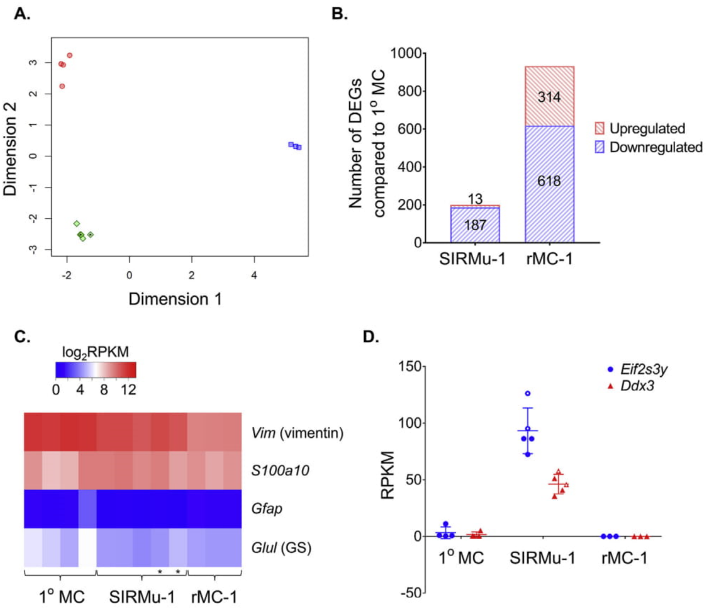

Fig. 4. mRNA sequencing of MCs. (**A**) Multidimensional scaling plot of normalized data for 12 RNA-seq samples. Red circles: primary (1°) MCs (4 biological replicates), Blue squares: rMC-1s (3 replicates), Green diamonds: SIRMu-1s (5 replicates). 2 SIRMu-1 samples grown in the presence of the antibiotic gentamicin and the antifungal amphotericin B are indicated by black dots. (**B**) Bar graph showing numbers of significantly differentially expressed genes (DEGs) which were either upregulated or downregulated at a fold-change of greater than 5 in SIRMu-1 and rMC-1 cells compared to 1° MCs. (**C**) Heatmap showing expression levels of MC marker genes. SIRMu-1 samples grown in the presence of gentamicin and amphotericin B are indicated by asterisks. RPKM, reads per kilobase per million. **(D)** Quantification of mRNA expression levels of two Y chromosome specific genes, *Eif2s3y* (blue circles) and *Ddx3* (red triangles), in the 3 MC lines. Expression level expressed in reads per kilobase per million (RPKM). Horizontal lines represent means and error bars ± SD. SIRMu-1 samples grown in the presence of gentamicin and amphotericin B are indicated by white dots.

encoding vimentin, S100, and GFAP to the primary MCs and rMC-1 cells, with transcripts encoding GFAP expressed at low levels (Fig. 4C). SIRMu-1 and rMC-1 cells also express GS transcripts, but at a lower level compared to the primary MCs (Fig. 4C). All cell types express CRALBP transcripts at very low levels with an average of 0.06, 0.15, and 1.16 cpm in primary MCs, SIRMu-1 and rMC-1 cells, respectively. These results are consistent with protein expression from immunocytochemical and western blotting analyses (Figs. 1, 2 and 4C). The relatively small difference in GS mRNA levels observed between primary MCs and the two immortalized lines shown in Fig. 4C is not of the same magnitude as the greater difference in protein levels demonstrated by western blotting in Fig. 2D, which is likely to be a consequence of post-transcriptional regulation.

Importantly, SIRMu-1 and rMC-1 cells express very low to undetectable levels of transcripts encoding rhodopsin, blue cone opsin, tau, CD11b, and RPE65, markers used in the immunofluorescence analysis that are characteristic of other retinal cell types including rod and cone photoreceptors, neurons, microglia, and RPE cells. Of note, while SIRMu-1 cells express transcripts encoding NG2, a pericyte marker, the levels are many fold lower than the vimentin transcripts in these cells (Fig. 4C), and primary MCs and rMC-1 cells also express NG2 at low levels. Together these data show that the SIRMu-1 cells display a MC-like transcriptomic profile, and also authenticate the MC characteristics of the rMC-1 cells used in the present study.

Finally, we examined the expression of gender-specific genes between the three different MC types. Compared to primary MCs, which were derived from mixed litters presumed to contain both male and female pups, the SIRMu-1 cells show an upregulation of two Y chromosome-specific genes, *Eif2s3y* and *Ddx3* (Fig. 4D), consistent with the SIRMu-1 cell line originating from a male pup. In contrast, *Eif2s3y* and *Ddx3* were not expressed at significant levels in the rMC-1 cell samples (Fig. 4D), nor were any other Y chromosome-specific genes, consistent with the rMC-1 cell line being derived from a female rat.

3.5. Transfection efficiency

One key advantage of most immortalized cell lines is high transfection efficiency with standard transfection reagents, such as cationic lipids, compared to primary cells. To determine transfection efficiency of the SIRMu-1 cell line, various commercially-available lipid-based transfection reagents were used to transfect SIRMu-1 cells with a fluorescence reporter gene, and transfection efficiency was measured using fluorescence microscopy (Table 2). The transfection efficiency of the SIRMu-1 cells is between 7 and 14%, which is similar to that achieved with the rMC-1 cells (6–24%), and approximately 10-fold higher than what we observed with the primary MCs (1.9%).

4. Discussion

Immortalized rat MC lines generated via transformation, such as rMC-1 (Sarthy et al., 1998), RMC HPV-16 E6/E7 (Roque et al., 1997) and TR-MUL5 (Tomi et al., 2003), have been used extensively for the analysis of MC function. Similar to the spontaneously immortalized human MC line MIO-M1 (Limb et al., 2002) and the spontaneously immortalized murine MC line QMMuC-1 (Augustine et al., 2018) serving as an alternative model for studying human and mouse MCs, respectively, the spontaneously immortalized SIRMu-1 cells described

Table 2
Transfection efficiency of SIRMu-1 and rMC-1 cells.

Transfection reagent	SIRMu-1[a]	rMC-1[a]
FuGENE HD	14 ± 7	16 ± 1
FuGENE 6	7 ± 6	6 ± 2
Lipofectamine 2000	13 ± 3	24 ± 6
PEI[b]	12 ± 2	15 ± 2

[a] Data are presented as mean ± SD of % transfection efficiency from 3 independent experiments.

[b] PEI, polyethylenimine.

here provide an alternative system for investigating MC function in rat cells not transformed with viral oncogenes. Although the mechanism of spontaneous immortalization remains to be ascertained, the SIRMu-1 cells appear capable of proliferating indefinitely.

SIRMu-1 cells, like transformed rMC-1 cells, display key characteristics of primary MCs, including the expression of an array of well-characterized MC marker proteins (Figs. 1B and 2) and genes (Fig. 4C). The presence of transcripts encoding the MC markers vimentin, GS and CRALBP (Fig. 4C) in all 3 types of MCs investigated in the present study is consistent with published reports on rat and mouse MC transcriptomes (Roesch et al., 2008; Ueno et al., 2017; Zhao et al., 2015). Furthermore, the lack of expression of key markers indicative of other major retinal cell types (Fig. 3) supports the conclusion that SIRMu-1 cells were derived from primary MCs.

Of note, the results are also consistent with the SIRMu-1 cells having been derived from mature MCs. The SIRMu-1 cells originated from a rat mixed retinal culture made from 2 to 4 day post-natal pups. While the generation of MCs is spread over a long period of retinal development between embryonic day 18 and post-natal day 12, in the rat retina one of the major peaks of MC genesis is between post-natal days 2–4 (Rapaport et al., 2004), where we produce mixed retinal cultures. At post-natal days 2–4, 50% of MCs have developed (Rapaport et al., 2004), supporting the presence of a significant proportion of mature MCs in these cultures. More importantly, similar to the primary MCs and the rMC-1 cells derived from adult rats, the SIRMu-1 cells express CRALBP and GS, which are markers associated with mature MCs (Bunt-Milam and Saari, 1983; Ji et al., 2017; Linser and Moscona, 1979; Sarthy, 1985; Sarthy et al., 1998). The SIRMu-1 cells also display a characteristic cellular morphology of cultured primary adult rat MCs. (Roque et al., 1997; Sarthy, 1985; Sarthy et al., 1998).

While most MC markers were expressed at similar levels when comparing the two immortalized lines and the primary MCs, at both the mRNA and protein levels, the SIRMu-1 and the rMC-1 cell lines express GS at a lower level than the primary MCs (Figs. 2D and 4C). GS catalyzes the conversion of glutamate to glutamine in MCs, playing an important role in the neurotransmitter recycling process, an essential function of MCs in support of retinal neurons (Bringmann et al., 2006; Vecino et al., 2016). The decreased GS expression levels may reflect changes due to extended propagation in culture in the absence of retinal neurons, consistent with previous studies (Germer et al., 1997; Hauck et al., 2003; Lewis et al., 1989, 1999; Roque et al., 1997). Similarly, this may also explain the low expression levels of the MC marker CRALBP in all 3 types of MCs investigated (Fig. 2D). CRALBP in MCs *in vivo* is involved in the recycling of photopigments derived from photoreceptors (Das et al., 1992); the absence of functional light-sensitive photoreceptors and prolonged culture likely leads to a decrease in CRALBP expression (Hauck et al., 2003; Lewis et al., 1989; Pfeffer et al., 2016). In addition, our finding that the cultured MCs express GFAP (Figs. 2B and 4C) is consistent with a number of published studies (Limb et al., 2002; Roque et al., 1997; Sarthy et al., 1998). Given that expression of GFAP can be induced in MCs under reactive gliosis and/or during injury or stress (Bringmann et al., 2006), the presence of GFAP in the SIRMu-1 cell cultures and cultured MCs in other studies above likely reflects differences in culturing MCs compared to their *in vivo* retinal environment. However, the relatively low GFAP expression levels in all 3 MC types in this study suggest that the culture conditions employed do not cause major stress to the cells.

Overall, the transcriptome of the SIRMu-1 cells closely resembles the transcriptome of primary MCs. The rMC-1 cells are also transcriptomically similar to the primary MCs but to a lesser degree than are the SIRMu-1 cells. While the rMC-1 cells do have a greater number of genes showing differential expression when compared to the primary MCs than the SIRMu-1 cells (Fig. 4B), this may be in part a function of the more consistent gene expression profiles among the independent rMC-1 samples (revealed in the close clustering for rMC-1 samples in Fig. 4A). Not surprisingly, genes encoding proteins involved in DNA replication and cell cycle/division were overrepresented in the rapidly-proliferating rMC-1 transcriptomes compared to the primary MCs (Supplementary Fig. S1B). In contrast, DNA replication and cell cycle/division were not overrepresented in the list of genes differentially expressed between the rapidly-proliferating SIRMu-1 cells and the primary MCs, even when the stringency of differential expression was reduced to 2-fold (data not shown). This may reflect differences between transformation with viral oncogenes and the spontaneous immortalization observed here on cell proliferation, or it may be that a transcriptomic analysis of more SIRMu-1 samples is required to detect significant changes in expression of genes contributing to cellular proliferation. Furthermore, the rMC-1 cells were derived from adult rats (Sarthy et al., 1998) which may contribute to the bigger transcriptomic differences observed here between these cells and the primary neonatal rat MCs used in this study, compared to between the SIRMu-1 and the primary MCs. It is important to note, however, that the SIRMu-1 cells retaining the distinct large, flat, ghost-like shape are morphologically similar to both cultured primary adult rat MCs (Roque et al., 1997; Sarthy, 1985; Sarthy et al., 1998) and cultured primary neonatal rat MCs (Wood et al., 2005) (Fig. 1A), in contrast to the smaller, fibroblast-like morphology of the rMC-1 cells (Sarthy et al., 1998) (Fig. 1A). Given the well-established sex-related differences in retinal function (Chaychi et al., 2015; Wagner et al., 2008), the male genotype of SIRMu-1 cells compared to the female genotype of rMC-1 cells (Fig. 4D) also represents another important difference. It is also noteworthy that while the SIRMu-1 cells are transcriptomically and morphologically similar to primary MCs, other metabolic or functional properties of these cells are not compared.

In summary, we present the establishment and characterization of the SIRMu-1 cell line, which to our knowledge is the first spontaneously immortalized cell line derived from primary rat MCs. SIRMu-1 cells display similar morphology and gene expression profiles to primary MCs, but proliferate more rapidly, have an effectively indefinite life span, and are more amenable to transfection. Thus, these SIRMu-1 cells comprise a valuable new tool for investigation of MC function and roles in retinal health and disease.

Data accessibility

The RNA-seq data discussed in this article have been deposited in NCBI Gene Expression Omnibus (Edgar et al., 2002) and are accessible through GEO ID: GSE123161. (https://www.ncbi.nlm.nih.gov/geo/query/acc.cgi?acc=GSE123161).

Declarations of interest for all authors

None.

Funding

This work was supported by a project grant from the National Health and Medical Research Council of Australia (109932). The funding source has no involvement in the conduct of experiments, data analysis and interpretation, the preparation of the manuscript and the decision to submit the work for publication.

Author contributions

T.K. conceived the project, planned experiments, carried out experimental work, interpreted the results, and wrote the paper. C.D.H. planned experiments, interpreted the results, and wrote the paper. J.P.M.W. planned experiments, provided primary cell cultures, carried out experimental work, interpreted the results, and edited the paper. T.M. provided primary cell cultures, and edited the paper. R.J.C. and D.J.P. conceived and supervised the project, planned experiments, interpreted the results, and edited the paper.

Acknowledgements

The authors thank Joel Geoghegan, Andreas Schreiber, Wendy Parker and Ming Lin (ACRF Cancer Genomics Facility, Adelaide, SA, Australia) for their assistance with the RNA-seq, and members of the Peet and Whitelaw laboratories and Onruedee Khantisitthiporn (University of Adelaide, SA, Australia) for helpful discussion and technical assistance.

Appendix A. Supplementary data

Supplementary data to this article can be found online at https://doi.org/10.1016/j.exer.2019.01.013.

References

Augustine, J., Pavlou, S., O'Hare, M., Harkin, K., Stitt, A., Curtis, T., Xu, H., Chen, M., 2018. Characterization of a spontaneously immortalized murine muller glial cell line QMMuC-1. Invest. Ophthalmol. Vis. Sci. 59, 1666–1674.

Benjamini, Y., Hochberg, Y., 1995. Controlling the false discovery rate: a practical and powerful approach to multiple testing. J. Roy. Stat. Soc. B (Method) 57, 289–300.

Bissell, M.J., Hatie, C., Rubin, H., 1972. Patterns of glucose metabolism in normal and virus-transformed chick cells in tissue culture. J. Natl. Cancer Inst. 49, 555–565.

Bringmann, A., Pannicke, T., Grosche, J., Francke, M., Wiedemann, P., Skatchkov, S.N., Osborne, N.N., Reichenbach, A., 2006. Muller cells in the healthy and diseased retina. Prog. Retin. Eye Res. 25, 397–424.

Bunt-Milam, A.H., Saari, J.C., 1983. Immunocytochemical localization of two retinoid-binding proteins in vertebrate retina. J. Cell Biol. 97, 703–712.

Chaychi, S., Polosa, A., Lachapelle, P., 2015. Differences in retinal structure and function between aging male and female sprague-dawley rats are strongly influenced by the estrus cycle. PLoS One 10, e0136056.

Das, S.R., Bhardwaj, N., Kjeldbye, H., Gouras, P., 1992. Muller cells of chicken retina synthesize 11-cis-retinol. Biochem. J. 285 (Pt 3), 907–913.

Derouiche, A., Rauen, T., 1995. Coincidence of L-glutamate/L-aspartate transporter (GLAST) and glutamine synthetase (GS) immunoreactions in retinal glia: evidence for coupling of GLAST and GS in transmitter clearance. J. Neurosci. Res. 42, 131–143.

Dobin, A., Davis, C.A., Schlesinger, F., Drenkow, J., Zaleski, C., Jha, S., Batut, P., Chaisson, M., Gingeras, T.R., 2013. STAR: ultrafast universal RNA-seq aligner. Bioinformatics 29, 15–21.

Edgar, R., Domrachev, M., Lash, A.E., 2002. Gene Expression Omnibus: NCBI gene expression and hybridization array data repository. Nucleic Acids Res. 30, 207–210.

Franze, K., Grosche, J., Skatchkov, S.N., Schinkinger, S., Foja, C., Schild, D., Uckermann, O., Travis, K., Reichenbach, A., Guck, J., 2007. Muller cells are living optical fibers in the vertebrate retina. Proc. Natl. Acad. Sci. U. S. A 104, 8287–8292.

Germer, A., Jahnke, C., Mack, A., Enzmann, V., Reichenbach, A., 1997. Modification of glutamine synthetase expression by mammalian Muller (glial) cells in retinal organ cultures. Neuroreport 8, 3067–3072.

Hauck, S.M., Suppmann, S., Ueffing, M., 2003. Proteomic profiling of primary retinal Muller glia cells reveals a shift in expression patterns upon adaptation to in vitro conditions. Glia 44, 251–263.

Jadhav, A.P., Roesch, K., Cepko, C.L., 2009. Development and neurogenic potential of Muller glial cells in the vertebrate retina. Prog. Retin. Eye Res. 28, 249–262.

Jayaram, H., Jones, M.F., Eastlake, K., Cottrill, P.B., Becker, S., Wiseman, J., Khaw, P.T., Limb, G.A., 2014. Transplantation of photoreceptors derived from human Muller glia restore rod function in the P23H rat. Stem Cells Transl. Med. 3, 323–333.

Ji, H.P., Xiong, Y., Zhang, E.D., Song, W.T., Gao, Z.L., Yao, F., Sun, H., Zhou, R.R., Xia, X.B., 2017. Which has more stem-cell characteristics: muller cells or Muller cells derived from in vivo culture in neurospheres? Am. J. Transl. Res. 9, 611–619.

Kittipassorn, T., Haydinger, C.D., Wood, J.P.M., Mammone, T., Casson, R.J., Peet, D.J., 2018. RNA sequencing data of cultured primary rat Müller cells, the spontaneously immortalized rat Müller cell line, SIRMu-1, and the SV40-transformed rat Müller cell line, rMC-1. Submitted to Elsevier, Data in Brief.

Labin, A.M., Ribak, E.N., 2010. Retinal glial cells enhance human vision acuity. Phys. Rev. Lett. 104, 158102.

Lawrence, J.M., Singhal, S., Bhatia, B., Keegan, D.J., Reh, T.A., Luthert, P.J., Khaw, P.T., Limb, G.A., 2007. MIO-M1 cells and similar muller glial cell lines derived from adult human retina exhibit neural stem cell characteristics. Stem Cell. 25, 2033–2043.

Lewis, G., Mervin, K., Valter, K., Maslim, J., Kappel, P.J., Stone, J., Fisher, S., 1999. Limiting the proliferation and reactivity of retinal Muller cells during experimental retinal detachment: the value of oxygen supplementation. Am. J. Ophthalmol. 128, 165–172.

Lewis, G.P., Erickson, P.A., Guerin, C.J., Anderson, D.H., Fisher, S.K., 1989. Changes in the expression of specific Muller cell proteins during long-term retinal detachment. Exp. Eye Res. 49, 93–111.

Lewis, G.P., Kaska, D.D., Vaughan, D.K., Fisher, S.K., 1988. An immunocytochemical study of cat retinal Muller cells in culture. Exp. Eye Res. 47, 855–868.

Limb, G.A., Salt, T.E., Munro, P.M., Moss, S.E., Khaw, P.T., 2002. In vitro characterization of a spontaneously immortalized human Muller cell line (MIO-M1). Invest. Ophthalmol. Vis. Sci. 43, 864–869.

Linser, P., Moscona, A.A., 1979. Induction of glutamine synthetase in embryonic neural retina: localization in Muller fibers and dependence on cell interactions. Proc. Natl. Acad. Sci. U. S. A 76, 6476–6480.

Mansour, H., Chamberlain, C.G., Weible 2nd, M.W., Hughes, S., Chu, Y., Chan-Ling, T., 2008. Aging-related changes in astrocytes in the rat retina: imbalance between cell proliferation and cell death reduces astrocyte availability. Aging Cell 7, 526–540.

Mayerson, P.L., Hall, M.O., Clark, V., Abrams, T., 1985. An improved method for isolation and culture of rat retinal pigment epithelial cells. Invest. Ophthalmol. Vis. Sci. 26, 1599–1609.

McCarthy, D.J., Chen, Y., Smyth, G.K., 2012. Differential expression analysis of multifactor RNA-Seq experiments with respect to biological variation. Nucleic Acids Res. 40, 4288–4297.

Mi, H., Huang, X., Muruganujan, A., Tang, H., Mills, C., Kang, D., Thomas, P.D., 2017. PANTHER version 11: expanded annotation data from Gene Ontology and Reactome pathways, and data analysis tool enhancements. Nucleic Acids Res. 45, D183–D189.

Osborne, N.N., 1990. Stimulatory and inhibitory actions of excitatory amino acids on inositol phospholipid metabolism in rabbit retina. Evidence for a specific quisqualate receptor subtype associated with neurones. Exp. Eye Res. 50, 397–405.

Pfeffer, B.A., Xu, L., Porter, N.A., Rao, S.R., Fliesler, S.J., 2016. Differential cytotoxic effects of 7-dehydrocholesterol-derived oxysterols on cultured retina-derived cells: dependence on sterol structure, cell type, and density. Exp. Eye Res. 145, 297–316.

Pirisi, L., Yasumoto, S., Feller, M., Doniger, J., DiPaolo, J.A., 1987. Transformation of human fibroblasts and keratinocytes with human papillomavirus type 16 DNA. J. Virol. 61, 1061–1066.

Ramirez, M., Hernandez-Montoya, J., Sanchez-Serrano, S.L., Ordaz, B., Ferraro, S., Quintero, H., Pena-Ortega, F., Lamas, M., 2012. GABA-mediated induction of early neuronal markers expression in postnatal rat progenitor cells in culture. Neuroscience 224, 210–222.

Rapaport, D.H., Wong, L.L., Wood, E.D., Yasumura, D., LaVail, M.M., 2004. Timing and topography of cell genesis in the rat retina. J. Comp. Neurol. 474, 304–324.

Ritchie, M.E., Phipson, B., Wu, D., Hu, Y., Law, C.W., Shi, W., Smyth, G.K., 2015. Limma powers differential expression analyses for RNA-sequencing and microarray studies. Nucleic Acids Res. 43, e47.

Robinson, M.D., McCarthy, D.J., Smyth, G.K., 2010. edgeR: a Bioconductor package for differential expression analysis of digital gene expression data. Bioinformatics 26, 139–140.

Roesch, K., Jadhav, A.P., Trimarchi, J.M., Stadler, M.B., Roska, B., Sun, B.B., Cepko, C.L., 2008. The transcriptome of retinal Muller glial cells. J. Comp. Neurol. 509, 225–238.

Roque, R.S., Agarwal, N., Wordinger, R.J., Brun, A.M., Xue, Y., Huang, L.C., Nguyen, L.P., Shay, J.W., 1997. Human papillomavirus-16 E6/E7 transfected retinal cell line expresses the Muller cell phenotype. Exp. Eye Res. 64, 519–527.

Sarthy, P.V., 1985. Establishment of Muller cell cultures from adult rat retina. Brain Res. 337, 138–141.

Sarthy, V.P., Brodjian, S.J., Dutt, K., Kennedy, B.N., French, R.P., Crabb, J.W., 1998. Establishment and characterization of a retinal Muller cell line. Invest. Ophthalmol. Vis. Sci. 39, 212–216.

Savage, F.J., Day, J.E., Hogg, P., Grierson, I., 1988. Tissue culture of retinal glial cells. Eye 2 (Suppl. l), S164–S179.

Schindelin, J., Arganda-Carreras, I., Frise, E., Kaynig, V., Longair, M., Pietzsch, T., Preibisch, S., Rueden, C., Saalfeld, S., Schmid, B., Tinevez, J.Y., White, D.J., Hartenstein, V., Eliceiri, K., Tomancak, P., Cardona, A., 2012. Fiji: an open-source platform for biological-image analysis. Nat. Methods 9, 676–682.

Tomi, M., Funaki, T., Abukawa, H., Katayama, K., Kondo, T., Ohtsuki, S., Ueda, M., Obinata, M., Terasaki, T., Hosoya, K., 2003. Expression and regulation of L-cystine transporter, system xc-, in the newly developed rat retinal Muller cell line (TR-MUL). Glia 43, 208–217.

Ueno, K., Iwagawa, T., Ochiai, G., Koso, H., Nakauchi, H., Nagasaki, M., Suzuki, Y., Watanabe, S., 2017. Analysis of Muller glia specific genes and their histone modification using Hes1-promoter driven EGFP expressing mouse. Sci. Rep. 7, 3578.

Vecino, E., Rodriguez, F.D., Ruzafa, N., Pereiro, X., Sharma, S.C., 2016. Glia-neuron interactions in the mammalian retina. Prog. Retin. Eye Res. 51, 1–40.

Wagner, H., Fink, B.A., Zadnik, K., 2008. Sex- and gender-based differences in healthy and diseased eyes. Optometry 79, 636–652.

Wood, J.P., Chidlow, G., Graham, M., Osborne, N.N., 2005. Energy substrate requirements for survival of rat retinal cells in culture: the importance of glucose and monocarboxylates. J. Neurochem. 93, 686–697.

Wood, J.P., Mammone, T., Chidlow, G., Greenwell, T., Casson, R.J., 2012. Mitochondrial inhibition in rat retinal cell cultures as a model of metabolic compromise: mechanisms of injury and neuroprotection. Invest. Ophthalmol. Vis. Sci. 53, 4897–4909.

Wood, J.P., Schmidt, K.G., Melena, J., Chidlow, G., Allmeier, H., Osborne, N.N., 2003. The beta-adrenoceptor antagonists metipranolol and timolol are retinal neuroprotectants: comparison with betaxolol. Exp. Eye Res. 76, 505–516.

Zerbino, D.R., Achuthan, P., Akanni, W., Amode, M.R., Barrell, D., Bhai, J., Billis, K., Cummins, C., Gall, A., Girón, C.G., Gil, L., Gordon, L., Haggerty, L., Haskell, E., Hourlier, T., Izuogu, O.G., Janacek, S.H., Juettemann, T., To, J.K., Laird, M.R., Lavidas, I., Liu, Z., Loveland, J.E., Maurel, T., McLaren, W., Moore, B., Mudge, J., Murphy, D.N., Newman, V., Nuhn, M., Ogeh, D., Ong, C.K., Parker, A., Patricio, M., Riat, H.S., Schuilenburg, H., Sheppard, D., Sparrow, H., Taylor, K., Thormann, A., Vullo, A., Walts, B., Zadissa, A., Frankish, A., Hunt, S.E., Kostadima, M., Langridge, N., Martin, F.J., Muffato, M., Perry, E., Ruffier, M., Staines, D.M., Trevanion, S.J., Aken, B.L., Cunningham, F., Yates, A., Flicek, P., 2018. Ensembl 2018. Nucleic Acids Res. 46, D754–D761.

Zhao, M., Andrieu-Soler, C., Kowalczuk, L., Paz Cortes, M., Berdugo, M., Dernigoghossian, M., Halili, F., Jeanny, J.C., Goldenberg, B., Savoldelli, M., El Sanharawi, M., Naud, M.C., van Ijcken, W., Pescini-Gobert, R., Martinet, D., Maass, A., Wijnholds, J., Crisanti, P., Rivolta, C., Behar-Cohen, F., 2015. A new CRB1 rat mutation links Muller glial cells to retinal telangiectasia. J. Neurosci. Official J. Soc. Neurosci. 35, 6093–6106.

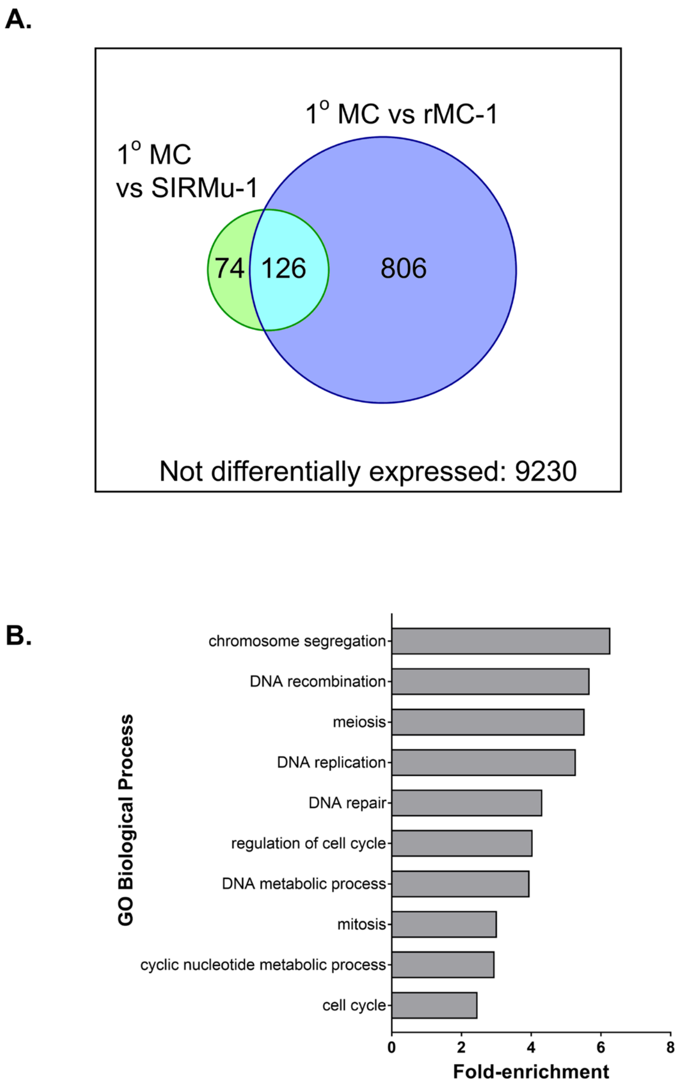

Supplementary Fig. S1. Differentially expressed genes in SIRMu-1 and rMC-1 cells, compared to primary (1°) MCs. **(A)** Venn diagram displaying the number of significantly differentially expressed genes at a fold-change of greater than 5 in each immortalized cell line compared to 1° MCs. **(B)** Gene ontology (GO) analysis of RNA-seq data. Bar graph showing significantly overrepresented ($FDR < 0.05$) PANTHER GO-Slim Biological Process terms among genes differentially expressed in rMC-1 cells relative to primary MCs, compared to the background *R. norvegicus* genome.

Supplementary table S1. See Appendix 7.5

3.3.2 Paper 5: RNA sequencing data of cultured primary rat Müller cells, the spontaneously immortalized rat Müller cell line, SIRMu-1, and the SV40-transformed rat Müller cell line, rMC-1.

Kittipassorn, T., Haydinger, C.D., Wood, J.P.M., Mammone, T., Casson, R.J., and Peet, D.J. (2019b). RNA sequencing data of cultured primary rat Müller cells, the spontaneously immortalized rat Müller cell line, SIRMu-1, and the SV40-transformed rat Müller cell line, rMC-1. Data in Brief 23, 103721.

https://doi.org/10.1016/j.dib.2019.103721

Statement of Authorship

Title of Paper	RNA sequencing data of cultured primary rat Müller cells, the spontaneously immortalized rat Müller cell line, SIRMu-1, and the SV40-transformed rat Müller cell line, rMC-1.
Publication Status	☑ Published ☐ Accepted for Publication ☐ Submitted for Publication ☐ Unpublished and Unsubmitted work written in manuscript style
Publication Details	Kittipassorn, T., Haydinger, C.D., Wood, J.P.M., Mammone, T., Casson, R.J., Peet, D.J., 2019. RNA sequencing data of cultured primary rat Müller cells, the spontaneously immortalized rat Müller cell line, SIRMu-1, and the SV40-transformed rat Müller cell line, rMC-1. Data Brief 23, 103721.

Principal Author

Name of Principal Author (Candidate)	Thaksaon Kittipassorn		
Contribution to the Paper	Conceived the project. Planned experiments and conducted experimental work. Generated Table 1. Contributed to preparing mRNA sequencing data for submission to the NCBI Gene Expression Omnibus (GEO) repository. Wrote the manuscript. Reviewed and edited the manuscript.		
Overall percentage (%)	65%		
Certification:	This paper reports on original research I conducted during the period of my Higher Degree by Research candidature and is not subject to any obligations or contractual agreements with a third party that would constrain its inclusion in this thesis. I am the primary author of this paper.		
Signature		Date	01/05/2019

Co-Author Contributions

By signing the Statement of Authorship, each author certifies that:

i. the candidate's stated contribution to the publication is accurate (as detailed above);

ii. permission is granted for the candidate in include the publication in the thesis; and

iii. the sum of all co-author contributions is equal to 100% less the candidate's stated contribution.

Name of Co-Author	Cameron D Haydinger		
Contribution to the Paper	Planned experiments. Prepared and submitted mRNA sequencing data to the NCBI Gene Expression Omnibus (GEO) repository. Reviewed and edited the manuscript.		
Signature		Date	01/05/2019

Name of Co-Author	John PM Wood		
Contribution to the Paper	Planned experiments. Provided primary cell cultures. Reviewed and edited the manuscript.		
Signature		Date	190219

Name of Co-Author	Teresa Mammone		
Contribution to the Paper	Provided primary cell cultures. Reviewed and edited the manuscript.		
Signature		Date	19.02.2019

Name of Co-Author	Robert J Casson		
Contribution to the Paper	Conceived and supervised the project. Planned experiments. Reviewed and edited the manuscript.		
Signature		Date	14/02/2019

Name of Co-Author	Daniel J Peet		
Contribution to the Paper	Conceived and supervised the project. Planned experiments. Reviewed and edited the manuscript.		
Signature		Date	14/2/2019

Data in brief 23 (2019) 103721

Contents lists available at ScienceDirect

Data in brief

journal homepage: www.elsevier.com/locate/dib

Data Article

RNA sequencing data of cultured primary rat Müller cells, the spontaneously immortalized rat Müller cell line, SIRMu-1, and the SV40-transformed rat Müller cell line, rMC-1

Thaksaon Kittipassorn [a, 1], Cameron D. Haydinger [a], John P.M. Wood [b], Teresa Mammone [b], Robert J. Casson [b], Daniel J. Peet [a, *]

[a] *School of Biological Sciences, Molecular Life Sciences Building, University of Adelaide, Adelaide, SA 5005, Australia*
[b] *Department of Ophthalmology and Visual Sciences, Adelaide Health and Medical Sciences Building, University of Adelaide, Adelaide, SA 5000, Australia*

ARTICLE INFO

Article history:
Received 12 January 2019
Received in revised form 23 January 2019
Accepted 25 January 2019
Available online 7 March 2019

ABSTRACT

Müller cells (MCs), the major type of glial cell of the vertebrate retina, have a vital role in retinal physiology and pathology. They provide structural and functional support for retinal neurons, including photoreceptors, and are implicated in various retinal diseases. Primary and immortalized MCs are important experimental tools for MC research. Here we present high throughput RNA sequencing data of 3 populations of cultured rat MCs: primary cells, the spontaneously immortalized rat MC line, SIRMu-1, and the SV40-transformed rat MC line, rMC-1. These data were deposited in NCBI Gene Expression Omnibus (GEO ID: GSE123161). For data analysis, interpretation and discussion, please refer to the research article, “Characterization of the novel spontaneously immortalized rat Müller cell line SIRMu-1” (Kittipassorn et al., 2019). This dataset is valuable for gaining insight

---

[*] Corresponding author.
E-mail addresses: thaksaon.kit@mahidol.ac.th (T. Kittipassorn), cameron.haydinger@adelaide.edu.au (C.D. Haydinger), john.wood2@sa.gov.au (J.P.M. Wood), teresa.mammone@adelaide.edu.au (T. Mammone), robert.casson@adelaide.edu.au (R.J. Casson), daniel.peet@adelaide.edu.au (D.J. Peet).
[1] Other affiliation/permanent address. Department of Physiology, Faculty of Medicine Siriraj Hospital, Mahidol University, 2 Wanglang Road, Bangkoknoi, Bangkok 10700, Thailand.

https://doi.org/10.1016/j.dib.2019.103721

into gene expression profiles of different types of cultured MCs and the roles of MCs in health and disease.

Specifications table

Subject area	*Biology, Ophthalmology*
More specific subject area	*Retinal Müller cell (MC) gene expression*
Type of data	*In the article* - *RNA sample information table* *In NCBI Gene Expression Omnibus* - *Raw: fastq files (one per sample)* - *Processed: csv files (one per sample) containing reads per gene (un-normalized and before any filtering)* - *Summary: tsv file containing TMM-normalized* log2 *counts per million reads (cpm) for all samples*
How data was acquired	*mRNA sequencing by an Illumina NextSeq 500 system*
Data format	*Raw and processed data*
Experimental factors	*3 different populations of cultured MCs*
Experimental features	*Total RNA was extracted from cultured primary rat MC cells, the spontaneously immortalized rat MC line, SIRMu-1* [1], *and the SV40-transformed rat MC line, rMC-1* [2]. *cDNA libraries were prepared from enriched polyA RNA and sequenced.*
Data source location	*Adelaide, Australia*
Data accessibility	*Data available in the article and in NCBI Gene Expression Omnibus* [3] *(GEO ID:* GSE123161*)* *(*https://www.ncbi.nlm.nih.gov/geo/query/acc.cgi?acc=GSE123161*).*
Related research article	*Kittipassorn, T., Haydinger, C.D., Wood, J.P.M., Mammone, T., Casson, R.J., Peet, D.J., Characterization of the novel spontaneously immortalized rat Müller cell line SIRMu-1, Exp. Eye. Res. 181 (2019) 127-135.* *https://doi.org/10.1016/j.exer.2019.01.013* [1]

Value of the data

- Commonly and differentially expressed genes can be identified between 3 distinct MC populations, providing invaluable information about the similarity between the different cells, as well as important functional differences.
- The rat MC transcriptomic data can be compared with MCs from a range of species from other published analyses to elucidate unique and similar gene expression patterns, signaling pathways and functions of MCs in different organisms.
- The ability to determine the origin and nature of a novel cell line.
- The data facilitate informed selection based on gene expression of appropriate MC lines to be used as an experimental tool.

1. Data

The data presented here are mRNA sequencing analyses of 3 populations of cultured rat MCs: primary cells, the novel spontaneously immortalized rat MC line, SIRMu-1 [1], and the SV40-transformed rat MC line, rMC-1 [2]. RNA samples were extracted from 4 biological replicates of primary MCs, 5 biological replicates of SIRMu-1 cells, and 3 biological replicates of rMC-1 cells. Table 1 in this article provides details on each sample, including the passage number and growth conditions of cells from which the samples were isolated. The data relating to this article are stored in NCBI Gene Expression Omnibus [3] (GEO ID: GSE123161), including: fastq files containing raw sequencing reads (one per sample, 12 in total); csv files containing numbers of reads per gene (un-normalized and

Table 1
RNA sample information.

Cell type	Sample name	Source	Passage no.[a] of cells used for RNA extraction	Gentamicin and amphotericin B present in culture medium?
Primary MC	P1T1_4	First litter, culture tray 1	4	Yes
	P1T2_4	First litter, culture tray 2	4	Yes
	P2a_3	Second litter	3	Yes
	P3b_3	Third litter	3	Yes
SIRMu-1	S4_6	A frozen vial, passage no. 4	6	No
	S4_11	Same as S4_6	11	No
	S4_11A	Same as S4_6	11	Yes
	S10_11	A frozen vial, passage no. 10	11	No
	S10_20A	Same as S10_11	20	Yes
rMC-1	R22_23	A frozen vial, passage no. 22	23	No
	R22_26	Same as R22_23	26	No
	R24_26	A frozen vial, passage no. 24	26	No

[a] No., number.

unfiltered, one per sample, 12 in total); a tsv file containing TMM-normalized log2 counts per million reads for all 12 samples. Please refer to the related research article [1] for details on data processing.

2. Experimental design, materials and methods

2.1. Cell culture

Primary rat MC cultures were prepared as described previously [1]. Briefly, mixed retinal cultures, consisting of retinal neurons and glial cells, were generated from 2 to 4 day post-natal Sprague-Dawley rat pups. Handling of these animals complied with the Australian Code of Practice for the Care and Use of Animals for Scientific Purposes 2004, and the ARVO Statement for the Use of Animals in Ophthalmic and Vision Research. The cultures were maintained in minimal essential medium (MEM, +Earle's Salts, -L-glutamine, #11090, Life Technologies Australia, Scoresby, VIC, Australia) containing 10% fetal bovine serum (FBS), 87 mg/L gentamicin sulfate, 2.2 mg/L amphotericin B, 25 mM glucose and 2 mM L-glutamine. 25 mM glucose is routinely used in our laboratories with neurons/glial cultures as a lower glucose concentration can lead to problems with cell attachment. After 7 days without any disturbance, the medium of the mixed retinal cultures was changed and the cultures were maintained for 28–42 days with medium changed every 3 days until almost all other cells died, leaving a near homogenous population of MCs. The isolated primary MCs were cultured in the same medium as above but with 20% FBS and passaged at 1:2 when confluent, approximately every 7 days. The SIRMu-1 cell line was cultured in the same medium as the primary MCs with the exception of gentamicin and amphotericin B (unless otherwise stated), and was passaged at 1:4 every 3–4 days. For the rMC-1 cell line (a kind gift of Dr Vijay Sarthy, Northwestern University, Chicago, IL, USA, obtained from Dr Binoy Appukuttan, Flinders University, Adelaide, SA, Australia), the same medium as the SIRMu-1 cells was used but with 10% FBS. rMC-1 cells were passaged at 1:10 every 2–3 days.

2.2. RNA extraction

Total RNA was extracted from 4 biological replicates of primary MCs, 5 replicates of SIRMu-1 cells, and 3 replicates of rMC-1 cells (Table 1), using a mirVana miRNA Isolation Kit (#AM1561, Life Technologies Australia) according to the manufacturer's instructions. The antibiotic gentamicin and the antifungal amphotericin B are routinely used to culture primary MCs to prevent contamination as the cells come directly from animals, but these drugs are not used for the culture of immortalized cells. To control for potential differences in transcriptome due to the absence or presence of gentamicin and amphotericin B in culture medium, 2 of the 5 SIRMu-1 samples were extracted from cells grown in medium containing the two drugs, while the other 3 SIRMu-1 samples and all rMC-1 samples were from cells grown without the drugs (Table 1).

2.3. Library preparation and mRNA sequencing

RNA samples were submitted to the Australian Cancer Research Foundation (ACRF) Cancer Genomics Facility (Adelaide, SA, Australia). Sample quality was determined on an Agilent 2100 bioanalyzer with an Agilent RNA 6000 Nano kit (#5067-1511, Agilent Technologies, Santa Clara, CA, USA) to confirm that RIN values were above 7 (unless concentrations too low to accurately determine RIN), and concentrations determined using a Qubit RNA HS assay kit (#Q32852, Life Technologies Australia). Libraries were prepared by a KAPA stranded RNAseq HyperPrep kit (#KK8544, KAPA, Cape Town, South Africa) using 5 ng of enriched polyA RNA. RNA was fragmented (approximate insert length: 200 basepairs) and converted to cDNA. End-repair and A-tailing were then performed. Adapters compatible with Illumina sequencing were ligated to the cDNA using a concentration of 1.5 μM with an approximate adapter to molar insert ratio of 200:1. Next, a post-ligation clean-up was carried out to remove excess adapters. The libraries were amplified with 10 cycles of PCR and cleaned with 1X ratio of beads. Library yields and sizes were confirmed on an Agilent 2100 bioanalyzer with an Agilent High Sensitivity DNA kit (#5067-4626, Agilent Technologies) and diluted to 4 nM stocks. Libraries were pooled in equimolar ratios and sequenced using a 75 cycle high output kit (#FC-404-2005, Illumina, San Diego, CA, USA) on an Illumina NextSeq 500 system.

Acknowledgements

The authors thank Joel Geoghegan, Andreas Schreiber, Ming Lin, and Wendy Parker (ACRF Cancer Genomics Facility, Adelaide, SA, Australia) for their assistance with the RNA sequencing. This work was supported by a National Health and Medical Research Council of Australia project grant (1099932). The funding source has no involvement in the conduct of experiments, data collection, manuscript preparation and the decision to submit the work for publication.

Transparency document

Transparency document associated with this article can be found in the online version at https://doi.org/10.1016/j.dib.2019.103721.

References

[1] T. Kittipassorn, C.D. Haydinger, J.P.M. Wood, T. Mammone, R.J. Casson, D.J. Peet, Characterization of the novel spontaneously immortalized rat Müller cell line SIRMu-1, Exp. Eye Res. 181 (2019) 127–135. https://doi.org/10.1016/j.exer.2019.01.013.
[2] V.P. Sarthy, S.J. Brodjian, K. Dutt, B.N. Kennedy, R.P. French, J.W. Crabb, Establishment and characterization of a retinal Müller cell line, Investig. Ophthalmol. Vis. Sci. 39 (1) (1998) 212–216.
[3] R. Edgar, M. Domrachev, A.E. Lash, Gene Expression Omnibus: NCBI gene expression and hybridization array data repository, Nucleic Acids Res. 30 (1) (2002) 207–210. https://doi.org/10.1093/nar/30.1.207.

Chapter 4

Metabolic characterisation of retinal Müller cells

CHAPTER 4: Metabolic characterisation of retinal Müller cells

4.1 Introduction

Studies have suggested that the retina displays a preference for undertaking glycolytic metabolism even in the presence of an adequate supply of oxygen; this is synonymous with the Warburg effect, an unusual form of glucose metabolism (reviewed in Paper 1 (Ng et al., 2015) (Appendix 7.1)) (Cohen and Noell, 1960; Tornquist and Alm, 1979; Warburg, 1925; Warburg et al., 1924; Warburg et al., 1930; Winkler, 1981, 1995). The Warburg effect is commonly found in cancer and other highly proliferating cells (Abdel-Haleem et al., 2017; Hsu and Sabatini, 2008; Koppenol et al., 2011; Palsson-McDermott and O'Neill, 2013; Rodriguez-Prados et al., 2010; Vander Heiden et al., 2009; Warburg, 1956; Warburg et al., 1927), but has also been observed in freshly-isolated guinea pig MCs (Poitry-Yamate et al., 1995), cultured primary human MCs (Winkler et al., 2000), and immortalised rMC-1 cells (Winkler et al., 2003).

An initial aim of this chapter was to investigate whether cultured primary rat MCs also display the Warburg effect similarly to species described above. This investigation included comparison of whether the SV40-transformed rMC-1 line (Sarthy et al., 1998) and the novel spontaneously immortalised SIRMu-1 line identified and characterised in Chapter 3 (Kittipassorn et al., 2019a) display similar glucose metabolism to primary MCs.

Key parameters of glucose metabolism include oxygen consumption or carbon dioxide production as indicators of OXPHOS, and lactate production or extracellular acidification as commonly-used indicators of glycolytic flux. In the current literature, the Warburg effect is often defined as upregulated aerobic glycolysis (Koppenol et al., 2011; Potter et al., 2016; Vander Heiden et al., 2009) but it is variable as to what constitutes “upregulation”, i.e. upregulated to what extent. Therefore, in the context of this thesis, the Warburg effect is defined as when cells primarily depend on glycolysis rather than OXPHOS for ATP production, and hence undergo a high rate of glycolysis, including high lactate production, relative to oxygen consumption under normoxic conditions.

To investigate whether a cell type displays the Warburg effect, oxygen consumption, extracellular acidification and lactate production need to be determined. Firstly, the techniques required for the measurement of these parameters were developed and optimised as they had not previously been utilised in our laboratory. Secondly, the techniques were used to analyse metabolism of glucose in MCs.

4.2 Chapter aims

This chapter addresses Aim 2 of the thesis: to determine whether cultured rat MCs display the Warburg effect, with specific aims as follows:

Aim 2.1: To develop and optimise techniques for metabolic analysis

Aim 2.2: To characterise metabolism of glucose in cultured primary rat MCs

Aim 2.3: To characterise metabolism of glucose in the SV40-transformed rat MC line rMC-1 and the spontaneously immortalised rat MC line SIRMu-1 compared to primary MCs

4.3 Experimental approach and overview

To develop techniques to analyse cellular metabolism of glucose, the highly specialised Seahorse XF extracellular flux analyser (Agilent Technologies) with Seahorse Cell Mito Stress Test assays to measure oxygen consumption and extracellular acidification were employed and optimised. After successful optimisation, the Seahorse extracellular flux assays were utilised, together with colourimetric plate-based lactate assays to determine lactate production, for analysis of the three different rat MCs: primary MCs and the immortalised rMC-1 and SIRMu-1 cell lines.

Metabolic analysis showed that cultured primary rat MCs and rMC-1 cells display the Warburg effect and are metabolically similar. In contrast, the SIRMu-1 cells are highly oxidative.

4.4 Results

4.4.1 Optimisation of metabolic analysis techniques

Colourimetric plate-based lactate assays (BioVision) were well-established and did not require significant optimisation. For oxygen consumption and extracellular acidification, two techniques were assessed: fluorescence plate reader-based assays (Luxcel Biosciences) and the Seahorse XFe96 extracellular flux analyser (Agilent Technologies). These assay systems were chosen as they are commonly used in published metabolic studies (Divakaruni et al., 2014; Favre et al., 2010; Hynes et al., 2013; Mookerjee et al., 2017; Mookerjee et al., 2015; Papkovsky and Zhdanov, 2015; Zhdanov et al., 2011). Both fluorescence plate reader-based assays and the Seahorse extracellular flux analyser are high throughput techniques, which enable measurement of samples in a 96-well plate format, and do not require large amounts of biological samples. They therefore have advantages over classical methods, such as the Clark electrode (Li and Graham, 2012) which is more difficult to use and requires a large number of cells that must be able to withstand extended suspension to enable measurement of oxygen consumption (Divakaruni et al., 2014).

MitoXpress Xtra oxygen consumption assays (Luxcel Biosciences) and pH-Xtra glycolysis assays (Luxcel Biosciences) are multi-well plate-based fluorescence assays that can be used to measure oxygen consumption and extracellular acidification, respectively. The MitoXpress Xtra assay utilises an oxygen-sensing fluorophore which is quenched by oxygen. Therefore, when the fluorophore is added to the culture medium surrounding the cells, the amount of fluorescence emitted is inversely proportional to the oxygen concentration within the medium and hence, is directly proportional to the oxygen consumption of the cells. The pH-Xtra glycolysis assay utilises a H^+-sensing fluorophore. When the fluorophore is added to the culture medium surrounding the cell, the amount of fluorescence emitted is directly proportional to the level of acidification of the medium. These assays were optimised and could be used to measure cellular OCRs and ECARs. However, the assays had limited sensitivity with a relatively long time period required to show changes in oxygen consumption and extracellular acidification. In addition, OCRs and ECARs had to be measured using two distinct assay kits described above, in two different trays of cells. Therefore, OCRs and ECARs of the same biological samples could not be measured and directly compared. With these limitations, these assays were not pursued any further.

The Seahorse XF extracellular flux analyser is considered the gold standard for measuring oxygen consumption and extracellular acidification in living cells. The Seahorse XFe96 system consists of a specialised 96-well cell culture microplate, a sensor cartridge with 96 probes (one probe per well, each containing two fluorophores, one sensing changes in oxygen concentration in assay medium and the other sensing changes in pH), the actual Seahorse extracellular flux analyser and the Wave control software. To perform an assay, cells are seeded into the specialised culture plate in a monolayer and placed in the analyser along with a sensor cartridge. Changes in oxygen and pH are measured in the assay medium in each well in real time by each of the probes of the sensor cartridge for multiple cycles. In each cycle, probes are lowered to 200 μm above the monolayer of cells in the cell culture plate, creating a transient micro-chamber within each well, in which changes in oxygen concentration and pH are measured simultaneously in the same biological sample and reported as OCR and ECAR, respectively. The probes are then lifted and the assay medium in the whole wells mixed so that the levels of oxygen and pH are returned to baseline levels. In the next cycle, the probes get lowered into the corresponding wells of the cell plate again and the measurements repeated. There are also four drug ports surrounding each of the sensor probes in the sensor cartridge. The four ports lie above the corresponding well of the cell culture tray during the assay and each port can be programmed to inject a drug into the well at a specified time. With these numerous advantages, investigation into the ability of the Seahorse analyser to efficiently and accurately analyse oxygen consumption and extracellular acidification in cells was undertaken.

4.4.2 Measuring oxygen consumption and extracellular acidification by a Seahorse extracellular flux analyser

The main focus of the thesis is to assess oxygen consumption and extracellular acidification of cells in the basal state, particularly OCRs that are due to mitochondrial respiration and $ECAR_{basal}$. These data can be directly obtained from a Seahorse XF Cell Mito Stress Test, which is specifically designed for assessing mitochondrial metabolism as well as basal cellular glycolytic activity and glycolytic reserve (see figure 2.1 and section 2.3.3.1 in Chapter 2 for details).

In a Cell Mito Stress Test, inhibitors targeting the ETC (Fig. 2.1B) are serially injected into wells at specific time points to determine cellular responses, generating the typical Seahorse metabolic OCR profile (Fig. 2.1A, upper panel). The OCR from the cells prior to treatment represents respiration rate in the basal state, i.e. OCR_{basal}. The first compound, oligomycin, inhibits ATP synthase (complex V) (Fig. 2.1B), resulting in a decrease in oxygen consumption (Fig. 2.1A, upper panel). The second compound, FCCP, uncouples oxygen consumption from ATP synthesis (Fig. 2.1B), resulting in maximal oxygen consumption (Fig. 2.1A, upper panel). The third injection is comprised of rotenone and antimycin A (Rot/AA), which inhibit complexes I and III, respectively (Fig. 2.1B), and thereby completely inhibit OXPHOS, leaving remaining OCR due to non-mitochondrial respiration (Fig. 2.1A, upper panel). Using these inhibitors, several metabolic parameters can be derived, including basal mitochondrial respiration (OCR_{mito}), oxygen consumption that is coupled to ATP production ($OCR_{coupled}$) and non-mitochondrial respiration ($OCR_{non\text{-}mito}$) (see figure 2.1 and sections 2.3.3.1 and 2.3.3.4 in Chapter 2).

As the Seahorse analyser measures OCRs and ECARs simultaneously, a kinetic profile of ECARs that corresponds to the OCRs can also be obtained (Fig. 2.1A, middle panel). The ECAR from the cells prior to treatment represents extracellular acidification in the basal state, i.e. $ECAR_{basal}$. Oligomycin, which inhibits ATP synthase, results in an increase in ECAR, indicating cellular glycolytic reserve, i.e. an increased glycolytic activity to compensate for the loss of ATP production from the inhibition of OXPHOS (see figure 2.1 and section 2.3.3.2 in Chapter 2).

To get accurate and reliable results from these Seahorse assays, cell-specific optimisation of seeding density and concentrations of the mitochondrial inhibitors as well as normalisation factors are required.

4.4.2.1 Optimising FCCP concentrations

High doses of FCCP are required for complete uncoupling of oxygen consumption from ATP production, and the concentration required varies significantly between cell types. However, if concentrations of FCCP used are too high, this compound becomes toxic to cells leading to a decrease in observed OCR responses. Therefore, FCCP concentrations need to be optimised to determine the lowest FCCP concentration that gives the highest response (highest OCR). Therefore, initial Cell Mito Stress Tests were performed to determine the optimal FCCP concentrations for primary MCs (Fig. 4.1A) and rMC-1 cells (Fig. 4.1B). Assay medium used was a standard media as per the manufacturer's recommendations: Seahorse XF base medium with glucose (10 mM), glutamine (2 mM) and sodium pyruvate (1 mM). For both cell populations, the OCRs were elevated with increasing concentrations of FCCP from 0.125 up to 0.5 μM, with the 0.5 and 1 μM concentrations resulting in similar OCRs, indicating that the response has reached a plateau. Of note, in rMC-1 cells 2 μM FCCP was also tested (Fig. 4.1B), and led to a decreased response which indicated that when used at 2 μM, FCCP was toxic. As 0.5 μM was the lowest concentration that produced the highest response, it was chosen for subsequent experiments.

Importantly, the experiments also show that OCRs and ECARs could be quantitatively and simultaneously measured in real time, and responses of the cells to each compound of the Cell Mito Stress Tests could be immediately detected (Fig. 4.1). In addition, the responses observed were consistent with expected typical Seahorse Cell Mito Stress Test OCR and ECAR profiles (Fig. 2.1A upper and middle panels), with OCR decreasing and ECAR increasing after the addition of oligomycin, OCR increasing after the addition of FCCP, and OCR decreasing after the addition of Rot/AA.

4.4.2.2 Optimising cell seeding density

Optimal cell seeding density is another important prerequisite for metabolic analysis using the Seahorse analyser. Optimal seeding density is one which results in the cells not being completely confluent at the time of the assay (resulting in weak or dead cells as well as an unintentionally hypoxic environment, all of which could affect metabolism) and which gives OCR_{basal} and $ECAR_{basal}$ in an optimal range (OCR_{basal} of 20-160 pmol/min and $ECAR_{basal}$ of 10-90 mpH/min, Agilent Technologies user manual). In this thesis, the MCs investigated are all adherent cells, so the cells were seeded the day before each assay. It is noteworthy that for some cell types there may not be an optimal seeding density that fulfils all of the above requirements, as this is dependent on the characteristics of a specific cell population, including culture composition (homogeneous or heterogeneous), cell size, proliferation rate, preference for glycolysis or OXPHOS and metabolic activity.

Cell seeding densities for primary MCs (Fig. 4.2A) and rMC-1 cells (Fig. 4.2B) were optimised. After it was established and characterised (Paper 4 (Kittipassorn et al., 2019a) in Chapter 3), the novel SIRMu-1 cell line was also included in the analysis (Fig. 4.2C). As the ultimate aim was to analyse glucose metabolism of MCs, the assay medium used here was Seahorse XF base medium with 10 mM glucose as the sole substrate. Although 10 mM glucose is above normal blood glucose levels (Potter et al., 2016; Wang et al., 1997a, b), it is recommended by the manufacturer to use in the assay medium as a saturating concentration is necessary to ensure that cellular metabolism is not limited by the amount of the energy substrate. For primary MCs, two cell seeding densities (15,000 and 20,000 cells/well) were tested, with 15,000 cells/well resulting in the cells being 80-100% confluent before the assay and giving OCR_{basal} and $ECAR_{basal}$ within the desired ranges (Fig. 4.2A). This density was then chosen for subsequent experiments. Similar results were obtained with rMC-1 cells where 15,000 cells/well was found to be the optimal cell seeding density (Fig. 4.2B). For SIRMu-1 cells, four cell seeding densities (5000; 10,000; 15,000 and 20,000 cells/well) were investigated (Fig 4.2C). The 5000 cell/well seeding density resulted in 95-100% cell confluency but both OCR_{basal} and $ECAR_{basal}$ were lower than the recommended ranges. The other higher seeding densities led to OCR_{basal} being within the range, but the cells appeared overgrown at the time of the assay (slightly overgrown in the 10,000 cells/well group and highly overgrown in the other two groups). In addition, even with the cells being overgrown, all of the three higher seeding densities gave $ECAR_{basal}$ values that were lower than the desired range. Therefore, as there was no seeding density that perfectly fit the criteria, the density of 10,000 cells/well was chosen for subsequent experiments as it gave optimal OCR_{basal} and the cells were only slightly overgrown. These results also indicate that SIRMu-1 cells display very low ECARs compared to the other two MCs.

Figure 4.1

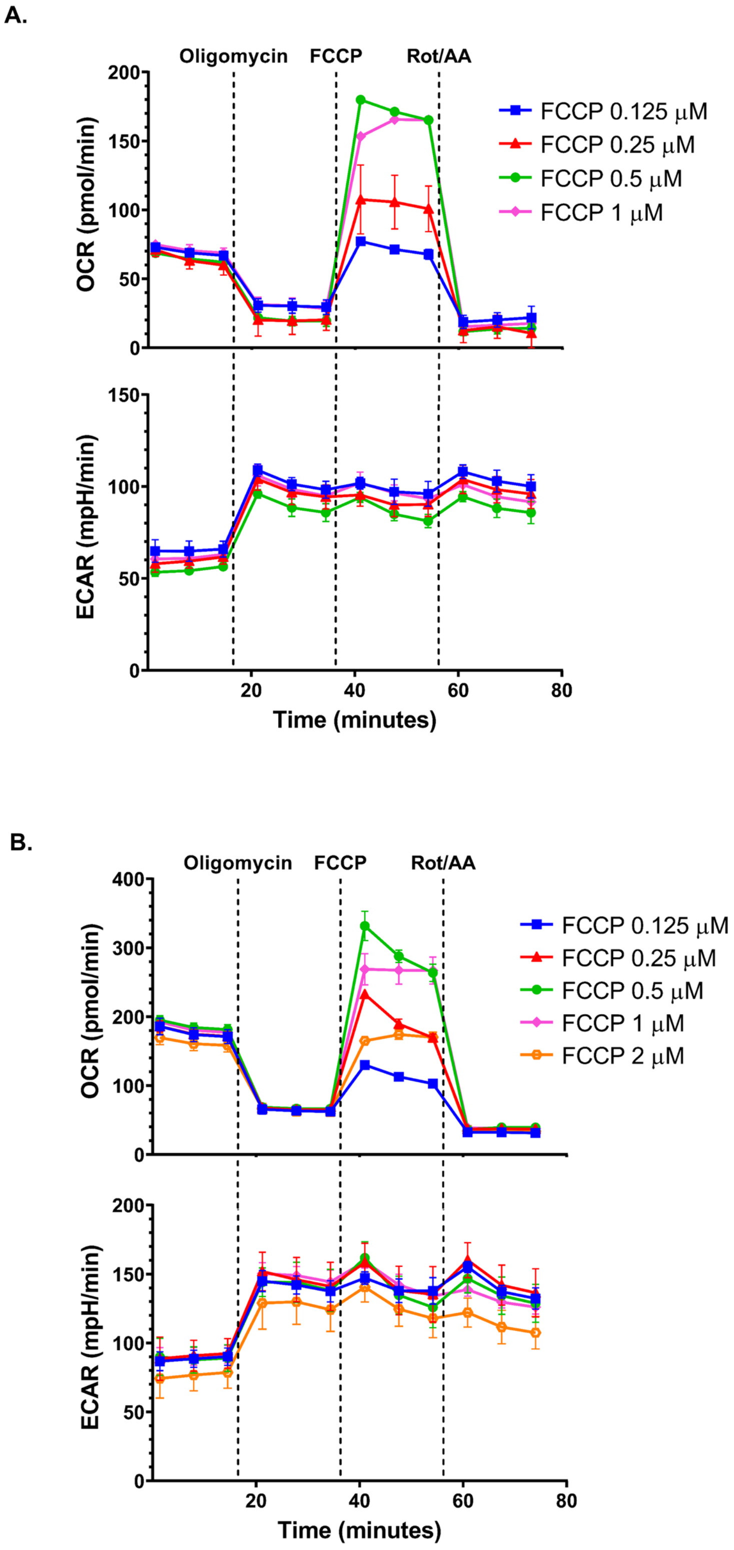
A.
Oligomycin
FCCP
Rot/AA
OCR (pmol/min)
0
50
100
150
200
FCCP 0.125 μM
FCCP 0.25 μM
FCCP 0.5 μM
FCCP 1 μM
ECAR (mpH/min)
0
50
100
150
20
40
60
80
Time (minutes)
B.
Oligomycin
FCCP
Rot/AA
OCR (pmol/min)
0
100
200
300
400
FCCP 0.125 μM
FCCP 0.25 μM
FCCP 0.5 μM
FCCP 1 μM
FCCP 2 μM
ECAR (mpH/min)
0
50
100
150
200
20
40
60
80
Time (minutes)

Figure 4.1. FCCP concentration optimisation in a Seahorse XF Cell Mito Stress test. Primary (1°) MC **(A)**, and rMC-1 **(B)** cells were seeded in a Seahorse 96-well cell culture plate at 20,000 and 40,000 cells per well respectively. On the following day, an XF Cell Mito Stress test was performed where oxygen consumption rates (OCRs) and extracellular acidification rates (ECARs) in the presence of glucose (10 mM), glutamine (2 mM) and sodium pyruvate (1 mM) were measured simultaneously by the Seahorse XFe96 extracellular flux analyser at a basal state and after the addition of oligomycin (2 µM), FCCP (various concentrations as indicated), and rotenone/antimycin A (Rot/AA, 0.5 µM). OCRs and ECARs were measured three times during each of the four conditions. Data from one experiment, presented as mean ± SD of each measurement point from a minimum of three replicate wells per group for the 1° MCs, and four replicate wells per group for the rMC-1.

Figure 4.2

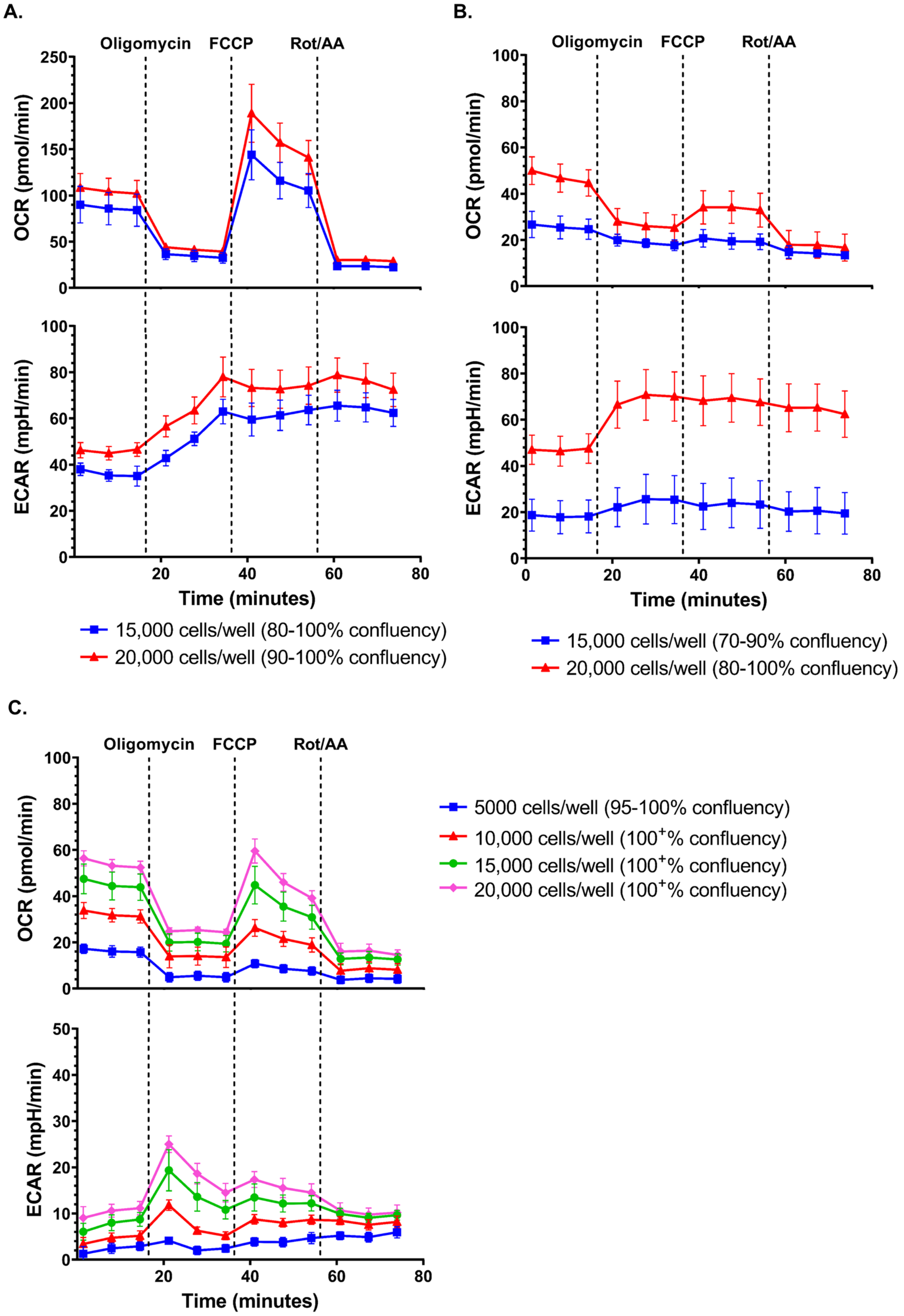
A.
Oligomycin
FCCP
Rot/AA
OCR (pmol/min)
250
200
150
100
50
0
ECAR (mpH/min)
100
80
60
40
20
0
20
40
60
80
Time (minutes)
15,000 cells/well (80-100% confluency)
20,000 cells/well (90-100% confluency)
B.
Oligomycin
FCCP
Rot/AA
OCR (pmol/min)
100
80
60
40
20
0
ECAR (mpH/min)
100
80
60
40
20
0
0
20
40
60
80
Time (minutes)
15,000 cells/well (70-90% confluency)
20,000 cells/well (80-100% confluency)
C.
Oligomycin
FCCP
Rot/AA
OCR (pmol/min)
100
80
60
40
20
0
ECAR (mpH/min)
50
40
30
20
10
0
20
40
60
80
Time (minutes)
5000 cells/well (95-100% confluency)
10,000 cells/well (100+% confluency)
15,000 cells/well (100+% confluency)
20,000 cells/well (100+% confluency)

Figure 4.2. Cell seeding density optimisation in a Seahorse XF Cell Mito Stress test. Primary (1°) MC **(A)**, rMC-1 **(B)**, and SIRMu-1 cells **(C)** were seeded in a Seahorse 96-well cell culture plate at different densities as indicated. On the following day cell confluency of each group was recorded (shown in brackets after a corresponding seeding density), and an XF Cell Mito Stress test was performed where oxygen consumption rates (OCRs) and extracellular acidification rates (ECARs) in the presence of glucose (10 mM) were measured simultaneously by the Seahorse XFe96 extracellular flux analyser at a basal state and after the addition of oligomycin (2 μM), FCCP (0.5 μM), and rotenone/antimycin A (Rot/AA, 0.5 μM). OCRs and ECARs were measured three times during each of the four conditions. Data from one experiment, presented as mean ± SD of each measurement point from a minimum of six replicate wells per group for the 1° MCs, a minimum of three replicate wells per group for the rMC-1, and a minimum of nine replicate wells per group for the SIRMu-1 cells.

4.4.2.3 Normalising OCR and ECAR data from Seahorse extracellular flux assays

To accurately interpret and compare cellular metabolic profiles between different cell types or treatment groups based on OCR and ECAR data from Seahorse assays, it is crucial to normalise for differences in cell number due to differences in seeding densities, proliferation rates, and more random differences in cell loss during incubation, washing and treatment. Commonly-used factors for normalisation are protein amount and the number of cells per well. Although total protein amount is easier to determine, the actual number of cells is arguably a better factor as different cell types or groups of the same cell type that have undergone different treatments can have different amounts of protein per cell. For normalisation, it is best to determine the number of cells per well at the end of an assay, rather than using the original cell seeding density, to account for differences in proliferation rates, and cell loss during incubation, washing and treatment.

A number of methods were used to try to accurately and efficiently determine cell numbers after each experiment. Firstly, attempts were made to count cells in each well after a Seahorse assay by trypsinising the cells and counting them using a hemocytometer or a cell counter. This was shown to be inaccurate and inconsistent. For example, there was considerable variation in apparent cell numbers when a single well was counted multiple times, or between replicate wells with very similar OCRs and ECARs, which could be due to the relatively small number of cells in each well, cell clumping, or inconsistencies in the technique. A second method used nuclear labelling of the cells followed by imaging using fluorescence microscopy and automated cell counting using the Fiji software (Schindelin et al., 2012). This method was more consistent than manual cell counting, although it was very inefficient as it required manually taking images of multiple wells. Thus, the number of cells for each experimental group was determined using this method from images taken from three representative wells in each group. Every well was also observed using a light microscope to ensure that the cell confluency of all wells in a group was similar and that wells used for cell counting were representative of that group. An average of the number of cells from the three representative wells was used to normalise OCR and ECAR data from all the replicate wells in that group.

We also tested the suitability of an ArrayScan XTI Live High Content Platform (ThermoFisher Scientific) which is capable of automatically imaging all the wells in a 96-well cell culture plate in a relatively short time while simultaneously counting the numbers of cell in each well. This method of determining cell number proved to be accurate, consistent and highly efficient. It also enabled the efficient determination of the number of cells in every individual well in each Seahorse assay and the ability to normalise OCR and ECAR data from each individual well with the actual number of cells in that well, rather than an average from representative wells. This preferred method of determining cell number was used for all experiments performed after we gained access to the ArrayScan in September 2018. The method by which cell numbers were determined in each Seahorse assay is specified in the legend of each subsequent figure.

4.4.2.4 Summary

With all parameters optimised, the Seahorse analyser was able to efficiently, consistently and accurately measure OCRs and ECARs of each type of the cultured MCs in real time. It was also capable of rapidly detecting responses of cells to each of the drugs added during the course of the experiments. The Cell Mito Stress Tests were also successfully performed, and expected responses of OCRs and ECARs to each drug obtained.

4.4.3 Metabolic analysis of primary and immortalised Müller cells

The optimised Seahorse Cell Mito Stress Test protocol as well as colorimetric lactate assays were used to analyse the glucose metabolism of primary MCs, the rMC-1 line and our novel SIRMu-1 line (Paper 4 (Kittipassorn et al., 2019a) in Chapter 3) (Fig. 4.3). A key aim was to investigate whether primary rat MCs cultured under current conditions displayed the Warburg effect similar to those previously reported (Poitry-Yamate et al., 1995; Winkler et al., 2000; Winkler et al., 2003), and to determine whether the two immortalised MC lines were metabolically similar to the primary MCs. Cervical cancer HeLa cells and primary MEFs were also analysed alongside the MCs. The well-characterised HeLa cells are known to be highly glycolytic and display the Warburg effect (Reitzer et al., 1979; Stanisz et al., 1983), while primary MEFs have been shown to have relatively high OCRs (Bryant et al., 2018; Wu et al., 2009).

Figure 4.3

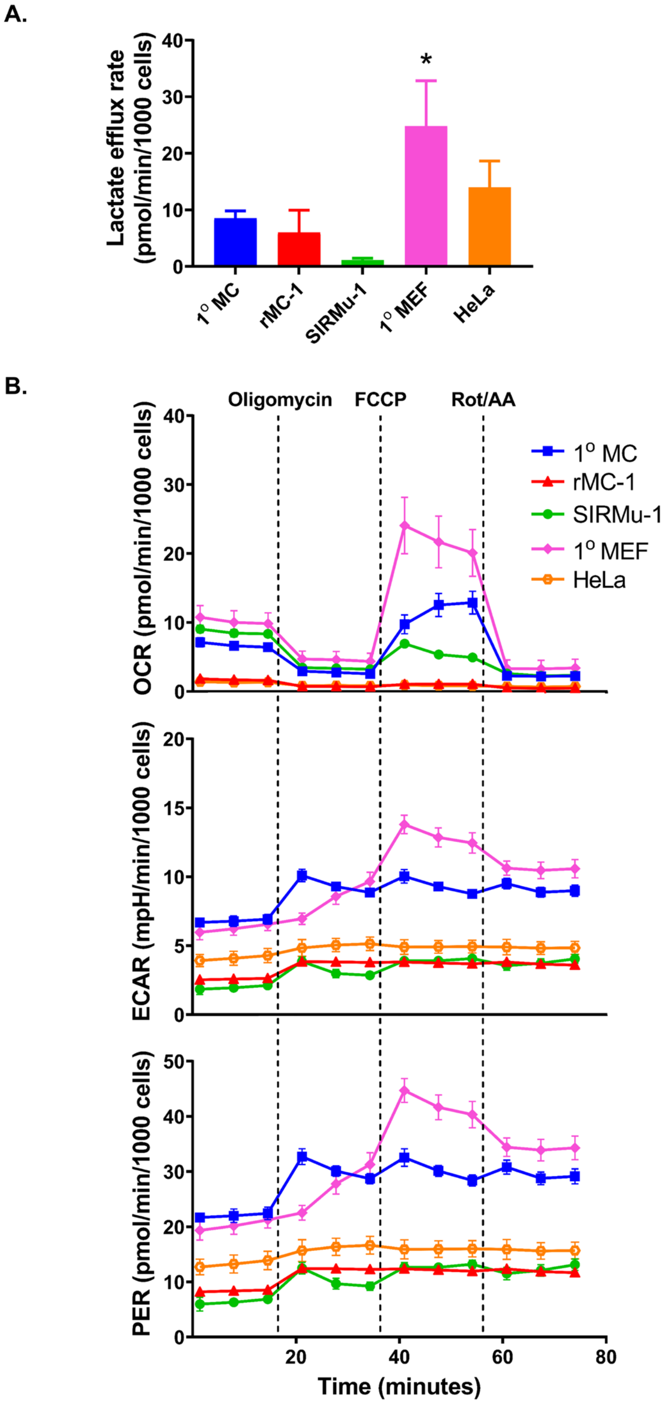
A.
Lactate efflux rate (pmol/min/1000 cells)
0
10
20
30
40
*
1° MC
rMC-1
SIRMu-1
1° MEF
HeLa
B.
Oligomycin
FCCP
Rot/AA
OCR (pmol/min/1000 cells)
0
10
20
30
40
1° MC
rMC-1
SIRMu-1
1° MEF
HeLa
ECAR (mpH/min/1000 cells)
0
5
10
15
20
PER (pmol/min/1000 cells)
0
10
20
30
40
50
20
40
60
80
Time (minutes)

Figure 4.3 (continued)

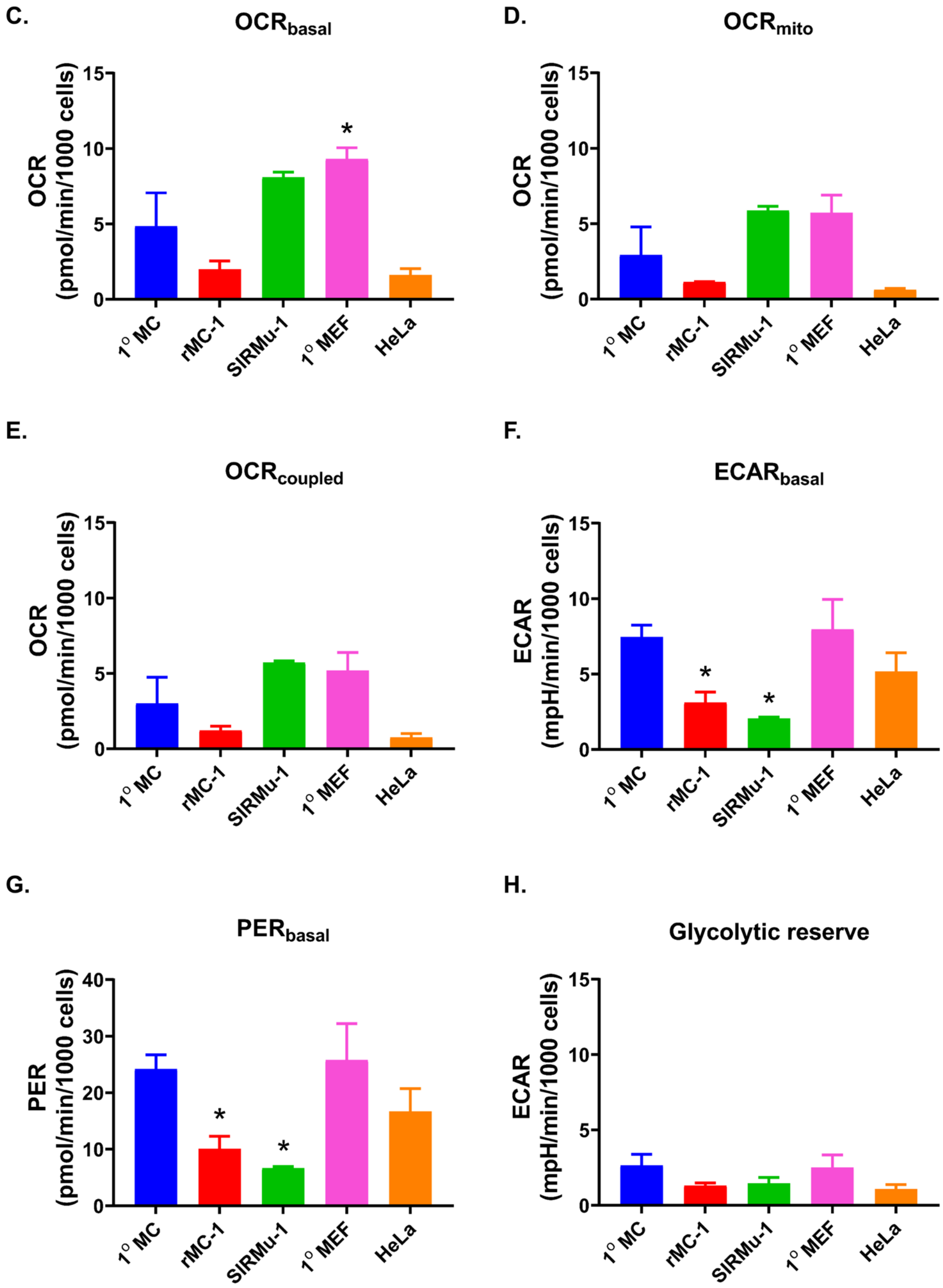

Figure 4.3. Metabolic profile of cultured primary and immortalised Müller cells (MCs) in normoxia. Primary (1°) MC (15,000 cells/well), rMC-1 (15,000 cells/well), SIRMu-1 (10,000 cells/well), 1° MEF (15,000 cells/well), and HeLa (10,000 cells/well) cells were seeded in a Seahorse 96-well cell culture plate. On the following day, cells were washed and incubated in fresh assay medium (XF base medium with 10 mM glucose) for an hour before the medium of each well was collected to use as samples for lactate assays. Cells were then subjected to an XF Cell Mito Stress test where oxygen consumption rates (OCRs) and extracellular acidification rates (ECARs) in the presence of glucose (10 mM) were measured by the Seahorse XFe96 extracellular flux analyser at a basal state and after the addition of oligomycin (2 μM), FCCP (0.5 μM), and rotenone/antimycin A (Rot/AA, 0.5 μM). OCRs and ECARs were measured three times during each of the four conditions. Three independent experiments (each with a minimum of six replicate wells per group) were performed. In the first experiment, cell numbers at the end of the assay could not be determined accurately due to technical problems. For the other two experiments, cell numbers were determined by fluorescence microscopy after Hoechst 33342 nuclear staining. **(A)** Lactate efflux rates determined from media samples collected before each Cell Mito Stress Test was performed, using lactate calorimetric assays, presented as mean ± SD from the three independent experiments, each performed using samples from three representative wells per group. **(B)** Representative graphs from one of the three independent experiments showing changes in OCRs, ECARs and proton efflux rates (PERs) calculated from the changes in ECARs. Data presented as mean ± SD from at least six replicate samples. OCR and ECAR graphs from all three experiments can be found in Appendix 7.6. **(C)-(H)** Different metabolic parameters were determined from the OCR and ECAR readings: **(C)** basal OCR (OCR_{basal}), **(D)** OCR due to mitochondrial respiration (OCR_{mito}), **(E)** OCR coupled to ATP production ($OCR_{coupled}$), **(F)** basal ECAR ($ECAR_{basal}$), **(G)** basal PER (PER_{basal}), and **(H)** glycolytic reserve. Data in A and C-H are normalised to cell numbers and presented as mean ± SD from two independent experiments with accurate cell counts. Statistical significance comparing to 1° MCs was determined by one-way ANOVA followed by Dunnett's multiple comparison test. *$p<0.05$. An absence of asterisks indicates $p\geq0.05$.

4.4.3.1 Lactate production

Lactate production (indicated by lactate efflux rates in Fig. 4.3A) of the primary MCs is relatively similar to the HeLa cells, which are known to display the Warburg effect (Reitzer et al., 1979; Stanisz et al., 1983). The rMC-1 cells show very similar rates of lactate production to the primary MCs; however, the SIRMu-1 cells display much lower lactate production than primary MCs and all of the other cells types. Interestingly, the primary MEFs, which have been reported to have relatively high oxidative activity (Bryant et al., 2018; Wu et al., 2009), display the highest lactate production.

4.4.3.2 Oxygen consumption, extracellular acidification and proton efflux

Kinetic profiles determined for both OCRs and ECARs for all five cell types are shown in the top and middle panels in figure 4.3B and in Appendix 7.6. ECARs (mpH/min) indicate changes in the pH level in the assay medium and can be converted to absolute changes in H^+ or PERs (pmol H^+/min) using a buffer factor (mM/pH), which is the amount of H^+ that changes the pH level in the medium by one pH unit as measured in a Seahorse analysis system (see sections 2.3.1 and 2.3.3.3 in Chapter 2). The kinetic profiles of PERs are shown in the lower panel in figure 4.3B.

The primary MCs display an expected Cell Mito Stress Test profile (see Fig. 4.3B, compare with Fig. 2.1A), where OCRs decrease after the addition of oligomycin, increase after the addition of FCCP and are completely inhibited after the addition of Rot/AA (Fig. 4.3B). In addition to decreasing OCRs, as expected oligomycin leads to an increase in ECARs and PERs (Fig. 4.3B). Looking at the basal activity, the primary MCs show relatively high levels of OCR_{basal} and $ECAR_{basal}$, which are both higher than those of the rMC-1 cells (Fig. 4.3B), suggesting that the primary MCs are more metabolically active than the rMC-1 cells. The SIRMu-1 cells display similar OCRs to the primary MCs but much lower ECARs, suggesting that the primary MCs are more glycolytic than the SIRMu-1s. For the two non-MC cells, the HeLa cells consume very little oxygen while producing noticeable amount of extracellular acidification, corresponding to their having a predominantly glycolytic activity, while the primary MEFs, similar to the primary MCs, show considerable levels of OCR_{basal} and $ECAR_{basal}$, suggesting that they are also metabolically active.

From the OCR, ECAR and PER kinetic profiles including responses to the compounds added during the assay (Fig. 4.3B), additional important metabolic parameters can be determined using the methods as described (Fig. 4.3C-H) (section 2.3.3.4 in Chapter 2). The primary MCs show high levels of $ECAR_{basal}$ and PER_{basal}, relative to OCR parameters (OCR_{basal}, OCR_{mito} and $OCR_{coupled}$), suggesting a glycolytic phenotype. The rMC-1 cells also display high levels of $ECAR_{basal}$ and PER_{basal}, relatively to OCR. This suggests that the rMC-1 cells also have a glycolytic phenotype, similar to the primary MC. However, the rMC-1 cells show an overall lower trend for all of these parameters compared to the primary MCs (Fig. 4.3C-H), suggesting that the rMC-1 cells are less energetic than the primary MCs. The SIRMu-1 cells have the highest levels of the OCR parameters, but the lowest $ECAR_{basal}$ and PER_{basal}, among the three MC types (Fig. 4.3C-G). This indicate that the SIRMu-1 cells are heavily dependent on OXPHOS, which is a different metabolic phenotype from the other two MCs. As expected, the HeLa cells display the lowest OCRs and relatively high $ECAR_{basal}$ and PER_{basal}, consistent with the Warburg effect. Interestingly, while the MEFs do display high levels of OCR, they also display relatively high $ECAR_{basal}$, consistent with the results from the lactate assay. Glycolytic reserve (Fig. 4.3H) is higher in the primary MCs and the MEFs than in the rMC-1, the SIRMu-1 and the HeLa cells, which have very low glycolytic reserve. Although this is not statistically significant, it suggests that the primary MCs and MEFs have a higher capacity to upregulate their glycolytic activity when OXPHOS is inhibited.

4.4.3.3 Contribution of glycolysis and respiration to PER

Extracellular acidification and H^+ efflux are commonly used as indicators of glycolysis since the conversion of glucose to lactate via glycolysis yields H^+ (Divakaruni et al., 2014). However, CO_2 produced from OXPHOS also contributes to extracellular acidification as it can partially hydrate in the medium to produce H^+ and HCO_3^- (Mookerjee et al., 2015). Therefore, in order to accurately determine the glycolytic activity of cells, it is important to differentiate between acidification which is due to glycolysis and acidification which is due to mitochondrial respiration (Mookerjee et al., 2015). Based on absolute OCR_{mito} data (the difference between OCR_{basal} and $OCR_{non\text{-}mito}$, see Fig. 2.1 and section 2.3.3.4 in Chapter 2), the amount of H^+ in the medium derived from CO_2 can also be determined (Mookerjee et al., 2015) (detailed in section 2.3.3.5 in Chapter 2). This is the PER_{res}, and the difference between the PER_{basal} (calculated from $ECAR_{basal}$) and the PER_{res} is the PER_{glycol}

(Mookerjee et al., 2015). Hence, OCR_{mito} data enabled the determination of PER_{res} and consequently PER_{glyco}; this was one of the reasons that the Seahorse Cell Mito Stress Tests, in which three compounds targeting the ETC and OXPHOS are serially injected, were utilised in this thesis.

Values and % contribution to the PER_{basal} of PER_{glyco} of the five cell types investigated were determined (Fig. 4.4A-B). In primary MCs and HeLa cells, levels of PER_{glyco} are similar (Fig. 4.4A) with more than 85% of the PER_{basal} derived from glycolysis (Fig. 4.4B), consistent with both cell types having similar glycolytic activities and displaying the Warburg effect. Although rMC-1 cells have a lower absolute value of PER_{glyco} than primary MCs (Fig. 4.4A), they do show a highly similar contribution of glycolysis to the total acidification, with also more than 85% of the PER_{basal} having been derived from glycolysis (Fig. 4.4B); this suggests that the rMC-1 cells and the primary MCs display similar levels of dependency on glycolysis. On the other hand, SIRMu-1 cells show much lower levels of both the value and the % contribution to the PER_{basal} of the PER_{glyco}, when compared to the primary MCs (Fig. 4.4A and B), indicating a clear difference in glycolytic activity between the two cell types. Less than 20% of the PER_{basal} is derived from glycolysis in SIRMu-1 cells, again consistent with a much lower relative rate of glycolysis compared with OXPHOS. Of note, on average more than 65% of the PER_{basal} in MEFs is derived from glycolysis, showing a relatively high glycolytic activity, similar to primary MCs, rMC-1s and HeLa cells.

4.4.3.4 Contribution of glycolysis and respiration to ATP production and glucose consumption

Cells that exhibit the Warburg effect display high rates of glycolysis and predominantly depend upon this pathway for their ATP production, even when exposed to physiological oxygen levels (Hsu and Sabatini, 2008; Koppenol et al., 2011; Vander Heiden et al., 2009; Warburg, 1956; Warburg et al., 1927). Based on OCR and PER data and the type of substrate used in the assays (which was glucose in this case), the total amount and relative proportions of ATP produced and glucose consumed that were due to either glycolysis or respiration can be calculated (Mookerjee et al., 2017, 2018) (detailed in section 2.3.3.6 in Chapter 2). On average, in primary MCs, rMC-1s and HeLa cells, over 50% of

Figure 4.4

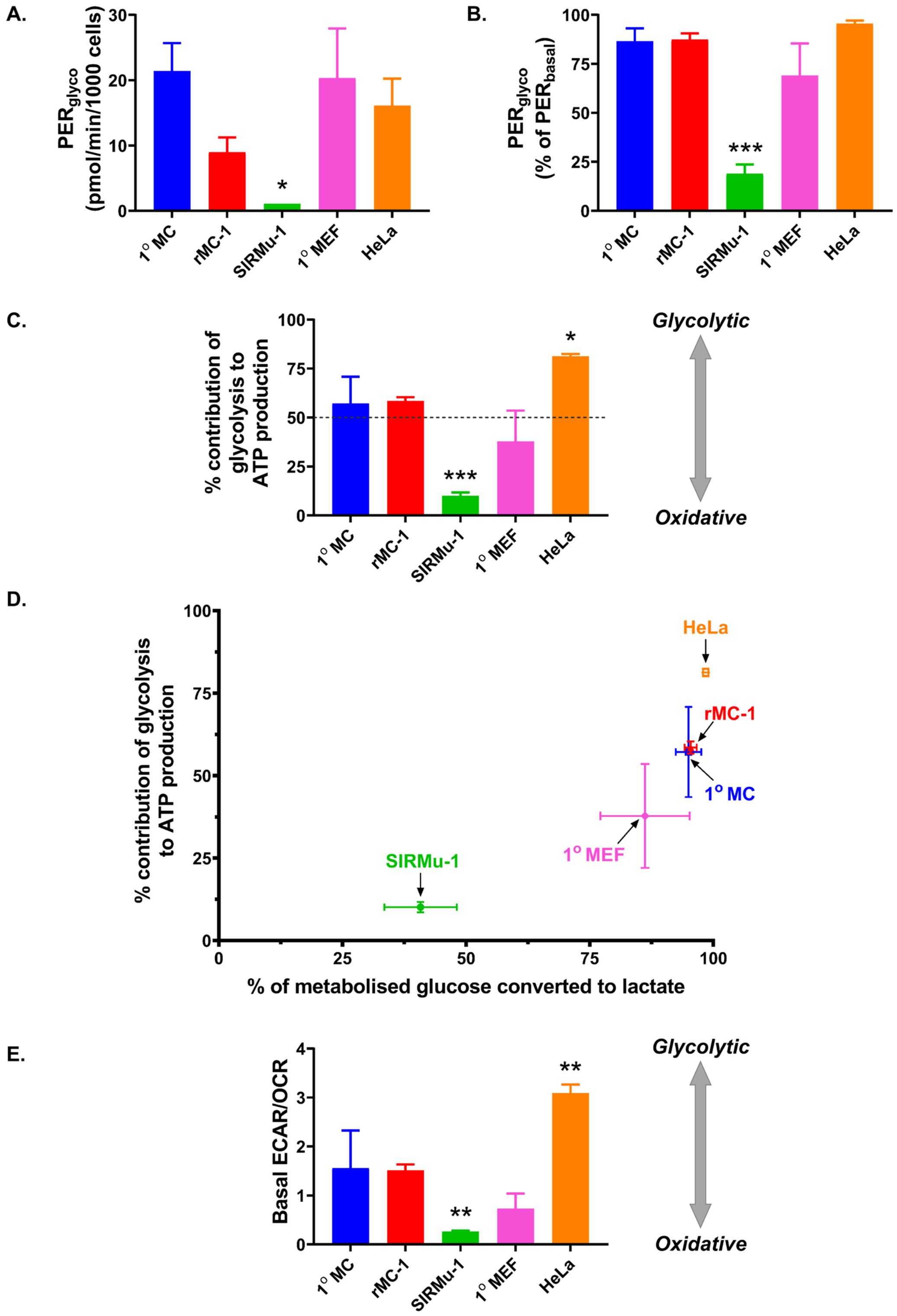
A.
PER_{glyco} (pmol/min/1000 cells)
30
20
10
0
*
1° MC
rMC-1
SIRMu-1
1° MEF
HeLa
B.
PER_{glyco} (% of PER_{basal})
100
75
50
25
0
***
1° MC
rMC-1
SIRMu-1
1° MEF
HeLa
C.
% contribution of glycolysis to ATP production
100
75
50
25
0
***
*
1° MC
rMC-1
SIRMu-1
1° MEF
HeLa
Glycolytic
Oxidative
D.
% contribution of glycolysis to ATP production
100
75
50
25
0
HeLa
rMC-1
1° MC
1° MEF
SIRMu-1
0
25
50
75
100
% of metabolised glucose converted to lactate
E.
Basal ECAR/OCR
4
3
2
1
0
**
**
1° MC
rMC-1
SIRMu-1
1° MEF
HeLa
Glycolytic
Oxidative

Figure 4.4. Metabolic parameters associated with glycolytic activity of cultured primary and immortalised Müller cells (MCs) in normoxia. Additional parameters were calculated based on oxygen consumption rates (OCRs), extracellular acidification rates (ECARs) and proton efflux rates (PERs) from the Cell Mito Stress tests in figure 4.3, where three independent experiments (each with a minimum of six replicate wells per group) were performed. The parameters are **(A)** PER due to glycolysis ($\text{PER}_{\text{glyco}}$) in pmol/min/1000 cells, **(B)** $\text{PER}_{\text{glyco}}$ (% contribution to PERbasal in figure 4.3G, **(C)** % contribution of glycolysis to ATP production, and **(D)** Basal ECAR/OCR ratios. **(E)** A graph showing a relationship between % contribution of glycolysis to ATP production from C and % of metabolised glucose converted to lactate. Data in A are normalised to cell numbers and presented as mean ± SD from the two independent experiments. Data in B-E are cell number-independent and presented as mean ± SD of three independent experiments. Statistical significance comparing to 1° MCs was determined by one-way ANOVA followed by Dunnett's multiple comparison test. *$p<0.05$, **$p<0.01$, ***$p<0.001$. An absence of asterisks indicates $p\geq0.05$.

ATP is produced from glycolysis, whereas in SIRMu-1s less than 15% is produced from glycolysis (Fig. 4.4C and 4.4D). This further supports that primary MCs, rMC-1s and HeLa cells depend on glycolysis, while the SIRMu-1 cells depend on OXPHOS. For MEFs, on average less than 50% of ATP is generated from glycolysis, confirming that they are more oxidative than glycolytic. The graph in figure 4.4D shows a relationship between the contributions of glycolysis to ATP production (data from fig. 4.4C) and the proportions of metabolised glucose that are converted into lactate in different cell types. The majority of glucose consumed in all cell types, except SIRMu-1 cells, is converted to lactate (Fig. 4.4D). In figure 4.4D, the locations on the graph of the primary MC and the rMC-1 data points are similar, with the majority of their ATP produced and glucose consumed due to glycolysis, further confirming their similar dependency on glycolysis. The graph also shows that HeLa cells are highly glycolytic, SIRMu-1 highly oxidative and MEFs intermediate.

Since both glycolysis and respiration contribute to ECARs, the glycolytic activity of cells in the basal state can be analysed qualitatively by normalising $ECAR_{basal}$ to OCR_{basal}, to give ECAR/OCR ratios, which are independent of cell number. Among the three MC populations, the primary MCs and the rMC-1s show similarly high ECAR/OCR ratios, while that of the SIRMu-1 cells is significantly lower compared to the primary MCs (Fig. 4.4E). HeLa cells have the highest ECAR/OCR ratio, indicating the highest glycolytic activity among all cell types investigated (Fig. 4.4E). Although slightly lower, the ECAR/OCR ratio of MEFs is not statistically significantly different from that of the primary MCs, suggesting intermediate glycolytic activity (Fig. 4.4E). The trend of ECAR/OCR ratios (Fig. 4.4E) among the five cell types are very similar to the contributions of glycolysis to ATP production (Fig. 4.4C), confirming that ECAR/OCR ratios are a good indicator of relative glycolytic activity. Importantly, again, the SIRMu-1 cells are clearly the most oxidative cell type analysed, with the HeLa cells being the most glycolytic and the other MCs intermediate.

4.4.3.5 Summary

Overall, primary MCs and rMC-1 cells appear to have very similar glucose metabolism. Both cell populations show high glycolytic activity, and hence display the Warburg effect, as indicated by similar lactate efflux rates, similar contributions of glycolysis to PER and ATP production, similar proportions of glucose converted to lactate and similar basal ECAR/OCR ratios (Fig. 4.3 and 4.4).

However, there are small differences including lower OCRs (although not statistically significant), lower glycolytic reserve (although not statistically significant), lower ECARs and lower PERs in the rMC-1 cells compared to the primary MCs (Fig. 4.3C-G). Altogether, this indicates that both the primary MCs and the rMC-1 cells display the Warburg effect and predominantly rely on glycolysis for ATP production, but the primary MCs are more metabolically active. On the other hand, glucose metabolism of the SIRMu-1 cells is very different from the primary MCs in that they are highly dependent on OXPHOS, as demonstrated by lower lactate efflux rates (although not statistically significant), higher OCRs (although not statistically significant), lower ECARs, lower PERs, lower contributions of glycolysis to PER and ATP production, lower proportions of glucose converted to lactate and lower basal ECAR/OCR ratios, compared to primary MCs (Fig. 4.3 and 4.4).

4.4.4 Analysing metabolic gene expression in Müller cells based on RNA sequencing data

To investigate whether the major difference in metabolism between the SIRMu-1 and the primary MCs (Fig. 4.3 and 4.4) could be explained by differential gene expression, the relative expression levels of 44 key genes involved in glucose metabolism in the SIRMu-1 cells were compared with the primary MCs (Table 4.1, Fig. 4.5) using the data from RNA-seq performed and described in Paper 4 (Kittipassorn et al., 2019a) and Paper 5 (Kittipassorn et al., 2019b) in Chapter 3. rMC-1 data compared to primary MCs were also analysed (Table 4.1, Fig. 4.5). Among the 44 genes analysed there was no gene that was uniquely differentially expressed in the SIRMu-1 cells compared to the primary MCs, even when differential expression was analysed using a minimum two fold-change threshold compared to primary MCs (Table 4.1 and the yellow left-hand side area of the Venn diagram in Fig. 4.5). There were two genes, *Slc2a9* (encoding glucose transporter 9 (GLUT9)) and *Slc16a3* (encoding monocarboxylate transporter 4, MCT4), that were differentially expressed in the SIRMu-1 cells relative to the primary MCs, but these were also differentially expressed in the rMC-1 cells compared to the primary MCs (Table 4.1 and the green middle area of the Venn diagram in Fig. 4.5). Therefore, the differential expression of these two genes is likely not an explanation for the major difference in glucose metabolism between the SIRMu-1s and the primary MCs, as the rMC-1s, which display a similar metabolism to primary MCs, also differentially express these genes compared to primary MCs.

Table 4.1. Differential expression of key genes involved in glucose metabolism in the SIRMu-1 and the rMC-1 cells relative to primary (1°) MCs from RNA sequencing data

Gene symbol	**Gene name**	**Differential gene expression compared to 1° MC**	
		SIRMu-1	**rMC-1**
Aldoa	aldolase, fructose-bisphosphate A	0	0
Aldoc	aldolase, fructose-bisphosphate C	0	0
Eno1	enolase 1	0	0
G6pd	glucose-6-phosphate dehydrogenase	0	0
Gapdh	glyceraldehyde-3-phosphate dehydrogenase	0	0
Gpd1	glycerol-3-phosphate dehydrogenase 1	0	1
Gpi	glucose-6-phosphate isomerase	0	0
Gsr	glutathione-disulfide reductase	0	0
Hk1	hexokinase 1	0	0
Hk2	hexokinase 2	0	0
Ldha	lactate dehydrogenase A	0	0
Ldhb	lactate dehydrogenase B	0	-1
Mpc1	mitochondrial pyruvate carrier 1	0	0
Mpc2	mitochondrial pyruvate carrier 2	0	0
Pdha1	pyruvate dehydrogenase (lipoamide) alpha 1	0	0
Pdk1	pyruvate dehydrogenase kinase 1	0	0
Pdk2	pyruvate dehydrogenase kinase 2	0	0
Pdk3	pyruvate dehydrogenase kinase 3	0	0
Pfkfb1	6-phosphofructo-2-kinase/fructose-2,6-biphosphatase 1	0	1
Pfkfb2	6-phosphofructo-2-kinase/fructose-2,6-biphosphatase 2	0	0
Pfkfb3	6-phosphofructo-2-kinase/fructose-2,6-biphosphatase 3	0	0
Pfkl	phosphofructokinase, liver type	0	0
Pfkm	phosphofructokinase, muscle	0	0
Pfkp	phosphofructokinase, platelet	0	0
Pgam1	phosphoglycerate mutase 1	0	0
Pgd	phosphogluconate dehydrogenase	0	0

Pgk1	phosphoglycerate kinase 1	0	0
Pgls	6-phosphogluconolactonase	0	0
Pkm	pyruvate kinase M	0	0
Rpe	ribulose-5-phosphate-3-epimerase	0	0
Rpia	ribose 5-phosphate isomerase A	0	0
Slc2a1	solute carrier family 2 member 1	0	0
Slc2a5	solute carrier family 2 member 5	0	0
Slc2a6	solute carrier family 2 member 6	0	0
Slc2a8	solute carrier family 2 member 8	0	0
Slc2a9	solute carrier family 2 member 9	-1	-1
Slc2a10	solute carrier family 2 member 10	0	-1
Slc2a12	solute carrier family 2 member 12	0	0
Slc2a13	solute carrier family 2 member 13	0	-1
Slc16a1	solute carrier family 16 member 1	0	1
Slc16a3	solute carrier family 16 member 3	-1	-1
Slc16a7	solute carrier family 16 member 7	0	0
Taldo1	transaldolase 1	0	0
Tkt	transketolase	0	0

A fold-change threshold of two was set to analyse differential expression of 44 genes involved in glucose metabolism in the SIRMu-1 cells compared to the primary MCs (results shown in the column named “SIRMu-1”), and in the rMC-1 cells compared to the primary MCs (results shown in the column named “rMC-1”). Genes not differentially expressed are denoted by 0, genes downregulated denoted by -1, and genes upregulated denoted by 1.

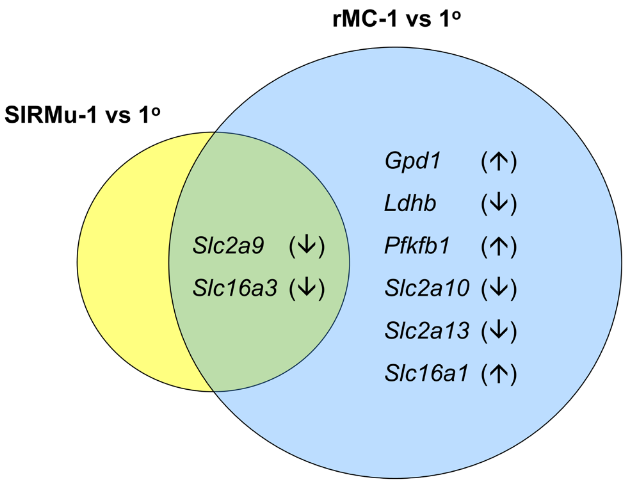

Figure 4.5. Differentially expressed genes involved in glucose metabolism of SIRMu-1 and rMC-1 cells compared to primary (1°) MCs. Venn diagram displays the names of genes significantly differentially expressed at a fold-change of greater than two in each immortalised cell line compared to 1° MCs. Differentially expressed genes were either upregulated (↑) or downregulated (↓). *Gpd1*, glycerol-3-phosphate dehydrogenase 1; *Ldhb*, lactate dehydrogenase B; *Pfkfb1*, 6-phosphofructo-2-kinase/fructose-2,6-biphosphatase 1; *Slc2a9*, solute carrier family 2 member 9; *Slc2a10*, solute carrier family 2 member 10; *Slc2a13*, solute carrier family 2 member 13; *Slc16a1*, solute carrier family 16 member 1; *Slc16a3*, solute carrier family 16 member 3.

As previously discussed, the rMC-1 cells have very similar glucose metabolism to the primary MCs although there are small differences with the rMC-1 cells exhibiting lower OCRs, lower ECARs and lower PERs (Fig. 4.3 and 4.4). There are only six genes that are uniquely differentially expressed in rMC-1 cells under these conditions compared to primary MCs, including *Gpd1* (encoding glycerol-3-phosphate dehydrogenase 1, an enzyme involved in carbohydrate and lipid metabolism), genes encoding enzymes involved in the glycolytic pathway (*Ldhb* encoding LDHB and *Pfkfb1* encoding phosphofructokinase 2), and genes encoding membrane transporters in the GLUT family (*Slc2a10* encoding GLUT10 and *Slc2a13* encoding GLUT13), and *Slc16a1* (encoding monocarboxylate transporter 1) (Table 4.1 and the blue right-hand area of the Venn diagram in Fig. 4.5), which likely contribute to the small metabolic differences between the rMC-1 cells and the primary MCs.

4.5 Discussion

4.5.1 Metabolic analysis techniques

Two of the key parameters for the analysis of glucose metabolism in MCs were oxygen consumption and extracellular acidification. To analyse these, two techniques were assessed: fluorescence plate reader-based assays (Luxcel Biosciences) and the Seahorse XFe96 extracellular flux analyser (Agilent Technologies). Although both are high throughput techniques that enable measurement of samples in a 96-well plate format and do not require large amounts of cells, the Seahorse extracellular flux analyser had a number of advantages over the fluorescence plate reader-based assays. With the Seahorse analysis, changes in oxygen concentration (reported as OCR) and pH (reported as ECAR) are measured simultaneously in the same biological samples, rapid cellular responses can be detected in real time due to a very small volume (about 2 μL) of the transient micro-chambers in which changes were measured, drug ports in sensor cartridges enable the addition of multiple drugs to the same well over the course of an assay, at specified times, and the responses of the same cells to each of the drugs determined, the system has an optimised set of protocols for sensitive, consistent and accurate measurements of both OCRs and ECARs, and the analysis is quantitative, allowing determination of absolute levels of OCRs and ECARs. This chapter presented the optimisation of metabolic assays performed using the Seahorse analyser and demonstrated that OCRs and ECARs could be measured efficiently, consistently and accurately.

Hence, this technique, together with assays to determine lactate production, were used to investigate whether primary MCs display the Warburg effect as previously published (Poitry-Yamate et al., 1995; Winkler et al., 2000) and whether the rMC-1 and the SIRMu-1 cells have similar glucose metabolism to primary MCs. HeLa cells and MEFs were also analysed alongside MCs. Importantly, these experiments enabled glucose metabolism in all cell types to be assessed in the same microplates and directly compared.

4.5.2 Interpreting metabolic data and characterising Müller cell glucose metabolism

The primary MCs display the Warburg effect, similar to HeLa cells but to a lesser degree, as they exhibit relatively high values of glycolytic parameters including lactate efflux rates, contribution of glycolysis to PER, contribution of glycolysis to ATP production, high proportions of glucose converted to lactate and high basal ECAR/OCR ratios (Fig. 4.3 and 4.4). These results are consistent with studies published previously in primary MCs of guinea pig (Poitry-Yamate et al., 1995) and of human (Winkler et al., 2000). In contrast, other types of primary cells, including normal human dermal fibroblasts (NHDF) (Zhang et al., 2012) and rat cortical neurons (Divakaruni et al., 2014), have been shown to be predominantly oxidative, confirming the primary MCs as a rare type of primary cells that uniquely display the Warburg effect.

Similar to the primary MCs investigated, the rMC-1 cells show high dependence upon glycolysis for metabolism, indicating that the rMC-1 cells also display the Warburg effect. This was in line with a published report that investigated lactate production by these cells (Winkler et al., 2003). Of note, rMC-1 cells show lower OCRs and ECARs than primary MCs, suggesting that although both rMC-1 cells and primary MCs predominantly depend on glycolysis for ATP production, the latter are more metabolically active. Nevertheless, both primary MCs and rMC-1s display the Warburg effect.

For the SIRMu-1 cells, almost all of their metabolic parameters are different from those of the primary MCs. Compared to primary MCs, SIRMu-1 cells have a lower PER_{glyco}, a lower contribution of glycolysis to ATP production, a lower proportion of glucose converted to lactate, lower basal ECAR/OCR ratios, lower $ECAR_{basal}$, lower lactate efflux rates and higher OCRs. Altogether this indicates that the highly-proliferative SIRMu-1 cells are predominantly oxidative and do not display the Warburg effect. This helps to validate the method as it shows that, unlike what has been previously suggested (Young, 2013), not all continuously proliferating cell lines appear as glycolytic when cultured under these conditions in which sufficient glucose is present, and that predominantly oxidative cells do exist in culture. This is also similar to a previously-published finding that the highly-proliferative human breast cancer MCF-7 cell line seems to be primarily oxidative (Zhang et al., 2012) and also supports the less well-known and more recent notions that the Warburg effect might not always exist in highly-proliferative cells and that different cell lines from the same tissue origin may have different metabolic phenotypes (Giang et al., 2013; Zhang et al., 2012) (reviewed in (Moreno-Sanchez et al., 2007). Here, the rMC-1 and the SIRMu-1 cell lines both originated from primary rat MCs but undertake very different types of glucose metabolism.

The considerable differences between primary MC and SIRMu-1 glucose metabolism are unlikely to be due primarily to differential expression of genes involved in glucose metabolism. Analysis of RNA-seq data on expression levels of 44 key glucose metabolic genes (Table 4.1, Fig. 4.5), including genes commonly important in the regulation of the switch between glycolysis and OXPHOS such as *Pdha1*, *pdk1* and *Ldha* (Luo et al., 2011), showed that there was no gene that was uniquely differentially expressed in the SIRMu-1 cells compared to the primary MCs. The major differences in primary MC and SIRMu-1 glucose metabolism might, instead, be primarily associated with differences in expression of genes indirectly involved in glucose metabolism, genes involved in other forms of metabolism or, more likely, post-transcriptional mechanisms (Arif et al., 2017).

It is noteworthy that in the SIRMu-1 cells PER_{glyco} contributes less than 20% to the PER_{basal}, calculated from the $ECAR_{basal}$. Similar results were previously reported including in the MCF-7 cell line, the human osteosarcoma Saos-2 cell line and the rat insulinoma INS-1E cell line where only a small fraction of the total production of H^+ was derived from glycolysis (Giang et al., 2013; Mookerjee et al., 2015). This emphasises that it is not ideal to use ECAR obtained from the extracellular flux analyser as a sole and direct indicator of cellular glycolytic activity, because in highly oxidative cells the majority of ECAR could be the result of H^+ released from the hydration of CO_2 produced from OXPHOS, and not the result of H^+ produced from the conversion of glucose to lactate via glycolysis.

It also emphasises that in order to accurately use ECAR to represent glycolytic flux, it is crucial to determine the proportion of ECAR that is due to glycolysis, or to interpret the ECAR data relative to the OCR, as demonstrated in this thesis and in a number of studies by others (Cao et al., 2014; Mookerjee et al., 2015; Nicholas et al., 2017; Zhang et al., 2012).

Interestingly, primary MEFs show both a relatively high glycolytic flux (as shown by high lactate efflux rates and high ECARs) and a high oxygen consumption, indicating highly metabolically active cells. However, they depend slightly more on respiration than glycolysis for ATP production (contribution of glycolysis to ATP production was on average less than 50% but not by much and the basal ECAR/OCR ratio was relatively low). This shows that a cell type can have a high glycolytic flux, due to being highly active cells, without having the majority of ATP being derived from glycolysis, which again highlights the importance of considering lactate production, ECAR and OCR altogether when analysing glucose metabolism of cells (Divakaruni et al., 2014; Mookerjee et al., 2017, 2018). In addition, the MEFs are primary cells and have a population doubling time of approximately seven to ten days, similar to the primary rat MCs whose doubling time is approximately seven days ((Kittipassorn et al., 2019a) in Chapter 3). Despite both cell types being primary cells with similarly slow proliferation rates, the primary MCs are more dependent on glycolysis for ATP production than the MEFs. On the other hand, although both the MEFs and the SIRMu-1 show dependency on OXPHOS (the SIRMu-1 more so than the MEFs), the former are slowly-proliferative cells while the latter highly-proliferative. This again demonstrates that proliferative capability does not always correlate with a certain metabolic phenotype and also argues against the proposal that the Warburg effect exists to facilitate biosynthesis primarily for cellular proliferation (reviewed in (Liberti and Locasale, 2016).

Of note, the FCCP concentration used in the above experiments for all five cell types was 0.5 μM, selected based on the optimal concentration of FCCP in primary MCs and rMC-1 cells determined previously in initial optimisation experiments (Fig. 4.1). After the SIRMu-1 cell line was established, it was also included in the metabolic analysis. The FCCP concentrations in SIRMu-1 cells were later tested (Appendix 7.7) using the same concentrations (0.125, 0.25, 0.5, 1, 2 μM) as investigated in primary MCs and rMC-1 cells (Fig. 4.1). It was found that the highest concentration used (2 μM) still gave a higher OCR response than the second highest concentration (1 µM), demonstrating that the optimal FCCP concentration for the SIRMu-1 cells is equal to or higher than 2 µM. This indicates that the maximal respiration (illustrated in Fig. 2.1) that can be obtained from the OCR kinetic graphs (Fig. 4.3 and Appendix 7.6) in the above experiments of MC metabolic analysis, where 0.5 µM concentration of FCCP was used, has to be interpreted cautiously for the SIRMu-1 cells, as they are less sensitive to FCCP than the primary MCs and the rMC-1 cells and the FCCP concentration used is not the optimal for this cell type, potentially leading to an underestimation of maximal respiration in the SIRMu-1 cells. In published studies, the FCCP concentration of 0.5 µM has been used with HeLa cells (Boehning et al., 2018; Faccenda et al., 2017) and the concentration of 1 µM has been used with MEFs (Bryant et al., 2018; Raini et al., 2017; Wu et al., 2009). Therefore, in a similar fashion to SIRMu-1, the OCR_{FCCP} of MEFs in the experiments in this thesis might not be the maximal respiration. Interestingly, even with the possibility of an underestimation of maximal respiration, the MEFs still have the greatest level of the spare oxidative capacity (the difference between the OCR_{basal} and the OCR_{FCCP}) among all the cell types under the conditions analysed (Fig. 4.3 and Appendix 7.6). This also shows that while the MEFs are highly active, it does not appear that they have high rates of glycolysis because their OXPHOS is at capacity. Importantly, however, the underestimation of maximal respiration in the SIRMu-1 cells and MEFs has no impact on the interpretation of the results in regard to basal cellular metabolic activity, which is the main focus of this thesis.

An important future experiment would be to incubate MCs with ^{13}C-glucose and track the fate of the labelled carbons into intermediates in the glycolytic pathway, the TCA cycle and other pathways, such as the PPP, as well as their incorporation into precursors for nucleic acid, amino acid and lipid production.

4.5.3 Conclusions

The Seahorse extracellular flux analyser was tested and successfully optimised for the measurement of oxygen consumption and extracellular acidification, and used for the metabolic characterisation of cultured MCs. Metabolic analysis demonstrated that the primary rat MCs display the Warburg effect. Of the two immortalised MC lines, the rMC-1s also display the Warburg effect, and were more metabolically similar to primary MCs than were the SIRMu-1 cells, which are heavily dependent on

OXPHOS and do not display the Warburg effect. Thus, primary MCs and rMC-1 cells were used as the preferred experimental system for the study of the role of PKM2 in the Warburg effect in the retina in Chapter 5.

Chapter 5

Role of pyruvate kinase M2 in the Warburg effect in retinal Müller cells

CHAPTER 5: Role of pyruvate kinase M2 in the Warburg effect in retinal Müller cells

5.1 Introduction

The non-proliferative mammalian retina displays the Warburg effect (reviewed in Paper 1 (Ng et al., 2015)) (Cohen and Noell, 1960; Tornquist and Alm, 1979; Warburg, 1925; Warburg et al., 1924; Warburg et al., 1930; Winkler, 1981, 1995), whereby cells predominantly utilise glycolysis for ATP production regardless of oxygen availability, which is surprisingly similar to proliferating cells including cancer cells (Hsu and Sabatini, 2008; Koppenol et al., 2011; Vander Heiden et al., 2009; Warburg, 1956; Warburg et al., 1927). Chapter 4 investigates one of the three main hypotheses of this thesis that cultured rat MCs display the Warburg effect, and the data support the hypothesis in cultured primary rat MCs and the rMC-1 immortalised MC line, consistent with previously published reports in freshly-isolated guinea pig MCs (Poitry-Yamate et al., 1995), cultured primary human MCs (Winkler et al., 2000), and rMC-1 cells (Winkler et al., 2003). The primary rat MCs and rMC-1 cells were therefore chosen as appropriate experimental tools to study the Warburg effect in the retina in this thesis.

Not much is known about factors driving the Warburg effect in the retina. On the contrary, a number of agents have been implicated in driving the Warburg effect in cancer and other proliferating cells (reviewed in (Chaneton and Gottlieb, 2012; Dayton et al., 2016b; Dejure and Eilers, 2017; Semenza, 2012; Ward and Thompson, 2012)). One such agent is a specific isoform of the glycolytic enzyme PK, PKM2 (Christofk et al., 2008a; Clower et al., 2010; Goldberg and Sharp, 2012; Palsson-McDermott et al., 2015; Siddiqui et al., 2018).

PK is an enzyme that catalyses the conversion of PEP into pyruvate in the glycolytic pathway (reviewed in (Mazurek, 2011). There are four PK isoforms, PKM1, PKM2, PKL and PKR, each with different tissue expression patterns (see section 1.4.1 in Chapter 1). PKM2 is the specific isoform that has been implicated in driving the Warburg effect in a number of cancer and proliferating cells (Christofk et al., 2008a; Clower et al., 2010; Goldberg and Sharp, 2012; Palsson-McDermott et al., 2015; Siddiqui et al., 2018), which is likely facilitated by its function in the nucleus where it acts as a coactivator for, among others, the transcription factor HIF-1, leading to upregulation of HIF-1 target genes, many of which are involved in glucose metabolism, and the consequent upregulation of glycolysis in concert with an inhibition of OXPHOS (Luo et al., 2011; Palsson-McDermott et al., 2015). This function in the nucleus and the contribution to the Warburg effect are unique to PKM2 but not its closely-related alternatively-spliced isoform, PKM1, which is encoded by the same gene *PKM*. Alternative splicing results in PKM1 and PKM2 having 11 common exons (exons 1-8, 11 and 12) and a mutually-exclusive exon: exon 9 for PKM1 and exon 10 for PKM2 (Noguchi et al., 1986) (Fig. 1.3). Exon 9 and exon 10 are of the same length; hence, both isoforms have the same numbers of amino acids (531). Each of exons 9 and 10 encodes 56 amino acids (Noguchi et al., 1986). Among these, only 22 amino acids are different between PKM1 and PKM2 for human and mouse, and 21 are different for rat, resulting in very similar predicted molecular weights between PKM1 and PKM2 in all three species (all are approximately 58 kDa; see section 1.4.1 in Chapter 1 for details). The amino acid residues in exon 10 of PKM2 that are different from exon 9 in PKM1 form a binding pocket for FBP (Dombrauckas et al., 2005; Noguchi et al., 1986), enabling allosteric regulation that is unique to PKM2. This implicates PKM2, but not PKM1, in regulating the fate of glucose within the cells (see section 1.4.3 in Chapter 1).

With these specific roles of PKM2 and the evidence of PKM2 expression in the mammalian retina (Morohoshi et al., 2012), it was hypothesised that PKM2 plays a similar role in driving the Warburg effect in MCs as it does in cancer cells, which is explored in this chapter.

5.2 Chapter aims

This chapter addresses Aim 3 of the thesis: to investigate whether PKM2 drives the Warburg effect in MCs.

Aim 3.1: To study the effect of PKM2 knockdown (KD) on the metabolism of glucose in MCs

Aim 3.2: To study the effect of PKM2 knockout (KO) on the metabolism of glucose in MCs

5.3 Experimental approach and overview

PKM expression in cultured MCs was firstly elucidated. Secondly, to determine its specific role in MCs, PKM2 was knocked down using a lentiviral shRNA-mediated system and the cells analysed for glucose metabolism. Thirdly, to complement and confirm the results of PKM2 KD, PKM2 KO MCs were created by employing CRISPR/Cas9 technology, and the KO cells subjected to similar metabolic analysis to the KD cells.

The results demonstrated that both cultured primary MCs and immortalised rMC-1 cells express PKM2. Attempts were then made to knock down PKM2 in primary MCs but were not successful due to low lentiviral transduction efficiency, despite trying different cell seeding densities and different batches and amounts of lentivirus. As rMC-1 cells display the Warburg effect, similar to primary MCs, they were chosen as the suitable MC cell line for analysis, and PKM2 KD and KO performed. Metabolic analyses showed that neither PKM2 KD nor PKM2 KO significantly affected glycolytic activity of rMC-1 cells, indicating that PKM2 is not a main driver of the Warburg effect in MCs.

5.4 Results

5.4.1 Pyruvate kinase M expression in Müller cells

5.4.1.1 Verifying antibodies

As PKM1 and PKM2 are encoded by the same gene, *PKM*, with the only difference being a mutually-exclusive exon (exon 9 for PKM1 and exon 10 for PKM2) (Noguchi et al., 1986), specific antibodies which had been verified in rat tissues were required to investigate expression of these PK isoforms in cultured rat MCs by western blotting. A number of commercial antibodies were available, but in many cases they had been poorly verified and their specificity was questionable (reviewed in (Chaneton and Gottlieb, 2012).

In preliminary studies, two commercially available anti-PKM2 antibodies were tested (Fig. 5.1), a polyclonal antibody from Cell Signaling Technology (CS) (#3198S) and a monoclonal antibody from Novus Biologicals (N) (#NBP1-48351). These data were presented in the candidate's Honours thesis

(Kittipassorn, 2013) and published during the course of the candidate's PhD in Paper 2 (Casson et al., 2016) (Appendix 7.2). Surprisingly, the two antibodies detected proteins of different sizes in human and mouse cell lines (human embryonic kidney HEK293T and mouse embryonic fibroblast NIH3T3 cells). The anti-PKM2 antibody from CS was generated using a synthetic peptide corresponding to sequences surrounding Serine 406 residue in the region encoded exclusively by exon 10 of human PKM2, while the immunogen used to generate the anti-PKM2 antibody from N was full length human PKM2 protein, which contains regions encoded by the common exons. In addition, CS performed specificity testing that indicated that the antibody only detected PKM2 and not PKM1 (personal communication with the manufacturer). It has also been shown independently that transfecting cells with a siRNA specific to PKM2 led to a KD of the protein detected by the same CS antibody on western blots (Goldberg and Sharp, 2012). Furthermore, this antibody was able to detect PKM2 in rat cells (Kittipassorn, 2013). Therefore, given the specificity and verification in rat cells of the anti-PKM2 antibody from CS, this antibody was selected for use in all experiments in this thesis.

In addition to an antibody specific to PKM2, an antibody specific to PKM1 was also thought to be beneficial in determining whether treatments targeting PKM2 also affected PKM1 expression. Therefore, three commercially-available anti-PKM1 antibodies were tested: a monoclonal antibody from CS (#7067), a polyclonal antibody from Proteintech (PT) (#15821-1-AP), and a polyclonal antibody from N (#NBP2-14833). Liver tissues which mainly express PKL (Imamura and Tanaka, 1972) were used as a negative control, while muscle tissues whose dominant PK isoform is PKM1 (Imamura and Tanaka, 1972) were used as a positive control. Tissues from both mouse and rat were used. None of the three antibodies detected a band of the approximate size of PKM1 (58 kDa) in mouse liver, but did all detect bands of approximately 58 kDa, matching the quoted size of this protein (see section 1.4.1 in Chapter 1), in mouse muscle samples (Fig. 5.2), as expected. These findings suggested that all three antibodies correctly and specifically detected mouse PKM1. However, none of the antibodies detected bands corresponding to PKM1 in rat muscle (Fig. 5.2).

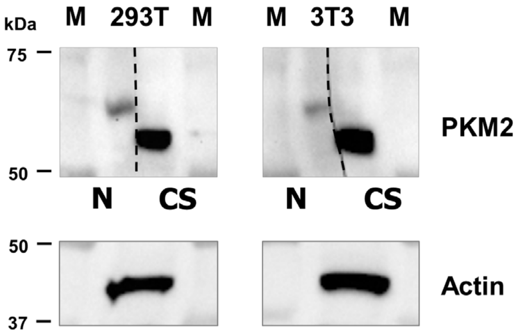

Figure 5.1. Validating anti-PKM2 antibodies. Western blots of whole cell extracts from HEK293T and NIH3T3 cell lines grown in hypoxia, probed for PKM2 using two commercially-available antibodies from Cell Signaling Technology (CS) (#3198S) and Novus Biologicals (N) (#NBP1-48351). Each of the two sample lanes was cut in the middle (dotted lines) and each half probed with each of the two antibodies as indicated. M, molecular weight markers. Reproduced from Paper 2 (Casson et al., 2016), and part of the candidate's Honours thesis (Kittipassorn, 2013).

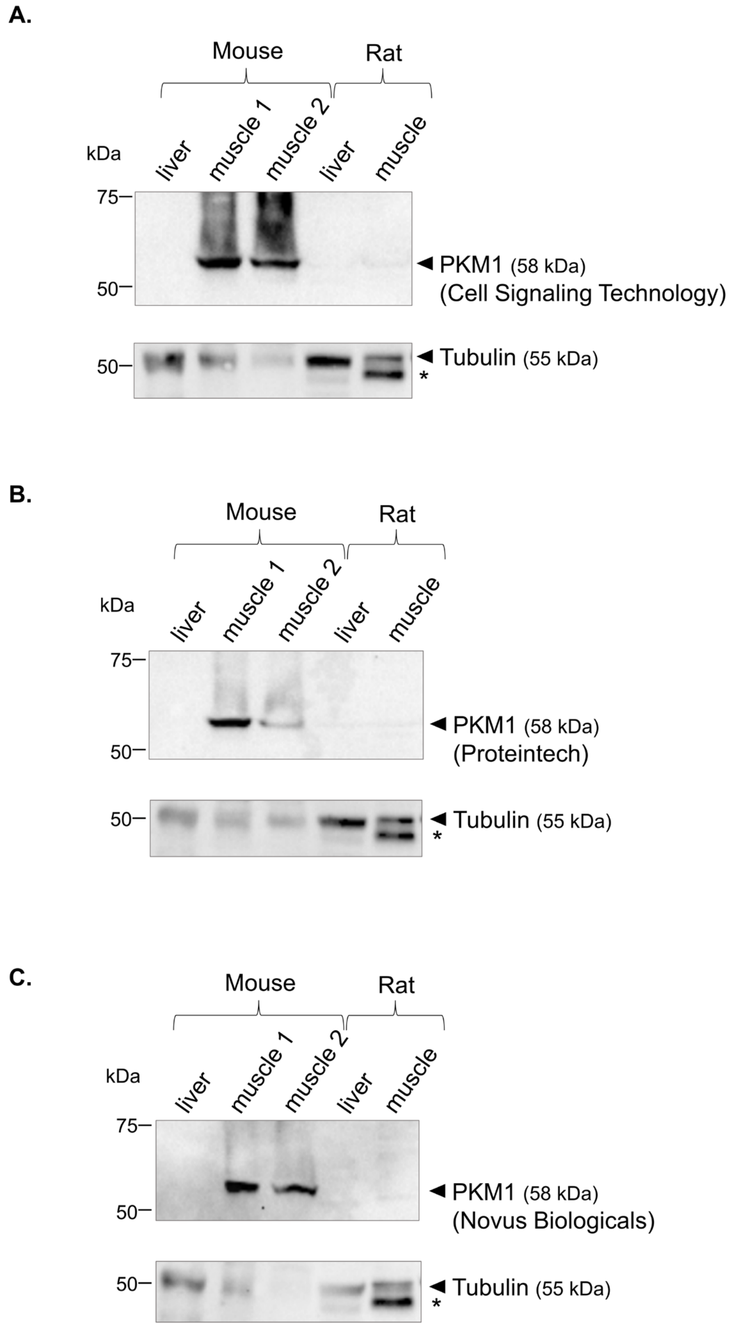

Figure 5.2. Validating anti-PKM1 antibodies. Western blots of protein extracts from mouse and rat liver and muscle tissues, probed for PKM1 using commercially-available antibodies from **(A)** Cell Signaling Technology (#7067), **(B)** Proteintech (#15821-1-AP), and **(C)** Novus Biologicals (#NBP2-14833). Expected size of each protein is shown in brackets. Arrows indicate target protein bands and asterisks non-specific bands. Each blot representative of two independent experiments.

Immunogens that were used to generate all three antibodies were peptides corresponding to part of the human PKM1 protein (Fig. 5.3). In the human PKM1 protein, residues 381-436 are encoded from exon 9, the exclusive exon of PKM1. The CS immunogen is a synthetic peptide of undefined length corresponding to residues surrounding Alanine 411 which is in the region encoded by exon 9 (manufacturer's data sheet). The PT immunogen corresponds to residues 398-417 which are also within the region encoded by exon 9 (manufacturer's data sheet and personal communication with the manufacturer). The N immunogen corresponds to a C-terminal region of the human PKM1, between residues 350-450 (exact length of immunogen not provided by manufacturer) which span regions encoded by exons 8, 9 and 11. The regions of the human PKM1 protein corresponding to these immunogens are highly conserved in primary amino acid sequence between human and mouse (Fig. 5.3B), but not as well conserved between human and rat (Fig. 5.3C), which could explain why none of these antibodies can detect rat PKM1.

Attempts were made to generate custom anti-PKM1 antibodies but these were not successful. Anti-total PKM antibody (CS #3190S), which detects both isoforms of PKM, was then instead used to determine total PKM levels, and by comparison with the anti-PKM2 antibodies the relative level of PKM1, as performed previously (Goldberg and Sharp, 2012). The immunogen used to generate this pan-specific antibody was a synthetic peptide corresponding to residues around Glycine 200 of human PKM2 (manufacturer's data sheet), which is in a region encoded by a common exon between PKM1 and PKM2, and is highly conserved between human and rat (Fig. 5.3C). Figure 5.4 shows western blots probed for total PKM (Fig. 5.4A) and PKM2 (Fig. 5.4B) on three different rat tissues: liver tissues which mainly express PKL and not PKM (Imamura and Tanaka, 1972) (reviewed in (Mazurek, 2011)), muscles which express PKM1 but not PKM2 (Imamura and Tanaka, 1972) (reviewed in (Mazurek, 2011)), and retinas that express both isoforms of PKM (Casson et al., 2016; Kittipassorn, 2013; Lindsay et al., 2014; Morohoshi et al., 2012). The blot incubated with the previously-verified anti-PKM2 antibody only showed positive protein determination in the rat retina sample (Fig. 5.4B, lane 3), as expected. The total PKM blot showed a band corresponding to PKM in both the rat muscle and the rat retina samples (Fig. 5.4A, lanes 2 and 3). Together these data demonstrate that the anti-total PKM antibody is able to detect both rat PKM1 and rat PKM2 proteins, and hence was used in subsequent experiments.

Figure 5.3

A.

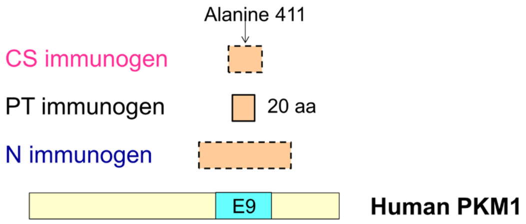

B.

```
mouse   1    MPKPHSEAGTAFIQTQQLHAAMADTFLEHMCRLDIDSAPITARNTGIICTIGPASRSVEM  60
             M KPHSEAGTAFIQTQQLHAAMADTFLEHMCRLDIDS PITARNTGIICTIGPASRSVE
human   1    MSKPHSEAGTAFIQTQQLHAAMADTFLEHMCRLDIDSPPITARNTGIICTIGPASRSVET  60

mouse   61   LKEMIKSGMNVARLNFSHGTHEYHAETIKNVREATESFASDPILYRPVAVALDTKGPEIR  120
             LKEMIKSGMNVARLNFSHGTHEYHAETIKNVR ATESFASDPILYRPVAVALDTKGPEIR
human   61   LKEMIKSGMNVARLNFSHGTHEYHAETIKNVRTATESFASDPILYRPVAVALDTKGPEIR  120

mouse   121  TGLIKGSGTAEVELKKGATLKITLDNAYMEKCDENILWLDYKNICKVVEVGSKIYVDDGL  180
             TGLIKGSGTAEVELKKGATLKITLDNAYMEKCDENILWLDYKNICKVVEVGSKIYVDDGL
human   121  TGLIKGSGTAEVELKKGATLKITLDNAYMEKCDENILWLDYKNICKVVEVGSKIYVDDGL  180

mouse   181  ISLQVKEKGADFLVTEVENGGSLGSKKGVNLPGAAVDLPAVSEKDIQDLKFGVEQDVDMV  240
             ISLQVK+KGADFLVTEVENGGSLGSKKGVNLPGAAVDLPAVSEKDIQDLKFGVEQDVDMV
human   181  ISLQVKQKGADFLVTEVENGGSLGSKKGVNLPGAAVDLPAVSEKDIQDLKFGVEQDVDMV  240

mouse   241  FASFIRKAADVHEVRKVLGEKGKNIKIISKIENHEGVRRFDEILEASDGIMVARGDLGIE  300
             FASFIRKA+DVHEVRKVLGEKGKNIKIISKIENHEGVRRFDEILEASDGIMVARGDLGIE
human   241  FASFIRKASDVHEVRKVLGEKGKNIKIISKIENHEGVRRFDEILEASDGIMVARGDLGIE  300

mouse   301  IPAEKVFLAQKMMIGRCNRAGKPVICATQMLESMIKKPRPTRAEGSDVANAVLDGADCIM  360
             IPAEKVFLAQKMMIGRCNRAGKPVICATQMLESMIKKPRPTRAEGSDVANAVLDGADCIM
human   301  IPAEKVFLAQKMMIGRCNRAGKPVICATQMLESMIKKPRPTRAEGSDVA[NAVLDGADCIM  360

mouse   361  LSGETAKGDYPLEAVRMQHLIAREAEAAMFHRLLFEELVRASSHSTDLMEAMAMGSVEAS  420
             LSGETAKGDYPLEAVRMQHLIAREAEAAMFHR LFEELVRASSHSTDLMEAMAMGSVEAS
human   361  LSGETAKGDYPLEAVRMQHLIAREAEAAMFHRKLFEE[LVRASSHSTDLMEAMAMGSV]EAS  420

mouse   421  YKCLAAALIVLTESGRSAHQVARYRPRAPIIAVTRNPQTARQAHLYRGIFPVLCKDAVLN  480
             YKCLAAALIVLTESGRSAHQVARYRPRAPIIAVTRNPQTARQAHLYRGIFPVLCKD V
human   421  YKCLAAALIVLTESGRSAHQVARYRPRAP]IAVTRNPQTARQAHLYRGIFPVLCKDPVQE  480

mouse   481  AWAEDVDLRVNLAMDVGKARGFFKKGDVVIVLTGWRPGSGFTNTMRVVPVP  531
             AWAEDVDLRVN AM+VGKARGFFKKGDVVIVLTGWRPGSGFTNTMRVVPVP
human   481  AWAEDVDLRVNFAMNVGKARGFFKKGDVVIVLTGWRPGSGFTNTMRVVPVP  531
```

C.

```
rat     1    MPKPDSEAGTAFIQTQQLHAAMADTFLEHMCRLDIDSAPITARNTGIICTIGPASRSVEM  60
             M KP SEAGTAFIQTQQLHAAMADTFLEHMCRLDIDS PITARNTGIICTIGPASRSVE
human   1    MSKPHSEAGTAFIQTQQLHAAMADTFLEHMCRLDIDSPPITARNTGIICTIGPASRSVET  60

rat     61   LKEMIKSGMNVARLNFSHGTHEYHAETIKNVRAATESFASDPILYRPVAVALDTKGPEIR  120
             LKEMIKSGMNVARLNFSHGTHEYHAETIKNVR ATESFASDPILYRPVAVALDTKGPEIR
human   61   LKEMIKSGMNVARLNFSHGTHEYHAETIKNVRTATESFASDPILYRPVAVALDTKGPEIR  120

rat     121  TGLIKGSGTAEVELKKGATLKITLDNAYMEKCDENILWLDYKNICKVVEVGSKIYVDDGL  180
             TGLIKGSGTAEVELKKGATLKITLDNAYMEKCDENILWLDYKNICKVVEVGSKIYVDDGL
human   121  TGLIKGSGTAEVELKKGATLKITLDNAYMEKCDENILWLDYKNICKVVEVGSKIYVDDGL  180

rat     181  ISLQVKEKGADYLVTEVENGGSLGSKKGVNLPGAAVDLPAVSEKDIQDLKFGVEQDVDMV  240
             ISLQVK+KGAD+LVTEVENGGSLGSKKGVNLPGAAVDLPAVSEKDIQDLKFGVEQDVDMV
human   181  ISLQVKQKGADFLVTEVENGGSLGSKKGVNLPGAAVDLPAVSEKDIQDLKFGVEQDVDMV  240

rat     241  FASFIRKAADVHEVRKVLGEKGKNIKIISKIENHEGVRRFDEILEASDGIMVARGDLGIE  300
             FASFIRKA+DVHEVRKVLGEKGKNIKIISKIENHEGVRRFDEILEASDGIMVARGDLGIE
human   241  FASFIRKASDVHEVRKVLGEKGKNIKIISKIENHEGVRRFDEILEASDGIMVARGDLGIE  300

rat     301  IPAEKVFLAQKMMIGRCNRAGKPVICATQMLESMIKKPRPTRAEGSDVANAVLDGADCIM  360
             IPAEKVFLAQKMMIGRCNRAGKPVICATQMLESMIKKPRPTRAEGSDVANAVLDGADCIM
human   301  IPAEKVFLAQKMMIGRCNRAGKPVICATQMLESMIKKPRPTRAEGSDVA[NAVLDGADCIM  360

rat     361  LSGETAKGDYPLEAVRMQHLIAREAEAAVFHRLLFEELARASSQSTDPLEAMAMGSVEAS  420
             LSGETAKGDYPLEAVRMQHLIAREAEAA+FHR LFEEL RASS STD +EAMAMGSVEAS
human   361  LSGETAKGDYPLEAVRMQHLIAREAEAAMFHRKLFEE[LVRASSHSTDLMEAMAMGSV]EAS  420

rat     421  YKCLAAALIVLTESGRSAHQVARYRPRAPIIAVTRNPQTARQAHLYRGIFPVLCKDAVLD  480
             YKCLAAALIVLTESGRSAHQVARYRPRAPIIAVTRNPQTARQAHLYRGIFPVLCKD V +
human   421  YKCLAAALIVLTESGRSAHQVARYRPRAP]IAVTRNPQTARQAHLYRGIFPVLCKDPVQE  480

rat     481  AWAEDVDLRVNLAMNVGKARGFFKKGDVVIVLTGWRPGSGFTNTMRVVPVP  531
             AWAEDVDLRVN AMNVGKARGFFKKGDVVIVLTGWRPGSGFTNTMRVVPVP
human   481  AWAEDVDLRVNFAMNVGKARGFFKKGDVVIVLTGWRPGSGFTNTMRVVPVP  531
```

Figure 5.3. Immunogens used to generate anti-PKM1 antibodies used in figure 5.1. (A) A schematic diagram showing immunogens against human PKM1 protein that were used to generate the three anti-PKM1 antibodies used in figure 5.1 from Cell Signaling Technology (CS) (#7067), Proteintech (PT) (#15821-1-AP), and Novus Biologicals (N) (#NBP2-14833). Data on the CS and the NB immunogens from the manufacturers' data sheets. Data on the PT immunogen from the manufacturers' data sheets and personal communication with the manufacturer. Dashed boxes represent immunogens with length not provided. aa, amino acids. In **(B)** and **(C)** the amino acid sequence of human PKM1 (NCBI Reference Sequence: NP_872270.1) is aligned with that of mouse (NCBI Reference Sequence: NP_001240812.1) and rat (GenBank: AAB93666.1), respectively, using the NCBI BLAST services. Exon 9 (residues 381-436) is highlighted in yellow. CS immunogen is a synthetic peptide (length not provided) corresponding to residues surrounding Alanine 411 (pink circle). PT immunogen is a 20-amino acid-long peptide corresponding to residues 398-417 (green brackets). N immunogen (length not provided) locates between residues 350-450 (blue brackets). E, exon.

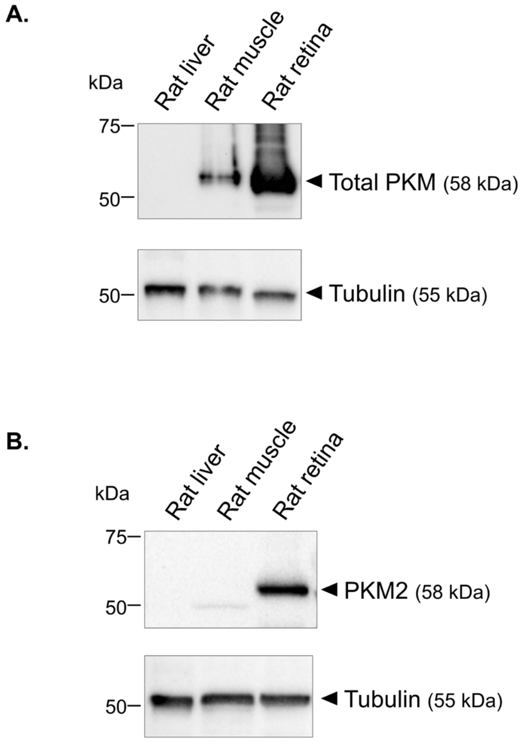

Figure 5.4. Anti-total PKM and anti-PKM2 antibodies. Western blots of protein extracts from rat liver, muscle and retina tissues, probed for total PKM **(A)** and PKM2 **(B)**. Expected size of each protein is shown in brackets. Arrows indicate target protein bands and asterisks non-specific bands.

5.4.1.2 Expression of pyruvate kinase M2 and total pyruvate kinase M in Müller cells

Using the verified antibodies, the expression of PKM2 and total PKM in three different rat MCs (primary, rMC-1 and SIRMu-1) as well as primary MEFs and HeLa cells was investigated (Fig. 5.5). These same cells were also used in the subsequent metabolic analyses presented in figures 4.5 and 4.6.

The western blots demonstrated that all cell types express PKM2, with a very low levels in SIRMu-1s and MEFs and at least an order of magnitude higher in the other three cell lines (Fig 5.5). A similar trend was observed with the levels of total PKM. Interestingly, PKM proteins of human (HeLa), mouse (MEF) and rat (three different MCs) all produced bands with small differences in apparent size, but all have the same number of amino acids (Fig 5.3). We had previously observed these slight differences in size and we hypothesised that they may be due to differences in sequence and/or post-translational modifications between species, affecting electrophoretic migration and apparent molecular weight.

5.4.2 Effect of pyruvate kinase M2 knockdown on the Warburg effect in Müller cells

To determine the specific role of PKM2 in glucose metabolism in MCs, we attempted to transiently knock down PKM2 protein in primary MCs, using the miR30-based shRNA system as described previously (Bersten et al., 2015). The glucose metabolism in these cells with PKM2 knocked down could then be analysed using lactate assays and Seahorse Cell Mito Stress Tests, as described in Chapter 4.

5.4.2.1 Determining knockdown efficiency of shRNAs targeting pyruvate kinase M2 mRNA

For the KD of PKM2, four different shRNAs targeting exon 10 of rat PKM2 were designed (shPKM2s 1572, 1452, 1499 or 1501) and cloned into the pLV410 lentiviral expression vector together with the nuclear fluorescent protein Tomato (Bersten et al., 2015) (see section 2.6.1 in Chapter 2). The lentiviral system was chosen rather than transient transfection to increase efficiency, specifically for use with the primary MCs. As primary MCs are more difficult to grow and transfect, with a short life span (Chapter 3 and Paper 4 (Kittipassorn et al., 2019a)), initial testing of the KD efficiency of the

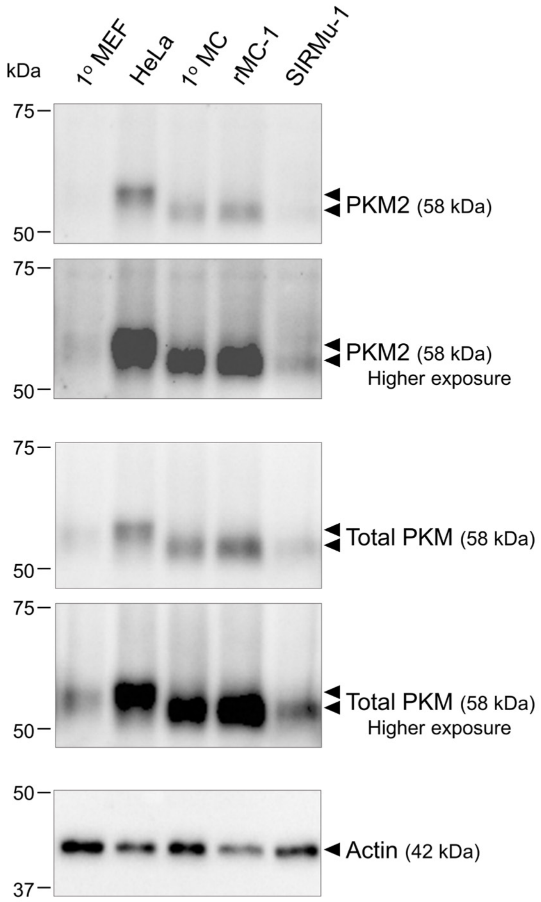

Figure 5.5. PKM2 and total PKM expression in Müller cells (MCs), MEFs and HeLa cells. Western blots of whole cell extracts from primary (1°) MEFs, HeLa cells, 1° MCs, rMC-1s and SIRMu-1s, probed for PKM2 and total PKM**.** Expected size of each protein is shown in brackets. Arrows indicate target protein bands and asterisks non-specific bands. Each blot representative of three independent experiments.

shRNAs was performed using the immortalised rMC-1 cell line. High transduction efficiencies of 50-85% were achieved with the rMC-1 cells at 48 hours after transduction, as determined by fluorescence microscopy (see section 2.6.4 in Chapter 2) to quantify the number of cells with the constitutive Tomato fluorescent protein expression from the pLV410 expression vector.

To determine the efficiencies of each of the shRNAs, rMC-1 cells transduced with lentivirus encoding either a non-targeting shRNA (shControl) or one of four shPKM2s (shPKM2s 1572, 1452, 1499 or 1501), incubated for 48 hours, and then whole cell extracts analysed by western blotting (Fig. 5.6). Although not statistically significant, the results clearly show that shPKM2 1452 was the most efficient with an average of 67% decrease in PKM2 protein level compared to the shControl. shPKM2s 1572 and 1499 were less efficient with an average of 37% and 41% decrease in PKM2 protein levels, respectively, compared to the shControl. shPKM2 1501 did not produce a consistent decrease in PKM2 levels; hence, shPKM2s 1452, 1572, and 1499 were chosen for subsequent experiments.

5.4.2.2 Transduction efficiency in primary Müller and rMC-1 cells

After testing the shPKM2s and successfully knocking down PKM2 in rMC-1 cells, similar experiments were performed on primary MCs. Figure 5.7 presents representative images taken three days after primary MCs (Fig. 5.7B upper panel) and rMC-1 cells (Fig. 5.7A lower panel) were seeded in a 96-well cell culture plate and transduced with lentivirus encoding a nuclear Tomato fluorescence protein and either a non-targeting shRNA (shControl) or one of three shRNAs targeting PKM2 (shPKM2s 1452, 1572, 1499). Hoechst 33342 nuclear staining indicates the total cell numbers and nuclear Tomato-positive cells indicate transduced cells. The representative primary MC images (Fig. 5.7A upper panel) are from a well with a 7.3% transduction efficiency, while the average transduction efficiencies for all shRNAs ranged from 3 to 14% (Fig. 5.7B). The rMC-1 images (Fig. 5.7A lower panel) are from a well with a 64% transduction efficiency while the average transduction efficiencies for all shRNAs ranged from 42-74% (Fig. 5.7B). Attempts were made to increase transduction efficiency in primary MCs, including employing different cell seeding densities and different batches and amounts of lentivirus; however, no experiments showed transduction efficiencies consistently above 50% and in most cases transduction efficiencies were less than 25%. These low transduction efficiencies in primary MCs were clearly inadequate for knocking down PKM2 for metabolic analysis

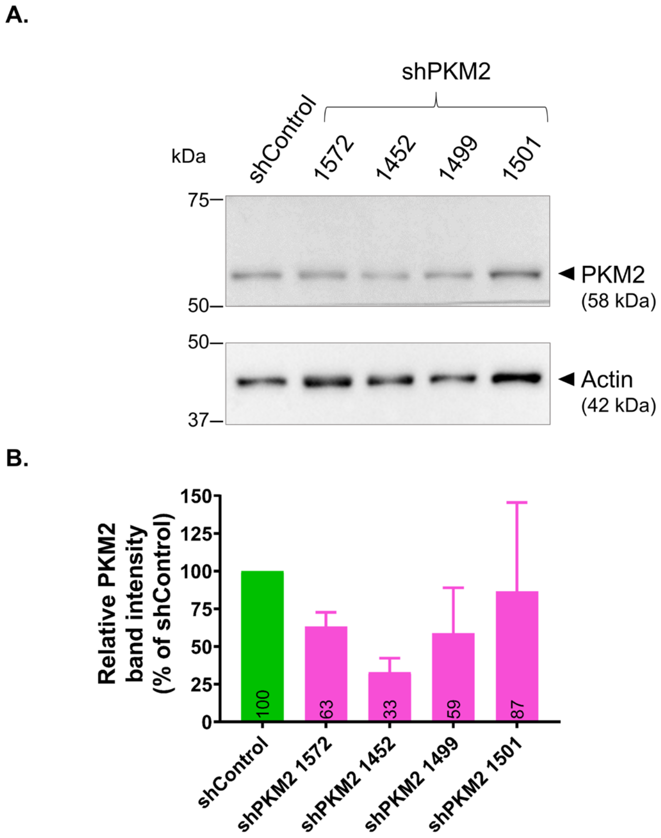

Figure 5.6. Determining knockdown efficiency of short hairpin RNAs (shRNAs) targeting *Pkm2* mRNA. (A) Western blot of whole cell extracts from rMC-1 cells transduced with lentivirus encoding either shControl (non-targeting shRNA) or one of four shRNAs targeting *Pkm2* mRNA (shPKM2s 1572, 1452, 1499 or 1501) and incubated for 48 hours, probed for PKM2. Blot representative of three independent experiments. In two experiments rMC-1 cells were seeded at 100,000 cells per well in a 24-well tray and transduced with 1.2 mL lentivirus per well. The third experiment was performed in a 6-well tray with the equivalent cell seeding density (500,000 cells per well) and lentivirus amount (6 mL per well). Expected band size of each protein is shown in brackets. Arrows indicate target protein bands. **(B)** A graph showing PKM2 band intensity normalised to the loading control actin. The relative PKM2 band intensity of the shControl is set to 100%. Data presented as mean ± S.D. from three independent experiments, with the mean of each group labelled within each bar. Statistical significance comparing to the shControl group was determined by one-way ANOVA followed by Dunnett's multiple comparison test. $p \geq 0.05$ for all comparisons.

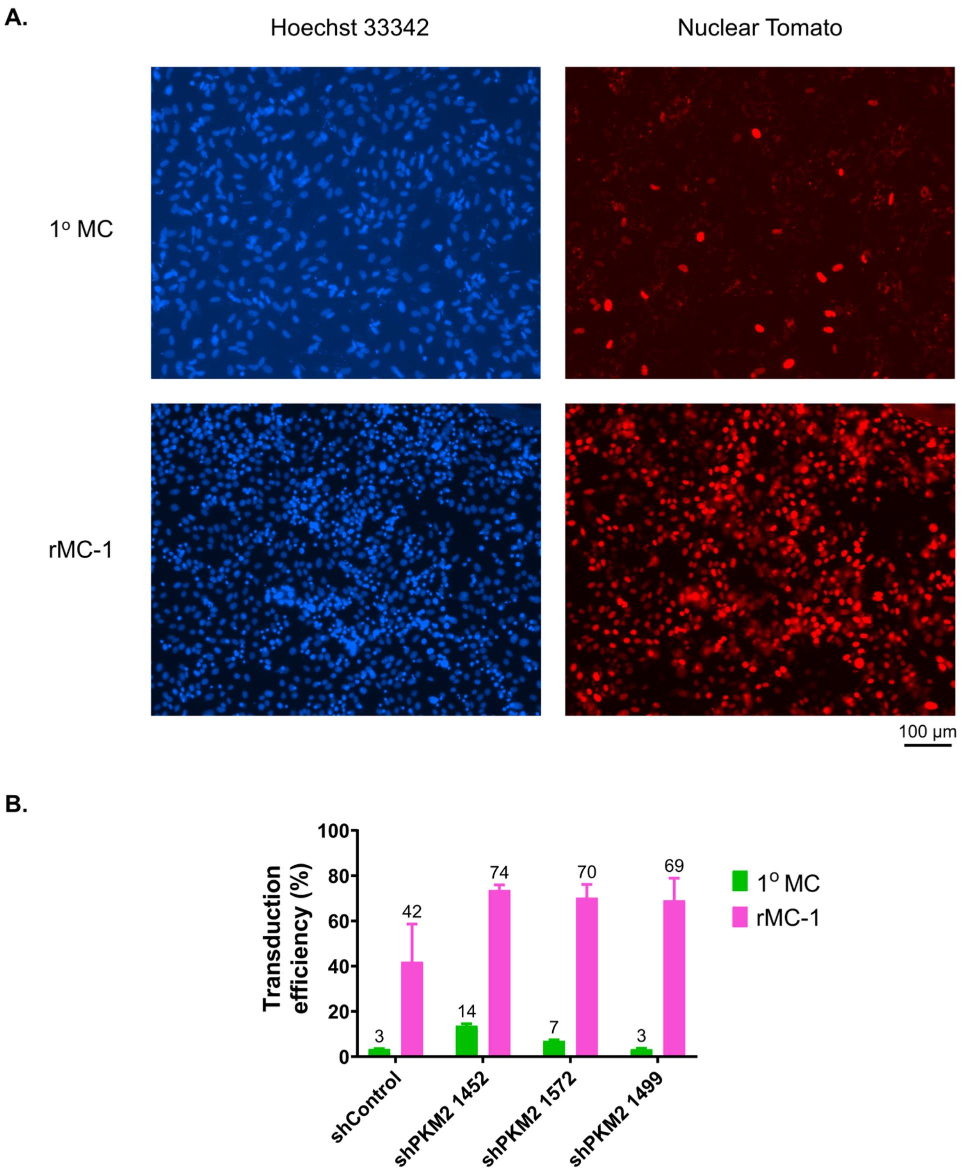

Figure 5.7. Transduction efficiency of primary Müller cells (1° MCs) and rMC-1 cells. 1° MCs (15,000 cells per well) and rMC-1 cells (3750 cells per well) were seeded in growth medium (80 µL per well) in a Seahorse 96-well cell culture plate and transduced with lentivirus (270 µL per well) encoding a nuclear Tomato fluorescence protein and either a non-targeting shRNA (shControl) or one of three shRNAs targeting PKM2 (shPKM2s 1452, 1572, 1499). Three days after transduction, cells were stained with Hoechst 33342 nuclear staining and transduction efficiency assessed. **(A)** Representative fluorescence images from 1° MCs (upper panel) and rMC-1 cells (lower panel) transduced with shPKM 1572, showing nuclear Tomato-positive cells (right panel), which indicate transduced cells, in comparison to total cell numbers indicated by nuclear staining (left panel). Scale bar = 100 µm and applies to all images. **(B)** Transduction efficiency of each of the four shRNAs in 1° MCs and rMC-1 cells. Data from one experiment (no statistical test performed) and presented as mean ± SD of two replicate wells per groups for 1° MCs and three replicate wells per group for rMC-1 cells, with the mean of each group labelled above each bar.

(i.e. with the best shRNA at best a 70% KD in 25% of cells could be achieved). Since the transduced cells express nuclear Tomato fluorescent protein, an attempt was made to enrich the transduced cells in a primary MC population by using FACS. However, the primary MCs were injured and did not recover after FACS; this was not unexpected for primary cells, which do not usually tolerate stress as well as immortalised cells. Given the difficulties in achieving adequate levels of transduction in the primary MCs, and the similarities in glycolytic dependency for ATP production and PKM2 expression between the primary MCs and the rMC-1 cells, the rMC-1 cells alone were used to investigate the role of PKM2 in MCs using shRNA-mediated KD.

5.4.2.3 Effect of pyruvate kinase M2 knockdown in the Warburg effect in rMC-1 cells

To determine the effect of knocking down PKM2 protein levels on glucose metabolism, rMC-1 cells were transduced with lentivirus encoding either a non-targeting shRNA (shControl) or one of the three best shPKM2 (shPKM2s 1572, 1452, or 1499), incubated for three days, and then lactate assays and Seahorse Cell Mito Stress Tests performed, as described in Chapter 4 (Fig. 5.8). Lentivirus for all shRNAs resulted in comparable transduction efficiencies (Fig 5.8A). Western blotting (Fig. 5.8B, 5.8C and Appendix 7.8) showed that all shPKM2s produced PKM2 KD but with varying efficiencies and consistencies among three independent experiments, with the shPKM2 1452 being the most efficient and consistent (on average ~80% KD). However, there was no significant difference in glycolytic indicators, including lactate efflux rates (Fig. 5.8D), kinetic profiles of ECARs and OCRs (Fig. 5.8E and Appendix 7.8), % contribution of glycolysis to ATP production (Fig. 5.8F) or basal ECAR/OCR ratios (Fig. 5.8G) between any of the three shRNAs targeting PKM2 and shControl. As a comparison, figure 5.8H shows a significantly decreased ECAR/OCR ratio in rMC-1 cells treated with oxamate, a LDHA inhibitor, demonstrating the loss of the Warburg effect due to inhibition of aerobic glycolysis. These results demonstrate that the rMC-1 cells with greatly decreased PKM2 levels still display high glycolytic activity, relative to OXPHOS, to the same extent as control cells with normal levels of PKM2, and are not consistent with PKM2 driving the Warburg effect in MCs.

Figure 5.8

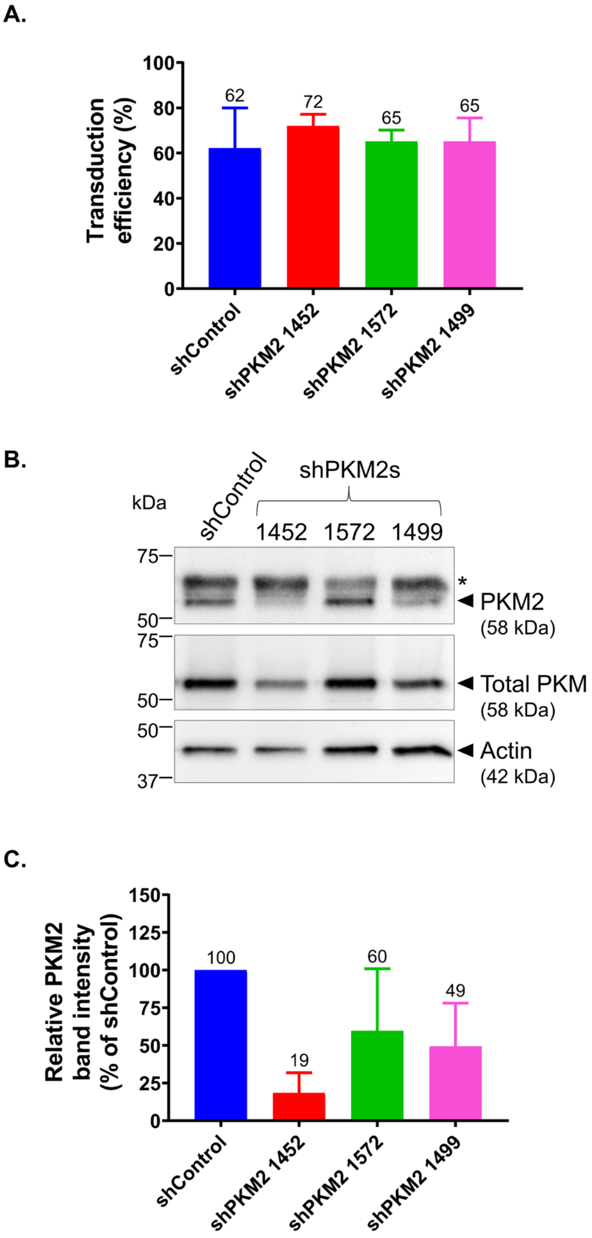
A.
Transduction efficiency (%)
100
80
60
40
20
0
62
72
65
65
shControl
shPKM2 1452
shPKM2 1572
shPKM2 1499
B.
kDa
shControl
shPKM2s
1452
1572
1499
75
50
75
50
50
37
*
PKM2
(58 kDa)
Total PKM
(58 kDa)
Actin
(42 kDa)
C.
Relative PKM2 band intensity (% of shControl)
150
125
100
75
50
25
0
100
19
60
49
shControl
shPKM2 1452
shPKM2 1572
shPKM2 1499

Figure 5.8 (continued)

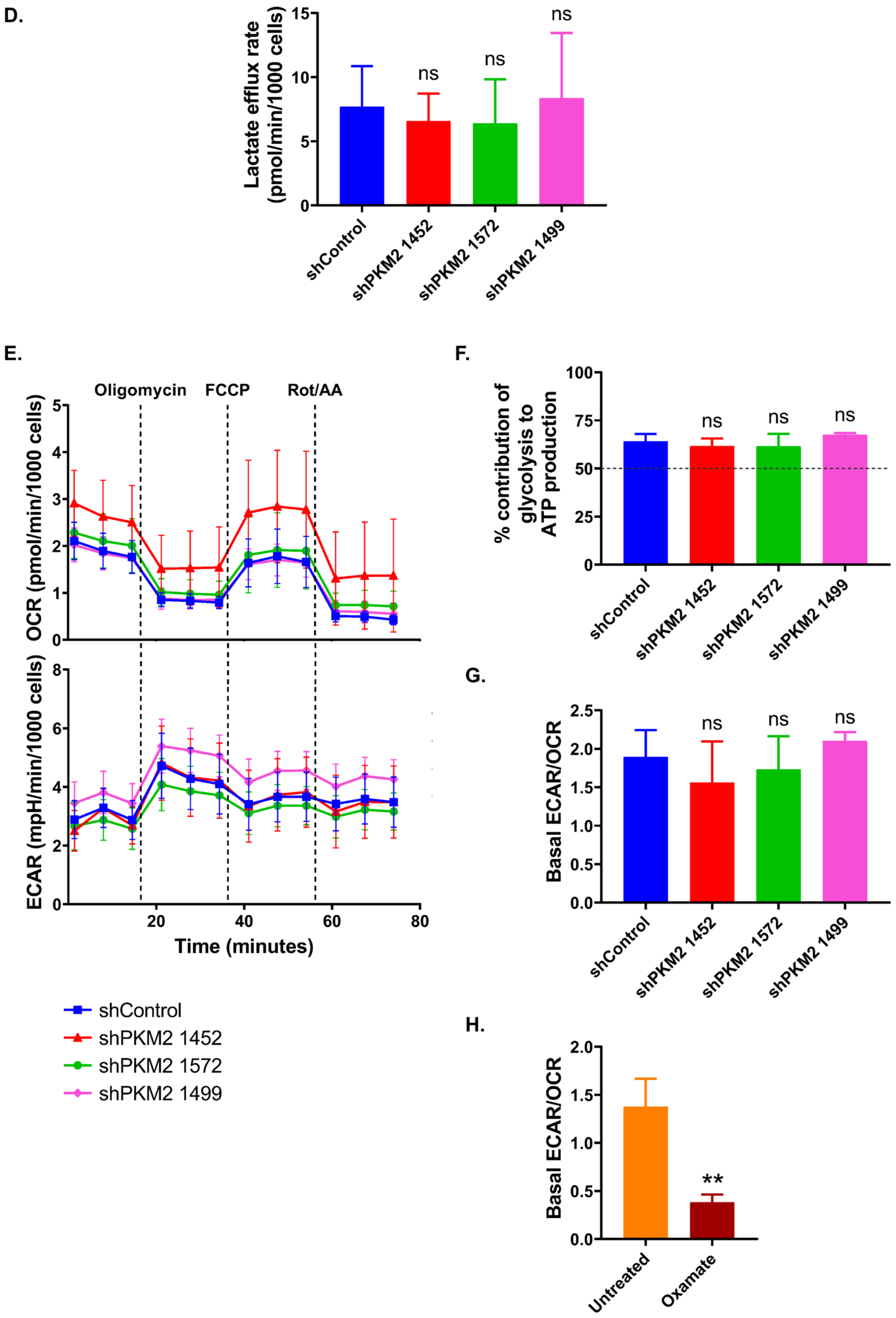

Figure 5.8. Effect of PKM2 knockdown in the Warburg effect in rMC-1 cells. (A) – (G) rMC-1 (3750 cells/well) were seeded in a Seahorse 96-well cell culture plate and transduced with lentivirus encoding either a non-targeting shRNA (shControl) or one of three shRNAs targeting PKM2 (shPKM2s 1452, 1572, 1499). Three days after transduction, cells were washed and incubated in fresh assay medium (XF base medium with 10 mM glucose) for an hour before the medium collected for lactate assays. Cells were then subjected to a Seahorse XF Cell Mito Stress Test in the presence of glucose (10 mM), using oligomycin (2 µM), FCCP (0.5 µM), and rotenone/antimycin A (Rot/AA, 0.5 µM). OCRs and ECARs were measured three times during each of the four conditions. Three independent experiments (each with a minimum of six replicate wells per group) were performed. In two experiments, cell numbers and transduction efficiency for each shRNA at the end of the assay were determined in three representative wells by fluorescence microscopy after Hoechst 33342 nuclear staining, while cells in experimental wells (used for OCR and ECAR readings) were harvested and protein extracted for western blot analysis. In the third experiment, cell numbers in all experimental wells were determined by the ArrayScan after Hoechst 33342 staining. Proteins for western blot analysis were extracted from a replicate Seahorse cell culture plate. Transduction efficiency for each shRNA was determined from a representative well in the replicate Seahorse cell culture plate. **(A)** Transduction efficiency of lentivirus of each shRNAs presented as mean ± SD of three independent experiments, with the mean of each shRNA labelled above each bar. (**B**) Western blot, probed for PKM2 and total PKM. Expected band size of each protein is shown in brackets. Arrows indicate target protein bands and asterisks non-specific bands. Western blots representative of three independent experiments, with other blots shown in Appendix 7.8. **(C)** PKM2 band intensity normalised to the loading control actin. The relative PKM2 band intensity of the shControl is set to 100%. **(D)** Lactate efflux rates determined from media samples collected before each Cell Mito Stress Test, presented as mean ± SD from three independent experiments, each performed using samples from three representative wells per group. **(E)** Representative graphs from one of the three independent experiments showing changes in OCRs and ECARs. Data presented as mean ± SD from at least six replicate samples. OCR and ECAR graphs from all three experiments can be found in Appendix 7.8. **(F)** % contribution of glycolysis to ATP production and **(G)** Basal ECAR/OCR ratios were determined based on OCR and ECAR readings. Data in A, C, D, F and G are presented as mean ± SD from three independent experiments. Statistical significance comparing to the shControl group was determined by one-way ANOVA followed by Dunnett's multiple comparison test. ns, not significant. **(H)** Effect of oxamate treatment on basal ECAR/OCR ratios in rMC-1 cells. Cells were seeded at 15,000 cells per well in a Seahorse cell culture plate. On the following day, cells were washed and incubated in fresh assay medium (XF base medium with 10 mM glucose) with or without oxamate for approximately three hours, and subjected to an XF Cell Mito Stress Test. Data presented as mean ± SD from three independent experiments (each with a minimum of two replicate wells per group). Statistical significance comparing to the untreated rMC-1 cells was determined by an unpaired two-tailed student's t-test. **p<0.01

While the KD did significantly reduce the levels of PKM2, it is important to consider the possibility that PKM2 is in excess in these cells, and the residual PKM2 (20-60% on average from the three shPKM2) is still able to drive the Warburg effect in MCs. Therefore, to further investigate whether PKM2 is required for driving the Warburg effect in MCs, and more specifically whether the residual level of PKM2 after the KD was enough to maintain its function, complete PKM2 KO rMC-1 cells were generated.

5.4.3 Effect of pyruvate kinase M2 knockout on the Warburg effect in Müller cells

PKM2 KO rMC-1 cell lines were generated using CRISPR/Cas9 technology and subsequently characterised in terms of their glucose metabolism.

5.4.3.1 Generating rMC-1 cell lines with pyruvate kinase M2 knocked out using CRISPR/Cas9

PKM2 and its splice variant PKM1 are encoded from the same gene *Pkm* (Noguchi et al., 1986). With alternative splicing, *Pkm2* mRNA contains the exclusive exon 10 and *Pkm1* contains the exclusive exon 9 (Fig. 1.3) (Chaneton and Gottlieb, 2012; Noguchi et al., 1986). A strategy was devised to generate PKM2 KO rMC-1 cells by removing exon 10 from the *Pkm* gene while keeping exon 9 intact, so that a complete loss of the PKM2 protein could be achieved without affecting PKM1.

To use CRISPR/Cas9 technology to remove exon 10 of the *Pkm* gene, a strategy was employed where a pair of gRNAs were used: one targeting the intron between exon 9 and exon 10 and the other the intron between exon 10 and exon 11 (Fig. 5.9A) (see also Fig. 2.3 and section 2.7.1 in Chapter 2). Cas9 nuclease would cause a double stranded break at both sites targeted by the two gRNAs and the portion between the two cut sites, which contains exon 10, could be removed during subsequent repair. To control for non-specific off-target effects, two different pairs of gRNAs were designed, and each used to generate distinct lines of PKM2 KO cells. Two gRNAs (gRNAs A1 and A2) were designed to target the intron between exon 9 and exon 10, and another two gRNAs (gRNAs B1 and B2) were designed to target the intron between exon 10 and exon 11 (Fig. 5.9A). gRNA A1 was paired with B1 to generate a PKM2 KO I cell population, and gRNA A2 was paired with B2 to generate a PKM2 KO II population (Fig. 5.9A). A primer pair that flanks the cut sites of the gRNAs was designed for use in PCR screening of KO cells.

5.4.3.2 Screening and verifying pyruvate kinase M2 knockout rMC-1 cell lines

rMC-1 cells were co-transfected with a plasmid encoding a puromycin resistance gene for selection, and a dual-gRNA expressing Cas9 nuclease plasmid (Adikusuma et al., 2017) containing either no gRNAs (an empty vector (EV) to generate a WT control pool of cells), gRNAs A1 and B1 (to generate the KO I pool), or gRNAs A2 and B2 (to generated the KO II pool). Transfected cells of each pool (EV, KO I or KO II) were selected with puromycin for 48 hours, and the gDNA extracted from surviving cells and screened by PCR (Fig 5.9B, the lanes labelled “Pool”). Amplified gDNA from the EV pool shows an unmodified WT PCR product of approximately 1100 base pairs (bp) as expected, the same as a sample from parent rMC-1 cells (untreated). The KO I pool produced a WT band of approximately 1100bp, an expected KO I PCR product of approximately 580 bp, and an additional band of approximately 850 bp (Fig. 5.9A and B), suggesting that there are both WT (cells that were successfully transfected but the Cas9-mediated deletion was unsuccessful) and KO alleles mixed within the pool. Similar results were found with the KO II pool which produced a WT band of approximately 1100bp, an expected KO II PCR product of approximately 470 bp, and another band of approximately 800 bp (Fig. 5.9A and B). Note that the additional bands in both KO I and KO II pools may be due to the loss of only part of exon 10 during the DNA repair process. Importantly, the bands corresponding to the expected KO products were clear, indicating successful and relatively efficient loss of exon 10 in each pool of cells.

Prior to further analysis, monoclonal lines were generated from each pool and propagated. gDNA of 15 monoclonal lines from each KO pool was extracted and screened by PCR (Fig. 5.9B, the lanes labelled “monoclones”). Monoclonal lines were also generated from the WT control EV pool and five lines also screened by PCR. All EV monoclonal lines showed a WT band of approximately 1100 bp as expected. Importantly, a number of the KO I and KO II monoclonal lines produced bands of approximately 580 and 470 bp, respectively, consistent with the loss of exon 10. Three lines each from KO I and KO II were selected, first based on the absence of a band corresponding to the WT allele, and second the presence of one or more bands corresponding to the size of expected products

Figure 5.9

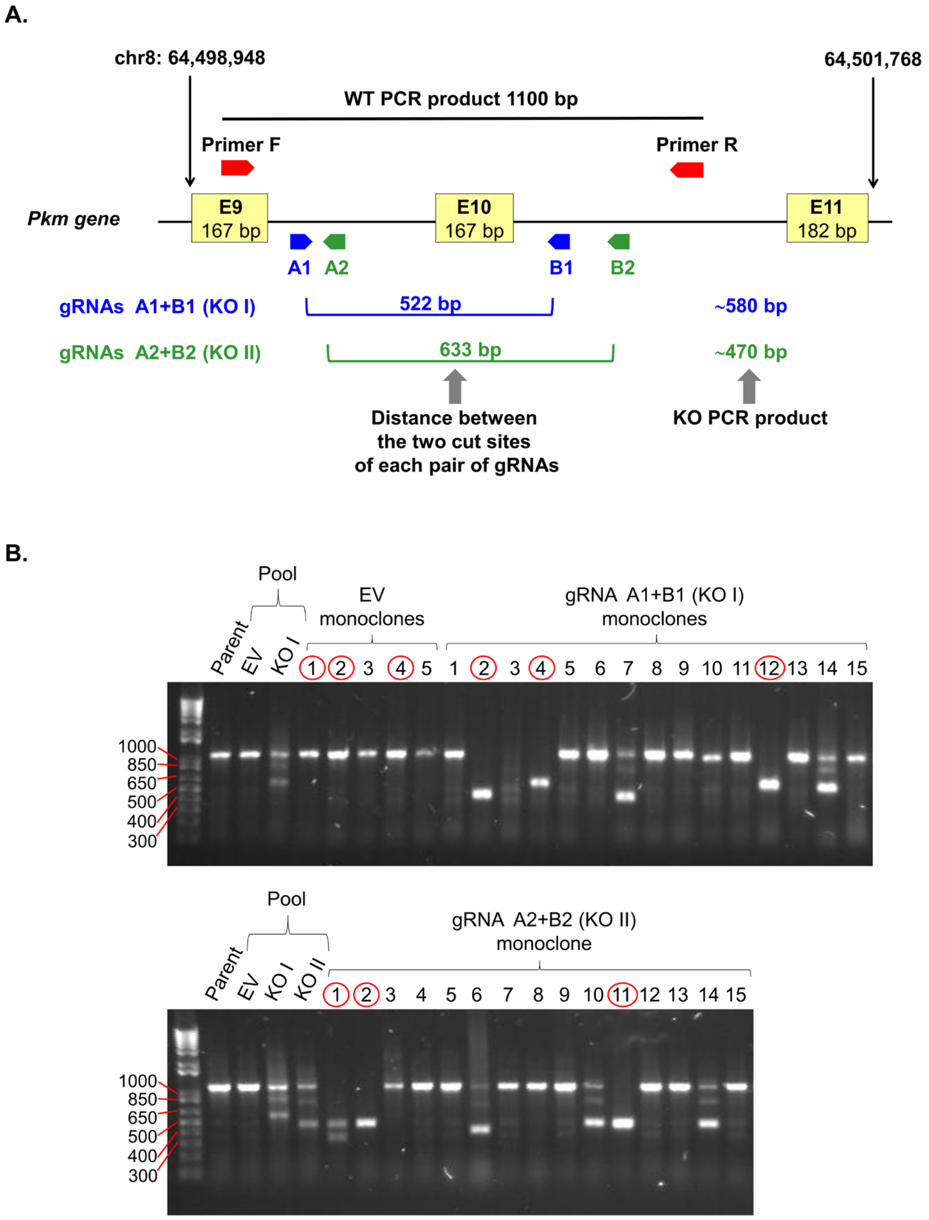
A.
chr8: 64,498,948
64,501,768
WT PCR product 1100 bp
Primer F
Primer R
Pkm gene
E9
167 bp
E10
167 bp
E11
182 bp
A1
A2
B1
B2
gRNAs A1+B1 (KO I)
522 bp
~580 bp
gRNAs A2+B2 (KO II)
633 bp
~470 bp
Distance between the two cut sites of each pair of gRNAs
KO PCR product
B.
Pool
Parent
EV
KO I
EV monoclones
1 2 3 4 5
gRNA A1+B1 (KO I) monoclones
1 2 3 4 5 6 7 8 9 10 11 12 13 14 15
1000
850
650
500
400
300
Pool
Parent
EV
KO I
KO II
gRNA A2+B2 (KO II) monoclone
1 2 3 4 5 6 7 8 9 10 11 12 13 14 15
1000
850
650
500
400
300

C.

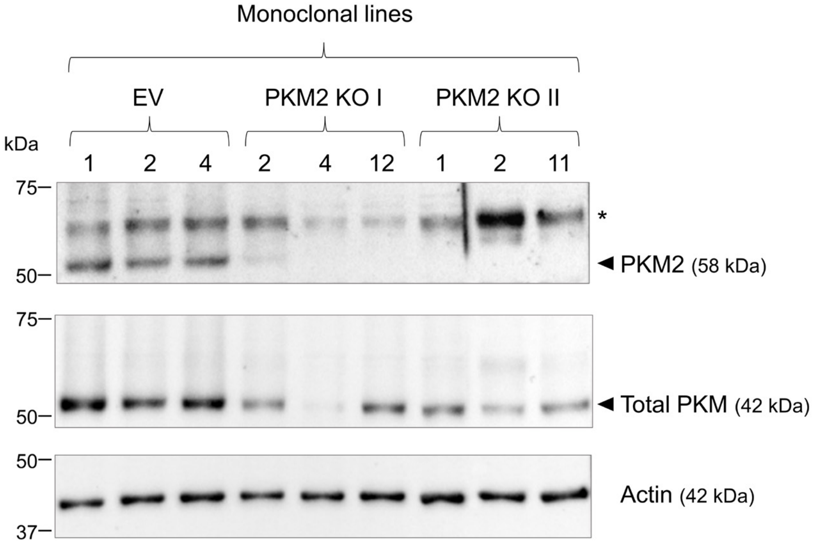

Figure 5.9. Generating and screening PKM2 knockout (KO) rMC-1 cell lines. (A) Schematic diagram illustrating a strategy to generate PKM2 KO cells by removing exon (E) 10 from the *Pkm* gene, using CRISPR/Cas9 technology. E10 was removed using a dual-guide RNA expressing Cas9 nuclease plasmid (Adikusuma et al., 2017) containing a pair of guide RNA (gRNAs). Two gRNAs (gRNAs A1 and A2) were designed to target the intron between E9 and E10, and another two gRNAs (gRNAs B1 and B2) were designed to target the intron between E10 and E11. gRNA A1 was paired with B1 to generate a KO I cell population (indicated by blue arrows and text). gRNA A2 was paired with B2 to generate a KO II population (indicated by green arrows and text). Distance between the two cut sites for each pair of gRNAs is shown. Forward (F) and reverse (R) primers were designed to screen for removal of E10, with PCR products of wildtype (WT) and KO indicated. Positions of the start of E9 and the end of E11 on chromosome (chr) 8 and the length of each exon are also illustrated. Black lines between exons indicate introns. bp, base pairs. The diagram is not to scale. **(B)** and **(C)** rMC-1 cells were co-transfected with a plasmid encoding a puromycin resistant gene for selection and one of three Cas9 nuclease plasmids: an empty vector (EV) without gRNA (to generate a WT control pool of cells), a vector with gRNAs A1 and B1 (to generate the KO I pool), or a vector with gRNAs A2 and B2 (to generated the KO II pool). Approximately 48 hours after transfection, transfected cells were selected with puromycin. gDNA was extracted from the three pools of cells and PCR performed **(B)**. Five monoclonal lines were then isolated from the WT pool (EV) and 15 monoclonal lines from each of the KO pools. gDNA were extracted from these lines and used for PCR **(B)**. Selected lines based on the PCR results (circled in red in C) were grown and proteins extracted and subjected to western blotting, probed for PKM2 and total PKM **(C)**. Expected size of each protein is shown in brackets. Arrows indicate target protein bands and asterisks non-specific bands.

or smaller, if additional deletions had occurred during repair. The selected cell lines were lines 2, 4, 12 for the KO I pool and lines 1, 2, 11 for the KO II (Fig. 5.9B). Three EV cell lines were randomly selected (lines 1, 2 and 4), and there was no obvious change in growth rate between the six KO lines compared to the EV lines.

Whole cell extracts were made from each of these selected cell lines and subjected to western blotting (Fig. 5.9C). With the exception of the KO I line 2, PKM2 was not detected in any of the KO lines, consistent with the KO of PKM2. All of the KO cell lines displayed varying levels of total PKM, corresponding to PKM1, and these levels were lower than the total PKM in the EV control lines, also consistent with the KO of PKM2.

The monoclonal line from each of the KO pools that displayed the most similar level of total PKM to the EV control lines (line 12 for KO I, line 1 for KO II) was chosen, and the amplified DNA analysed by Sanger sequencing. Figure 5.10 schematically illustrates the modified alleles, based on sequencing results, of the monoclonal PKM2 KO I line 12 and the monoclonal PKM2 KO II line 1. One allele of the KO I line 12 has lost 524 bp and the other 569 bp (Fig. 5.10). For the KO II line 1, one allele has lost 771 bp and the other 633 bp (Fig. 5.10). Both alleles of each cell line have exon 10 completely removed, and the 3’ end of exon 9 remains intact, confirming the complete KO of PKM2.

These two monoclonal PKM2 KO lines, and the corresponding EV control line, were then analysed metabolically using lactate assays and Seahorse Cell Mito Stress Tests. In the remainder of this thesis, the KO I line 12 is referred to as the KO I line, and the KO II line 1 is referred to as the KO II line. The EV line 1 was chosen as a control for subsequent experiments and is referred to as the WT line.

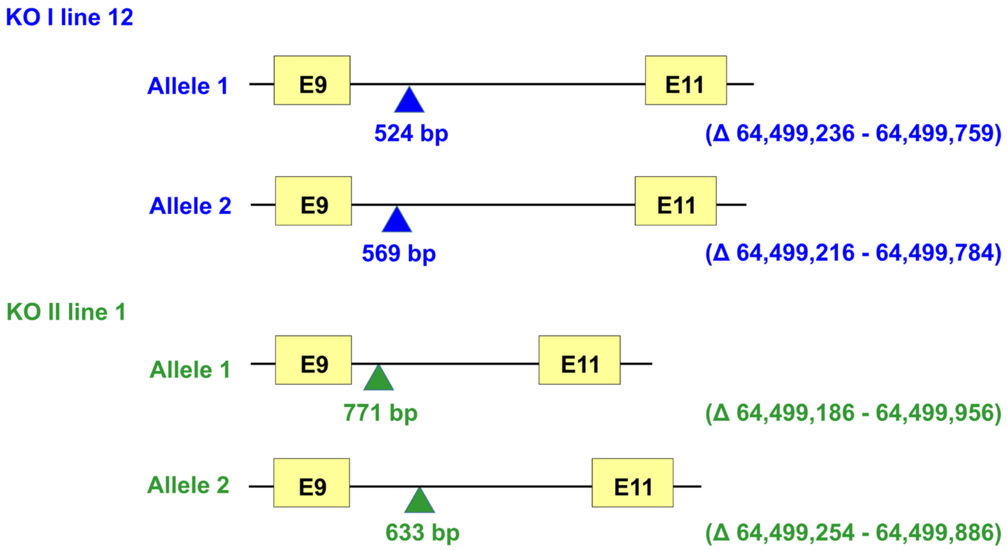

Figure 5.10. Modified *Pkm* alleles of selected monoclonal PKM2 knockout (KO) rMC-1 cell lines. Schematic diagrams showing the modified alleles of the KO I line 12 and the KO II line 1 based on Sanger sequencing results. Triangles and text underneath indicate the portion of each allele that was removed and its length, respectively. Positions on chromosome 8 of the deleted nucleotides are shown in brackets.

5.4.3.3 Effect of pyruvate kinase M2 knockout on the Warburg effect in rMC-1 cells

Lactate assays and Seahorse Cell Mito Stress Tests were performed on the two distinct PKM2 KO rMC-1 cell lines in comparison to the WT line (Figure 5.11). Western blots confirmed that the two KO lines lacked PKM2, and had reduced total PKM, compared to the WT control (Fig. 5.11A). Parameters indicative of glycolytic activity, namely lactate efflux rates (Fig. 5.11B), ECAR and OCR kinetic profiles (Fig. 5.11C and Appendix 7.9), % contribution of glycolysis to ATP production (Fig. 5.11D), and basal ECAR/OCR ratios (Fig. 5.11E), were not significantly changed in either the KO I line or the KO II line compared to the WT cells, and similar to previous observations with untreated rMC-1 and primary MCs (Fig. 4.6 and 4.7). While there was a small apparent change in lactate production, this is not statistically significant and did not alter either the contribution of glycolysis to ATP production or the basal ECAR/OCR ratio, which were very similar to the WT cells. Thus, any effects on metabolism with the loss of PKM2 are subtle, and the Warburg effect is essentially similar to the WT cells. These data are consistent with the PKM2 KD results (Fig. 5.8), and support the conclusion that PKM2 is not a major driver of the Warburg effect in rMC-1 cells. Of note, the KO I line had a small but statistically significant lower OCR_{basal}, OCR_{FCCP} and $OCR_{coupled}$ compared to the WT cells, but these results were not consistent with those of the other PKM2 KO line (KO II) in which there was either no significant change (for OCR_{basal} and OCR_{FCCP}) or an increase ($OCR_{coupled}$) compared to the WT, suggesting that these are likely off-target effects (Appendix 7.9B and C). Importantly, the inconsistencies of these results between the two KO lines indicate that these changes are not specific to PKM2 KO.

5.5 Discussion

5.5.1 Pyruvate kinase M2 expression in cultured Müller cells and correlation with glycolytic dependency

Firstly, PKM2 expression in different cultured rat MCs was determined using a verified PKM2-specific antibody (Kittipassorn, 2013) (Paper 2 (Casson et al., 2016) (Appendix 7.2)) (Fig. 5.4B). The specificity of the antibody is particularly crucial as PKM2 and PKM1 have very similar amino acid sequences and predicted molecular weights (See section 1.4.1 in Chapter 1). This issue also exists in published studies that used anti-PKM2 antibodies that have not been verified, the results of which have to be interpreted with caution (reviewed in (Chaneton and Gottlieb, 2012)).

Using the verified antibody, this thesis shows that the three MCs (primary, rMC-1 and SIRMu-1), primary MEFs and HeLa cells all express PKM2 but to different degrees (Fig. 5.5). PKM2 expression in primary rat MCs is consistent with the results of western blotting and immunocytochemistry presented in the candidate’s Honours thesis (Kittipassorn, 2013) and with PKM2 expression in cultured primary mouse MCs (Lindsay et al., 2014). PKM2 expression in rMC-1 and HeLa cells is also in agreement with published reports (Bluemlein et al., 2011; Christofk et al., 2008a; Lindsay et al., 2014). This thesis adds to that knowledge by showing that the SIRMu-1 cells also express PKM2 and that each of the five cell types investigated expresses PKM2 to a different degree. SIRMu-1 cells and primary MEFs express PKM2 at a level at least ten times lower than the other three cell types. Interestingly, PKM2 protein levels correlate with the cellular dependency on glycolysis for ATP production as presented in Chapter 4 (Fig. 4.4). HeLa cells, rMC-1 cells and primary MCs with higher PKM2 levels are more dependent on glycolysis for ATP production than on OXPHOS (on average over 50% of ATP is derived from glycolysis). MEFs and SIRMu-1 cells that have much lower levels of PKM2 are oxidative and on average less than 50% of ATP is derived from glycolysis. This agrees with a previously published finding where activated CD4 and CD8 T cells were shown to be more glycolytic and express higher levels of PKM2 than resting T cells (Cao et al., 2014). This correlation suggests that PKM2 might be involved in the control of glycolytic activity in cells. However, it does not indicate a causal relationship and further investigations are required.

In addition to PKM2 expression, it was also of interest to determine corresponding PKM1 expression. Unfortunately, a verified PKM1-specific antibody that works with rat PKM1 was not available (Fig. 5.2), consistent with that described in a collaborative study (Paper 2 (Casson et al., 2016)) (Appendix 7.2). A verified anti-total PKM antibody was instead used, similar to that used previously by others (Goldberg and Sharp, 2012). This antibody targets a common area of PKM1 and PKM2 proteins and can detect both isoforms (Fig. 5.4). Total PKM expression is higher in HeLa cells, rMC-1 cells and primary MCs than in MEFs and SIRMu-1 cells, following the same trend as PKM2 levels. Total PKM expression was also assessed at the mRNA level using the RNA-seq data presented in Paper 4

Figure 5.11

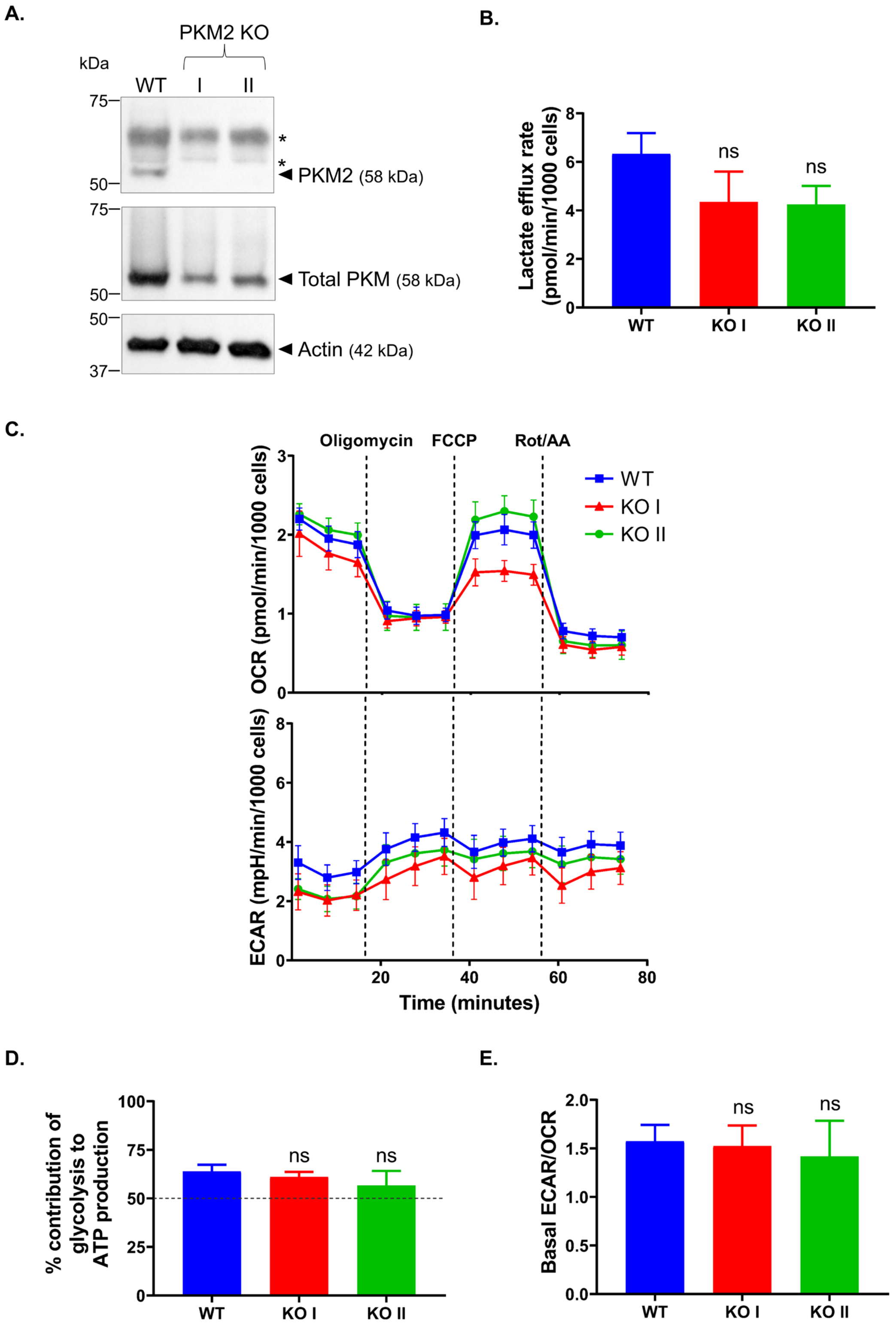
A.
PKM2 KO
kDa
WT
I
II
75
50
*
*
◀ PKM2 (58 kDa)
75
50
◀ Total PKM (58 kDa)
50
37
◀ Actin (42 kDa)
B.
Lactate efflux rate (pmol/min/1000 cells)
8
6
4
2
0
ns
ns
WT
KO I
KO II
C.
Oligomycin
FCCP
Rot/AA
OCR (pmol/min/1000 cells)
3
2
1
0
WT
KO I
KO II
ECAR (mpH/min/1000 cells)
8
6
4
2
0
20
40
60
80
Time (minutes)
D.
% contribution of glycolysis to ATP production
100
75
50
25
0
ns
ns
WT
KO I
KO II
E.
Basal ECAR/OCR
2.0
1.5
1.0
0.5
0.0
ns
ns
WT
KO I
KO II

Figure 5.11. Effect of PKM2 knockout (KO) on the Warburg effect in rMC-1 cells. Experiments were performed on three rMC-1 monoclonal cell lines: WT (the empty vector EV1 line), PKM2 KO I (the KO I line 12) and PKM2 KO II (the KO II line 1). **(A)** Western blot of whole cell extracts probed for PKM2 and total PKM. Results representative of three independent experiments. Expected size of each protein is shown in brackets. Arrows indicate target protein bands and asterisks non-specific bands. **(B) – (E)** The WT, the PKM2 KO I and the PKM2 KO II rMC-1 cell lines were seeded at 15,000 cells/well in a Seahorse 96-well cell culture plate. On the following day, cells were washed and incubated in fresh assay medium (XF base medium with 10 mM glucose) for an hour before the medium of each well was collected to use as samples for lactate assays. Cells were then subjected to an XF Cell Mito Stress test using oligomycin (2 μM), FCCP (0.5 μM), and rotenone/antimycin A (Rot/AA, 0.5 μM). OCRs and ECARs were measured three times during each of the four conditions. Three independent experiments (each with a minimum of eight replicate wells per group) were performed. Cell numbers from all three experiments were determined by the ArrayScan after Hoechst 33342 nuclear staining. **(B)** Lactate efflux rates determined from media samples collected before each Cell Mito Stress Test was performed, presented as mean ± SD from the three independent experiments, each performed using samples from three representative wells per group. **(C)** Representative graphs from one of the three independent experiments showing changes in OCRs and ECARs. Data presented as mean ± SD from at least eight replicate samples. OCR and ECAR graphs from all three experiments can be found in Appendix 7.9. **(D)** % contribution of glycolysis to ATP production and **(E)** Basal ECAR/OCR ratios were determined based on OCR and ECAR readings. Data in B, D and E are presented as mean ± SD from the three independent experiments. Statistical significance comparing to WT was determined by one-way ANOVA followed by Dunnett's multiple comparison test. ns, not significant.

(Kittipassorn et al., 2019a) and Paper 5 (Kittipassorn et al., 2019b) in Chapter 3. Unlike the clear difference in the protein levels, even when the stringency of the analysis was reduced to just a two-fold difference in expression levels, there was no significant difference in the expression of the PKM transcripts between SIRMu-1 cells and primary MCs (Table 4.1), which could be due to post-transcriptional regulation. A similar observation has previously been demonstrated with glutamine synthetase (GS), where the difference in its mRNA level in SIRMu-1 cells compared with primary MCs was of a lower degree than the difference in protein levels (data presented and discussed in Paper 4 (Kittipassorn et al., 2019a) in Chapter 3). Quantification of the amounts of each isoform could not be determined from the RNA-seq data.

5.5.2 Role of pyruvate kinase M2 in the Warburg effect in cultured Müller cells

To investigate the role of PKM2 in the Warburg effect in MCs (Aim 3 of the thesis), PKM2 KD and KO were performed. Methods and agents that specifically target PKM2 but not PKM1 were critical as the two isoforms are closely related. Although there were varying KD efficiencies (on average ~40-80%), metabolic analysis of the rMC-1 cells with PKM2 knocked down clearly demonstrated that the KD did not significantly affect the glycolytic activity of rMC-1 cells as shown by no statistically significant changes in any of the glycolytic parameters (lactate efflux rates, % contribution of glycolysis to ATP production and basal ECAR/OCR ratios) between the KD cells and the control (Fig. 5.8), suggesting that PKM2 is not a main driver of the Warburg effect in cultured MCs.

Next, rMC-1 cells with PKM2 knocked out were generated in order to differentiate between two possibilities: that PKM2 is not a major driver of the Warburg effect in MCs or that the residual amount of PKM2 (on average ~20-60%) was adequate to maintain its function of promoting the Warburg effect. A study has shown that a 90% decrease in PKM2 levels is required to illicit a 50% decrease in cell viability in HCT116 cells (Goldberg and Sharp, 2012)). Although cell viability is not the same biological effect as that being investigated in this thesis, given that the average KDs achieved were less than 90%, this study emphasises the importance of the KO approach.

Two distinct monoclonal lines of rMC-1 cells with PKM2 knocked out were generated by removing the PKM2-specific exon 10 from the *Pkm* gene disturbing the PKM1-specific exon 9. Both lines had a complete loss of PKM2 protein and similar levels of total PKM (Fig. 5.9 and 5.11). The levels of total PKM in both KO lines were lower than that of the WT control line but were still present. As PKM2 was completely lost, the presence of the total PKM bands in the KO lines shows that the knocking out of PKM2 by manipulating the *Pkm* gene did not stop the expression of PKM1.

The KO lines were subjected to metabolic analysis (Fig. 5.11). PKM2 KO did not significantly affect the glycolytic activity of the rMC-1 cells, similar to the results of the PKM2 KD cells, confirming that PKM2 is not a main driver of the Warburg effect in cultured MCs. This also suggests that the correlation between PKM2 protein levels and glycolytic dependency of cells is not a causal relationship. It is possible that PKM2 does play a subtle role in glucose metabolism that cannot be detected in this series of experiments, but clearly not the major role it is postulated to play in some cancer and other proliferating cells that display the Warburg effect (Christofk et al., 2008a; Clower et al., 2010; Goldberg and Sharp, 2012; Palsson-McDermott et al., 2015) (reviewed in (Chaneton and Gottlieb, 2012; Dayton et al., 2016b)).

Although it is unlikely that PKM1 expression levels were decreased in the PKM2 KD and KO cells as the materials and methods used to knock down and knock out PKM2 were highly specific, a limitation of this thesis is that it cannot be directly shown that PKM1 expression levels were not reduced with the KD and the KO of PKM2 due to the unavailability of PKM1-specfic antibodies. Nevertheless, since neither PKM2 KD nor KO affects the Warburg effect in rMC-1 cells, and the changes in PKM2 protein levels (a decrease for the KD and an absence for the KO) were conclusively verified, it is clear that PKM2 is not a main driver of the Warburg effect in these cells *in vitro*.

5.5.3 Pyruvate kinase M2 expression in Müller cells *in vivo*

At the commencement of this PhD project, there was limited information on PKM2 expression in different cell types of the retina *in situ* or *in vivo.* More recent studies have addressed this matter by immunohistochemical analysis of retinal sections (Paper 2 (Casson et al., 2016) (Appendix 7.2))

(Lindsay et al., 2014; Rueda et al., 2016). Unlike the cultured rat MCs depicted in this thesis, there is no discernible expression of PKM2 in MCs in mouse and rat retinal sections (Paper 2 (Casson et al., 2016) (Appendix 7.2)) (Lindsay et al., 2014; Rueda et al., 2016). On the contrary, there is some expression of PKM2 in MCs in human and marmoset retinas, indicating differences between species (Paper 2 (Casson et al., 2016) (Appendix 7.2)). Interestingly, PKM2 is strongly expressed in photoreceptors in all four species (Paper 2 (Casson et al., 2016) (Appendix 7.XX)) (Chinchore et al., 2017; Lindsay et al., 2014; Rajala et al., 2018a; Rajala et al., 2016; Rueda et al., 2016). For PKM1, there is expression in photoreceptors but no discernible expression in MCs in mouse retinas (Paper 2 (Casson et al., 2016) (Appendix 7.2)) (Lindsay et al., 2014; Rueda et al., 2016). PKM1 is also expressed in photoreceptors in marmosets and humans, while PKM1 localisation in rat retinas remains largely unknown due to the unavailability of verified antibodies (Paper 2 (Casson et al., 2016) (Appendix 7.2)). Detailed data on PKM1 and PKM2 expression and localisation in the retina are presented and discussed in Paper 2 (Casson et al., 2016) (Appendix 7.2). Interestingly, analysing microarray gene expression data from a previously published study (Roesch et al., 2008), Lindsay et al. reported that freshly isolated mouse MCs express a low level of *Pkm* transcripts while photoreceptors express a much higher level (Lindsay et al., 2014). The mouse MCs were freshly isolated and had not been in culture before the gene expression study was performed and therefore were highly relevant to MCs *in situ* (Roesch et al., 2008). This not only suggests that photoreceptors strongly express PKM, in agreement with the immunohistochemical data (Paper 2 (Casson et al., 2016) (Appendix 7.2)) (Lindsay et al., 2014; Rueda et al., 2016), but it also shows that there is some PKM expression in freshly isolated rodent MCs and this indicates the possibility that the absence of discernible PKM expression in MCs in retinal sections of rodents shown by immunohistochemistry (Casson et al., 2016; Lindsay et al., 2014; Rueda et al., 2016) could be because the levels are too low to be detected by this method. However, it has to be kept in mind that it could also be due to a poor correlation between mRNA and the protein levels because of post-transcriptional regulation, and the possibility that freshly isolated MCs are still not exactly the same as MCs *in situ.* Nevertheless, rat MCs *in situ* do not strongly express PKM2 in contrast to the cultured rat MCs shown in this thesis. Of note, there are very limited data on expression analysis of *Pkm* transcripts in the retina by in situ hybridisation; one study has shown in mouse retinas that PKM2 is expressed in the photoreceptor layer and that PKM1 is expressed in the INL, in which MC bodies are usually located.

(Chinchore et al., 2017). In addition, the same study has shown by PCR analysis that *Pklr* transcripts are not expressed in the retina (Chinchore et al., 2017).

Changes in protein expression in MCs after a period of being cultured have been shown previously although PKM2 expression was not directly assessed (Hauck et al., 2003). The difference in PKM2 expression in MCs *in situ* from published studies (Paper 2 (Casson et al., 2016) (Appendix 7.2)) (Lindsay et al., 2014; Rueda et al., 2016) and in culture as demonstrated in this thesis could be because cultured cells adopt PKM2 expression for a survival advantage *in vitro*. It could be argued that this is the case for the rMC-1 cells and the primary MCs. The rMC-1 cells proliferate effectively indefinitely and although primary MCs are short-lived, they do survive in culture for a period of time (typically four to eight weeks) (Paper 4 (Kittipassorn et al., 2019a) in Chapter 3). However, the SIRMu-1 cells, which also proliferate essentially indefinitely and are resilient in culture, and primary MEFs, which have a short life span but also survive in culture, express a much lower level of PKM2; this does not entirely support the above argument that PKM2 expression provides survival or proliferation advantages.

This is in part similar to a study by Israelsen et al. where cell lines were generated from mammary tumours of *Pkm2*$^{fl/fl}$ mice with a conditional deletion of PKM2 in the tumours by Cre recombinase-mediated exon 10 excision (Israelsen et al., 2013). These cell lines unexpectedly retain at least one *Pkm2*^{fl} allele and express high levels of PKM2 protein even though PKM2 deletion was observed in the parent tumours. The study then suggests that transition of cells from *in vivo* to tissue culture preferably selects for the few cells in which both Pkm alleles had not undergone recombination. However, upon deleting the remaining *Pkm2*^{fl} allele in the cell lines *in vitro*, they found that the loss of PKM2 did not change oxygen consumption or gene expression induced by hypoxia or β-catenin and concluded that these functions or *in vitro* proliferation were not the basis of the selection for the few PKM2-expressing cells during the generation of the tumour cell lines.

Overall, whether or not PKM2 expression correlates with or provides an advantage for cell survival *in vitro* requires further investigation, similar to the topic of the conflicting roles of PKM2 in cellular proliferation *in vivo* and tumourigenesis discussed in the literature (Christofk et al., 2008a; Dayton et al., 2016a; Goldberg and Sharp, 2012; Israelsen et al., 2013). Furthermore, to conclusively determine the role of PKM2 in MCs *in vivo*, MC-specific PKM2 KO mice could be generated by crossing mice that specifically express Cre recombinase in MCs with floxed *Pkm2* mice, and the retinas analysed for MC functions.

5.5.4 Cultured Müller cells as a model to study the Warburg effect in the retina and beyond

The apparent difference in PKM2 expression between MCs *in situ* and in culture has made cultured rat MCs a less physiologically relevant model for the study of the role of PKM2 in the Warburg effect in the retina. It does not indicate, however, that cultured MCs are not a useful tool for the study of the Warburg effect in the retina at all, as they may have other qualities that are similar to MCs *in vivo* which remain to be determined. Furthermore, primary MCs are still one of the very few cell types that are slowly-proliferative and yet display the Warburg effect, rendering them a unique system for the study of both the Warburg effect in general, and the reasons behind the existence of this phenomenon that are independent of the proliferation demands of the cells.

Importantly, this thesis adds to the body of knowledge in the field of glucose metabolism and shows that the role of PKM2 in the Warburg effect might not be as universal as previously postulated (Christofk et al., 2008a; Clower et al., 2010; Goldberg and Sharp, 2012; Palsson-McDermott et al., 2015) (reviewed in (Chaneton and Gottlieb, 2012; Dayton et al., 2016b)) and that it might be cell type-dependent. In addition, it would still be beneficial to determine why PKM2 does not play a crucial role in driving the Warburg effect in primary MCs, such as determining the predominant allosteric form (tetrameric, dimeric or monomeric), the state of PKM2 phosphorylation and other post-translational modifications, and the interaction of PKM2 with HIF-1 and PHD3 in the primary MCs, which would all contribute to the knowledge of PKM2 function. As PKM2 has been reported to contribute to the Warburg effect in cancer and proliferating cells by acting as a coactivator of HIF-1 and upregulating glycolysis (Luo et al., 2011; Palsson-McDermott et al., 2015), PKM2 not significantly affecting the Warburg effect in cultured MCs described here could be either because HIF-1 also does not play a crucial role in the Warburg effect, or because PKM2 does not interact and/or is not acting as a coactivator of HIF-1 in this system. The former could be investigated by assessing metabolic changes in rMC-1 cell lines with HIF-1 knocked out, which will be carried out as part of future work in our laboratory. If HIF-1 KO does lead to significant changes in the Warburg effect in rMC-1 cells, the next step will be to determine whether PKM2 interacts with HIF-1 in cultured MCs. Being a unique cell type that proliferates slowly and displays the Warburg effect, it would also be beneficial to use cultured MCs to investigate the role in the Warburg effect of other potential drivers that have been implicated in cancer cells, including the PI3K pathway (Makinoshima et al., 2015; Ward and Thompson, 2012) and Myc (Dejure and Eilers, 2017).

In terms of the study of the Warburg effect in the retina *in vivo* and the role of PKM2, photoreceptors might be a more physiologically relevant model as they strongly express PKM2 *in situ* (Paper 2 (Casson et al., 2016) (Appendix 7.2)) (Lindsay et al., 2014; Rajala et al., 2018a; Rajala et al., 2016; Rueda et al., 2016), have recently been shown to be a major source of lactate production in the retina (Lindsay et al., 2014), make up the majority of cells in the retina (Jeon et al., 1998; Macosko et al., 2015) and are arguably the most important cell types being the light-sensing cells. In fact, recent studies have investigated the role of PKM2 in the Warburg effect and other biological aspects in photoreceptors (Chinchore et al., 2017; Rajala et al., 2018a; Rajala et al., 2018b; Rajala et al., 2016). This will be further discussed in Chapter 6.

5.5.5 Conclusions

Cultured primary MCs, rMC-1 and HeLa cells, which depend on glycolysis for ATP production, strongly express PKM2. MEFs and SIRMu-1 cells, which predominantly use OXPHOS, also express PKM2 but at much lower levels. This suggests a correlation between PKM2 protein levels and the glycolytic dependency of cells. PKM2 KD and KO do not significantly affect the Warburg effect in rMC-1 cells. This is not consistent with one of the main hypotheses of this thesis that PKM2 drives the Warburg effect in cultured MCs, and it also indicates that the role of PKM2 in the Warburg effect may be cell-type dependent. Unlike cultured rat MCs, there is no discernible PKM2 expression in rat MCs *in situ* (Paper 2 (Casson et al., 2016) (Appendix 7.2)) (Lindsay et al., 2014; Rueda et al., 2016). This makes cultured MCs a less physiologically relevant model for the study of the role of PKM2 in the Warburg effect in the retina. However, cultured MCs could still be a good experimental tool to study the role of factors other than PKM2 in the Warburg effect in the retina as well as to investigate the Warburg effect in general.

Chapter 6

Final discussion and future perspectives

CHAPTER 6: Final discussion and future perspectives

The hypotheses examined in this PhD project were 1) that the SIRMu-1 cell line originated from primary MCs, 2) that cultured rat MCs displayed the Warburg effect, and 3) that PKM2 drove the Warburg effect in cultured MCs. These hypotheses logically defined the aims of the thesis to be 1) to establish and characterise the novel spontaneously immortalised rat MC line SIRMu-1, 2) to determine whether cultured rat MCs displayed the Warburg effect, and 3) to investigate whether PKM2 drove this Warburg effect in MCs. All aims were successfully addressed. For Aim 1, the SIRMu-1 cell line was established and verified to originate from primary MCs (Chapter 3). For Aim 2 (Chapter 4), metabolic analysis, consisting of lactate assays and Seahorse extracellular flux analyser assays which measured OCRs and ECARs, showed that cultured primary rat MCs and immortalised rMC-1 cells do predominantly use glycolysis to produce ATP, even in the presence of abundant oxygen, and hence, do indeed display the Warburg effect (Fig. 4.3 and 4.4), supporting the second hypothesis. Note that in contrast, the SIRMu-1 cells unexpectedly did not display the Warburg effect and are highly oxidative (Fig. 4.3 and 4.4), and therefore only the primary MCs and rMC-1 cells were used to explore the role of PKM2 in the Warburg effect in MCs (Chapter 5). The results for Aim 3, however, demonstrated that PKM2 KD and KO did not significantly affect the glycolytic activity of rMC-1 cells (Fig. 5.8 and 5.11), and it was thus concluded that PKM2 does not act as a main driver of the Warburg effect in cultured MCs.

6.1 The novel spontaneously-immortalised SIRMu-1 Müller cell line as an experimental tool for ophthalmology research and other fields

The SIRMu-1 cells were verified to originate from primary MCs but exhibit characteristics of immortalised cells, including rapid proliferation, an effectively indefinite life span and relatively high transfection efficiency (Paper 4 (Kittipassorn et al., 2019a) in Chapter 3). Therefore, they are a useful experimental tool for MC research. The SIRMu-1 cell line has a more similar overall transcriptome to primary MCs than does the rMC-1 line (Sarthy et al., 1998), another well-established immortalised MC line (Paper 4 (Kittipassorn et al., 2019a) in Chapter 3). This suggests that in general the SIRMu-1 cells are a more suitable experimental model for gene expression studies in MCs. For specific genes, however, it has to be verified which cell line expresses the genes of interest at a more similar level to the primary MCs and MCs *in vivo*. While the SIRMu-1 cells have very similar morphology to primary MCs, the rMC-1 cells are morphologically different from the primary MCs. This indicates that the SIRMu-1 cells may be a more appropriate experimental tool for the study of MC morphology and cytoskeleton (Scaife and Langdon, 2000). Furthermore, the SIRMu-1 cells were shown to be derived from a male rat, while the rMC-1 are female rat-derived cells (Paper 4 (Kittipassorn et al., 2019a) in Chapter 3); both can be useful and complementary for gender-specific ophthalmologic studies.

As a corollary, the SIRMu-1 cells spontaneously became immortalised without having been intentionally transformed with exogenous reagents. Thus, these cells can theoretically be used to study spontaneous cellular immortalisation, and more specifically, underlying mechanisms and differential gene expression related to this event (e.g. using RNA seq data from this study, described in Paper 4 (Kittipassorn et al., 2019a) and Paper 5 (Kittipassorn et al., 2019b) in Chapter 3). Underlying mechanisms of spontaneous immortalisation were not investigated in this thesis as they did not fall under the original remit of the study.

This thesis also showed that the immortalised, highly-proliferative SIRMu-1 cells exhibit a relative preference for oxidative metabolism, which is vastly different from the short-lived, slowly-proliferative, highly-glycolytic primary MCs from which they originated (Fig. 4.3 and 4.4). Although this indicates that the SIRMu-1 cells are not a suitable experiment tool to represent cultured primary MCs in the study of glucose metabolism as discussed in this thesis, it suggests another potential use for the SIRMu-1 cells as a valuable model for other aspects of cellular metabolism research. They can be used to study if and how OXPHOS is related to proliferation, or how cells can switch between glycolytic dependency to more oxidative metabolism, especially when their overall transcriptome is very similar to that of primary MCs from which they originated (Paper 4 (Kittipassorn et al., 2019a)) and when there was no significant difference in the expression of key genes involved in glucose metabolism (Table 4.1 and Fig 4.8). For example, it would be informative to assess the number of mitochondria per cell in SIRMu-1 cells compared with that of primary MCs to determine whether the more oxidative metabolism of SIRMu-1 cells is due to the higher number of mitochondria.

6.2 Investigating cellular metabolism

Cells that display the Warburg effect have upregulated aerobic glycolysis and common phenotypes are high lactate production, low oxygen consumption and high extracellular acidification (Hsu and Sabatini, 2008; Koppenol et al., 2011; Vander Heiden et al., 2009; Warburg, 1956; Warburg et al., 1927). It is important to determine all the characteristic parameters together to obtain a comprehensive profile of metabolism of the cell type of interest because cells that have a high lactate production might not always primarily depend on glycolysis for ATP production, as seen with the primary MEFs in this thesis (Fig. 4.3 and 4.4).

When analysing and drawing conclusions from metabolic studies of glucose, both in this thesis and beyond, the experimental conditions and their relevance to *in vivo* conditions needs to be taken into account. For example, one key condition is the concentration of glucose used. Low glucose concentrations in culture medium can cause issues with attachment of cells in primary mixed retinal cultures, from which the primary MCs are derived, and hence we and others use media containing 25 mM glucose to promote cell attachment in primary neuron/glial cultures and primary MC cultures (Eide and McMurray, 2005; Wood et al., 2005) (Paper 4 (Kittipassorn et al., 2019a) in Chapter 3). All other cell types that were used for experiments alongside primary MCs were also maintained in medium containing 25 mM glucose to keep the growth conditions consistent with primary MCs. However, all cells were cultured in medium with 5.5 mM glucose, which is more physiologically relevant (Potter et al., 2016; Wang et al., 1997a, b) and recommended for use by the Seahorse analyser's manufacturer, or at least 24 hours before being seeded for Seahorse assays, which is at least 40 hours before the start of the assay. During the Seahorse assays 10 mM glucose, a saturating concentration, was used in the assay medium as recommended by the manufacturer to ensure that cellular metabolism was not restricted by the amount of substrate. Of note, in the current study cells cultured in 5.5 mM glucose showed no obvious difference in cellular morphology or proliferation compared to cells cultured in 25 mM glucose. However, a study has reported that cultured rMC-1 cells grown in a high glucose concentration (30 mM) for seven days show reduced basal OCR, maximal OCR and basal ECAR, as well as changes in mitochondrial morphology, compared to cells grown in 5 mM glucose (Tien et al., 2017). A limitation of this thesis is that it is not known whether the use of 25 mM glucose also affected cellular metabolism in our system and if so, whether culturing the cells in 5.5 mM glucose for at least 40 hours before the start of the Seahorse assays was long enough to re-adjust the cells to an arguably more physiological state. An informative follow-up experiment would be to maintain the cells in 5.5 mM glucose, with the caution of the cell attachment issues in the primary cultures, subject them to Seahorse assays and compared the results with those of this thesis to determine the influence of glucose concentration in the media on glucose metabolism. Importantly, the use of 25 mM glucose in media does not affect the validity of the findings in this thesis. The primary MCs and the rMC-1 cells clearly display the Warburg effect in the culture and experimental conditions of this thesis and therefore are a suitable model for the study of the Warburg effect.

6.3 Investigating retinal metabolism

The second hypothesis of this thesis was that cultured rat MCs displayed the Warburg effect. Metabolic analyses showed that the cultured primary MCs and rMC-1 cells do display the Warburg effect, consistent with the hypothesis (Fig. 4.3 and 4.4). This also further supports the well-characterised notion that MCs *in vitro* display the Warburg effect, as demonstrated previously in freshly-isolated guinea pig MCs (Poitry-Yamate et al., 1995), cultured primary human MCs (Winkler et al., 2000), and rMC-1 cells (Winkler et al., 2003). Unexpectedly, the expression of the glycolytic enzyme PKM2 in cultured rodent MCs shown in this thesis (Fig. 5.5) and in work by others (Lindsay et al., 2014) is in contrast to the absence of discernible expression of PKM2 in rodent MCs *in situ* (Paper 2 (Casson et al., 2016) (Appendix 7.2)) (Lindsay et al., 2014; Rueda et al., 2016). This suggests that the metabolism of MCs in culture and *in vivo* could be different, at least in some aspects, and metabolic properties of MCs *in vivo* remain to be further elucidated.

Lindsay et al. demonstrated that cultured primary mouse MCs do not incorporate ^{13}C from glucose into lactate as fast as whole intact retinas (Lindsay et al., 2014). In the same study, using mouse retinas with an inherent photoreceptor degeneration caused by deficiency of the photoreceptor-specific gene Aryl hydrocarbon interacting protein like 1 (*Aipl1*) (Ramamurthy et al., 2004), they showed that lactate production was reduced by 74% in AIPL1$^{-/-}$ retinas compared to retinas from control mice (Lindsay et al., 2014). They concluded that these results were consistent with photoreceptors, and not MCs, being the major source of lactate production, and hence the Warburg effect, in the retina *in vivo* (Lindsay et al., 2014).

This alone does not indicate that MCs do not display the Warburg effect at all; they might do so but to a lesser degree than photoreceptors, and it is also worth considering that the photoreceptors make up a much larger proportion of the retina by cell number than the MCs. Another possibility is that photoreceptors are not the direct primary source of lactate production but rather their degeneration affected other retinal cell types, including MCs, which could have affected their metabolism. Abnormal changes to MCs have been reported in retinal diseases associated with photoreceptor cell death, such as retinal detachment (reviewed in (Bringmann et al., 2006)). Therefore, investigating metabolism of MCs *in vivo* is important and could be performed by comparing lactate production in retinal explants from a transgenic mouse model with inducible MC ablation, as described previously (Shen et al., 2012), with those from control mice. Even if photoreceptors are the major source of lactate production in the retina as suggested by Lindsay et al. (Lindsay et al., 2014), it is still possible that MCs contribute to the other 26% of lactate production and display the Warburg effect *in vivo*.

However, studies have shown that MCs in the rodent retina have low or no expression levels of glycolytic enzymes, including PKM1, PKM2, hexokinase 2 (HK2), and LDHA, as well as a low LDH activity (Paper 2 (Casson et al., 2016) (Appendix 7.2)) (Lindsay et al., 2014; Rueda et al., 2016), which suggests a limited capacity of MCs for glycolysis and argues against MCs displaying the Warburg effect *in vivo*. In addition, MCs in the rodent retina have a low expression level of cytochrome c oxidase subunit IV (COX IV) and a low COX activity, suggesting a limited capacity for OXPHOS (Rueda et al., 2016). If MCs really do have limited capacities for glycolysis and OXPHOS as suggested by these studies on enzyme expression and activity, the question is, how do MCs *in vivo* fulfill their energy requirements?

With low or no expression of either PKM1 or PKM2, MCs may produce pyruvate to fuel their mitochondria via an alternative PK-independent reaction, where PEP donates its phosphate to phosphoglycerate mutase (PGM) resulting in a production of pyruvate (Vander Heiden et al., 2010b).

It has also been proposed that MCs take up lactate produced by photoreceptors via MCT4 and convert it into pyruvate (Lindsay et al., 2014). Expression of MCT4 protein and/or mRNA in MCs has been shown previously (Chidlow et al., 2005), and supported by the RNA-seq analysis in this thesis (Table 4.1 in Chapter 4 and Supplementary table S1 from (Kittipassorn et al., 2019a) in Appendix 7.5). In addition, MCs may depend on the TCA cycle to produce guanosine triphosphate (GTP), and depend on high-energy phosphate transferring kinases to produce ATP. They express relatively high levels of enzymes involved in the TCA cycle, including oxoglutarate/alpha-ketoglutarate dehydrogenase (OGDH) and succinate thiokinase (STK), and high-energy phosphate transferring kinases, including nucleoside-diphosphate kinase (NDPK) and adenylate kinase 1 (AK1) (Rueda et al., 2016). MCs also highly express glutamate dehydrogenase (Rueda et al., 2016) and may use it to convert glutamate to α-ketoglutarate which can feed the TCA cycle. Moreover, as MCs express mitochondrial fatty acid β-oxidation enzymes (Atsuzawa et al., 2010), they may utilise fatty acid β-oxidation to produce acetyl CoA for the TCA cycle. Of note, in contrast to MCs in the rodent retina, MCs in the marmoset and the human retina show a discernible expression of PKM2 (Paper 2 (Casson et al., 2016) (Appendix 7.2)), suggesting that the glycolytic capacity of MCs *in vivo* varies between species. It would also be interesting to determine whether cultured primary human MCs and immortalised human MC cells, such as the MIO-M1 line (Limb et al., 2002), express PKM2 like the human MCs *in situ* (Paper 2 (Casson et al., 2016) (Appendix 7.2)).

More recently, the focus of retinal metabolism research has shifted from MCs to photoreceptors. As light-sensing cells, they are arguably the most crucial cell types in the retina. There are two main types of photoreceptors, rods and cones, and together they make up the majority of cell populations in the retina. Using microscopy techniques, Jeon et al. reported that photoreceptors comprise 82% (rods 79.9%, cones 2.1%) of all cells in the mouse retina (Jeon et al., 1998). Similarly, Macosko et al. reported that photoreceptors comprise 69.8% (rods 65.6%, cones 4.2%) of all cells in mouse retinas by single cell RNA-seq (Macosko et al., 2015).

As mentioned, photoreceptors have been proposed to be the major source of lactate production, and hence the Warburg effect, in the retina (Lindsay et al., 2014). In support of this, photoreceptors show abundant expression of glycolytic enzymes, especially the isoforms that have been shown to promote the Warburg effect, including PKM2, HK2 and LDHA, indicating that they have a high capacity for glycolysis (Paper 2 (Casson et al., 2016) (Appendix 7.2)) (Chinchore et al., 2017; Lindsay et al., 2014; Rajala et al., 2018a; Rajala et al., 2016; Reidel et al., 2011; Rueda et al., 2016). Photoreceptors also have abundant mitochondria (Stone et al., 2008) and express considerable levels of COX IV and enzymes involved in the TCA cycle, including OGDH and STK, indicating that they also potentially have a high capacity for OXPHOS (Rueda et al., 2016). Thus, given their abundance, their major contribution to retinal lactate production *in vivo*, and the expression levels of key metabolic enzymes, photoreceptors are an appropriate focus for the study of retinal metabolism.

6.4 The role of PKM2 in the Warburg effect in the mammalian retina

The third aim of this thesis was to investigate whether PKM2 drove the Warburg effect in MCs, using cultured rat MCs as an experimental tool. The results showed that while PKM2 is expressed in cultured rat MCs, it is not a key driver of the Warburg effect (Chapter 5). As mentioned, recent studies have shown that there is no discernible PKM2 expression in MCs but there is strong PKM2 expression in photoreceptors in the rodent retina (Paper 2 (Casson et al., 2016) (Appendix 7.2)) (Chinchore et al., 2017; Lindsay et al., 2014; Rajala et al., 2018a; Rajala et al., 2016; Rueda et al., 2016).

While not commonly expressed in MCs, a number of studies support a role for PKM2 in the Warburg effect in rod photoreceptor cells in mammalian retinas. Chinchore and colleagues demonstrated that freshly-isolated retinas of mice with a rod-specific conditional deletion of *Pkm2* exhibit a small but significant reduction in lactate production compared to control mice (Chinchore et al., 2017). Rajala et al. showed that the amount of carbon from glucose that was incorporated into pyruvate and lactate in isolated retinas of rod-specific PKM2 KO mice was less than in the controls, while there was an accumulation of PEP (Rajala et al., 2018a).

In addition to metabolism, PKM2 has also been shown to play a role in the viability, structure and function of photoreceptors. Rod-specific PKM2 KO, with aging, leads to photoreceptor cell death, reduced thickness of photoreceptor end tips, reduced GLUT1 expression, and reduced electroretinography (ERG) responses (Rajala et al., 2018a). Similarly, cone-specific PKM2 KO results in cone degeneration and function loss in aged mice (Rajala et al., 2018b). Furthermore, shRNA-mediated PKM2 KD led to photoreceptors with shorter outer segments, a phenotype which could be rescued with dark rearing, possibly because there is less outer segment shedding in the dark (LaVail, 1980) and less biogenesis is required (Chinchore et al., 2017).

Interestingly, it has been reported that there are IgG antibodies recognising PKM2 in the serum of patients with dry and wet age-related macular degeneration (AMD) with a higher reactivity in wet than dry AMD, but it is unknown whether these directly contribute to, or are secondary products of AMD (Morohoshi et al., 2012). The authors proposed that anti-PKM2 IgG could be used as a biomarker for the progression of AMD (Morohoshi et al., 2012).

With mounting evidence for a role for PKM2 in the retina, it is worth noting that novel cancer treatments targeting PKM2 (reviewed in (Tennant et al., 2010)) might adversely affect the retina.

6.5 Investigating other potential drivers of the Warburg effect in the mammalian retina

In addition to PKM2, various other factors have been implicated in driving the Warburg effect in cancer and proliferating cells, such as LDHA, HK2, HIF-1, and the PI3K signalling pathway (reviewed in (Upadhyay et al., 2013; Vander Heiden et al., 2009)), some of which have been recently studied in photoreceptors and MCs.

Photoreceptors strongly express LDHA and HK2 (Paper 2 (Casson et al., 2016) (Appendix 7.2) (Chinchore et al., 2017; Petit et al., 2018; Rueda et al., 2016). A rod-specific LDHA KO resulted in a reduced retinal lactate production, indicating a role of LDHA in the Warburg effect in rod photoreceptors (Chinchore et al., 2017). A shRNA-mediated LDHA KD led to a decrease in photoreceptor outer segment length which could be partially rescued with dark rearing, in which less outer segment shedding (LaVail, 1980) and biogenesis may be required, similar to the effect of PKM2 KD in the same study described above (Chinchore et al., 2017). Rod-specific HK2 KO resulted in decreased retinal lactate production and reduced expression of LDHA and PKM2, suggesting a decrease in the Warburg effect (Petit et al., 2018). In addition, HK2 loss in rod cells did not impact photoreceptor structure or survival but did affect rod ERG function, indicating a possible role for the Warburg effect in rod function (Petit et al., 2018). Unlike rods, HK2 KO in cones did not affect cellular function but its impact on the Warburg effect here is not known, as cones only make up 3% of photoreceptors which make it difficult to observe cone-dependent changes when measuring lactate in whole retinas (Petit et al., 2018).

HIF-1 and other HIFs (HIF-2 and HIF-3) play an important role in retinal development, physiology and disease (reviewed in Paper 3 (Peet et al., 2017) (Appendix 7.3)). A potential role for HIF-1 in establishing the Warburg effect in the retina is supported by the report of HIF-1α expression in normoxic human and rat retinas shown by immunohistochemistry and western blotting (Hughes et al., 2010), although this result has to be approached with caution as it is not uncommon for anti-HIF-1α antibodies to cross-react non-specifically. Interestingly, both the rod-specific KO of HIF-2α alone or of HIF-2α and HIF-1α combined did not affect photoreceptor development, morphology and ERG functions in mouse (Kast et al., 2016). Metabolic changes were not directly assessed in this study, but the data may imply that either the loss of the HIFs do not affect the Warburg effect in rod photoreceptors, or the presence of the Warburg effect is not essential for rod survival and function (reviewed in Paper 3 (Peet et al., 2017) (Appendix 7.3)). This is, in part, surprising as a number of downstream target genes of HIF-1, such as LDHA, PKM2, and HK2, when lost, lead to a decrease in retinal lactate production and changes in photoreceptor structure or function (Chinchore et al., 2017; Petit et al., 2018). However, there is an additional possibility. In another report, a mouse model with a rod-specific loss of VHL, in which HIF-1 and HIF-2 are chronically activated, has an upregulation of *Pdk1* and *Glut1* in the retina, and a slowly progressing retinal degeneration that can be alleviated by expression of shRNA targeting *Hif-1α* (Barben et al., 2018). This does not conclusively demonstrate that the HIFs drive the Warburg effect in rods, but if they do, it may mean that a chronic activation of the HIFs lead to a chronically-upregulated Warburg effect which could impact rod cell survival, while a HIF KO (such as in (Kast et al., 2016)) may result in a decreased Warburg effect which would not affect rod survival. Nevertheless, this suggests that the role of the HIFs in photoreceptor metabolism, structure and function is complex, and is likely tightly-regulated.

It remains to be elucidated whether the HIFs are involved in driving the Warburg effect in photoreceptors.

A conditional deletion of *Hif-1α* has also been reported in MCs; it did not cause apparent morphological or functional defects under normal conditions, but in mice with oxygen-induced retinopathy the deletion of *Hif-1α* in MCs led to reduced retinal inflammation and vascular leakage (Lin et al., 2011). However, metabolic changes were not determined. In this study by Lin et al., the mouse model with HIF-1α KO in MCs was generated by crossing floxed *Hif-1α* mice with mice that express Cre recombinase in MCs as described previously (Ueki et al., 2009). These MC Cre mice were generated using a 3.0-kb human vitelliform macular dystrophy-2 (*VMD2*) promoter (Ueki et al., 2009). VMD2 is usually preferentially expressed in RPE (Esumi et al., 2004), and Ueki et al. aimed to generate RPE-specific Cre mice but unexpectedly obtained a transgenic line with prominent Cre activity in MCs. In this line, Cre activity in RPE was nearly absent, while there was some Cre activity in some neurons in the INL and some photoreceptors. This suggests that the results reported by Lin et al. above need to be interpreted cautiously as the effects seen may have been the consequence of *Hif-1α* deletion in cell types other than MCs. In addition, further studies using this Cre mouse line to investigate the role of other agents in MC metabolism and function have to be designed and performed carefully due to the non-MC Cre activity. Alternatively, Rlbp1-CreER, a mouse model with inducible MC-specific Cre expression (Shen et al., 2012), generated using a part of the regulatory region of the retinaldehyde binding protein 1 gene (*Rlbp1*), is a valuable and, perhaps, a more suitable tool for MC-specific gene editing to study the role of genes of interest in MCs.

Another pathway of interest in driving the Warburg effect in retinas is the PI3K signalling pathway. Loss of PI3K in cones leads to a reduced expression of genes encoding GLUT1, HK2, PKM2, and HIF-1α, possibly implying a decrease in the Warburg effect (Rajala et al., 2016).

In addition to investigating the drivers of the Warburg effect in the mammalian retina, it is also important to elucidate *why* the mammalian retina displays the Warburg effect. Despite suggestions being mooted (Casson et al., 2012; Ng et al., 2015), this is still unknown. One commonly-postulated explanation is that the Warburg effect is required to accommodate the high biosynthetic demand associated with the constant renewal of photoreceptor outer segments (reviewed in Paper 1 (Ng et al., 2015) (Appendix 7.1)) (Chinchore et al., 2017). An interesting experiment would be to determine whether glucose directly contributes to biosynthesis as a carbon source. This could be performed by following the incorporation of labelled carbon from glucose into the retina, and determining if and how much of the carbon is directly incorporated into the visual pigment rhodopsin and outer segment structures.

6.6 Implications for retinal diseases and cancer treatment research

There may not yet be a direct link between the disruption of the Warburg effect in the retina and retinal diseases in human, but it is clear that photoreceptors are metabolically demanding (Ames et al., 1992) and that the loss or degeneration of photoreceptors are the basis of many blinding retinal diseases, such as AMD and retinitis pigmentosa. In addition, although MC metabolism *in vivo* remains to be elucidated, it is well established that MCs play an important role in retinal diseases (reviewed in (Bringmann et al., 2006)) and MC loss or damage has been shown to lead to photoreceptor apoptosis and vascular pathologies (Dubois-Dauphin et al., 2000; Shen et al., 2012). Therefore, the regulation of photoreceptor and MC metabolism is crucial to retinal health. Furthermore, various factors that have been studied in regard to retinal metabolism also play important roles in other aspects of retinal physiology. For example, HIF-1 has been shown to regulate key metabolic genes, but HIF-1 and other HIFs have also been shown to play crucial roles in the formation and maintenance of retinal vasculature (reviewed in Paper 3 (Peet et al., 2017) (Appendix 7.3)). Altogether this highlights a complex interconnected relationship between potential drivers of the Warburg effect, their other roles in the retina, retinal metabolism and retinal diseases, as well as indicates that to manipulate one agent to treat one aspect of a condition it might adversely affect others. For instance, in diabetic retinopathy, if HIF-1 is to be inhibited to decrease VEGF expression and hence reduce neovascularisation, it may at the same time decrease LDHA, PKM2 and HK2 expression and hence affect photoreceptor metabolism, structure or function (Chinchore et al., 2017; Petit et al., 2018).

Moreover, if factors that play a role in retinal and cancer metabolism are conserved, treatments targeting cancer metabolism, both directly and indirectly, may adversely affect the retina. For example, cetuximab is a drug that, in combination with chemotherapy and/or radiotherapy, is approved for treating patients with colorectal cancers and head and neck cancers (Bonner et al., 2006; Cunningham et al., 2004) and has been shown to down-regulate HIF-1α and LDHA (Lu et al., 2013; Luwor et al., 2005), calling into question whether the drug could have unknown long-term adverse effects on the retina. This highlights the importance of understanding the mechanisms and reasons behind the Warburg effect in the retina in addition to the association with retinal diseases, as they could contribute to awareness of possible adverse effects of metabolism-targeting cancer treatments and to developing novel diagnostic and therapeutic strategies for retinal diseases.

6.7 Final conclusions

This thesis describes a useful novel SIRMu-1 MC cell line, highlights the importance of comprehensive metabolic analyses that cover various parameters in addition to lactate production, verifies that cultured primary rat MCs and rMC-1 cells display the Warburg effect, enhances our understanding of MC metabolism and demonstrates that the role of PKM2 in the Warburg effect is likely cell type-dependent. Furthermore, it emphasises the notion that cultured cells have both similar and different aspects compared to their *in vivo* counterparts and therefore, multiple established cell lines derived from the same cell type and species of origin may not always retain the same properties and should be verified before using as experimental models.

Chapter 7

Appendices

CHAPTER 7: Appendices

7.1 Paper 1: Cancer-like metabolism of the mammalian retina

Ng, S.K., Wood, J.P., Chidlow, G., Han, G., Kittipassorn, T., Peet, D.J., and Casson, R.J. (2015). Cancer-like metabolism of the mammalian retina. Clinical & Experimental Ophthalmology 43, 367-376.

http://dx.doi.org/10.1111/ceo.12462

Statement of Authorship

Title of Paper	Cancer-like metabolism of the mammalian retina
Publication Status	☑ Published ☐ Accepted for Publication ☐ Submitted for Publication ☐ Unpublished and Unsubmitted work written in manuscript style
Publication Details	Ng, S.K., Wood, J.P., Chidlow, G., Han, G., Kittipassorn, T., Peet, D.J., Casson, R.J., 2015. Cancer-like metabolism of the mammalian retina. Clin Exp Ophthalmol 43, 367-376.

Co-Author

Name of Co-Author (Candidate)	Thaksaon Kittipassorn		
Contribution to the Paper	Wrote the part on hypoxia-inducible factor-1 (HIF-1) in the article subsection "The metabolic reprogramming". Reviewed and edited the manuscript.		
Overall percentage (%)	5%		
Certification:	This is an original article, my contribution to which was made during the period of my Higher Degree by Research candidature and is not subject to any obligations or contractual agreements with a third party that would constrain its inclusion in this thesis. I am a co-author of this paper.		
Signature		Date	18/12/2018

Co-Author Contributions

By signing the Statement of Authorship, each author certifies that:

i. the candidate's stated contribution to the publication is accurate (as detailed above);

ii. permission is granted for the candidate in include the publication in the thesis; and

iii. the sum of all co-author contributions is equal to 100% less the candidate's stated contribution.

Name of Principal Author	Soo Khai Ng		
Contribution to the Paper	Conceived the project. Wrote the manuscript. Reviewed and edited the manuscript.		
Signature		Date	02/01/2019

Name of Co-Author	John PM Wood		
Contribution to the Paper	Conceived the project. Wrote the manuscript. Reviewed and edited the manuscript.		
Signature		Date	19/02/19

Name of Co-Author	Glyn Chidlow		
Contribution to the Paper	Conceived the project. Wrote the manuscript. Reviewed and edited the manuscript.		
Signature		Date	19/2/19

Name of Co-Author	Guoge Han		
Contribution to the Paper	Conceived the project. Wrote the manuscript. Reviewed and edited the manuscript. CO-AUTHOR COULD NOT BE CONTACTED, SO SIGNED BY PRINCIPLE SUPERVISOR		
Signature		Date	24/9/2019

Name of Co-Author	Daniel J Peet		
Contribution to the Paper	Conceived the project. Wrote the manuscript. Reviewed and edited the manuscript.		
Signature		Date	14/2/2019

Name of Co-Author	Robert J Casson		
Contribution to the Paper	Conceived the project. Wrote the manuscript. Reviewed and edited the manuscript.		
Signature		Date	18/12/2018

Clinical & Experimental Ophthalmology RANZCO The Royal Australian and New Zealand College of Ophthalmologists

Clinical and Experimental Ophthalmology 2015; 43: 367–376 doi: 10.1111/ceo.12462

Review

Cancer-like metabolism of the mammalian retina

Soo Khai Ng MBBS,[1] John PM Wood DPhil,[1] Glyn Chidlow DPhil,[1] Guoge Han MBBS,[1]
Thaksaon Kittipassorn MD,[2,3] Daniel J Peet PhD[2] and Robert J Casson DPhil FRANZCO[1]
[1]South Australian Institute of Ophthalmology and [2]School of Molecular and Biomedical Science (Biochemistry), University of Adelaide, Adelaide, South Australia, Australia; and [3]Department of Physiology, Faculty of Medicine Siriraj Hospital, Mahidol University, Bangkok, Thailand

ABSTRACT

The retina, like many cancers, produces energy from glycolysis even in the presence of oxygen. This phenomenon is known as aerobic glycolysis and eponymously as the Warburg effect. In recent years, the Warburg effect has become an explosive area of study within the cancer research community. The expanding knowledge about the molecular mechanisms underpinning the Warburg effect in cancer promises to provide a greater understanding of mammalian retinal metabolism and has motivated cancer researchers to target the Warburg effect as a novel treatment strategy for cancer. However, if the molecular mechanisms underlying the Warburg effect are shared by the retina and cancer, treatments targeting the Warburg effect may have serious adverse effects on retinal metabolism. Herein, we provide an updated understanding of the Warburg effect in mammalian retina.

Key words: aerobic glycolysis, HIF-1, mammalian retina, PKM2, Warburg effect.

INTRODUCTION

In the 1920s, Otto Warburg and his team at the Kaiser Wilhelm Institute showed that cancer cells tend to convert glucose to lactate despite the presence of oxygen. He called this phenomenon 'aerobic glycolysis', a term that is now synonymous with the 'Warburg effect' (Fig. 1). Warburg believed that this phenomenon was abnormal: a breach of the 'Pasteur effect', where oxygen inhibits glycolysis, or conversely, hypoxia stimulates glycolysis.[1,2] He further believed that the switch from oxidative phosphorylation (OXPHOS) to glycolysis caused cancer,[3] a concept that was criticized during his lifetime, but that has recently had a resurgence. His team also noted that normal mammalian retinal explants displayed aerobic glycolysis.[4] This finding, however, did not fit neatly with Warburg's beliefs about cancer pathogenesis and was attributed as experimental artefact. Several decades thereafter, other researchers confirmed that the mammalian retina indeed displays a strong Warburg effect.[5,6]

In recent years, the Warburg effect has become an explosive area of study within the cancer research community, with many publications in the world's leading scientific journals,[7–10] resulting in a deeper understanding of the Warburg effect at the molecular level. This new knowledge has also led to better comprehension of the Warburg effect in mammalian retina.[11] However, the fact that the retina also displays the Warburg effect is rarely acknowledged in the cancer literature. The authors of a *Nature Reviews Cancer* publication incorrectly stated that 'aerobic glycolysis is uniquely observed in cancer'.[12] But the Warburg effect is widely described in other cell types, namely embryonic stem cells, human T lymphocytes, neutrophils, dendritic cells and macrophages.[13,14]

In this review, we aim to provide an updated understanding of the Warburg effect in the mammalian retina.

■ **Correspondence:** Dr Soo K Ng, South Australian Institute of Ophthalmology, University of Adelaide, Adelaide, SA 5000, Australia. Email: soo.ng8098@gmail.com

Received 13 April 2014; accepted 7 October 2014.

Competing/conflicts of interest: No stated conflict of interest.

Funding sources: No stated funding sources.

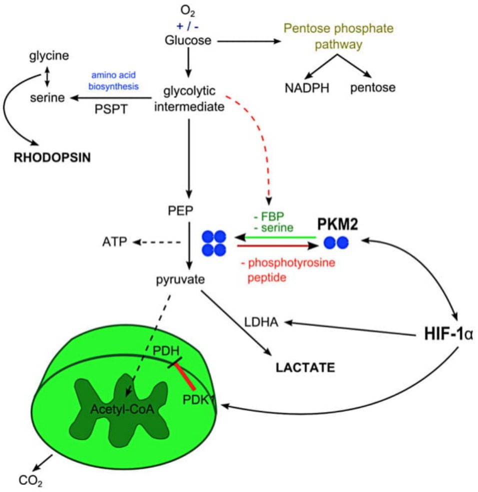

Figure 1. Metabolic budget system and the Warburg effect. Pyruvate kinase M2 (PKM2) exists as an active tetrameric form and an inactive dimeric form. Its transition is regulated by fructose 1,6 biphosphate (FBP), serine, reactive oxygen species and phosphotyrosine peptide. PKM2 is also a co-activator of hypoxia-inducible factor-1α (HIF-1α). We propose that glucose-derived amino acids are required for rhodopsin synthesis and that the Warburg effect is HIF dependent. ATP, adenosine triphosphate; LDHA, lactate dehydrogenase A; NADPH, nicotinamide adenine dinucleotide phosphate, reduced; PDH, pyruvate dehydrogenase; PDK1, pyruvate dehydrogenase kinase 1; PEP, phosphoenolpyruvate; PSPT, phosphoserine phosphatase.

AEROBIC GLYCOLYSIS

Cellular metabolism and the Warburg effect

All life on Earth uses adenosine triphosphate (ATP) to transfer energy. ATP is generated via two related metabolic pathways: OXPHOS and glycolysis.[15] Glycolysis converts a single molecule of glucose into two molecules of pyruvate, generating two ATP molecules.[15] The final step requires pyruvate kinase (PK), which exists as several isoforms, notably PKM1 and PKM2.[16] In the presence of oxygen, pyruvate is usually converted to acetyl CoA, which then enters the Krebs cycle, forming electron donors for OXPHOS, generating approximately 32 net ATP molecules.[17] When oxygen is scarce or falls short of demand, pyruvate is shunted away from OXPHOS and is converted into lactate by lactate dehydrogenase (LDH) to regenerate nicotinamide adenine dinucleotide (NAD+).[17,18] Each of the steps within the glycolytic pathway is catalysed by a specific enzyme or enzyme complex.[15] Some of these enzymes may have a role in transcription regulation, cell motility and apoptosis regulation.[19–21]

In tumours, proliferating tissue and the isolated mammalian retina, conversion of pyruvate to lactate occurs despite the presence of oxygen.[3,6,22] This is the so-called Warburg effect. The biological drive that causes tumours and some other non-neoplastic cells to apparently forsake optimal ATP production remains somewhat speculative. Warburg initially hypothesized that the reliance on the glycolytic metabolism was secondary to development of mitochondrial defects within cancer cells, which impaired OXPHOS.[3] Albeit plausible, this hypothesis was rejected when subsequent studies demonstrated normal functioning mitochondria in most cancer cells.[23,24] A more tenable explanation for the existence of the Warburg effect concerns the biosynthetic requirements of proliferating cells.

The metabolic requirements of tumour and proliferating cells

Vander Heiden *et al.* publishing in *Science* summarized a widely accepted explanation for the existence of the Warburg effect in cancer.[10] In proliferating cells, glucose not only produces ATP, but also provides metabolic intermediates for biosynthesis (Fig. 1).[10] Intracellular glucose can also be directed towards biosynthesis: into the pentose phosphate pathway to generate nucleotides and nicotinamide adenine dinucleotide phosphate, reduced, or to make the amino acids, serine and glycine, branching from glycolysis at phosphoglycerate.[10,25] The enzyme phosphoserine phosphatase is the final step in glucose-serine conversion (Fig. 1).[26]

Proliferating cells have the ability to increase glycolytic ATP production under hypoxic conditions, but provided glucose is abundant, in normoxia, they direct metabolic pathways away from OXPHOS towards biomass synthesis. The ability to oscillate between biosynthesis and energy production provides proliferating tissue with a powerful metabolic strategy known as the 'metabolic budget system',[27] a phenomenon that goes hand in hand with the Warburg effect (Fig. 1). This strategy can be viewed as the presence of the Warburg effect in a tissue using glucose for biosynthesis.[27] Such a phenomenon, however, has not yet been reported, to our knowledge, in a non-proliferating tissue, such as the retina.

The metabolic reprogramming

The programming of cellular metabolism involves the interplay of various growth factor signalling pathways.[28,29] Many of these pathways, including Jak STAT3,[30] P13K/Akt,[31] mammalian target of rapamycin,[30,32] the proto-oncogene and tumour suppressor genes,[33,34] have been implicated in the Warburg effect. However, the focus has recently converged on PK isoform M2 (PKM2) and hypoxia-inducible factor-1 (HIF-1) as the key regulators of the Warburg effect.[35]

HIF-1 is a dimeric transcription factor responsible for driving cellular responses to hypoxia.[36] It comprises an oxygen-regulated alpha subunit (HIF-1α) and a constitutive beta subunit (HIF-1b).[36] When oxygen is sufficient, the expression and activity of HIF-1α are inhibited.[37] In hypoxia, HIF-1α is stabilized and transcriptionally active; it partners with HIF-1 to transactivate a large set of target genes leading to various changes in cellular processes including the upregulation of glycolysis and the inhibition of OXPHOS.[36,37] Its activity is also present in normoxia in many cancers.[37]

PK is a glycolytic enzyme that catalyses the conversion of phosphoenolpyruvate into pyruvate, generating one molecule of ATP in the rate-limiting final step of glycolysis.[34,38] There are four isoforms of PK in mammals: L – liver, R – red blood cell, M1 – adult (muscle and brain) and M2 – embryonic and tumour.[39] Uniquely, PKM2 has an allosteric pocket not present in the other isoforms that permits binding to phosphotyrosine peptides and fructose 1,6 biphosphate.[8,40] This structural configuration renders PKM2 vulnerable to various regulatory inputs. Whereas PKM1 forms a stable, constitutively active tetramer, PKM2 oscillates between the active tetrameric and the inactive dimeric (or monomeric) forms.[27,41] The dimeric form has a low affinity for the substrate phosphoenolpyruvate and lower activity than the tetrameric form.[41] When the dimeric form dominates, phosphoenolpyruvate conversion becomes inefficient, and as a consequence glycolytic intermediates upstream of phosphoenolpyruvate accumulate and are available for biomass synthesis and cell proliferation.[27] As the glycolytic intermediate, fructose 1,6 biphosphate accumulates, the reaction favours conversion of the dimeric form back to the tetrameric form and pyruvate is produced efficiently again.[27,41] These regulations of PKM2, labelled as the 'metabolic budget system', are proposed to control the anabolic biosynthesis *versus* energy production in tumour metabolism.[27] PKM2 activities are also susceptible to other post-translational modifications.[42,43]

Although it was initially assumed that the switch from expression of physiological PKM1 to PKM2 is responsible for the Warburg effect in tumour cells,[8] subsequent experiments demonstrated PKM2 as the predominant PK isoform in both tumour and normal tissues.[44] PKM2 is also a direct target gene of HIF-1 and was proposed to act as a co-activator of HIF-1α in the mediation of the Warburg effect.[9,45] Other experiments have reported non-metabolic functions of PKM2 such as the ability to function as protein kinase, which may confer additional benefits in the promotion of the Warburg effect.[46,47]

More recent studies provide further detail and indicate that PKM2 knockdown may not be a viable treatment strategy in established tumours because alternative pathways are invoked providing metabolic nourishment as required.[42,48,49] Cortes-Cros *et al*. observed that PKM2 knockdown did not affect the growth of established tumours.[48] In addition, the authors highlighted ongoing pyruvate production along with increased serine and glycine biosynthesis in dual PKM1 and PKM2 knockdown tumour cells.[48] One explanation involves the shunting of accumulated upstream glycolytic intermediates into the serine synthetic pathway, in which serine is produced and subsequently converted into pyruvate.[25] However, the metabolic phenotype of these tumours, whether they have converted from glycolytic to aerobic metabolism, remains unclear. The existence of alternative glycolytic pathways involving not yet characterized enzymes had also been proposed.[50] Israelsen *et al*. then reported paradoxical acceleration of tumour growth with the loss of PKM2 in mouse model of breast cancer.[49] The authors interpreted these findings as an indication that 'regulation of PKM2 activity supports the different metabolic requirements of proliferating and nonproliferating tumor cells'. Similarly, Anastasiou *et al*. demonstrated that high PK activity impedes xenograft tumour growth.[42]

Collectively, these results highlighted two interesting points. Firstly, PKM2 expression is not entirely essential in established tumours. Secondly, overall high PK activity actually hinders tumour growth. This paradigm actually supports the notion of the 'metabolic budget system': high PK activity leads to depletion of glycolytic intermediates available for biosynthesis and therefore impairs cellular proliferation and growth.[10,27,42] Because the activities of PKM2, determined by its conformation in either the highly active tetramer or the inactive dimer, are highly malleable to various regulatory inputs, preferential PKM2 expression confers an advantageous metabolic flexibility to the differential metabolic needs of proliferating cells and tumours through various proliferative phases.[49]

MAMMALIAN RETINAL METABOLISM

Glycolysis in mammalian retina

The retina has prodigious energy demands to maintain the neurons in an excitable state for phototransduction and neurotransmission, in addition to the maintenance of normal cellular function.[51]

The initial discovery of the high level of lactate production from explanted retina by Warburg and his team sparked the unprecedented impetus for huge interest in the metabolism of mammalian retina.[3] Numerous experiments have subsequently reinforced Warburg's original findings and demonstrated the role and the importance of glycolysis in mammalian retina.[5,51–53]

In 1951, Noell demonstrated the direct dependence of mammalian (rabbits and cats) retinal function on glycolysis.[5] The visual functions in these mammals, as measured by the electroretinogram, resisted the effect of anoxia but were highly susceptible to iodoacetate inhibition of glycolysis.[5] Iodoacetate is an agent that selectively inhibits glycolysis while preserving mitochondrial OXPHOS.[5,52] Loss of electrical activity and selective disappearance of the rod photoreceptor cells were observed following iodoacetate inhibition.[52] In another *in vivo* study, Tornquist and Alm measured the arterio-venous differences in glucose, oxygen and lactate levels for both choroidal and retinal blood in pigs.[54] They recorded high concentration of lactate in the venous blood.[54] Additionally, the total amount of oxygen extracted from choroidal and retinal blood flow combined only accounted for complete oxidation of 37% of all the extracted glucose, reflecting the high glycolytic activities.[54] The majority of the glycolytic substrate was derived from the choroidal circulation, indicating the greater metabolic activity in the outer retina.[54]

In 1975, Winkler reported the capability of isolated rat retina to support electrical activity in the photoreceptors anaerobically, provided glucose was abundant.[55] Of note, the electrical activity was maintained at 80% for 30 min of anoxia but fell to 40% of the aerobic value when the glucose supply was reduced.[55] Winkler later reported the effect of oxygen tension on retinal lactate production, ATP production and electroretinography, obtaining some data about metabolism in different retinal layers.[6] These experiments indicated a Pasteur effect in photoreceptors, but neither glycolysis alone nor OXPHOS alone maintained the electrophysiological function of the isolated retina at a normal level.

The fact that glycolysis within the mammalian retina occurs in the aerobic setting was substantiated by Wang and Bill who showed the lack of effect from induced hyperoxia in rabbit retina on the lactate production and glucose consumption.[56] In Winkler's *in vitro* study of glucose metabolism in both normal and dystrophic rat retinas, 90% of the glucose utilized aerobically was used in glycolysis.[57] Furthermore, Ames *et al.* demonstrated, in isolated rabbit retina, corresponding changes in the lactate level with neurotransmission, independent of oxygen consumption.[51] The author postulated that neurotransmission through the inner retina was highly dependent on glycolysis.[51]

Higher glycolytic activities in the outer retina

Most of the aerobic glycolysis reportedly takes place in the outer retina, mainly in the photoreceptors.[58–61] Graymore observed a greater than 50% reduction in the glycolytic activity within dystrophic rat retinas lacking photoreceptor cells when compared to normal rat retina.[58,59] Wang *et al.* reported the glucose consumptions in pig retina *in vivo* by measuring the arteriovenous differences in the glucose concentrations.[60,61] The inner retina metabolized 21% of the glucose via glycolysis and 69% via oxidative metabolism in contrast to the outer retina that metabolized 61% of the glucose via glycolysis and only 12% via oxidative metabolism.[60,61] These results are consistent with the differential oxygen consumption reported in mammalian retina.[62–64] The deep inner plexiform layer, the outer plexiform layer and the inner segments of photoreceptor have much higher oxygen consumptions as opposed to the outer segments of the photoreceptors and the outer nuclear layers in vascularized mammalian retina.[62–64]

Relative contribution of glycolysis *versus* OXPHOS in different retinal cells

Almost all metabolic evidence for the Warburg effect in the retina comes from experiments on whole retinas. The photoreceptors have been technically the easiest to experimentally isolate. However, data about the metabolic profile of other cell types or retinal layers are limited.[5,51–53] Furthermore, variations appear to exist across different mammalian species and among different experimental designs.[51,53,60,65] Reported contributions of aerobic glycolysis to retinal glucose metabolism ranges from 40% to 80% in rabbit,[51,53] 60% in pig,[65] 90% in rat,[57] to 99% in cultured human retinal Müller cells.[66]

Noell demonstrated that retinal ganglion cells (RGCs) are susceptible to hypoxia and are the 'weakest link in the chain' of visual perception when oxygen is scarce.[67] Whether the RGCs have a Pasteur effect is unclear. However, the neuroprotective effect of glucose was supported by our previous research that indicated that an elevated vitreal glucose level at the time of acute[68] or chronic retinal ischaemia[69] or experimental glaucoma[70] provides robust protection to the RGCs. We recently demonstrated that, *in vitro*, this is predominantly due to glycolytic ATP production.[71] The protective effect is abolished if the vitreous glucose is elevated post-ischaemia.[66] These results suggest that the RGCs can upregulate glycolysis during ischaemia to generate ATP (the Pasteur effect). Winkler *et al.* attempted to determine whether cultured RGCs displayed the Pasteur effect,[72] but unfortunately their methodology was flawed because they used an RGC-5 cell line, which was later recognized to be of photoreceptor origin.[73,74] Hence, information about the Pasteur effect in RGCs remains incomplete.

Nevertheless, experimental evidence has indicated that neither OXPHOS nor glycolysis is dispensable for optimal retinal metabolism and functioning.[6,51] The requirement for mitochondrial OXPHOS in mammalian retinal function is seen in a retinitis pigmentosa model.[75] The *IDH3B* gene encodes for the B-subunit of NAD-specific isocitrate dehydrogenase (NAD-IDH), which is required to catalyse the oxidation of isocitrate to α-ketoglutarate in the citric acid cycle of mitochondrial OXPHOS. *IDH3B* mutations in familial retinitis pigmentosa result in the impairment of mitochondrial OXPHOS. This may, in part, contribute to progressive rod and cone photoreceptors degeneration, characteristic of the disease.[75] The notion of mitochondrial dysfunction and associated oxidative stress in retinitis pigmentosa is also supported by other experiments.[76–78]

Explanation for the Warburg effect in mammalian retina

We have recently published a teleological explanation for the presence of the Warburg effect in the mammalian retina: even though the adult mammalian retina is non-proliferative, it shares similar biosynthesis requirements to neoplastic tissue because of the prodigious turnover of the opsin protein in the disc membranes of the photoreceptor outer segments.[11] Each mammalian rod outer segment consists of a stack of ~1500 distinct discs enclosed by the plasma membrane.[79,80] Approximately 60% of the dry weight of the disc membrane is protein, and opsin comprises 90% of the protein content.[81] Hence, the retinal-bound opsin, rhodopsin forms a large structural component of the rod disc membrane. Rhodopsin is a G protein-coupled receptor comprising 348 amino acids, with a rich glycine and serine component.[82]

In a landmark experiment using radioactively labelled methionine and radiographic tracing, Richard Young showed that rhodopsin was constantly renewed as the disc membranes moved in a sclerad direction along the rod outer segment towards the retinal pigment epithelium in mouse, rat and frog retinas.[83] The rhodopsin turnover rate as measured by the position of radioactive band displacement was notably faster in rats than in frogs.[83] Thus, we propose that the reason that the Warburg effect has evolved in the mammalian retina is simply because it has similar metabolic requirements to a proliferating tissue, owing to the constant rhodopsin turnover. The rhodopsin turnover rate parallels the degree of aerobic glycolysis found in different species.[83] Furthermore, the relatively low rate of photoreceptor turnover in lower vertebrates is temperature dependent, increasing at higher temperatures,[83] reflecting the temperature-dependent Warburg effect.[4]

Also consistent with this postulate was the observation by Agathocleus *et al.* who reported facultative aerobic glycolytic metabolism of developing *Xenopus laevis* frog and zebrafish retinas to match the biosynthetic requirements.[84] Glycolysis inhibition resulted in cellular apoptosis, but OXPHOS interference had no deleterious consequence.[84] Nevertheless, a switch to greater reliance of OXPHOS was noted in mature retina.[84]

An alternate explanation for the high glycolytic process in the photoreceptors may involve the highly compartmentalized cellular configurations, with the confinement of mitochondria to the inner segment, absent from the outer segment.[80,85] The dense aggregation of mitochondria in the ellipsoid region of the inner segment reflects the considerable reliance of this portion on oxidative energy.[85–87] Supporting this was the finding of high concentration of malate dehydrogenase (an enzyme involved in OXPHOS) in the monkey photoreceptors inner segment, a level 30 times higher than the outer segment.[88] On the contrary, measured LDH was significantly lower in the inner segment as compared with the outer segment.[88] The exclusion of mitochondria from the photoreceptor outer segment possibly necessitates its reliance on glycolysis for cellular energy.[88] However, conceivably OXPHOS-derived ATP could be shuttled from the inner segment to the outer segment.

Aerobic glycolysis and lactate from Müller cells

In addition to the biosynthetic requirements of the photoreceptors, aerobic glycolysis and lactate production from Müller cell cultures has also been described.[65] The Müller cells are the predominant glial cells of the retina and have been proposed as the primary storage sites for glycogen.[89] The human Müller cells metabolize glucose primarily via aerobic glycolysis, accounting for 99% of total glucose metabolism and the remaining 1% undergoes mitochondrial OXPHOS.[65] This observation is consistent with the so-called astrocyte neuronal lactate shuttle hypothesis in the brain.[90] The astrocyte neuronal lactate shuttle hypothesis asserts that brain neurones use astrocyte-derived lactate as a primary energy source and that the delivery of lactate is calibrated by neuronal activity.[90] There is evidence for and against this hypothesis, and the matter remains highly controversial.[91] Conceivably, a similar phenomenon exists in the retina with the Müller cells taking the place of the astrocytes.

Experimental findings also unveiled the multipotent differentiative capability of the adult human Müller cells, whereby it can undergo differentiation into retinal neurons, astrocytes, oligodendrocytes[92] and also rod photoreceptors.[93] Reportedly, the differentiation into rod photoreceptors is sixfold faster than conventional pluripotent stem cells.[93] The unique capability of adult human Müller cells to proliferate and differentiate likely explains its inherent metabolic preference for aerobic glycolysis, which is better suited for this role. Recent evidence indicates that Müller cell ablation in a transgenic model causes photoreceptor degeneration related to loss of neurotrophic support.[94] Whether the mechanisms driving lactate production in Müller cell cultures also involve PKM2 is completely unknown.

LDH in cancer and the retina

LDH is a tetrameric enzyme comprising two major subunits A and/or B, (encoded by the *Ldh-A* and *Ldh-B* genes) resulting in five isoenzymes (A4, A3B1, A2B2, A1B3 and B4) that catalyse the forward and backward conversion of pyruvate to lactate. LDHA (LDH-5, M-LDH or A4), which is the predominant form in skeletal muscle, kinetically favours the conversion of pyruvate to lactate.[95,96] LDHB (LDH-1, H-LDH or B4), which is found in heart muscle, converts lactate to pyruvate that is further oxidized in mitochondria.[95,96] Cancers also utilize the LDHA form (even when oxygen is abundant); hence, the quantification of LDHA in cancer has become a routine surrogate marker of the Warburg effect, providing diagnostic and prognostic clinical information.[97]

The mammalian retina also expresses relatively high levels of LDHA, typical of a tumour.[98–100] Saavedra *et al.* reported the exceptionally high amount of LDH_k (synonymous with LDH-5) activity in rat, mouse and guinea pig retina, equivalent to the level measured in human cancer cells.[99,100] Lower vertebrates such as turtle, toad and frog that do not display the Warburg effect have correspondingly much lower LDH-5 activities.[100] Graymore, publishing in *Nature* in 1964, noted that the expression of the LDHA isoenzyme in the retina was reduced in rats with inherited retinitis pigmentosa characterized pathologically by loss of the photoreceptors.[98] This observation indicated that the photoreceptors were principally responsible for the retinal lactate production and also supported evidence that the photoreceptors were particularly susceptible to glycolytic inhibition.[5]

PKM2 and HIF-1α in mammalian retina

We have recently demonstrated the presence of PKM2 and constitutive expression of low level HIF-1α in the rat retina (Casson RJ, unpublished data, 2014). Hughes *et al.* have earlier reported the presence of stabilized HIF-1α in normal physiological human and rat retinas.[101] The presence of PKM2 in mouse retina was demonstrated by Morohoshi *et al.* using purified immunoglobulin G specific for the M2 isoform from individuals with age-related macular degeneration.[102] The authors proposed that PKM2 may correlate with the severity and progression of age-related macular degeneration.[102] Conceivably, the presence of PKM2 antibodies in age-related macular degeneration has a causal relation but, to our knowledge, remains untested. These findings of the coexpression of PKM2 and HIF-1α in normal mammalian retina suggest that these molecular factors likely have similar role in driving the Warburg effect.

Anti cancer therapy targeting glycolysis and the Warburg effect

Advances in the understanding of the molecular mechanism of the Warburg effect in cancer have motivated efforts to develop targeted therapies.[103–111] Variable successes have been reported with PKM2 modulation *in vitro* and *in vivo* animal studies.[42,49,109–111] Besides targeting PKM2, many other drugs that target different stages of glycolysis are also under preclinical development.[103–108] However, the extent of toxicities of these drugs towards normal, metabolically active tissues utilizing glycolysis in human is largely unknown.

The obligatory reliance of mammalian retinal metabolism, particularly photoreceptors, on glycolysis as highlighted in this review raises concerns about the potential adverse effects of PKM2 inhibition. Any disruption to key metabolic pathways essential for physiological maintenance of continuous photoreceptor renewal, energy production, phototransduction and neurotransmission will likely result in deleterious effects.[112]

Ongoing research promises a better understanding of retina biology and metabolism with the potential for breakthrough treatment of various retinal diseases. At the same time, targeting the Warburg effect and PKM2 as a therapeutic strategy for cancer should proceed cautiously.

REFERENCES

1. Dixon KC. The pasteur effect and its mechanism. *Biol Rev* 1937; **12**: 393–503.
2. Winkler BS, Sauer MW, Starnes CA. Modulation of the Pasteur effect in retinal cells: implications for

understanding compensatory metabolic mechanisms. *Exp Eye Res* 2003; **76**: 715–23.
3. Warburg O. On the origin of cancer cells. *Science* 1956; **123**: 309–14.
4. Wind F. In: Warburg O, ed. *The Metabolism of Tumors: Investigations from the Kaiser Wilhelm Institute for Biology*. Berlin-Dahlem, London: Constable & Co. Ltd., 1930; 282.
5. Noell WK. The effect of iodoacetate on the vertebrate retina. *J Cell Physiol* 1951; **37**: 283–307.
6. Winkler BS. Glycolytic and oxidative metabolism in relation to retinal function. *J Gen Physiol* 1981; **77**: 667–92.
7. Cairns RA, Harris IS, Mak TW. Regulation of cancer cell metabolism. *Nat Rev Cancer* 2011; **11**: 85–95.
8. Christofk HR, Vander Heiden MG, Harris MH *et al*. The M2 splice isoform of pyruvate kinase is important for cancer metabolism and tumour growth. *Nature* 2008; **452**: 230–3.
9. Luo W, Hu H, Chang R *et al*. Pyruvate kinase M2 is a PHD3-stimulated coactivator for hypoxia-inducible factor 1. *Cell* 2011; **145**: 732–44.
10. Vander Heiden MG, Cantley LC, Thompson CB. Understanding the Warburg effect: the metabolic requirements of cell proliferation. *Science* 2009; **324**: 1029–33.
11. Casson RJ, Chidlow G, Han G, Wood JP. An explanation for the Warburg effect in the adult mammalian retina. *Clin Exp Ophthalmol* 2013; **41**: 517.
12. Gatenby RA, Gillies RJ. Why do cancers have high aerobic glycolysis? *Nat Rev Cancer* 2004; **4**: 891–9.
13. Palsson-McDermott EM, O'Neill LA. The Warburg effect then and now: from cancer to inflammatory diseases. *Bioessays* 2013; **35**: 965–73.
14. Krawczyk CM, Holowka T, Sun J *et al*. Toll-like receptor-induced changes in glycolytic metabolism regulate dendritic cell activation. *Blood* 2010; **115**: 4742–9.
15. Romano AH, Conway T. Evolution of carbohydrate metabolic pathways. *Res Microbiol* 1996; **147**: 448–55.
16. Imamura K, Tanaka T. Multimolecular forms of pyruvate kinase from rat and other mammalian tissues. I. Electrophoretic studies. *J Biochem* 1972; **71**: 1043–51.
17. Berg JM, Tymoczko JL, Stryer L. *Biochemistry*. 5th edition. New York: W H Freeman; 2002. Section 18.6, The Regulation of Cellular Respiration Is Governed Primarily by the Need for ATP. http://www.ncbi.nlm.nih.gov/books/NBK22448/
18. Lehninger A, N DL, Cox MM. *Principles of Biochemistry*, 2nd edn. New York: Worth, 1993.
19. Zheng L, Roeder RG, Luo Y. S phase activation of the histone H2B promoter by OCA-S, a coactivator complex that contains GAPDH as a key component. *Cell* 2003; **114**: 255–66.
20. Rathmell JC, Fox CJ, Plas DR, Hammerman PS, Cinalli RM, Thompson CB. Akt-directed glucose metabolism can prevent Bax conformation change and promote growth factor-independent survival. *Mol Cell Biol* 2003; **23**: 7315–28.
21. Sun YJ, Chou CC, Chen WS, Wu RT, Meng M, Hsiao CD. The crystal structure of a multifunctional protein: phosphoglucose isomerase/autocrine motility factor/neuroleukin. *Proc Natl Acad Sci U S A* 1999; **96**: 5412–7.
22. Jones RG, Thompson CB. Revving the engine: signal transduction fuels T cell activation. *Immunity* 2007; **27**: 173–8.
23. Weinhouse S. The Warburg hypothesis fifty years later. *Z Krebsforsch Klin Onkol Cancer Res Clin Oncol* 1976; **87**: 115–26.
24. Fantin VR, St-Pierre J, Leder P. Attenuation of LDH-A expression uncovers a link between glycolysis, mitochondrial physiology, and tumor maintenance. *Cancer Cell* 2006; **9**: 425–34.
25. Ward PS, Thompson CB. Metabolic reprogramming: a cancer hallmark even Warburg did not anticipate. *Cancer Cell* 2012; **21**: 297–308.
26. Collet JF, Stroobant V, Van Schaftingen E. Mechanistic studies of phosphoserine phosphatase, an enzyme related to P-type ATPases. *J Biol Chem* 1999; **274**: 33985–90.
27. Mazurek S. Pyruvate kinase type M2: a key regulator of the metabolic budget system in tumor cells. *Int J Biochem Cell Biol* 2011; **43**: 969–80.
28. Lum JJ, Bui T, Gruber M *et al*. The transcription factor HIF-1alpha plays a critical role in the growth factor-dependent regulation of both aerobic and anaerobic glycolysis. *Genes Dev* 2007; **21**: 1037–49.
29. Majumder PK, Febbo PG, Bikoff R *et al*. mTOR inhibition reverses Akt-dependent prostate intraepithelial neoplasia through regulation of apoptotic and HIF-1-dependent pathways. *Nat Med* 2004; **10**: 594–601.
30. Ramanathan A, Schreiber SL. Direct control of mitochondrial function by mTOR. *Proc Natl Acad Sci U S A* 2009; **106**: 22229–32.
31. Buzzai M, Bauer DE, Jones RG *et al*. The glucose dependence of Akt-transformed cells can be reversed by pharmacologic activation of fatty acid beta-oxidation. *Oncogene* 2005; **24**: 4165–73.
32. Cunningham JT, Rodgers JT, Arlow DH, Vazquez F, Mootha VK, Puigserver P. mTOR controls mitochondrial oxidative function through a YY1-PGC-1alpha transcriptional complex. *Nature* 2007; **450**: 736–40.
33. Dang CV. Rethinking the Warburg effect with Myc micromanaging glutamine metabolism. *Cancer Res* 2010; **70**: 859–62.
34. Bach M, Hawlina M, Holder GE *et al*. Standard for pattern electroretinography. International Society for Clinical Electrophysiology of Vision. *Doc Ophthalmol* 2000; **101**: 11–8.
35. Wang HJ, Hsieh YJ, Cheng WC *et al*. JMJD5 regulates PKM2 nuclear translocation and reprograms HIF-1alpha-mediated glucose metabolism. *Proc Natl Acad Sci U S A* 2014; **111**: 279–84.
36. Goda N, Kanai M. Hypoxia-inducible factors and their roles in energy metabolism. *Int J Hematol* 2012; **95**: 457–63.

37. Ke Q, Costa M. Hypoxia-inducible factor-1 (HIF-1). *Mol Pharmacol* 2006; **70**: 1469–80.
38. Eigenbrodt E, Reinacher M, Scheefers-Borchel U, Scheefers H, Friis R. Double role for pyruvate kinase type M2 in the expansion of phosphometabolite pools found in tumor cells. *Crit Rev Oncog* 1992; **3**: 91–115.
39. Jurica MS, Mesecar A, Heath PJ, Shi W, Nowak T, Stoddard BL. The allosteric regulation of pyruvate kinase by fructose-1,6-bisphosphate. *Structure* 1998; **6**: 195–210.
40. Dombrauckas JD, Santarsiero BD, Mesecar AD. Structural basis for tumor pyruvate kinase M2 allosteric regulation and catalysis. *Biochemistry* 2005; **44**: 9417–29.
41. Spoden GA, Rostek U, Lechner S, Mitterberger M, Mazurek S, Zwerschke W. Pyruvate kinase isoenzyme M2 is a glycolytic sensor differentially regulating cell proliferation, cell size and apoptotic cell death dependent on glucose supply. *Exp Cell Res* 2009; **315**: 2765–74.
42. Anastasiou D, Yu Y, Israelsen WJ *et al*. Pyruvate kinase M2 activators promote tetramer formation and suppress tumorigenesis. *Nat Chem Biol* 2012; **8**: 839–47.
43. Lv L, Li D, Zhao D *et al*. Acetylation targets the M2 isoform of pyruvate kinase for degradation through chaperone-mediated autophagy and promotes tumor growth. *Mol Cell* 2011; **42**: 719–30.
44. Bluemlein K, Gruning NM, Feichtinger RG, Lehrach H, Kofler B, Ralser M. No evidence for a shift in pyruvate kinase PKM1 to PKM2 expression during tumorigenesis. *Oncotarget* 2011; **2**: 393–400.
45. Luo W, Semenza GL. Pyruvate kinase M2 regulates glucose metabolism by functioning as a coactivator for hypoxia-inducible factor 1 in cancer cells. *Oncotarget* 2011; **2**: 551–6.
46. Keller KE, Tan IS, Lee YS. SAICAR stimulates pyruvate kinase isoform M2 and promotes cancer cell survival in glucose-limited conditions. *Science* 2012; **338**: 1069–72.
47. Yang W, Zheng Y, Xia Y *et al*. ERK1/2-dependent phosphorylation and nuclear translocation of PKM2 promotes the Warburg effect. *Nat Cell Biol* 2012; **14**: 1295–304.
48. Cortes-Cros M, Hemmerlin C, Ferretti S *et al*. M2 isoform of pyruvate kinase is dispensable for tumor maintenance and growth. *Proc Natl Acad Sci U S A* 2013; **110**: 489–94.
49. Israelsen WJ, Dayton TL, Davidson SM *et al*. PKM2 isoform-specific deletion reveals a differential requirement for pyruvate kinase in tumor cells. *Cell* 2013; **155**: 397–409.
50. Vander Heiden MG, Locasale JW, Swanson KD *et al*. Evidence for an alternative glycolytic pathway in rapidly proliferating cells. *Science* 2010; **329**: 1492–9.
51. Ames A III, Li YY, Heher EC, Kimble CR. Energy metabolism of rabbit retina as related to function: high cost of Na + transport. *J Neurosci* 1992; **12**: 840–53.
52. Noell WK. The visual cell: electric and metabolic manifestations of its life processes. *Am J Ophthalmol* 1959; **48** (Pt 2): 347–70.
53. Cohen LH, Noell WK. Glucose catabolism of rabbit retina before and after development of visual function. *J Neurochem* 1960; **5**: 253–76.
54. Tornquist P, Alm A. Retinal and choroidal contribution to retinal metabolism in vivo. A study in pigs. *Acta Physiol Scand* 1979; **106**: 351–7.
55. Winkler BS. The electroretinogram of the isolated rat retina. *Vision Res* 1972; **12**: 1183–98.
56. Wang L, Bill A. Effects of constant and flickering light on retinal metabolism in rabbits. *Acta Ophthalmol Scand* 1997; **75**: 227–31.
57. Winkler BS. A quantitative assessment of glucose metabolism in the isolated rat retina. In: Christen Y, Doly M, Droy-Lefaix M-T, eds. *A Quantitative Assessment of Glucose Metabolism in the Isolated Rat Retina*. Amsterdam: Elsevier, 1995; 78–96.
58. Graymore C. Metabolism of the developing retina. III. Respiration in the developing normal rat retina and the effect of an inherited degeneration of the retinal neuroepithelium. *Br J Ophthalmol* 1960; **44**: 363–9.
59. Graymore C. Metabolism of the developing retina. I. Aerobic and anaerobic glycolysis in the developing rat retina. *Br J Ophthalmol* 1959; **43**: 34–9.
60. Wang L, Tornquist P, Bill A. Glucose metabolism in pig outer retina in light and darkness. *Acta Physiol Scand* 1997; **160**: 75–81.
61. Wang L, Tornquist P, Bill A. Glucose metabolism of the inner retina in pigs in darkness and light. *Acta Physiol Scand* 1997; **160**: 71–4.
62. Linsenmeier RA. Effects of light and darkness on oxygen distribution and consumption in the cat retina. *J Gen Physiol* 1986; **88**: 521–42.
63. Haugh LM, Linsenmeier RA, Goldstick TK. Mathematical models of the spatial distribution of retinal oxygen tension and consumption, including changes upon illumination. *Ann Biomed Eng* 1990; **18**: 19–36.
64. Yu DY, Cringle SJ. Oxygen distribution and consumption within the retina in vascularised and avascular retinas and in animal models of retinal disease. *Prog Retin Eye Res* 2001; **20**: 175–208.
65. Winkler BS, Arnold MJ, Brassell MA, Puro DG. Energy metabolism in human retinal Muller cells. *Invest Ophthalmol Vis Sci* 2000; **41**: 3183–90.
66. Bui BV, He Z, Vingrys AJ, Nguyen CT, Wong VH, Fortune B. Using the electroretinogram to understand how intraocular pressure elevation affects the rat retina. *J Ophthalmol* 2013; **2013**: 262467.
67. Noell WK. Site of asphyxial block in mammalian retinae. *J Appl Physiol* 1951; **3**: 489–500.
68. Casson RJ, Chidlow G, Wood JP, Osborne NN. The effect of hyperglycemia on experimental retinal ischemia. *Arch Ophthalmol* 2004; **122**: 361–6.
69. Holman MC, Chidlow G, Wood JP, Casson RJ. The effect of hyperglycemia on hypoperfusion-induced injury. *Invest Ophthalmol Vis Sci* 2010; **51**: 2197–207.

70. Ebneter A, Chidlow G, Wood JP, Casson RJ. Protection of retinal ganglion cells and the optic nerve during short-term hyperglycemia in experimental glaucoma. *Arch Ophthalmol* 2011; **129**: 1337–44.
71. Han G, Wood JP, Chidlow G, Mammone T, Casson RJ. Mechanisms of neuroprotection by glucose in rat retinal cell cultures subjected to respiratory inhibition. *Invest Ophthalmol Vis Sci* 2013; **54**: 7567–77.
72. Winkler BS, Starnes CA, Sauer MW, Firouzgan Z, Chen SC. Cultured retinal neuronal cells and Muller cells both show net production of lactate. *Neurochem Int* 2004; **45**: 311–20.
73. Van Bergen NJ, Wood JP, Chidlow G *et al*. Recharacterization of the RGC-5 retinal ganglion cell line. *Investe Ophthalmol Vis Sci* 2009; **50**: 4267–72.
74. Wood JP, Chidlow G, Tran T, Crowston JG, Casson RJ. A comparison of differentiation protocols for RGC-5 cells. *Invest Ophthalmol Vis Sci* 2010; **51**: 3774–83.
75. Hartong DT, Dange M, McGee TL, Berson EL, Dryja TP, Colman RF. Insights from retinitis pigmentosa into the roles of isocitrate dehydrogenases in the Krebs cycle. *Nat Genet* 2008; **40**: 1230–4.
76. Donovan M, Carmody RJ, Cotter TG. Light-induced photoreceptor apoptosis in vivo requires neuronal nitric-oxide synthase and guanylate cyclase activity and is caspase-3-independent. *J Biol Chem* 2001; **276**: 23000–8.
77. Sanz MM, Johnson LE, Ahuja S, Ekstrom PA, Romero J, van Veen T. Significant photoreceptor rescue by treatment with a combination of antioxidants in an animal model for retinal degeneration. *Neuroscience* 2007; **145**: 1120–9.
78. Sanvicens N, Gomez-Vicente V, Masip I, Messeguer A, Cotter TG. Oxidative stress-induced apoptosis in retinal photoreceptor cells is mediated by calpains and caspases and blocked by the oxygen radical scavenger CR-6. *J Biol Chem* 2004; **279**: 39268–78.
79. Krebs W, Kuhn H. Structure of isolated bovine rod outer segment membranes. *Exp Eye Res* 1977; **25**: 511–26.
80. Young RW. The renewal of rod and cone outer segments in the rhesus monkey. *J Cell Biol* 1971; **49**: 303–18.
81. Young RW. Proceedings: biogenesis and renewal of visual cell outer segment membranes. *Exp Eye Res* 1974; **18**: 215–23.
82. Hargrave PA, Fong SL, Hugh McDowell J *et al*. The partial primary structure of bovine rhodopsin and its topography in the retinal rod cell disc membrane. *Neurochem Int* 1980; **1C**: 231–44.
83. Young RW. The renewal of photoreceptor cell outer segments. *J Cell Biol* 1967; **33**: 61–72.
84. Agathocleous M, Love NK, Randlett O *et al*. Metabolic differentiation in the embryonic retina. *Nat Cell Biol* 2012; **14**: 859–64.
85. De Robertis E. Electron microscope observations on the submicroscopic organization of the retinal rods. *J Biophys Biochem Cytol* 1956; **2**: 319–30.
86. Sjostrand FS. The ultrastructure of the innersegments of the retinal rods of the guinea pig eye as revealed by electron microscopy. *J Cell Physiol* 1953; **42**: 45–70.
87. Sjostrand FS. The ultrastructure of the outer segments of rods and cones of the eye as revealed by the electron microscope. *J Cell Physiol* 1953; **42**: 15–44.
88. Lowry OH, Roberts NR, Lewis C. The quantitative histochemistry of the retina. *J Biol Chem* 1956; **220**: 879–92.
89. Kuwabara T, Cogan DG. Retinal glycogen. *Arch Ophthalmol* 1961; **66**: 680–8.
90. Pellerin L, Magistretti PJ. Glutamate uptake into astrocytes stimulates aerobic glycolysis: a mechanism coupling neuronal activity to glucose utilization. *Proc Natl Acad Sci U S A* 1994; **91**: 10625–9.
91. Chih CP, Roberts EL Jr. Energy substrates for neurons during neural activity: a critical review of the astrocyte-neuron lactate shuttle hypothesis. *J Cereb Blood Flow Metab* 2003; **23**: 1263–81.
92. Das AV, Mallya KB, Zhao X *et al*. Neural stem cell properties of Muller glia in the mammalian retina: regulation by Notch and Wnt signaling. *Dev Biol* 2006; **299**: 283–302.
93. Giannelli SG, Demontis GC, Pertile G, Rama P, Broccoli V. Adult human Muller glia cells are a highly efficient source of rod photoreceptors. *Stem Cells* 2011; **29**: 344–56.
94. Chung SH, Shen W, Gillies MC. Laser capture microdissection-directed profiling of glycolytic and mTOR pathways in areas of selectively ablated Muller cells in the murine retina. *Invest Ophthalmol Vis Sci* 2013; **54**: 6578–85.
95. Cahn RD, Zwilling E, Kaplan NO, Levine L. Nature and development of lactic dehydrogenases: the two major types of this enzyme form molecular hybrids which change in makeup during development. *Science* 1962; **136**: 962–9.
96. Plagemann PG, Gregory KF, Wroblewski F. The electrophoretically distinct forms of mammalian lactic dehydrogenase. 1. Distribution of lactic dehydrogenase. 1. Distribution of lactic dehydrogenases in rabbit and human tissue. *J Biol Chem* 1960; **235**: 2282–7.
97. Miao P, Sheng S, Sun X, Liu J, Huang G. Lactate dehydrogenase a in cancer: a promising target for diagnosis and therapy. *IUBMB Life* 2013; **65**: 904–10.
98. Graymore C. Possible significance of the isoenzymes of lactic dehydrogenase in the retina of the rat. *Nature* 1964; **201**: 615–6.
99. Saavedra RA, Anderson GR. A cancer-associated lactate dehydrogenase is expressed in normal retina. *Science* 1983; **221**: 291–2.
100. Saavedra RA, Cordoba C, Anderson GR. LDHk in the retina of diverse vertebrate species: a possible link to the Warburg effect. *Exp Eye Res* 1985; **41**: 365–70.
101. Hughes JM, Groot AJ, van der Groep P *et al*. Active HIF-1 in the normal human retina. *J Histochem Cytochem* 2010; **58**: 247–54.
102. Morohoshi K, Ohbayashi M, Patel N, Chong V, Bird AC, Ono SJ. Identification of anti-retinal antibodies

in patients with age-related macular degeneration. *Exp Mol Pathol* 2012; **93**: 193–9.

103. Yang CM, Liu YZ, Liao JW, Hu ML. The in vitro and in vivo anti-metastatic efficacy of oxythiamine and the possible mechanisms of action. *Clin Exp Metastasis* 2010; **27**: 341–9.
104. Evans MJ, Saghatelian A, Sorensen EJ, Cravatt BF. Target discovery in small-molecule cell-based screens by in situ proteome reactivity profiling. *Nat Biotechnol* 2005; **23**: 1303–7.
105. Le A, Cooper CR, Gouw AM *et al.* Inhibition of lactate dehydrogenase A induces oxidative stress and inhibits tumor progression. *Proc Natl Acad Sci U S A* 2010; **107**: 2037–42.
106. Sonveaux P, Vegran F, Schroeder T *et al.* Targeting lactate-fueled respiration selectively kills hypoxic tumor cells in mice. *J Clin Invest* 2008; **118**: 3930–42.
107. Oudard S, Carpentier A, Banu E *et al.* Phase II study of lonidamine and diazepam in the treatment of recurrent glioblastoma multiforme. *J Neurooncol* 2003; **63**: 81–6.
108. De Lena M, Lorusso V, Latorre A *et al.* Paclitaxel, cisplatin and lonidamine in advanced ovarian cancer. A phase II study. *Eur J Cancer* 2001; **37**: 364–8.
109. Vander Heiden MG, Christofk HR, Schuman E *et al.* Identification of small molecule inhibitors of pyruvate kinase M2. *Biochem Pharmacol* 2010; **79**: 1118–24.
110. Chen J, Xie J, Jiang Z, Wang B, Wang Y, Hu X. Shikonin and its analogs inhibit cancer cell glycolysis by targeting tumor pyruvate kinase-M2. *Oncogene* 2011; **30**: 4297–306.
111. Boxer MB, Jiang JK, Vander Heiden MG *et al.* Evaluation of substituted N,N'-diarylsulfonamides as activators of the tumor cell specific M2 isoform of pyruvate kinase. *J Med Chem* 2010; **53**: 1048–55.
112. Ng SK, Wood JP, Chidlow G, Peet DJ, Casson RJ. Potential adverse effects to the retina of cancer therapy targeting pyruvate kinase M2. *Acta Oncol (Madr)* 2014; **1–2**.

7.2 Paper 2: M-Type Pyruvate Kinase Isoforms and Lactate Dehydrogenase A in the Mammalian Retina: Metabolic Implications

Casson, R.J., Wood, J.P., Han, G., Kittipassorn, T., Peet, D.J., and Chidlow, G. (2016). M-Type Pyruvate Kinase Isoforms and Lactate Dehydrogenase A in the Mammalian Retina: Metabolic Implications. Investigative Ophthalmology & Visual Science 57, 66-80.

http://dx.doi.org/10.1167/iovs.15-17962

Statement of Authorship

Title of Paper	M-Type Pyruvate Kinase Isoforms and Lactate Dehydrogenase A in the Mammalian Retina: Metabolic Implications
Publication Status	☑ Published ☐ Accepted for Publication ☐ Submitted for Publication ☐ Unpublished and Unsubmitted work written in manuscript style
Publication Details	Casson, R.J., Wood, J.P., Han, G., Kittipassorn, T., Peet, D.J., Chidlow, G., 2016. M-Type Pyruvate Kinase Isoforms and Lactate Dehydrogenase A in the Mammalian Retina: Metabolic Implications. Investigative ophthalmology & visual science 57, 66-80.

Co-Author

Name of Co-Author (Candidate)	Thaksaon Kittipassorn		
Contribution to the Paper	Generated Supplementary Figure 3 and wrote the parts of the manuscript associated with the figure (the explanation in the text of the main manuscript, the figure legend and a part of the Supplementary materials and methods). Reviewed and edited the manuscript. Please note that the experiment for Supplementary Figure 3 was performed during the period of my Honours degree at the University of Adelaide.		
Overall percentage (%)	5% contribution during the period of my PhD candidature		
Certification:	This paper reports on original research conducted during the period of my Higher Degree by Research candidature and is not subject to any obligations or contractual agreements with a third party that would constrain its inclusion in this thesis. I am a co-author of this paper.		
Signature		Date	18/12/2018

Co-Author Contributions

By signing the Statement of Authorship, each author certifies that:

i. the candidate's stated contribution to the publication is accurate (as detailed above);

ii. permission is granted for the candidate in include the publication in the thesis; and

iii. the sum of all co-author contributions is equal to 100% less the candidate's stated contribution.

Name of Principal Author	Robert J Casson		
Contribution to the Paper	Conceived the project. Planned experiments. Interpreted the results. Wrote, reviewed and edited the manuscript.		
Signature		Date	18/12/2018

Name of Co-Author	John PM Wood		
Contribution to the Paper	Conceived the project. Planned experiments. Conducted experiment work. Interpreted the results. Wrote, reviewed and edited the manuscript.		
Signature		Date	1902/19

Name of Co-Author	Guoge Han		
Contribution to the Paper	Conceived the project. Planned experiments. Conducted experiment work. Interpreted the results. Wrote, reviewed and edited the manuscript.		
Signature		Date	

Name of Co-Author	Daniel J Peet		
Contribution to the Paper	Conceived the project. Planned experiments. Interpreted the results. Reviewed and edited the manuscript.		
Signature		Date	14/2/2019

Name of Co-Author	Glyn Chidlow		
Contribution to the Paper	Conceived the project. Planned experiments. Conducted experiment work. Interpreted the results. Wrote, reviewed and edited the manuscript.		
Signature		Date	19/2/19

Name of Co-Author	John PM Wood		
Contribution to the Paper	Conceived the project. Planned experiments. Conducted experiment work. Interpreted the results. Wrote, reviewed and edited the manuscript.		
Signature		Date	

Name of Co-Author	Guoge Han		
Contribution to the Paper	Conceived the project. Planned experiments. Conducted experiment work. Interpreted the results. Wrote, reviewed and edited the manuscript.		
Signature	[redacted]	Date	20/01/2024

Name of Co-Author	Daniel J Peet		
Contribution to the Paper	Conceived the project. Planned experiments. Interpreted the results. Reviewed and edited the manuscript.		
Signature		Date	

Name of Co-Author	Glyn Chidlow		
Contribution to the Paper	Conceived the project. Planned experiments. Conducted experiment work. Interpreted the results. Wrote, reviewed and edited the manuscript.		
Signature		Date	

M-Type Pyruvate Kinase Isoforms and Lactate Dehydrogenase A in the Mammalian Retina: Metabolic Implications

Robert J. Casson,[1,2] John P. M. Wood,[1,2] Guoge Han,[1,2] Thaksaon Kittipassorn,[2,3] Daniel J. Peet,[3] and Glyn Chidlow[1,2]

[1]Ophthalmic Research Laboratories, Hanson Institute Centre for Neurological Diseases, Adelaide, South Australia, Australia
[2]South Australian Institute of Ophthalmology, University of Adelaide, Adelaide, South Australia, Australia
[3]School of Biological Science, University of Adelaide, Adelaide, South Australia, Australia

Correspondence: Robert J. Casson, South Australian Institute of Ophthalmology, Adelaide, SA 5000, Australia;
robert.casson@adelaide.edu.au.

Submitted: August 15, 2015
Accepted: December 2, 2015

Citation: Casson RJ, Wood JPM, Han G, Kittipassorn T, Peet DJ, Chidlow G. M-type pyruvate kinase isoforms and lactate dehydrogenase A in the mammalian retina: metabolic implications. *Invest Ophthalmol Vis Sci*. 2016;57:66–80. DOI:10.1167/iovs.15-17962

Purpose. Like cancer cells, photoreceptor cells produce lactate aerobically, requiring lactate dehydrogenase A (LDH-A). Cancer cells also use glycolytic intermediates for biosynthesis. The molecular switch controlling glycolytic flow is thought to be an isoenzyme of pyruvate kinase (PKM2). Here, we determined the expression and localization of PKM2 and LDH-A in mammalian retina and make comparisons with the brain.

Methods. Single- and double-labeling immunohistochemistry for PKM2, pyruvate kinase M1 (PKM1), and LDH-A were performed using retinal sections from C57BL/6 mice, Sprague-Dawley rats, rabbits, marmosets, and humans. Pyruvate kinase M1 and PKM2 mRNA and protein expression levels were quantified in rodent retina and brain by using qPCR and immunoblotting. The quaternary forms of PKM2 in rat retina were also determined.

Results. Pyruvate kinase M2 was present in some glial cells and rod and cone photoreceptors in the retina of all species but was exclusively localized to glia in the brain. Pyruvate kinase M1 was confined to neurons in the retina and brain. Lactate dehydrogenase A was principally found in photoreceptors and inner portion of the avascular rabbit retina. Western blotting and qPCR confirmed high levels of PKM2 and LDH-A in the retina. There was a 6- to 9-fold greater expression of PKM2 mRNA in the rodent retina than in the brain. Both the dimeric (inactive, biosynthesis-driving form) and the active tetrameric (glycolytic-driving) forms of PKM2 were present in retina but not in brain.

Conclusions. Mammalian photoreceptors contain dimeric and tetrameric PKM2 and LDH-A. This is consistent with the ability to switch between energy production and biosynthesis like a proliferating tissue, possibly due to demands of opsin synthesis.

Keywords: lactate dehydrogenase, metabolism, optic nerve, PKM2, retina

Retinal photoreceptors have a metabolism that is in some ways more reminiscent of a neoplastic cell than a central nervous system neuron.[1] That is, they face prodigious energy demands to maintain their "dark current"[2] and large biosynthesis requirements due to the rapid shedding and renewal of their outer segments.[3] Like cancer cells, photoreceptor cells rely heavily on both glycolysis and oxidative phosphorylation to meet energy demands, and like cancer cells, isolated retina has a high glycolytic flux and lactate production even in the presence of oxygen, a phenomenon known as aerobic glycolysis or the Warburg effect.[4,5] Limited evidence indicates that the retinal Warburg effect is actually predominantly localized to photoreceptors with minimal contribution from the inner retina.[4,6–8] Relatively high levels of lactate production by retinal cells in the presence of oxygen define the presence of the Warburg effect but are difficult to measure in vivo. It is also difficult to define the specific cellular source of lactate production. A surrogate marker in vivo, thus, is the presence of lactate dehydrogenase (LDH), consisting of the subunits LDH-A and LDH-B. The LDH-A isoform catalyzes the conversion of pyruvate to lactate, reforming nicotinamide adenine dinucleotide (NAD$^+$) to support ongoing glycolysis. Lactate dehydrogenase A is used as a cancer biomarker and is under consideration as a therapeutic target for cancer.[9] To our knowledge, the cell-specific localization of LDH-A in the retina has never been reported.

Glycolysis in cancer cells, in addition to providing energy, is also able to provide anabolic building blocks for cellular proliferation.[10] The requirement of a proliferating cell for both glycolysis-derived biosynthesis and adenosine triphosphate (ATP) production in the presence of oxygen has been termed a "metabolic budget system" (MBS).[11] Pyruvate kinase (PK) catalyzes the final step of glycolysis, converting phosphoenolpyruvate to pyruvate. The molecular switch responsible for the MBS is an isoenzyme of PK known as PKM2.[11] An alternative isoform, PKM1, is found in nonproliferating tissue.[12] Structurally, both PKM1 and PKM2 exist as homotetramers, configurations that favor glycolytic flux. Pyruvate kinase M2, however, unlike PKM1, is under allosteric control by the upstream glycolytic intermediate fructose-1,6-biphosphate[12] and the amino acid serine.[13] Allosteric modulation causes the PKM2 tetramer to dissociate to a dimer. Dimeric PKM2 is much less efficient at converting phosphoenolpyruvate to pyruvate, and its presence therefore slows the rate of glycolytic flux; the resultant accumulation of upstream glycolytic intermediates can then be used for anabolic reactions. The presence of a dimeric form of PKM2 within a cell, therefore, implies a reduced rate of glycolysis and an increased level of biosynthesis derived from glycolytic intermediates. Recent data indicate that rodent photoreceptors contain PKM2,[14] and intriguingly, that anti-PKM2 antibodies are present in the serum of individuals with age-related macular degeneration.[15]

In order to advance our understanding of the unique metabolism of the retina, a detailed characterization of the levels of expression, cellular distribution, and species correspondence among PKM1, PKM2, and LDH-A in the retina versus that in brain is needed. In this study, we investigated expression of PKM1, PKM2, and LDH-A in the retina, optic nerve, and cerebral cortex of mouse, rat, rabbit, common marmoset (*Callithrix jacchus*), and human.

Materials and Methods

Animals and Tissue Processing

This study was approved by the SA Pathology/Central Heath Network (CHN) Animal Ethics Committee (Adelaide, Australia) and conformed to the Australian Code of Practice for the Care and Use of Animals for Scientific Purposes, 2004, and with the Association for Research in Vision and Ophthalmology statement for the use of animals in vision and ophthalmic research. Adult Sprague-Dawley rats (approximately 250 g) and C57BL/6 mice were housed in a temperature- and humidity-controlled room with a 12L:12D cycle (lights on 7 AM) and were provided with food and water ad libitum. Light-adapted rodents were killed by transcardial perfusion with physiological saline under deep anesthesia between 2 and 9 PM. Both eyes with optic nerves attached were enucleated immediately. The brain was also taken when necessary. Rabbit eyes were obtained locally and fixed within 30 minutes of the animal's death.

Human ocular tissue for analysis was obtained from the Eye Bank of South Australia, Flinders Medical Centre (Adelaide, Australia), following guidelines of the Southern Adelaide Clinical Human Research Ethics Committee; all tissues had been screened to ensure there was no underlying ocular disease, and all were from Caucasian donors 50 to 65 years of age. Following ethical approval from the SA Pathology/CHN Animal Ethics Committee (Adelaide, Australia), we obtained ocular tissue from three adult marmosets (*Callithrix jacchus*) belonging to the colony housed at the Queen Elizabeth Hospital (South Australia, Australia) that were being euthanized. We are grateful to Toby Coates for participating in this tissue-sharing initiative, which has obvious benefits from an ethical perspective.

There was no consistent orientation of rodent, primate, or human globes with regard to nasal-temporal or dorsal-ventral quadrants of the retina analyzed. Sections were typically taken at the level of the optic nerve head and, hence, consisted of at least two quadrants. We cannot categorically rule out expression differences between different regions of the retina in any species; however, no such differences were apparent in any of our examinations.

Globes and optic nerves that were subsequently used for immunohistochemistry were fixed by immersion in Davidson's solution for 24 hours and then transferred to 70% ethanol until processing. Davidson's solution (2 parts formaldehyde [37%], 3 parts 100% ethanol, 1 part glacial acetic acid, and 3 parts water) is the preferred fixative for whole eyes as it provides optimal tissue morphology while avoiding retinal detachment. Brains were immersion-fixed in 10% buffered formalin until processing. Following fixation, the brain was positioned in a Kopf rat brain blocker (Kopf Instruments, Tujunga, CA, USA), and 2-mm coronal slices were taken starting from the dorsal and proceeding to the caudal portion of the brain. Brain slices along with the globe and optic pathway were then processed for routine paraffin-embedded sectioning. Globes were embedded sagittally and optic nerves longitudinally. In all cases, 4-μm sections were cut.

Immunohistochemistry

Colorimetric immunohistochemistry was performed as previously described.[16–18] Briefly, tissue sections were deparaffinized, endogenous peroxidase activity was blocked, and high-temperature antigen retrieval was performed. Subsequently, sections were incubated in primary antibody (Supplementary Table S1), followed by consecutive incubations with biotinylated secondary antibody and streptavidin-peroxidase conjugate. Color development was achieved using NovaRed (Sao Paolo, Brazil) substrate kit.

For double-labeling fluorescent immunohistochemistry, visualization of one antigen was achieved using a 3-step procedure (primary antibody, biotinylated secondary antibody, streptavidin-conjugated AlexaFluor 488 or 594 [Thermo Fisher Scientific, Waltham, MA, USA]), and the second antigen was labeled by a 2-step procedure (primary antibody, secondary antibody conjugated to AlexaFluor 488 or 594). Sections were prepared as described above and then incubated overnight at room temperature in the appropriate combination of primary antibodies. On the following day, sections were incubated with the appropriate biotinylated secondary antibody for the 3-step procedure plus the correct secondary antibody conjugated to AlexaFluor 488 or 594 for the 2-step procedure, followed by streptavidin-conjugated AlexaFluor 488 or 594. Sections were then mounted using antifade mounting medium and were examined using confocal fluorescence microscopy.

Western Blotting

Western blotting was performed as previously described.[17] Briefly, tissue extracts were sonicated in homogenization buffer, diluted with an equal volume of sample buffer, and boiled for 3 minutes. Electrophoresis was performed using 10% denaturing polyacrylamide gels. After proteins were separated, they were were transferred to polyvinylidene fluoride membranes for immunoprobing. Membranes were incubated consecutively with the appropriate primary antibody (Supplementary Table S1), biotinylated secondary antibody, and streptavidin-peroxidase conjugate. Color development was achieved using 3-amino-9-ethylcarbazole. Detection of β-actin or glyceraldehyde-3-phosphate dehydrogenase (GAPDH) was assessed in all samples as a positive gel-loading control.

Determination of oligomerization status for PK isoforms was undertaken by chemically cross-linking individual monomeric subunits in tissue homogenates as follows: Tissues were solubilized by sonication in 100 mM sodium phosphate buffer, pH 7.4, plus 150 mM NaCl, to a final concentration of 10 μg of protein/μL; each sample was divided into 2 tubes containing a equal volumes of the homogenate. The cross-linking agent disuccinimidyl suberate (DSS) was added to one tube from each sample to a final concentration of 1 mM. Addition of an equal volume of vehicle to the second tube from each sample served as the non–cross-linked control. All samples were incubated at 37°C for 1 hour, and then free DSS was quenched by addition of 1/5 volume of 1 M Tris-HCl (pH 7.5). The protease inhibitor phenyl methyl sulphonyl fluoride was added

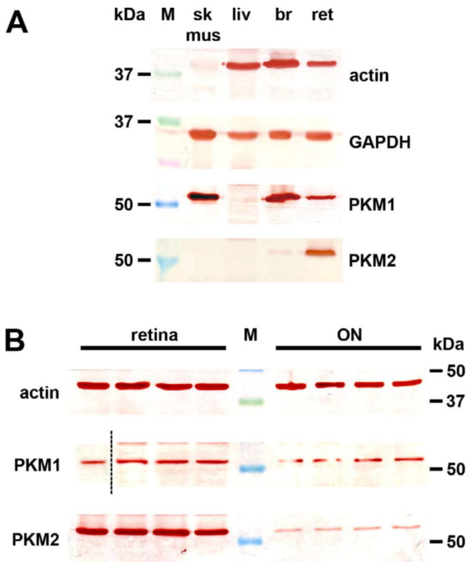

FIGURE 1. Western blot analysis of PKM1 and PKM2 expression in mouse tissues. (**A**) Skeletal muscle (sk mus), liver (liv), brain (br), and retina (ret) tissue extracts were probed for actin, GAPDH, PKM1, and PKM2. Note the absence of actin and PKM2 in skeletal muscle, the absence of PKM1 and PKM2 in liver, and the low level of PKM2 in brain. (**B**) Evaluation of PKM1 and PKM2 expression in retina (*lanes* 1–4) and optic nerve (*lanes* 6–9) from tissue extracts obtained from four different mice. Pyruvate kinase M1 and PKM2 are detectable in all samples but in greater amounts in the retina. The *dotted line* indicates that the first sample was not run in the adjacent lane. M, molecular weight markers.

to a final concentration of 100 µM, and an equal total volume of sample buffer (62.5 mM Tris-HCl, pH 7.4, containing 4% sodium dodecyl sulfate [SDS], 10% glycerol, 10% β-mercaptoethanol, and 0.002% bromophenol blue) was added before all samples were heated to 80°C for 10 minutes. Proteins were resolved on 6% SDS-PAGE gels, and Western blots for different PK isoforms were prepared as described above.

Real-Time RT-PCR

Reverse transcription (RT) polymerase chain reaction (RT-PCR) studies were carried out as described previously.[19] Briefly, entire retinas and optic nerves were dissected, total RNA was isolated, and first-strand cDNA was synthesized from DNase-treated RNA. Real-time PCR reactions were carried out in 96-well optical reaction plates by using the cDNA equivalent of 20 ng of total RNA for each sample in a total volume of 20 µL containing 1× SYBR Green PCR Master Mix (Bio-Rad, Gladesville, Australia) and forward and reverse primers. Thermal cycling conditions were 95°C for 3 min and 40 cycles of amplification at 95°C for 12 seconds, annealing temperature (Supplementary Table S2) for 30 seconds and 72°C for 30 seconds. After the final cycle of the PCR, primer specificity was checked by the dissociation (melting) curve method. In addition, specific amplification was confirmed by electrophoresis of PCR products on 3% agarose gels. PCR assays were performed using the IQ5 iCycler machine (Bio-Rad), and all samples were run in duplicate. Threshold cycles were calculated using IQ5 iCycler software (Bio-Rad). All values were normalized using the endogenous reference gene GAPDH, and results are means ± standard error of the mean (SEM). Primer pairs (Supplementary Table S2) were designed from sequences contained in the GenBank database, using the primer design software Primer 3 (Whitehead Institute for Biomedical Research; http://bioinfo.ut.ee/primer3-0.4.0/primer3/, in the public domain) and were selected to amplify sequences that spanned at least 1 intron. Primer sequences were analyzed for melting temperature (T_m) and secondary structure and primer-dimer formation by using NetPrimer analysis software (http://www.premierbiosoft.com/netprimer, in the public domain; Premier Biosoft, Palo Alto, CA, USA) and verified for their specificity to the target sequence. Results showed that all mRNAs were amplified with high efficiency and linearity during RT-PCR. Mean amplification efficiencies, as determined by plotting cycle threshold as a function of initial cDNA quantity, ranged from 1.9 to 2.0.

Antibody Characterization

Full details of all antisera and antibodies used are shown in Supplementary Table S1. Validation of antibodies to PKM1, PKM2, and LDH-A are detailed in *Results*. Validation of antibodies to β-actin, GAPDH, calretinin, PKCα, and glutamine synthetase are detailed in Supplementary Materials and Methods S1.

RESULTS

PKM1

Validation of Antibodies. All antibodies were validated prior to use. Three commercial antibodies, raised against peptides corresponding to the human PKM1 sequence (Supplementary Table S1) clearly recognized a protein of the expected size (~60 kDa) by Western blotting in mouse skeletal muscle (positive control tissue), brain, retina, and optic nerve but not in liver (negative control tissue). All antibodies provided high signal-to-noise cell-specific immunolabeling in mouse, monkey, and human tissue sections, including positive labeling in extraocular muscle, whereas incubation with preimmune serum alone elicited no labeling. The patterns of immunolabeling of the three antibodies were almost indistinguishable (compare Figs. 1 and 2 for data generated using the antibody from Cell Signaling [Cell Signaling Technology, Inc., Danvers, MA, USA] with data in Supplementary Fig. S1, which features data produced by antibodies from Proteintech [Proteintech Group, Inc., Chicago, IL, USA] and Novus [Novus Biologicals, Littleton, CO, USA]). Thus, it could be concluded that in mouse, marmoset, and human tissues, the data generated were specific to PKM1. Of note, PKM1 antibodies failed to elicit the expected band by Western blotting using rat samples; moreover, no specific staining was detectable in rat tissue sections (data not shown). The explanation for the lack of reactivity of the PKM1 antibodies in rat tissue almost certainly resides in the composition of the single exon that differentiates the PKM1 from the PKM2 isoform. Human, marmoset, and mouse display a high degree of similarity in this exon, but the rat sequence is more divergent.

mRNA and Protein Expression and Immunolocalization. Pyruvate kinase M1 was expressed in high amounts in the brain and retina of mice and rats, with cycle thresholds (C_T) of 17 to 18 cycles, compared to approximately 16 cycles for the housekeeping (and fellow glycolytic) gene GAPDH. There was an approximately 2.5-fold greater expression of

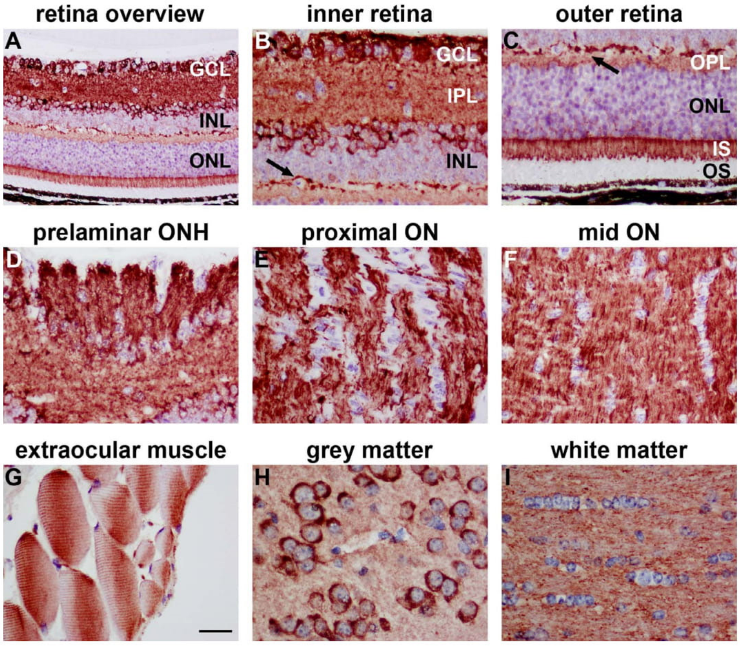

Figure 2. Representative images of PKM1 immunolabeling in mouse tissues. In the retina, positive labeling for PKM1 is localized principally to the inner retina, notably the IPL and populations of cells in the GCL and inner part of the INL (**A**, **B**). In the outer retina, PKM1 is restricted to putative axons in the OPL (*arrow*) and to photoreceptor inner segments (**A**, **C**). Pyruvate kinase M1 is robustly associated with RGC axons in the nerve fiber layer of the retina (**D**) and the optic nerve (**E**, **F**). Pyruvate kinase M1 is also expressed by extraocular muscle (**G**). In the brain, PKM1 is associated with neurons in gray matter (**H**) and axon bundles in white matter (**I**). *Scale bars*: 50 µm (**A**), 25 µm (**B–I**). IS, inner segments; ON, optic nerve; ONH, optic nerve head; ONL, outer nuclear layer; OS, outer segments.

PKM1 mRNA in cerebral cortex than in retina when normalized to GAPDH (Table 1). Consistent with this pattern, PKM1 protein, as detected by Western blotting, was more highly expressed in cortex than in retina (Fig. 1A). Analysis of retina and optic nerve samples from four mice revealed similar PKM1 expression in all samples (Fig. 1B).

By immunohistochemistry, PKM1 was principally localized to the inner retina of the mouse, specifically to populations of cells in the ganglion cell layer (GCL) and the inner part of the inner nuclear layer (INL), together with dendritic connections in the inner plexiform layer (IPL) (Fig. 2). In the outer retina, PKM1 immunostaining was evident in the outer plexiform

Table 1. Levels of PKM1, PKM2, and LDH-A mRNAs in Retina and Cortex of Rats and Mice

Gene	Tissue	GAPDH C_T	Target Gene C_T	ΔC_T*	mRNA Level†
PKM1 mouse	Retina	16.5 ± 0.4	18.7 ± 0.5	2.2 ± 0.1	0.23 ± 0.02
	Cortex	16.4 ± 0.1	17.2 ± 0.2	0.9 ± 0.1	0.57 ± 0.04
PKM1 rat	Retina	16.2 ± 0.2	18.4 ± 0.3	2.2 ± 0.1	0.24 ± 0.02
	Cortex	17.4 ± 0.4	18.2 ± 0.5	0.8 ± 0.1	0.57 ± 0.04
PKM2 mouse	Retina	16.5 ± 0.4	17.2 ± 0.5	0.7 ± 0.1	0.64 ± 0.02
	Cortex	16.4 ± 0.1	20.4 ± 0.1	4.0 ± 0.1	0.07 ± 0.003
PKM2 rat	Retina	16.2 ± 0.2	17.3 ± 0.2	1.1 ± 0.1	0.48 ± 0.03
	Cortex	17.4 ± 0.4	21.2 ± 0.3	3.8 ± 0.1	0.08 ± 0.01
LDH-A mouse	Retina	16.5 ± 0.4	18.6 ± 0.3	2.1 ± 0.1	0.26 ± 0.02
	Cortex	16.4 ± 0.1	19.8 ± 0.1	3.4 ± 0.1	0.10 ± 0.003
LDH-A rat	Retina	16.2 ± 0.2	17.8 ± 0.2	1.6 ± 0.1	0.35 ± 0.03
	Cortex	17.4 ± 0.4	20.3 ± 0.6	2.9 ± 0.2	0.15 ± 0.01

C_T, cycle threshold.

* ΔC_T, target gene C_T = GAPDH C_T.

† Target mRNA level was expressed relative to that of GAPDH, where $n = 6$.

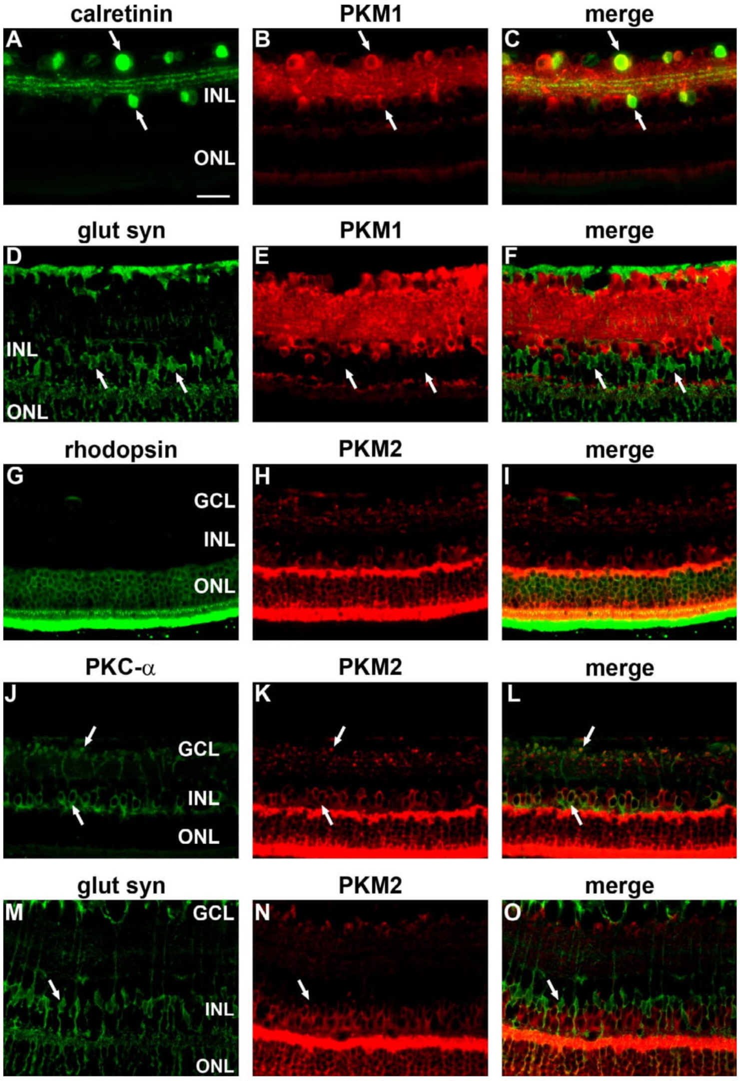

FIGURE 3. Double labeling immunofluorescence of PKM1 and PKM2 in mouse retina. Pyruvate kinase M1 colocalizes with some calretinin-positive neurons in the GCL and INL ([**A–C**] *arrows*). In contrast, PKM1 is not expressed by glutamine synthetase-positive Müller cells ([**D–F**] *arrows*). Pyruvate kinase M2 colocalizes with the rhodopsin labeling of photoreceptors (**G–I**). Pyruvate kinase M2 also colocalizes with some PKCα-positive bipolar cell bodies in the INL and their terminals adjacent to the GCL ([**J–L**] *arrows*). As with PKM1, there is no obvious association of PKM2 with glutamine synthetase-positive Müller cells ([**M–O**] *arrows*). *Scale bar*: 25 µm.

layer (OPL), in a location consistent with horizontal cell synapses, and in photoreceptor inner segments (Fig. 2). Pyruvate kinase M1 was robustly associated with retinal ganglion cell (RGC) axon bundles throughout the nerve fiber layer of the retina and the optic nerve, but there was no discernible expression of PKM1 by optic nerve glia (Fig. 2). Double-labeling experiments revealed that PKM1 colocalized with calretinin in the GCL and INL (Fig. 3). Calretinin-positive neurons are reported to be subsets of both amacrine cells and RGCs.[20] Pyruvate kinase M1 expression by RGCs and their

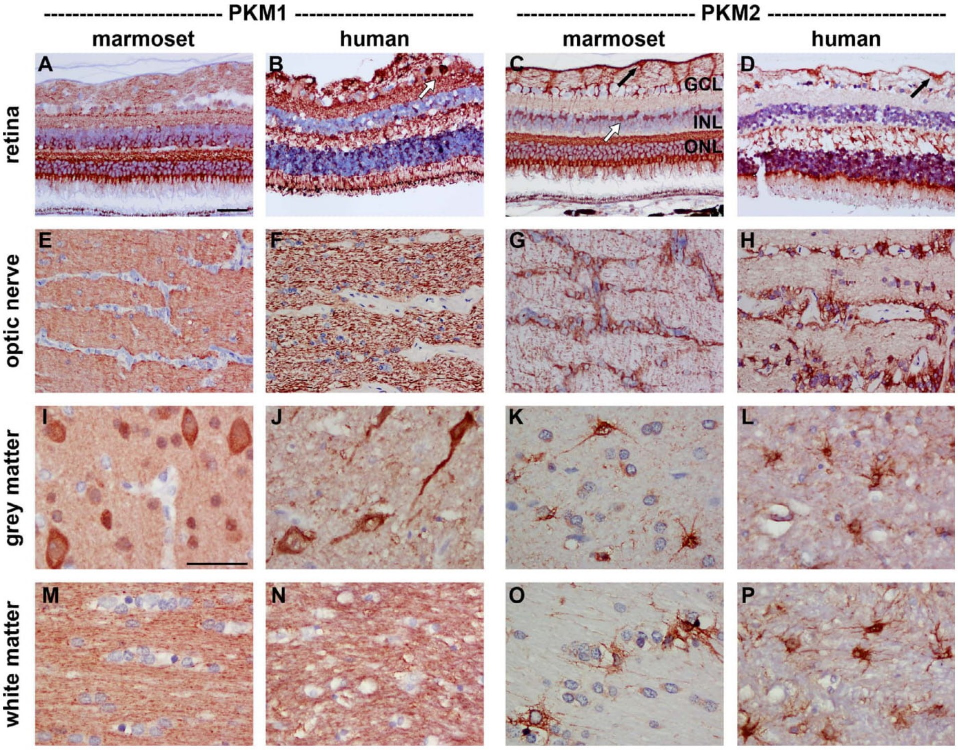

FIGURE 4. Representative images of PKM1 and PKM2 immunolabeling in marmoset and human tissues. In the marmoset and human retina, PKM1 is widely distributed, with positive labeling evident in the GCL (*arrow*), INL, and ONL, both plexiform layers, and nerve fiber layer (**A**, **B**). Pyruvate kinase M1 labels axon bundles in marmoset and human optic nerve (**E**, **F**). In marmoset and human brain, PKM1 is associated with neurons in gray matter (**I**, **J**) and axon bundles in white matter (**M**, **N**). In marmoset and human retina, PKM2 is restricted to photoreceptors (**C**, **D**), astrocytes (*black arrows*), and Müller cells (*white arrow*). In marmoset and human optic nerve (**G**, **H**), gray matter (**K**, **L**), and white matter (**O**, **P**), PKM2 is associated with astrocytes. *Scale bars*: 50 μm (**A**–**H**), 25 μm (**I**–**P**).

axons, as well as that of amacrine cells, was confirmed by colocalization with β_3-tubulin, Brn3a, and parvalbumin (data not shown). Notably, PKM1 did not colocalize with glutamine synthetase (Fig. 3) or S100 (data not shown), indicating a lack of discernible expression by Müller cells and astrocytes. In the mouse brain, PKM1 was localized to neurons in gray matter and axon bundles in white matter (Fig. 2). As in the retina and optic nerve, there was no observable expression of PKM1 by glial cells (Fig. 2).

In marmosets and humans, Western blotting (Supplementary Fig. S2) and immunohistochemistry (Fig. 4) indicated expression of PKM1 in retina, optic nerve, and brain. The distribution of PKM1 was fundamentally analogous to that observed in the rodent, with positive labeling evident in neurons and their axons, but not in glia. It should be noted, however, that in the marmoset and human retina, unlike the rodent retina, PKM1 distribution was more widespread, encompassing neurons in the inner and outer part of the INL as well as photoreceptor somata and inner segments.

Pyruvate Kinase M1

Validation of Antibodies. Initial analysis of antibodies from two different commercial sources demonstrated that, although both of the antibodies detected a band of approximately the expected size of 60 kDa, the antibodies detected distinct bands of slightly different apparent size (Supplementary Fig. S3). Hence the Novus antibody (Supplementary Table S1) was not used in this study, but two antibodies from Cell Signaling (Supplementary Table S1) were used for subsequent experiments as they were generated using peptides specific for the region of PKM2 divergent from PKM1, and specificity was independently verified using short interfering RNA (siRNA)-based knockdown of PKM2.[21] Further analysis showed the two Cell Signaling antibodies recognized a protein of the expected size by Western blotting in testis (positive control tissue) (Supplementary Fig. S4) and retina but not in liver or skeletal muscle (negative control tissues). Both of the antibodies provided high signal-to-noise, cell-specific immunolabeling in mouse, rat, rabbit, monkey, and human tissue sections. Neither of the antibodies elicited positive labeling in extraocular

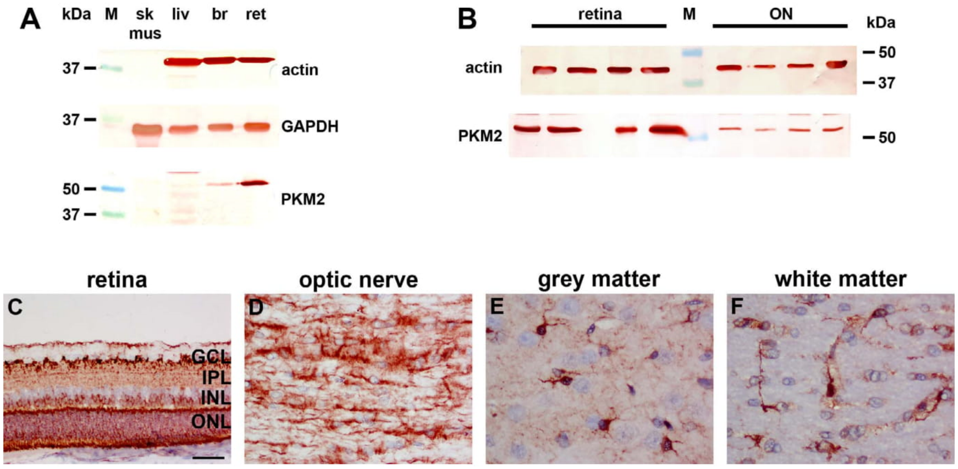

Figure 5. Analysis of PKM2 expression in rats. (**A**) Western blot analysis of PKM2 expression in rat tissues. Skeletal muscle (sk mus), liver (liv), brain (br), and retina (ret) tissue extracts probed for actin, GAPDH, and PKM2. Note the absence of actin and PKM2 in skeletal muscle, absence of PKM2 in liver, and low level of PKM2 in brain. (**B**) Evaluation of PKM2 expression in retina (lanes 1–4) and optic nerve (lanes 6–9) tissue extracts obtained from four different rats. Pyruvate kinase M2 is detectable in all samples but in greater amounts in the retina. (**C–F**) Representative images of PKM2 immunolabeling in rat tissues. In the retina, positive labeling for PKM2 is localized to a population of cells in the outer part of the INL and to photoreceptor cell bodies and their segments (**C**). In addition, PKM2 is associated with terminals in the IPL and to astrocytes (**C**). In the optic nerve, PKM2 is localized to cells with the morphology of astrocytes (**D**). In the brain, PKM2 is associated with astrocytes in gray matter (**E**) and white matter (**F**). *Scale bars*: 50 µm (**A**), 25 µm (**B–D**).

muscle (negative control), and incubation with preimmune serum alone also elicited no labeling. Patterns of immunolabeling of the two antibodies were indistinguishable. Thus, it can be concluded that, in all species, the data generated were specific to PKM2 (Figs. 1, 4, 5, 6, 7, 8).

mRNA and protein expression and immunolocalization. Relative to GAPDH expression, there was 6-fold greater expression of PKM2 mRNA in rat retina and 9-fold greater expression in mouse retina than that in cortex (Table 1). The abundance of the PKM2 transcript in the retina was evident by the low C_T findings in both mouse and rat ($C_T \sim 17$), less than 1 C_T greater than GAPDH. Consistent with mRNA data, PKM2 protein, as detected by Western blotting, was highly expressed in retinal samples and barely detectable in cortex (Figs. 1A, 5A). Analysis of retina and optic nerve samples from four rats and mice revealed PKM2 expression in all samples but much fainter bands in optic nerve samples (Figs. 1B, 5B).

Distribution of PKM2 in rodent retina contrasted markedly with that of PKM1. In both rats (Fig. 5) and mice (Fig. 6), robust labeling of PKM2 was evident in photoreceptor cell bodies and their inner and outer segments. Double-labeling experiments showed that PKM2 colocalized with rhodopsin (Fig. 3). Pyruvate kinase M2 was also associated with a population of cells in the outer part of the INL, in the histoanatomical location of bipolar cells, together with terminals in the IPL. Confirmation that these cells were bipolar cells was achieved by successful colocalization of PKM2 with the optic nerve bipolar cell marker PKCα (Fig. 3). Pyruvate kinase M2 was not associated with RGC axons in the nerve fiber layer of the retina nor in the optic nerve but was localized to astrocytes. Analogous to PKM1, PKM2 did not colocalize with glutamine synthetase (Fig. 3) or S100 (data not shown) in the INL, indicating a lack of discernible expression by Müller cells. Importantly, 5-fold dilution of the PKM2 antibody eliminated all labeling, with the exception of that associated with photoreceptors, suggesting that photoreceptors express higher levels of PKM2 than other retinal cells (data not shown). In the rodent brain, PKM2 was exclusively associated with astrocytes, in both gray and white matter (Figs. 5, 6).

It has been suggested that PKM2 expression in the retina is restricted to photoreceptors.[14] To corroborate our finding of PKM2 expression by nonrod photoreceptors, we analyzed 8-week-old rd1 mice, which feature completely degenerated rod photoreceptors but some residual M-, L-, and S-cone photoreceptors (Supplementary Fig. S5). First, we probed retinal extracts from rd1 mice and age-matched C57BL/6 (wild-type) mice for rhodopsin kinase, calretinin, PKM1, and PKM2 by Western blotting. Compared with wild-type retinas, there was an absence of rhodopsin kinase, as expected, and a lower but still clearly detectable amount of PKM2 in *rd1* retinas (Fig. 7A). Subsequently, we performed immunohistochemistry using tissue sections and showed, as expected, unambiguous PKM2 labeling of bipolar cells, astrocytes, and probably cones in both rd1 and wild-type retinas (Figs. 7B, 7C). The rod-dominant rodent retina, however, is not ideal for demonstrating that cones express PKM2. Moreover, although residual cones are present within the rd1 retina, they may well not be metabolically normal. Thus, to firmly establish whether cones express PKM2, we used primate retina (see below).

In marmosets and humans, Western blotting (Supplementary Fig. S2) and immunohistochemistry (Fig. 4) indicated expression of PKM2 in retina, optic nerve, and brain. Distribution of PKM2 was broadly similar to that observed in rodent, with positive labeling in the retina associated with photoreceptors and astrocytes and in the optic nerve and brain exclusively with astrocytes. Nevertheless, some differences were apparent with regard to retinal expression compared with that in rodents: first, in the marmoset, PKM2 was not

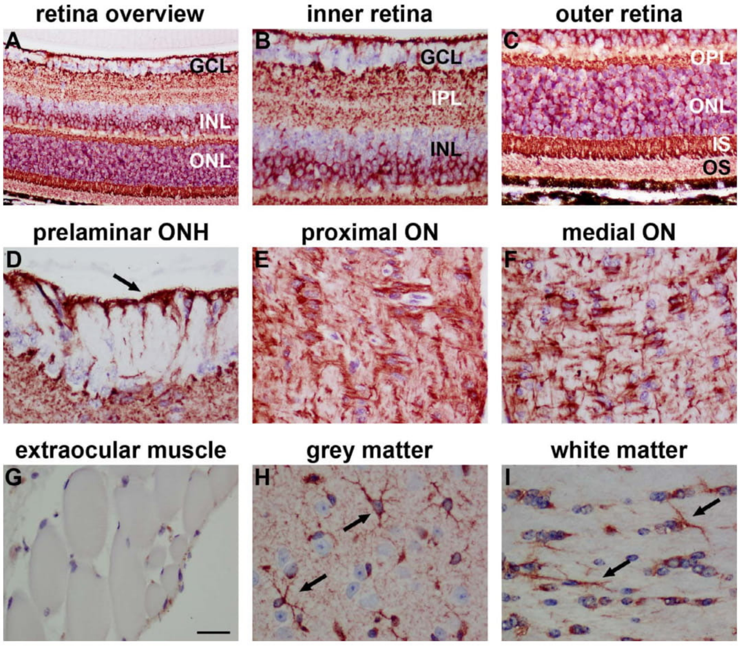

FIGURE 6. Representative images of PKM2 immunolabeling in mouse tissues. In the retina, positive labeling for PKM2 is localized to a population of cells in the outer part of the INL and to photoreceptor cell bodies and their segments (**A**–**C**). In addition, PKM2 is associated with terminals in the IPL (**A**, **B**) and to astrocytes ([**A**, **B**, **D**] *arrows*). Pyruvate kinase M2 is not associated with RGC axons in the nerve fiber layer of the retina or the optic nerve (**D**–**F**) but is localized to cells with the morphology of astrocytes (**D**–**F**). Pyruvate kinase M2 is not expressed by extraocular muscle (**G**). In the brain, PKM2 is associated with astrocytes in gray matter ([**H**] *arrows*) and white matter ([**I**] *arrows*). *Scale bars*: 50 μm (**A**), 25 μm (**B**–**I**).

expressed by neurons in the outer part of the INL, a finding that might be expected given the presence of PKM1 in these cells in the marmoset (Fig. 4); second, PKM2 was weakly but unambiguously associated with Müller cells (Figs. 4, 7; Supplementary Fig. S6). In order to shed light on PKM isoenzyme expression in cones, we examined distributions of PKM1 and PKM2 in the cone-rich parafovea of the marmoset. Data showed robust expression of both PKM1 and PKM2 by cone axons in Henle's fiber layer by photoreceptor somata and by cone inner segments, whereas double-labeling experiments showed that both isoenzymes colocalized with the cone marker peanut agglutinin (Figs. 7D–H).

Quaternary Forms of PKM2 in Retina. Structurally, both PKM1 and PKM2 exist as homotetramers, configurations which favor glycolytic flux. A major functional difference between PKM1 and PKM2, however, is that the latter isoform harbors a binding site for fructose-1,6-bisphosphate, which serves as an allosteric modulator and causes the PKM2 tetramer to dissociate to a dimer. Dimeric PKM2 is much less efficient at converting phosphoenolpyruvate to pyruvate, and its presence therefore slows the rate of glycolytic flux; the resultant accumulation of upstream glycolytic intermediates are then available for use in anabolic reactions. The presence of a dimeric form of PKM2 within a cell, therefore, implies a reduced rate of glycolysis and an increased level of biosynthesis derived from glycolytic intermediates. With this in mind, we analyzed the relative levels of quaternary forms of PKM2 in the rat retina using a crosslinking protein-immunoblotting approach. This clearly resolved the monomeric protein at the expected molecular weight (~60 kDa). In retinal samples subjected to the cross-linking reaction, protein species were also present at molecular masses which corresponded to both dimeric (~120 kDa) and tetrameric (~240 kDa) forms (Fig. 8).

Lactate Dehydrogenase A

Validation of Antibodies. Two commercial antibodies, raised against human LDH-A (Supplementary Table S1), clearly recognized a protein of the expected size (~35 kDa) by Western blotting in skeletal muscle and liver (positive control tissues) as well as retina, optic nerve and brain. Both antibodies provided high signal to noise, cell-specific immunolabeling in mouse, rat, rabbit, monkey, and human tissue sections, including staining of extraocular muscle (positive control), while incubation with preimmune serum alone also elicited no signal. The patterns of immunolabeling of the two antibodies were alike. Thus, it can be concluded that in all species, the data generated are specific to LDH-A (Figs. 9, 10, 11, 12; Supplementary Fig. S7).

mRNA and Protein Expression and Immunolocalization. Lactate dehydrogenase A was expressed in large amounts in retina of mice and rats, with cycle thresholds of ~18 cycles. There was an approximately 2.5-fold greater expression of LDH-A mRNA in rat and mouse retinas than in cortex after

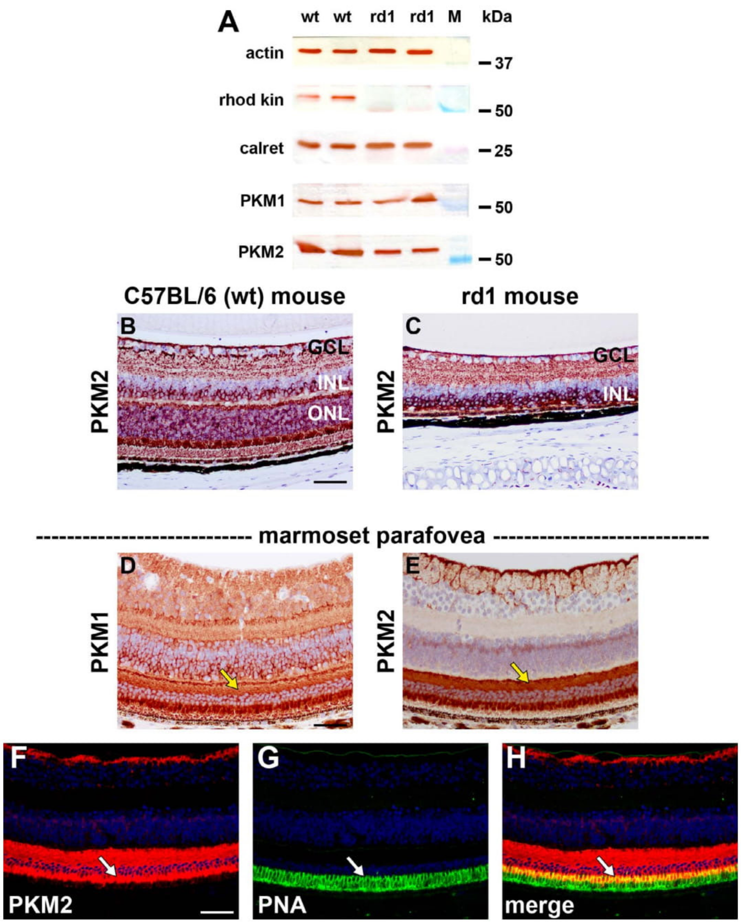

FIGURE 7. Analysis of PKM2 expression in mice lacking photoreceptors and in parafovea of the marmoset. (**A**) Retinal extracts from 8-week-old C57BL/6 (wild-type [wt]) and age-matched rd1 mice were probed for actin, rhodopsin kinase (rhod kin), calretinin (calret), PKM1, and PKM2 by Western blotting. Note the absence of rhodopsin kinase and the relatively lower level of PKM2 in Rd1 retinas. (**B**, **C**) Representative images of PKM2 immunolabeling in mouse retinas from 8-week-old C57BL/6 wt and age-matched rd1 mice. Both retinas display identical patterns of immunolabeling, except that rd1 mice lack a photoreceptor layer. (**D**, **E**) Representative images of PKM1 and PKM2 immunolabeling in the marmoset parafovea. Positive labeling is associated with cone axons in Henle's fiber layer (*yellow arrows*), photoreceptor somata in the outer nuclear layer, and cone inner segments. Double labeling immunofluorescence showed that PKM2 colocalized with the cone marker peanut agglutinin in inner segments ([**D**–**H**] *white arrows*). *Scale bars*: 25 μm. PNA, peanut agglutinin lectin.

normalization by GAPDH (Table 1). Consistent with this pattern, LDH-A protein, as detected by Western blotting, was more highly expressed in retina than in cortex (Fig. 9). Analysis of retina and optic nerve samples from four rats and mice revealed LDH-A expression in all samples but much fainter bands in the optic nerve samples (Fig. 9B; Supplementary Fig. S7).

The distribution of LDH-A in rodent retina paralleled that of PKM2 in many respects. Thus, in both rats (Fig. 10) and mice (data not shown), robust labeling of LDH-A was evident in photoreceptor cell bodies and their inner and outer segments. Lactate dehydrogenase A was likewise associated with bipolar cell bodies in the INL, together with their terminals in the IPL (Figs. 10, 11A–C). Lactate dehydrogenase A also did not colocalize with S100-positive Müller cells (Figs. 11A–C). Double labeling of PKM2 and LDH-A revealed the expected colocalization in photoreceptors and bipolar cells (Figs. 11G–I). Unlike PKM2, weak LDH-A immunoreactivity was associated with some cells, putatively amacrine cells, in the inner part of the INL.

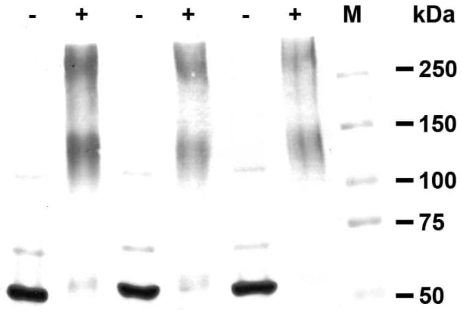

Figure 8. Relative levels of quaternary forms of PKM2 in rat retina, determined by using a cross-linking protein-immunoblotting approach (see Methods). Three individual retina homogenates were each split into 2 equal parts; 1 part was treated with the cross-linking reagent DSS (+), while the other was treated with vehicle (–). In vehicle-treated samples, there was clear resolution of monomeric PKM2 at the expected molecular weight (~60 kDa). In retinal samples subjected to the cross-linking reaction, protein species were also present at molecular masses that corresponded to both dimeric (~120 kDa) and tetrameric (~240 kDa) forms of PKM2.

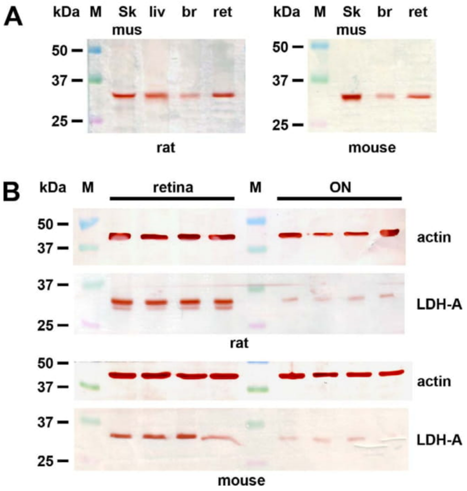

Figure 9. Western blot analysis of LDH-A expression in rat and mouse tissues. (**A**) Skeletal muscle (sk mus), liver (liv), brain (br), and retina (ret) tissue extracts probed for LDH-A. Note the lower level of LDH-A in brain samples. (**B**) Evaluation of LDH-A expression in retina (lanes 1–4) and optic nerve (lanes 6–9) tissue extracts obtained from 4 different rats and 4 different mice. Lactate dehydrogenase A is detectable in all samples but in much greater amounts in the retina.

Moreover, unlike PKM2, LDH-A did not localize to retinal or optic nerve astrocytes (Fig. 10). In the optic nerve, LDH-A expression was low with minimal expression by glial cells and indeterminate labeling of axons (Fig. 10).

In the marmoset retina (Fig. 12), LDH-A was very strongly expressed by photoreceptor cell bodies and their segments. Lactate dehydrogenase A labeling was also associated with a population of cells in the central part of the INL. These cells are not Müller cells as LDH-A failed to colocalize with CRALBP-positive Müller cells. Finally, weak LDH-A immunoreactivity was detectable in the GCL. In the optic nerve, LDH-A was not associated with glial cells, but axon bundles were lightly stained. The pattern of LDH-A immunolabeling in the human retina and optic nerve was similar to that observed in the marmoset, although the GCL and nerve fiber layer were more robustly labeled (Fig. 12).

PKM1, PKM2, and LDH-A Expression in Avascular Retina

As a final experiment, we investigated distribution patterns of LDH-A, and PKM1 and -2 in rabbit. Unlike rodents or primates, the rabbit has an avascular retina. Any differences between the vascular and avascular retina will impart a valuable perspective to the role of PKM and LDH-A in the retina. Data showed that distribution patterns of PKM1 in the avascular rabbit retina was analogous to those described in vascular retinas, namely expression by inner retinal neurons, photoreceptors, and axonal fibers in the optic nerve but negligible association with retinal or optic nerve glia (Supplementary Fig. S8). The distribution of PKM2 also displayed similarities in both avascular and vascular tissues, namely expression by photoreceptors and retinal and optic nerve glia. Nevertheless, PKM2 appears to be somewhat more abundant in the inner retina, notably Müller cell processes, of the rabbit and slightly less abundant in the outer retina compared to vascular retinas (Supplementary Fig. S8). The distribution of LDH-A showed the most marked dissimilarity between vascular and avascular retinas, being abundant in neurons and glia in the inner retina, but seemingly lacking in rod photoreceptors (Supplementary Fig. S8).

Discussion

The current study has demonstrated that PKM2 is abundantly expressed in the photoreceptors of mammalian species including humans. Our findings complement those of Lindsay et al.,[14] who likewise showed expression of PKM2 by rodent photoreceptors. The PKM2 and LDH-A expression profile of photoreceptors is typical of proliferating normal and neoplastic cells rather than terminally differentiated neurons. The metabolic implication of this isoenzyme pattern is that the cell has both large energy and biosynthesis demands that can only be met by a high glycolytic rate even in the presence of oxygen. To our knowledge, retinal photoreceptors are the only nondividing adult cell type to display this pattern.

There are four known isoforms of PK in mammalian cells encoded by two genes, *PKLR* and *PKM*. PKLR is expressed in the liver and erythrocytes. The PKM isoforms PKM1 and PKM2 are alternative splice products of the *PKM* gene. Christofk et al.[22] reported that the switch from expression of physiological PKM1 to PKM2 in cancer cells was responsible for the Warburg effect. However, Bluemlein et al.[23] undermined this conclusion by using proteomics to definitively show that PKM2 was present in tumors and normal control tissue. Subsequently, Luo et al.[24] combined these observations into a coherent explanation by reporting that the Warburg effect in cancer (HeLa) cells was mediated via PKM2 serving as a coactivator of hypoxia-inducible factor-1α (HIF-1α). They showed that prolyl hydroxylation of PKM2 promotes the interaction of PKM2 with HIF-1α, thereby stabilizing HIF-1α binding to the hypoxia response elements of target genes, including LDH-A. They suggested that

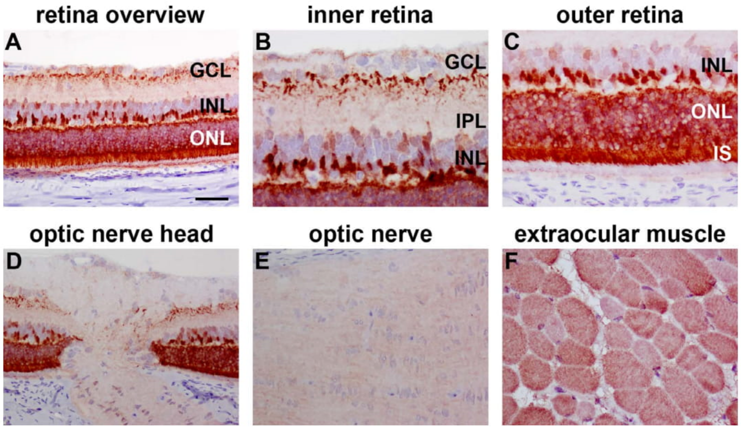

Figure 10. Representative images of LDH-A immunolabeling in rat retina and optic nerve. In the retina (**A–C**), positive labeling for LDH-A is localized to a population of cells, putatively bipolar cells, in the outer part of the INL together with terminals in the IPL. Lactate dehydrogenase A is also strongly expressed by photoreceptor cell bodies and their segments. Finally, weaker LDH-A labeling is associated with some cells in the inner part of the INL. Lactate dehydrogenase A is not localized to retinal astrocytes (**A**, **B**, **D**). In the optic nerve (**D**, **E**), LDH-A expression is low with minimal expression by axons and glial cells. As expected, LDH-A is expressed by extraocular muscle (**F**). *Scale bars*: 50 μm (**A**, **D**), 25 μm (**B**, **C**).

these molecules are not expressed together under physiological conditions in most tissues but occur in cancers due to the frequent presence of hypoxia and/or other HIF stabilization factors. Recent studies have demonstrated that PKM2 has nonmetabolic, epidermal growth factor–dependent actions that can promote tumorigenesis and the Warburg effect in certain cancer cell lines.[25–27] Other factors, particularly the oncogene c-Myc for which PKM2 can also serve as a transcriptional coactivator, are also mediators of the Warburg effect in some neoplastic cells. However, the emerging evidence indicates that PKM2 is a master regulator of the Warburg effect in cancer.[28,29]

With occasional exceptions,[30,31] cancer research reports are replete with references to PKM2 as “tumor specific” or as representing the “oncofetal” form of PK, which is replaced by PKM1 in adult tissue, despite the original report of PK isoenzymes demonstrating PKM2 in normal adult tissues (the retina was not studied),[32] and the recent report by Bluemlein et al.[23] demonstrating PKM2 in normal adult control tissues. Clearly, PKM2 is not tumor-specific. Recent strategies to target PKM2 as a novel cancer therapy[33] should proceed cautiously and at least include ophthalmic assessment in phase I trials.[34]

Although the changing quaternary structure of PKM2 regulates the flow of glycolysis and is under allosteric control by upstream glycolytic intermediates[12] and serine,[13] provided the cell has pyruvate, the catalytic activity of PKM2 is theoretically not a fundamental requirement for the Warburg effect (the production of lactate under aerobic conditions). Conversion of pyruvate to lactate in the cytosol rather than the entry of pyruvate into mitochondria, despite the presence of oxygen, is the fundamental requirement. Hence, biosynthesis demands are a plausible explanation but not a logical necessity for the existence of the Warburg effect. In fact, recent mathematical modeling that accounts for space limitations within the cell (and the large volume occupied by mitochondria relative to glycolytic enzymes) finds that a high glycolytic rate optimizes ATP production when glucose is abundant.[35] This finding explains the presence of the Warburg effect with glycolytic ATP production (and lactate production) in highly active skeletal muscle (which does not contain PKM2) when oxygen is not limiting.[36] The factors forcing conversion of pyruvate to lactate in this situation are not clear. Although cellular biosynthesis and PKM2 are not fundamental requirements for the Warburg effect, the convergence of evidence indicates that PKM2 has important roles in regulating the Warburg effect in cells with large biosynthesis and energy demands.

Pyruvate kinase M1 was confined to neurons and axons in the retina and brain in a pattern consistent with nonproliferating cells with a predominantly aerobic metabolism. X-ray crystallography has demonstrated that PKM1 exists as pairs of active dimers[37]; however, the isoform is not under allosteric control by glycolytic intermediates.[12] In contrast, PKM2 is believed to exist as an active tetrameric form and a relatively inactive dimeric form, termed M2-PK.[38] The presence of the dimeric form of PKM2 within a cell implies a reduced rate of glycolysis and an increased level of biosynthesis derived from glycolytic intermediates. Antibodies to “tumor M2-PK” are commercially available and are used in diagnostic testing of cancer; however, to our knowledge, the specificity of this antibody to the proposed dimeric form has not been validated. In our hands, tumor M2-PK antibody yielded data that are consistent with the antibody binding nonselectively to both PKM1 and PKM2 (data not shown). With this in mind, we investigated the quaternary forms of PKM2 in the rat retina using a crosslinking protein-immunoblotting approach. Using this methodology, we clearly demonstrated the dimeric form in retina. Hence, it seems likely that PKM2 is under allosteric control by fructose-1,6-biphosphate in the mammalian retina in a similar manner to proliferating tissue.[12]

As well as photoreceptors, PKM2 also colocalized with bipolar cells in the rodent retina and astrocytes in the retina, optic nerve, and brain. Interestingly, we could not demonstrate either PKM1 or PKM2 localization to retinal Müller cells in rats or mice. Our data are consistent with those of recent findings by Lindsay et al.,[14] who observed the same phenomenon in mice. In a comprehensive series of experiments they described novel metabolic pathways between retinal neurons and Müller

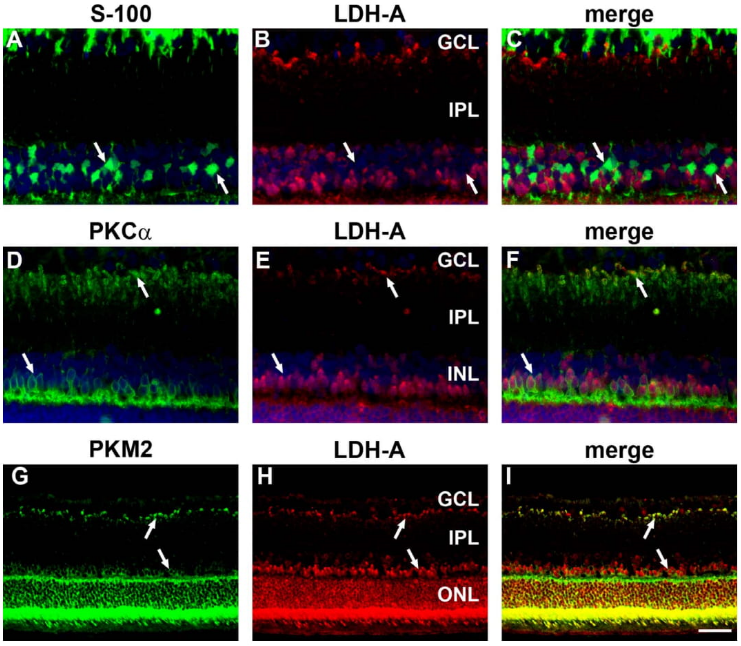

FIGURE 11. Double labeling immunofluorescence of LDH-A in rat retina. Lactate dehydrogenase A is not associated with S100-positive Müller cells ([**A–C**] *arrows*). In contrast, LDH-A colocalizes with some PKCα-positive bipolar cell bodies in the INL and their terminals adjacent to the GCL ([**D–F**] *arrows*). Expression of LDH-A overlaps considerably with that of PKM2, with colocalization in photoreceptors as well as in bipolar cell bodies and their terminals ([**G–I**] *arrows*). *Scale bars*: 25 µm (**A–F**); 50 µm (**G–I**).

cells deficient in pyruvate kinase.[14] However, our results show that PKM2 is expressed by Müller cells in marmosets, albeit at a considerably lower level than in photoreceptors, suggesting species differences in Müller cell metabolism. An evolutionary difference was also apparent with regard to bipolar cells: PKM2 was present in rodent bipolar cells, but primate bipolar cells expressed PKM1. The biosynthesis demands of the bipolar cells are likely to be less than the photoreceptors, and unlike astrocytes bipolar cells do not have the capacity to proliferate. Accordingly, an explanation for why rodent bipolar cells have a glycolytic enzyme pattern that is different to the pattern found in brain neurons and inner retinal neurons (amacrine cells, retinal ganglion cells) is not immediately apparent.

A limitation of the current study is that we did not obtain data at different times during the light/dark cycle. Hence, we have a static picture of the isoenzyme pattern. It is possible that this pattern or relative amounts of isoenzyme would fluctuate with disc shedding rates.[39] However, Lindsay et al.[14] recently reported that the pattern of PKM2 expression in mice was not affected by light; thus, it appears unlikely that a major diurnal change exists.

Lactate dehydrogenase is a tetrameric enzyme comprising two major subunits A and/or B, (encoded by the *Ldh-A* and *Ldh-B* genes, respectively) resulting in five isoenzymes (A4, A3B1, A2B2, A1B3, and B4) that catalyze the forward and backward conversion of pyruvate to lactate. Lactate dehydrogenase A (LDH-5, M-LDH, or A4) is the predominant form in skeletal muscle. Lactate dehydrogenase B (LDH-1, H-LDH, or B4) is found in heart muscle. Lactate dehydrogenase was one of the first enzymes recognized to have different isoforms,[40] and since their discovery, they have been conceptualized as having different physiological roles based on different enzyme kinetics: LDH-A predominantly catalyzing pyruvate to lactate, and critical for the Warburg effect, and LDH-B catalyzing the reverse reaction and predominating in well-oxygenated tissues. Lactate dehydrogenase enzyme kinetics have been widely studied, but reports are inconsistent, and simplistic notions that their kinetics affect physiological roles at equilibrium have recently been challenged.[41] However, under conditions of high glycolytic flux, varying kinetics are likely to significantly affect function,[41] and it would appear that LDH-A is a *sine qua non* for the Warburg effect.

In 1964, Graymore[42] noted that the expression of the LDH-A isoenzyme in the retina was reduced in rats with inherited "retinitis pigmentosa," characterized pathologically by loss of the photoreceptors. This observation was interpreted to imply that the photoreceptors were principally responsible for the retinal lactate production. This supported earlier evidence that the photoreceptors were particularly susceptible to glycolytic inhibition.[8] Similarly, Acosta et al.[43] demonstrated a high expression of LDH-A in mouse retina, in contrast to the minimal expression in brain. They noted that the high expression rate was lost in *rd1* mice after the onset of photoreceptor degeneration.[43] These observations were drawn from immunoblots, and almost all metabolic evidence for the

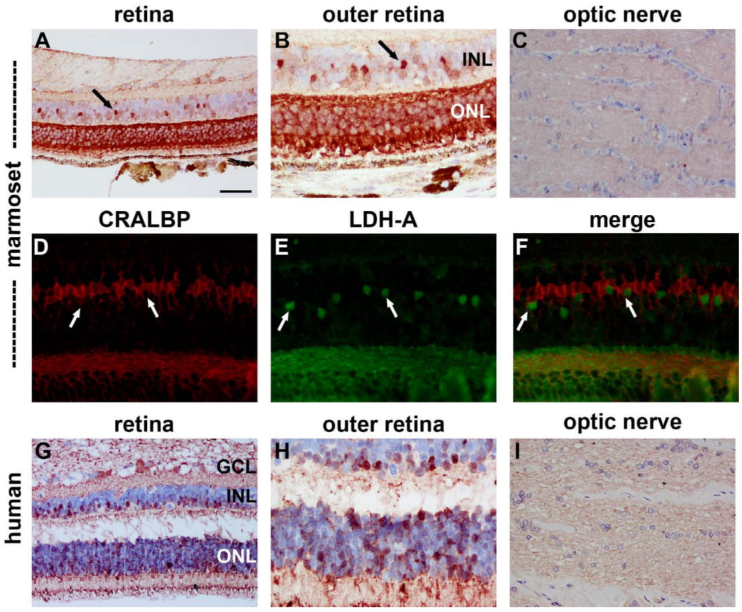

Figure 12. Representative images of LDH-A immunolabeling in marmoset and human retina and optic nerve. In marmoset retina, LDH-A is strongly expressed by photoreceptor cell bodies and their segments (**A**, **B**). Lactate dehydrogenase A labeling is also associated with a population of cells in the central part of the INL ([**A**, **B**] *black arrows*). These cells are not Müller cells as LDH-A fails to colocalize with CRALBP ([**D–F**] *white arrows*). Weak LDH-A immunoreactivity was detectable in the GCL (**A**). In the optic nerve, LDH-A was not associated with glial cells, but axon bundles were weakly positive (**C**). The pattern of LDH-A immunolabeling in the human retina and optic nerve was similar to that observed in the marmoset, although the GCL and nerve fiber layer were more robustly labeled (**G–I**). *Scale bars*: 50 μm (**A**, **C**, **G**, **I**), 25 μm (**B**, **D–F**, **H**).

Warburg effect in the retina comes from experiments on whole retinas, with no discrimination between the different retinal layers. Researchers have obtained some information about the relative glycolytic versus oxidative phosphorylation contribution of the outer retina compared to the inner retina from electrophysiological studies in the presence of retinal ischaemia,[4,44,45] but an understanding of retinal metabolism remains far from complete. Our results indeed confirm the hypothesis that photoreceptors express high levels of LDH-A. This was true for all species analyzed. Lactate dehydrogenase A, however, was not restricted to photoreceptors. Other neuronal classes, such as bipolar cells and, to a lesser degree, amacrine cells were also LDH-A-positive in certain species. In contrast, neither astrocytes nor Müller cells were associated with LDH-A immunolabeling in any species, suggesting that neither of these cell types produce significant quantities of lactate. Similarly in the optic nerve, LDH-A was not expressed by astrocytes or oligodendrocytes.

To impart perspective to our results, we explored the distribution patterns of LDH-A and PKM1 and -2 in the rabbit. Unlike rodents or primates, the rabbit has an avascular retina. Moreover, glycogen storage is abundant in the inner layers of the rabbit retina, and particularly concentrated in Müller cells, but is very limited in the rat or mouse.[46] Our results showed some discrepancies between avascular and vascular retinas, most notably concerning LDH-A, which was abundant in the inner retina but sparse in rod photoreceptors of the rabbit, results contradictory to those obtained in vascular retinas. These data agree with those of Ames et al.,[47] who investigated the energy requirements of the rabbit retina and concluded

Table 2. Relative Levels of PKM1, PKM2, and LDH-A Immunolabeling in Different Cell Rodent and Primate Populations

	Rodent			Primate		
Tissue	PKM1	PKM2	LDH-A	PKM1	PKM2	LDH-A
Inner retinal neurons	+++	+	+	+++	++	+
Photoreceptors	++	+++	+++	++	+++	+++
Retinal glia	−	+	−/+	−	++	−/+
Brain neurons	+++	−	ND	+++	−	ND
Brain glia	−	++	ND	−	++	ND

ND, not determined.

that the inner retina was supported almost entirely by anaerobic glycolysis to lactate, whereas the outer retina was normally supported by oxidative metabolism. Our results are also consistent with those of Poitry-Yamate et al.,[48] who showed that in the avascular guinea pig retina, Müller cells produce lactate that is released and metabolized by photoreceptors. Overall, then, it appears that in the avascular inner retina, the abundant supply of glycogen is metabolized to lactate via LDH-A, whereas the photoreceptors have minimal LDH-A and therefore likely do not produce lactate themselves. In contrast, in the vascular retina, photoreceptors have a high glycolytic rate and produce large quantities of lactate, presumably via their high level of LDH-A, whereas the inner retina is largely oxidative.

In conclusion, we characterized the cell-specific localization of PKM1, PKM2, and LDH-A in the retina of five mammalian species. An overview of the relative levels of PKM1, PKM2, and LDH-A immunolabeling in the different cell rodent and primate populations is shown in Table 2. The most striking finding was the consistently high expression of PKM2 in the photoreceptors across all species in a pattern similar to that reported in neoplastic tissue. Gardner et al.[49] recently showed the importance of glycolysis in retinal protein synthesis and uncovered an interaction between glycolysis and Akt/mTOR-regulation of anabolic pathways. Although Lindsay et al.[14] found no incorporation of radiolabelled glucose into serine in murine retinal explants over a 6-hour period, we propose that the prodigious biosynthesis requirements associated with in vivo disc shedding and turnover of opsin underpin the isoenzyme pattern we have observed. The cellular requirement for both energy and biomass production would explain the existence of the Warburg effect in the photoreceptors. Our findings suggest that photoreceptor metabolism may use PKM2 as the "molecular switch" between energy production and biomass production. The presence of PKM2 in rod photoreceptors of the avascular retina supports this hypothesis, but the relative lack of LDH-A in the same cell type casts some doubt on the universal requirement of aerobic glycolysis for photoreceptor homeostasis.

Acknowledgments

Supported by National Health and Medical Research Council Grant 626964 and the Ophthalmic Research Institute of Australia. The authors alone are responsible for the content and writing of the paper.

Disclosure: **R.J. Casson**, None; **J.P.M. Wood**, None; **G. Han**, None; **T. Kittipassorn**, None; **D.J. Peet**, None; **G. Chidlow**, None

References

1. Ng SK, Wood JP, Chidlow G, et al. Cancer-like metabolism of the mammalian retina. *Clin Experiment Ophthalmol*. 2015;43: 367–376.
2. Wong-Riley MT. Energy metabolism of the visual system. *Eye Brain*. 2010;2:99–116.
3. Young RW. The renewal of photoreceptor cell outer segments. *J Cell Biol*. 1967;33:61–72.
4. Winkler BS. Glycolytic and oxidative metabolism in relation to retinal function. *J Gen Physiol*. 1981;77:667–692.
5. Wind F. *The Metabolism of Tumors: Investigations from the Kaiser Wilhelm Institute for Biology.* Warburg O, ed. Berlin-Dahlem: Constable & Co. Ltd., 1930;282.
6. Graymore C, Tansley K. Iodoacetate poisoning of the rat retina. II. Glycolysis in the poisoned retina. *Br J Ophthalmol*. 1959;43:486–493.
7. Graymore C, Tansley K. Iodoacetate poisoning of the rat retina. I. Production of retinal degeneration. *Br J Ophthalmol*. 1959;43:177–185.
8. Noell WK. The impairment of visual cell structure by iodoacetate. *J Cell Physiol*. 1952;40:25–55.
9. Miao P, Sheng S, Sun X, Liu J, Huang G. Lactate dehydrogenase A in cancer: a promising target for diagnosis and therapy. *IUBMB Life*. 2013;65:904–910.
10. Vander Heiden MG, Cantley LC, Thompson CB. Understanding the Warburg effect: the metabolic requirements of cell proliferation. *Science*. 2009;324:1029–1033.
11. Mazurek S. Pyruvate kinase type M2: a key regulator of the metabolic budget system in tumor cells. *Int J Biochem Cell Biol*. 2011;43:969–980.
12. Jurica MS, Mesecar A, Heath PJ, Shi W, Nowak T, Stoddard BL. The allosteric regulation of pyruvate kinase by fructose-1,6-bisphosphate. *Structure*. 1998;6:195–210.
13. Chaneton B, Hillmann P, Zheng L, et al. Serine is a natural ligand and allosteric activator of pyruvate kinase M2. *Nature*. 2012;491:458–462.
14. Lindsay KJ, Du J, Sloat SR, et al. Pyruvate kinase and aspartate-glutamate carrier distributions reveal key metabolic links between neurons and glia in retina. *Proc Natl Acad Sci U S A*. 2014;111:15579–15584.
15. Morohoshi K, Ohbayashi M, Patel N, Chong V, Bird AC, Ono SJ. Identification of anti-retinal antibodies in patients with age-related macular degeneration. *Exp Mol Pathol*. 2012;93:193–199.
16. Chidlow G, Daymon M, Wood JP, Casson RJ. Localization of a wide-ranging panel of antigens in the rat retina by immunohistochemistry: comparison of Davidson's solution and formalin as fixatives. *J Histochem Cytol*. 2011;59:884–898.
17. Chidlow G, Holman MC, Wood JP, Casson RJ. Spatiotemporal characterization of optic nerve degeneration after chronic hypoperfusion in the rat. *Invest Ophthalmol Vis Sci*. 2010;51: 1483–1497.
18. Chidlow G, Wood JP, Casson RJ. Expression of inducible heat shock proteins Hsp27 and Hsp70 in the visual pathway of rats subjected to various models of retinal ganglion cell injury. *PLoS One*. 2014;9:e114838.
19. Chidlow G, Wood JP, Manavis J, Osborne NN, Casson RJ. Expression of osteopontin in the rat retina: effects of excitotoxic and ischemic injuries. *Invest Ophthalmol Vis Sci*. 2008;49:762–771.
20. Haverkamp S, Wassle H. Immunocytochemical analysis of the mouse retina. *J Comp Neurol*. 2000;424:1–23.
21. Goldberg MS, Sharp PA. Pyruvate kinase M2-specific siRNA induces apoptosis and tumor regression. *J Exp Med*. 2012;209: 217–224.
22. Christofk HR, Vander Heiden MG, Harris MH, et al. The M2 splice isoform of pyruvate kinase is important for cancer metabolism and tumour growth. *Nature*. 2008;452:230–233.
23. Bluemlein K, Gruning NM, Feichtinger RG, Lehrach H, Kofler B, Ralser M. No evidence for a shift in pyruvate kinase PKM1 to PKM2 expression during tumorigenesis. *Oncotarget*. 2011; 2:393–400.
24. Luo W, Hu H, Chang R, et al. Pyruvate kinase M2 is a PHD3-stimulated coactivator for hypoxia-inducible factor 1. *Cell*. 2011;145:732–744.
25. Yang W, Xia Y, Hawke D, et al. PKM2 phosphorylates histone H3 and promotes gene transcription and tumorigenesis. *Cell*. 2012;150:685–696.
26. Yang W, Zheng Y, Xia Y, et al. ERK1/2-dependent phosphorylation and nuclear translocation of PKM2 promotes the Warburg effect. *Nat Cell Biol*. 2012;14:1295–1304.

27. Yang W, Xia Y, Ji H, et al. Nuclear PKM2 regulates beta-catenin transactivation upon EGFR activation. *Nature*. 2011;480:118–122.
28. Wang HJ, Hsieh YJ, Cheng WC, et al. JMJD5 regulates PKM2 nuclear translocation and reprograms HIF-1alpha-mediated glucose metabolism. *Proc Natl Acad Sci U S A*. 2014;111:279–284.
29. Filipp FV. Cancer metabolism meets systems biology: pyruvate kinase isoform PKM2 is a metabolic master regulator. *J Carcinogenesis*. 2013;12:14.
30. Chaneton B, Gottlieb E. Rocking cell metabolism: revised functions of the key glycolytic regulator PKM2 in cancer. *Trends Biochem Sci*. 2012;37:309–316.
31. Israelsen WJ, Vander Heiden MG. Pyruvate kinase: function, regulation and role in cancer. *Semin Cell Dev Biol*. 2015;43:43–51.
32. Imamura K, Tanaka T. Multimolecular forms of pyruvate kinase from rat and other mammalian tissues. I. Electrophoretic studies. *J Biochem (Tokyo)*. 1972;71:1043–1051.
33. Yang W, Lu Z. Regulation and function of pyruvate kinase M2 in cancer. *Cancer Lett*. 2013;339:153–158.
34. Ng SK, Wood JP, Chidlow G, Peet DJ, Casson RJ. Potential adverse effects to the retina of cancer therapy targeting pyruvate kinase M2. *Acta Oncol*. 2015;54:136–137.
35. Vazquez A, Oltvai ZN. Molecular crowding defines a common origin for the Warburg effect in proliferating cells and the lactate threshold in muscle physiology. *PLoS One*. 2011;6:e19538.
36. Kemper WF, Lindstedt SL, Hartzler LK, Hicks JW, Conley KE. Shaking up glycolysis: sustained, high lactate flux during aerobic rattling. *Proc Natl Acad Sci U S A*. 2001;98:723–728.
37. McPherson A Jr, Rich A. Preliminary x-ray study of rabbit muscle pyruvate kinase. *J Biol Chem*. 1972;247:1334–1335.
38. Eigenbrodt E, Leib S, Kramer W, Friis RR, Schoner W. Structural and kinetic differences between the M2 type pyruvate kinases from lung and various tumors. *Biomed Biochim Acta*. 1983;42:S278–S282.
39. LaVail MM. Rod outer segment disk shedding in rat retina: relationship to cyclic lighting. *Science*. 1976;194:1071–1074.
40. Markert CL. Lactate dehydrogenase isozymes: dissociation and recombination of subunits. *Science*. 1963;140:1329–1330.
41. Quistorff B, Grunnet N. The isoenzyme pattern of LDH does not play a physiological role; except perhaps during fast transitions in energy metabolism. *Aging*. 2011;3:457–460.
42. Graymore C. Possible significance of the isoenzymes of lactic dehydrogenase in the retina of the rat. *Nature*. 1964;201:615–616.
43. Acosta ML, Fletcher EL, Azizoglu S, Foster LE, Farber DB, Kalloniatis M. Early markers of retinal degeneration in rd/rd mice. *Mol Vis*. 2005;11:717–728.
44. Bui BV, He Z, Vingrys AJ, Nguyen CT, Wong VH, Fortune B. Using the electroretinogram to understand how intraocular pressure elevation affects the rat retina. *J Ophthalmol*. 2013;2013:262467.
45. Tsai TI, Bui BV, Vingrys AJ. Effect of acute intraocular pressure challenge on rat retinal and cortical function. *Invest Ophthalmol Vis Sci*. 2014;55:1067–1077.
46. Kuwabara T, Cogan DG. Retinal glycogen. *Arch Ophthalmol*. 1961;66:680–688.
47. Ames A III, Li YY, Heher EC, Kimble CR. Energy metabolism of rabbit retina as related to function: high cost of Na+ transport. *J Neurosci*. 1992;12:840–853.
48. Poitry-Yamate CL, Poitry S, Tsacopoulos M. Lactate released by Muller glial cells is metabolized by photoreceptors from mammalian retina. *J Neurosci*. 1995;15:5179–5191.
49. Gardner TW, Abcouwer SF, Losiewicz MK, Fort PE. Phosphatase control of 4E-BP1 phosphorylation state is central for glycolytic regulation of retinal protein synthesis. *Am J Physiol Endocrinol Metab*. 2015;309:E546–E556.

7.3 Paper 3: HIF signalling: The eyes have it

Peet, D.J., Kittipassorn, T., Wood, J.P., Chidlow, G., and Casson, R.J. (2017). HIF signalling: The eyes have it. Experimental Cell Research 356, 136-140.

http://dx.doi.org/10.1016/j.yexcr.2017.03.030

Statement of Authorship

Title of Paper	HIF signalling: The eyes have it
Publication Status	☑ Published ☐ Accepted for Publication ☐ Submitted for Publication ☐ Unpublished and Unsubmitted work written in manuscript style
Publication Details	Peet, D.J., Kittipassorn, T., Wood, J.P., Chidlow, G., Casson, R.J., 2017. HIF signalling: The eyes have it. Exp Cell Res 356, 136-140.

Co-Author

Name of Co-Author (Candidate)	Thaksaon Kittipassorn		
Contribution to the Paper	Review and edited the manuscript. Helped with the manuscript outline and structure.		
Overall percentage (%)	10%		
Certification:	This is an original article, my contribution to which was made during the period of my Higher Degree by Research candidature and is not subject to any obligations or contractual agreements with a third party that would constrain its inclusion in this thesis. I am a co-author of this paper.		
Signature		Date	18/12/2018

Co-Author Contributions

By signing the Statement of Authorship, each author certifies that:

i. the candidate's stated contribution to the publication is accurate (as detailed above);
ii. permission is granted for the candidate in include the publication in the thesis; and
iii. the sum of all co-author contributions is equal to 100% less the candidate's stated contribution.

Name of Principal Author	Daniel J Peet		
Contribution to the Paper	Planned, wrote first draft, edited, revised and submitted the manuscript.		
Signature		Date	14/2/2019

Name of Co-Author	John PM Wood		
Contribution to the Paper	Reviewed and edited the manuscript.		
Signature		Date	190219

Name of Co-Author	Glyn Chidlow		
Contribution to the Paper	Reviewed and edited the manuscript.		
Signature		Date	19/2/19

Name of Co-Author	Robert J Casson		
Contribution to the Paper	Planned, reviewed and edited the manuscript.		
Signature		Date	18/12/2018

Experimental Cell Research 356 (2017) 136–140

Contents lists available at ScienceDirect

Experimental Cell Research

journal homepage: www.elsevier.com/locate/yexcr

HIF signalling: The eyes have it

D.J. Peet[a,*], T. Kittipassorn[a,b], J.P. Wood[c], G. Chidlow[c], R.J. Casson[c]

[a] School of Biological Sciences, University of Adelaide, Adelaide, South Australia, Australia
[b] Department of Physiology, Faculty of Medicine Siriraj Hospital, Mahidol University, Bangkok, Thailand
[c] South Australian Institute of Ophthalmology, University of Adelaide, Adelaide, South Australia, Australia

ARTICLE INFO

Keywords:
Hypoxia
Hypoxia inducible factors
Oxygen
Eye
Retina
Ischemia
Vasculature
Vascular endothelial growth factor

ABSTRACT

The hypoxia inducible factors (HIFs) promote changes in gene expression in response to hypoxia, and mediate key physiological responses such as angiogenesis. They play important roles in development and normal physiology, as well as in ischaemic and other pathologies. The human eye is a complex organ, with tight regulation of vascularisation and oxygen delivery, with the highly specialised retina containing both highly vascularised and avascular regions. This review, written to honour the significant contribution of Lorenz Poellinger to this field, covers the role of the HIFs in normal development of the eye, specifically the vasculature, as well as their roles in numerous retinal pathologies, including ischaemic retinopathies, and age-related macular degeneration (AMD). The characterisation of the HIFs in the eye has improved our understanding of the development, function, and numerous pathologies of the eye, and should inform future therapeutic approaches.

1. Introduction

Hypoxia-inducible factors (HIFs) are key regulators of the genomic response to hypoxia. They are ubiquitously expressed and play key roles in development, normal physiology and major human diseases [1]. The human eye is a complex organ interspersed with both highly vascular and avascular regions that are essential for visual function. Not surprisingly, the HIFs have been shown to have essential functions in numerous cells and tissues throughout the eye, and have also been implicated in many ophthalmologic pathologies, particularly in the retina.

2. Hypoxic signalling by the HIFs

The heterodimeric HIF transcription factors, members of the basic helix-loop-helix Per-Arnt-Sim (bHLH-PAS) family, are composed of an oxygen-regulated HIF-α subunit and a constitutively active aryl hydrocarbon receptor nuclear translocator (Arnt) subunit (also known as HIF-β) that form a functional HIF (reviewed in [1]). The HIF-α subunits are hydroxylated by three oxygen-dependent prolyl hydroxylases (PHD1-3, also known as EGLN1-3) in normoxia, leading to polyubiquitylation mediated by the von Hippel-Lindau (pVHL) tumour suppressor protein and subsequent rapid proteasome-mediated degradation. In addition, an asparaginyl hydroxylase factor inhibiting HIF (FIH) hydroxylates a transactivation domain in the HIF-α proteins, preventing coactivator recruitment and repressing transcriptional activity. In hypoxia the activity of the hydroxylases is reduced, and the HIF-α subunits avoid hydroxylation. The unhydroxylated proteins avoid ubiquitylation and degradation, translocate to the nucleus, partner with Arnt, bind hypoxic response elements in the regulatory regions of target genes, recruit transcriptional coactivators, and ultimately mediate the robust induction of a battery of target genes.

There are three genes encoding HIF-α proteins in mammals, *HIF-1a*, *EPAS1* (encodes HIF-2α) and *HIF-3a*, that can each dimerise with Arnt to form the functional HIF-1, HIF-2 or HIF-3 heterodimers, respectively. HIF-1α was the first oxygen-regulated subunit discovered [2], is ubiquitously expressed, and is the best characterised of the α subunits. HIF-2α is closely related to HIF-1α, sharing 48% amino acid sequence identity, a very similar domain structure, and hydroxylation-dependent regulation (reviewed in [3]). The expression pattern of HIF-2α is more restricted, being highest in blood vessels, but is also expressed in many other tissues. HIF-3α is the least characterised subunit, complicated by the numerous variants expressed, some of which activate and others repress hypoxically-induced gene expression [4].

HIF target genes mediate the adaptation to hypoxia, from the cellular level through to the whole organism. Target genes include *vascular endothelial growth factor* (*VEGF*) to promote angiogenesis [5] and *erythropoietin* (*Epo*) to promote erythropoiesis [6], as well as numerous genes involved in cell proliferation, survival, and metabolism

---

[*] Corresponding author.
E-mail address: daniel.peet@adelaide.edu.au (D.J. Peet).

http://dx.doi.org/10.1016/j.yexcr.2017.03.030
Received 3 March 2017; Accepted 14 March 2017
Available online 16 March 2017

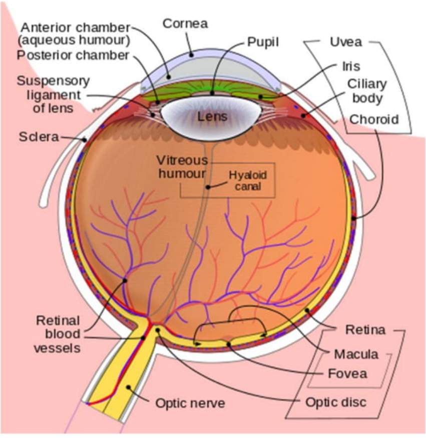

Fig. 1. Schematic diagram of the human eye. (By Rhcastilhos - Schematic_diagram_of_the_human_eye_with_English_annotations.svg, Public Domain, https://commons.wikimedia.org/w/index.php?curid=1597930).

to mediate the switch from oxidative phosphorylation to anaerobic glycolysis for ATP production. The majority of the cellular response to hypoxia is mediated by HIF-1 and HIF-2, and there are now hundreds of direct HIF target genes identified, including those induced by HIF-1α, HIF-2α or both [7,8].

3. Role of HIFs in the structure and physiology of the eye

The eye is an intricate arrangement of highly organised tissues, each comprised of multiple cell types (Fig. 1). Throughout the eye efficient oxygen delivery needs to be balanced by the consequence of vasculature obscuring the passage of light, as haemoglobin efficiently absorbs light. Consequently, some of the tissues in the eye are avascular, including the highly transparent cornea and lens, where the presence of blood vessels significantly compromises vision. Other tissues are highly vascularised, such as the choroid and the iris.

3.1. Retinal vasculature

The retina, the innermost layer of the eye that detects the light and converts it into electrical signals, is not only complex, comprised of 8 distinct cell types, but has unique vascular requirements related to its structure and function. It is essentially a layered, transparent, light-sensitive membrane containing the first, second and third order neurons of the visual pathway including photoreceptors, together with other accessory cells. These neurons are located in the outer nuclear, inner nuclear and ganglion cells layers, respectively, and are intercalated by two synaptic (plexiform) layers. Embryologically, the retina is an outpouching of the diencephalon. Like the remainder of the central nervous system it has a heavy metabolic load and prodigious energy demand. The human retina requires approximately 10 ml O_2/100 ml tissue/minute to maintain vision [9]. This is 2–3 times more than the estimated brain requirements, as evidenced by visual blackout preceding loss of consciousness under positive g conditions [9]. The intensive metabolic demands required for normal vision make the retina the most oxygen hungry tissue in the body.

To meet the nutrient requirements whilst optimizing optics, the human retina is vascularized with a dual blood supply from both the retinal and choroidal circulations. During the first trimester, the hyaloid artery within the developing vitreous cavity supplies nutrients to the retina. In the fourth month of gestation, endothelial cords arise from the optic nerve head to form an early central retinal artery. By the sixth month, these primitive vessels have canalized.

The circulation in mature retina, derived from the central retinal artery is a dichotomously branching, end-artery system supplying the inner and middle retina via superficial and deep capillary layers. The choriocapillaris (corresponding to the pia-arachnoid vessels in the rest of the brain) supplies oxygen and nutrients to the outer retina, including the classical photoreceptors, the rods and cones. The human retina, like all primates, also contains a specialized central zone, the macula, the centre of which is the fovea, where the cone photoreceptors are tightly packed, providing high acuity central vision. The inner region of the fovea is completely avascular (the foveal avascular zone). The choroid adjacent to the macula is thought to be vulnerable to ischemia because of the numerous watershed zones that converge in this region [10].

3.2. Role of HIFs in vasculature

As hypoxia is an important developmental cue to drive HIF-mediated angiogenesis, it is not surprising that the highly organised vascular development in the eye, specifically the retina, is dependent on the HIFs. Development of the retinal vasculature increases cellular oxygen tension with HIFα degradation and reduction in retinal VEGF [10]. Conditionally deleting VHL in retinal neurons or astrocytes and artificially maintaining HIFα causes pathological persistence of the hyaloidal vasculature [10]. Hence, it is generally accepted that HIF-induced spatiotemporal control of VEGF secretion is critical in the development of the superficial and deep layers of the retinal vasculature. However, HIF expression is not ubiquitously required in all retinal cell types for normal retinal development. Conditional deletions show that HIF-1α in retinal pigment epithelium [11] and Müller cells [12], and neither HIF-1α nor HIF-2α in astrocytes [13,14] or photoreceptors [15] are required for normal function or development of the mouse retina.

While the HIFs are broadly expressed at the mRNA level throughout the mature eye, their protein levels and activity are tightly regulated. This regulation enables the HIFs to control normal vascularisation where required, both promoting vascularisation mediated by VEGF and other angiogenic HIF target genes, but also preventing aberrant vascularisation in other parts of the eye. The highly specialised control of HIF activity in specific cell types within the eye was first highlighted by Lorenz Poellinger's group in a study identifying the novel mouse-specific inhibitory PAS domain protein (IPAS1) and characterising its role in the mouse cornea [16]. IPAS1, subsequently shown by Poellinger's group to be a splice variant of HIF-3α [17], lacks a transactivation domain and can function as a dominant negative regulator of HIF-1 by sequestering HIF-1α away from target genes. This protein is highly expressed in mouse corneal epithelium, and its transcription is induced by hypoxia [16]. Extended closure of the eye, as experienced during sleep, may result in hypoxia, inducing IPAS expression to prevent HIF-mediated vascularisation of the highly transparent cornea. A similar human splice variant of HIF-3α, HIF-3α4, also functions as a dominant negative of HIF-1 [18]. However, while a similar role in human corneal epithelium to IPAS in the mouse has been hypothesised [19], the presence or function of HIF-3α4 in the human cornea, or an alternative method for repressing HIF-1-mediated angiogenesis has yet to be confirmed.

3.3. Role of HIFs in specialised metabolism

The mammalian retina displays quite unusual cellular metabolism. Otto Warburg first highlighted the reliance on glycolysis for energy production in the retina, even in the presence of abundant oxygen [20]. This aerobic glycolysis, also known as the Warburg effect, in the retina was initially dismissed as an artefact, but as with cancer cells, the presence of the Warburg effect in the retina has subsequently become a research topic of significant interest in ophthalmological research [21]. Primary Müller cells display the Warburg effect very strongly when cultured [22], although more recent evidence supports the majority of lactate in the retina being produced by the photoreceptor cells, as photoreceptor-deficient retinas in mice produce 74% less lactate than normal retinas [23].

The HIFs are central for the metabolic reprogramming of cells in hypoxia, and have been implicated in driving the Warburg effect and other metabolic changes in cancer and other proliferating cells in normoxia (reviewed in [24]). They directly upregulate glucose transporters, many of the glycolytic enzymes, the production of lactate through lactate dehydrogenase, and inhibit oxidative phosphorylation through the induction of pyruvate dehydrogenase kinase. However, while a role for the HIFs in regulating the Warburg effect in the retina has been proposed [21], the targeted deletion of both HIF-1α and HIF-2α isoforms in rod photoreceptor cells in mice resulted in normal photoreceptor development and apparent normal function of retina [15]. This implies that either the HIFs are not involved in controlling this unusual metabolism in the retina, or displaying the Warburg effect is not required for rod photoreceptor function and survival.

4. HIF/VEGF-induced retinal pathologies

The roles of HIF in responding to hypoxia, and specifically its role in promoting angiogenesis, implicate HIF in numerous ischaemic and other ophthalmologic pathologies, specifically in the retina. Retinal ischemia ensues when the retinal circulation is insufficient to meet the metabolic demands of the retina [25]. Retinal ischemia is the underlying pathophysiology responsible for a considerable proportion of the global burden of visual impairment in children and adults.

4.1. Retinopathy of prematurity

Retinopathy of prematurity (ROP) is a severe, potentially blinding complication of oxygen delivery to premature neonates. In 1948, Michaelson published a landmark paper which utilized a technique to visualize blood vessels of the flat-mounted human fetal retina at various developmental stages [26]. From his observations, he presciently predicted that the retina produced a substance that he called Factor X (subsequently identified as VEGF), which controlled angiogenesis [26]. In ROP, hyperoxia causes downregulation of retinal VEGF and failure of normal vascularisation with consequent blinding pathology [27]. Better understanding of the role of the O_2/HIF/VEGF axis in the pathophysiology of ROP has motivated strict control and monitoring of neonatal oxygen administration in intensive care units and new treatments to promote physiologic retinal vascular development [28].

4.2. Retinal artery and venous occlusions

The retinal arteries are end-arteries; hence, occlusion causes complete inner retinal ischemia in its entire distribution. If nutrient supply is not rapidly restored, the inner retina is irreversibly damaged within approximately 100 min [29]. Energy substrate delivery via vitreal glucose has been shown to preserve inner retinal structure and function against ischaemic injury [30], and conversely hypoglycaemia exacerbates ischaemic retinal injury [31].

Retinal venous occlusions are a more common clinical occurrence than arterial occlusions and are frequently associated with neovascularization. A branch retinal vein occlusion (BRVO) resulting in retinal ischemia can cause retinal neovascularization with subsequent haemorrhage. For unclear reasons the neovascularization associated with a central retinal vein occlusion rarely occurs on the retina; however, a well-described condition following an ischaemic central retinal vein occlusion is the development of angiogenesis on the iris and in the angle of the eye, resulting in occlusion of the aqueous humour outflow pathways, intraocular pressure elevation and “neovascular glaucoma”.

Retinal venous occlusions are also commonly associated with macular edema. In experimental BRVO in mice, there is retinal swelling with marked coincidence with increased VEGF-A and HIF-1α followed by degeneration of the inner retina [32]. Recent evidence indicates that angiopoietin-like 4 (ANGPTL4) is up-regulated by HIF-1 in hypoxic Müller cells *in vitro* and the ischaemic inner retina *in vivo*, promoting capillary permeability by hypoxic Müller cells. Hence, HIF-dependent factors apart from VEGF may be involved in the pathogenesis of macular edema [33].

4.3. Diabetic retinopathy

Chronic hyperglycaemia associated with uncontrolled diabetic mellitus produces advanced glycation end products (AGEs) that cause retinal capillary occlusion and leakage. Capillary occlusion produces areas of ischaemic inner retina with consequent VEGF production and angiogenesis. In addition, there is evidence that AGEs directly stimulate VEGF expression through the activation of HIF-1 [34]. This can lead to the potentially blinding condition of “proliferative diabetic retinopathy”. Macular edema from VEGF-induced capillary leakage is the other common potentially blinding pathology.

4.4. Age-related macular degeneration (AMD)

AMD is the leading cause of blindness in the developed world. It manifests as two clinical-pathological phenotypes: exudative and non-exudative. The exudative type (Fig. 2), or wet AMD, is characterised by the presence of choroidal neovascularization (CNV). Increasing age is the principle risk factor and over the past decade there have been considerable advances in elucidating the underlying genetics, particularly the role of the complement pathway in the pathogenesis of CNV [35]. In addition, there is a convergence of evidence implicating ischemia and upregulated VEGF expression as an underlying mechanism of both exudative and non-exudative AMD [36]. Furthermore, the HIFs have been shown to be an important mediator of other age-related processes [37], including apoptosis [38], consistent with a role in AMD.

4.5. Current HIF/VEGF-related management of retinal ischemia

Although the ischaemic retina per se remains untreatable, the VEGF-driven neovascularization that contributes to the blinding sequelae has been traditionally managed by panretinal photocoagulation (PRP) [39]. The mechanism of action of PRP is controversial. There is some experimental evidence that by causing photoreceptor

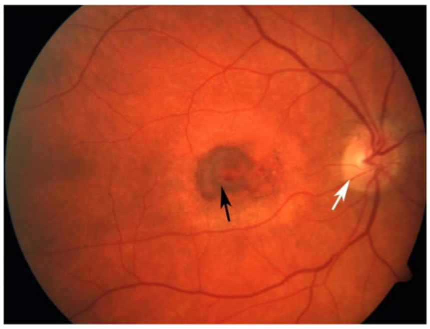

Fig. 2. Fundus photograph of an eye with exudative AMD. The current treatment for this condition includes intravitreal injections of anti-VEGF. Black arrow indicates haemorrhage at the macula from choroidal neovascularization, white arrow indicates optic disc.

destruction, PRP reduces the oxygen demands of the outer retina and provides choriocapillaris-derived oxygen for the inner retina, thereby stabilizing the HIFs and downregulating VEGF [40,41]. A related widely held belief within the ophthalmic community, albeit unsubstantiated, is that the retinal destruction reduces the "VEGF load" within the retina [42]. These pathophysiological notions have motivated the recent trial of intravitreal anti-VEGF (ranibizumab) as a treatment for retinal neovascularization associated with diabetic retinopathy. A recent large randomized study concluded that repeated intravitreal injections of ranibizumab were non-inferior to PRP in terms of visual acuity preservation over 2 years [42].

5. Future therapeutic opportunities

Characterising the role of the HIFs in the eye extends beyond an improved understanding of the development, function, and numerous pathologies of the eye, and may provide novel therapeutic approaches. There has been considerable interest in developing drugs to target the HIFs in ischaemic and other pathologies, both agonists and antagonists [43,44]. The most advanced of these activate the HIFs and induce erythropoiesis by specifically targeting the PHDs, and are currently in phase III clinical trials for the treatment of anaemia. HIF antagonists are also being developed for the treatment of cancer. Similar therapeutic approaches could be employed in retinal pathologies. VEGF, for example, has been actively targeted to reduce angiogenesis in diabetic retinopathy, but as broader drivers of angiogenesis, targeting the HIFs may produce more effective outcomes. The HIFs may also prove effective targets to reverse the neurodegeneration component of ischaemic retinal injury.

Finally, as a note of caution, the potential consequence to the eye, specifically the retina, with the use of any agonist or antagonist targeting HIF for pathologies unrelated to the eye needs to be carefully assessed, given the tight control and serious consequences of altering HIF activity.

Acknowledgements

This review was written in memory of Lorenz Poellinger, a close colleague and collaborator, who made a major contribution to this field and will be sadly missed. Supported by National Health and Medical Research Council of Australia grant 1099932 and the Ophthalmic Research Institute of Australia. The authors declare they have no conflicts of interest.

References

[1] W.G. Kaelin Jr, P.J. Ratcliffe, Oxygen sensing by metazoans: the central role of the HIF hydroxylase pathway, Mol. Cell 30 (2008) 393–402.
[2] G.L. Wang, B.H. Jiang, E.A. Rue, G.L. Semenza, Hypoxia-inducible factor 1 is a basic-helix-loop-helix-PAS heterodimer regulated by cellular O2 tension, Proc. Natl. Acad. Sci. USA 92 (1995) 5510–5514.
[3] B. Keith, R.S. Johnson, M.C. Simon, HIF1alpha and HIF2alpha: sibling rivalry in hypoxic tumour growth and progression, Nat. Rev. Cancer 12 (2011) 9–22.
[4] C.E. Dann 3rd, R.K. Bruick, J. Deisenhofer, Structure of factor-inhibiting hypoxia-inducible factor 1: an asparaginyl hydroxylase involved in the hypoxic response pathway, Proc. Natl. Acad. Sci. USA 99 (2002) 15351–15356.
[5] J.A. Forsythe, B.H. Jiang, N.V. Iyer, F. Agani, S.W. Leung, R.D. Koos, G.L. Semenza, Activation of vascular endothelial growth factor gene transcription by hypoxia-inducible factor 1, Mol. Cell Biol. 16 (1996) 4604–4613.
[6] P.H. Maxwell, C.W. Pugh, P.J. Ratcliffe, Inducible operation of the erythropoietin 3′ enhancer in multiple cell lines: evidence for a widespread oxygen-sensing mechanism, Proc. Natl. Acad. Sci. USA 90 (1993) 2423–2427.
[7] D.J. Manalo, A. Rowan, T. Lavoie, L. Natarajan, B.D. Kelly, S.Q. Ye, J.G. Garcia, G.L. Semenza, Transcriptional regulation of vascular endothelial cell responses to hypoxia by HIF-1, Blood 105 (2005) 659–669.
[8] J. Schodel, S. Oikonomopoulos, J. Ragoussis, C.W. Pugh, P.J. Ratcliffe, D.R. Mole, High-resolution genome-wide mapping of HIF-binding sites by ChIP-seq, Blood 117 (2011) e207–e217.
[9] B. Anderson Jr, H.A. Saltzman, Retinal oxygen utilization measured by hyperbaric blackout, Arch. Ophthalmol. 72 (1964) 792–795.
[10] T. Kurihara, Y. Kubota, Y. Ozawa, K. Takubo, K. Noda, M.C. Simon, R.S. Johnson, M. Suematsu, K. Tsubota, S. Ishida, N. Goda, T. Suda, H. Okano, von Hippel-Lindau protein regulates transition from the fetal to the adult circulatory system in retina, Development 137 (2010) 1563–1571.
[11] M. Lin, Y. Hu, Y. Chen, K.K. Zhou, J. Jin, M. Zhu, Y.Z. Le, J. Ge, J.X. Ma, Impacts of hypoxia-inducible factor-1 knockout in the retinal pigment epithelium on choroidal neovascularization, Investig. Ophthalmol. Vis. Sci. 53 (2012) 6197–6206.
[12] M. Lin, Y. Chen, J. Jin, Y. Hu, K.K. Zhou, M. Zhu, Y.Z. Le, J. Ge, R.S. Johnson, J.X. Ma, Ischaemia-induced retinal neovascularisation and diabetic retinopathy in mice with conditional knockout of hypoxia-inducible factor-1 in retinal Muller cells, Diabetologia 54 (2011) 1554–1566.
[13] A. Scott, M.B. Powner, P. Gandhi, C. Clarkin, D.H. Gutmann, R.S. Johnson, N. Ferrara, M. Fruttiger, Astrocyte-derived vascular endothelial growth factor stabilizes vessels in the developing retinal vasculature, PLoS One 5 (2010) e11863.
[14] A. Weidemann, T.U. Krohne, E. Aguilar, T. Kurihara, N. Takeda, M.I. Dorrell, M.C. Simon, V.H. Haase, M. Friedlander, R.S. Johnson, Astrocyte hypoxic response is essential for pathological but not developmental angiogenesis of the retina, Glia 58 (2010) 1177–1185.
[15] B. Kast, C. Schori, C. Grimm, Hypoxic preconditioning protects photoreceptors against light damage independently of hypoxia inducible transcription factors in rods, Exp. Eye Res. 146 (2016) 60–71.
[16] Y. Makino, R. Cao, K. Svensson, G. Bertilsson, M. Asman, H. Tanaka, Y. Cao, A. Berkenstam, L. Poellinger, Inhibitory PAS domain protein is a negative regulator of hypoxia-inducible gene expression, Nature 414 (2001) 550–554.
[17] Y. Makino, A. Kanopka, W.J. Wilson, H. Tanaka, L. Poellinger, Inhibitory PAS domain protein (IPAS) is a hypoxia-inducible splicing variant of the hypoxia-inducible factor-3alpha locus, J. Biol. Chem. 277 (2002) 32405–32408.
[18] M.A. Maynard, A.J. Evans, T. Hosomi, S. Hara, M.A. Jewett, M. Ohh, Human HIF-3alpha4 is a dominant-negative regulator of HIF-1 and is down-regulated in renal cell carcinoma, FASEB J. 19 (2005) 1396–1406.
[19] V.L. Dengler, M.D. Galbraith, J.M. Espinosa, Transcriptional regulation by hypoxia inducible factors, Crit. Rev. Biochem. Mol. Biol. 49 (2014) 1–15.
[20] F. Wind, The Metabolism of Tumors: Investigations from the Kaiser Wilhelm Institute for Biology, Constable & Co. Ltd, London, 1930.
[21] S.K. Ng, J.P. Wood, G. Chidlow, G. Han, T. Kittipassorn, D.J. Peet, R.J. Casson, Cancer-like metabolism of the mammalian retina, Clin. Exp. Ophthalmol. 43 (2015) 367–376.
[22] B.S. Winkler, M.J. Arnold, M.A. Brassell, D.G. Puro, Energy metabolism in human retinal Muller cells, Investig. Ophthalmol. Vis. Sci. 41 (2000) 3183–3190.
[23] K.J. Lindsay, J. Du, S.R. Sloat, L. Contreras, J.D. Linton, S.J. Turner, M. Sadilek, J. Satrustegui, J.B. Hurley, Pyruvate kinase and aspartate-glutamate carrier distributions reveal key metabolic links between neurons and glia in retina, Proc. Natl. Acad. Sci. USA 111 (2014) 15579–15584.
[24] G.L. Semenza, Regulation of metabolism by hypoxia-inducible factor 1, Cold Spring Harb. Symp. Quant. Biol. 76 (2011) 347–353.
[25] N.N. Osborne, R.J. Casson, J.P. Wood, G. Chidlow, M. Graham, J. Melena, Retinal ischemia: mechanisms of damage and potential therapeutic strategies, Prog. Retin Eye Res. 23 (2004) 91–147.
[26] I.C. Michaelson, The mode of development of the vascular system of the retina, with some observations on its significance for certain retinal disease, Trans. Ophthalmol. Soc. UK 68 (1948) 137–180.
[27] T. Alon, I. Hemo, A. Itin, J. Pe'er, J. Stone, E. Keshet, Vascular endothelial growth factor acts as a survival factor for newly formed retinal vessels and has implications for retinopathy of prematurity, Nat. Med. 1 (1995) 1024–1028.
[28] M.E. Hartnett, Advances in understanding and management of retinopathy of prematurity, Surv. Ophthalmol. (2016).
[29] S.S. Hayreh, T.A. Weingeist, Experimental occlusion of the central artery of the retina. IV: retinal tolerance time to acute ischaemia, Br. J. Ophthalmol. 64 (1980) 818–825.
[30] R.J. Casson, G. Chidlow, J.P. Wood, N.N. Osborne, The effect of hyperglycemia on experimental retinal ischemia, Arch. Ophthalmol. 122 (2004) 361–366.
[31] R.J. Casson, J.P. Wood, N.N. Osborne, Hypoglycaemia exacerbates ischaemic retinal injury in rats, Br. J. Ophthalmol. 88 (2004) 816–820.
[32] A. Ebneter, D. Kokona, N. Schneider, M.S. Zinkernagel, Microglia Activation and Recruitment of Circulating Macrophages During Ischemic Experimental Branch Retinal Vein Occlusion, Investig. Ophthalmol. Vis. Sci. 58 (2017) 944–953.
[33] X. Xin, M. Rodrigues, M. Umapathi, F. Kashiwabuchi, T. Ma, S. Babapoor-Farrokhran, S. Wang, J. Hu, I. Bhutto, D.S. Welsbie, E.J. Duh, J.T. Handa, C.G. Eberhart, G. Lutty, G.L. Semenza, S. Montaner, A. Sodhi, Hypoxic retinal Muller cells promote vascular permeability by HIF-1-dependent up-regulation of angiopoietin-like 4, Proc. Natl. Acad. Sci. USA 110 (2013) E3425–E3434.
[34] C. Treins, S. Giorgetti-Peraldi, J. Murdaca, E. Van Obberghen, Regulation of vascular endothelial growth factor expression by advanced glycation end products, J. Biol. Chem. 276 (2001) 43836–43841.
[35] R.J. Klein, C. Zeiss, E.Y. Chew, J.Y. Tsai, R.S. Sackler, C. Haynes, A.K. Henning, J.P. SanGiovanni, S.M. Mane, S.T. Mayne, M.B. Bracken, F.L. Ferris, J. Ott, C. Barnstable, J. Hoh, Complement factor H polymorphism in age-related macular degeneration, Science 308 (2005) 385–389.
[36] B. Feigl, Age-related maculopathy - Linking aetiology and pathophysiological changes to the ischaemia hypothesis, Prog. Retin. Eye Res. 28 (2009) 63–86.
[37] A.P. Gomes, N.L. Price, A.J. Ling, J.J. Moslehi, M.K. Montgomery, L. Rajman, J.P. White, J.S. Teodoro, C.D. Wrann, B.P. Hubbard, E.M. Mercken, C.M. Palmeira, R. de Cabo, A.P. Rolo, N. Turner, E.L. Bell, D.A. Sinclair, Declining NAD(+) induces a pseudohypoxic state disrupting nuclear-mitochondrial communication during aging, Cell 155 (2013) 1624–1638.
[38] L.A. Kubasiak, O.M. Hernandez, N.H. Bishopric, K.A. Webster, Hypoxia and acidosis activate cardiac myocyte death through the Bcl-2 family protein BNIP3,

Proc. Natl. Acad. Sci. USA 99 (2002) 12825–12830.
[39] Photocoagulation treatment of proliferative diabetic retinopathy. Clinical application of Diabetic Retinopathy Study (DRS) findings, DRS Report Number 8. The Diabetic Retinopathy Study Research Group, Ophthalmology, 88 1981, pp. 583–600.
[40] M.B. Landers 3rd, E. Stefansson, M.L. Wolbarsht, Panretinal photocoagulation and retinal oxygenation, Retina 2 (1982) 167–175.
[41] E. Stefansson, The therapeutic effects of retinal laser treatment and vitrectomy A theor.y based on oxygen and vascular physiology, Acta Ophthalmol. Scand. 79 (2001) 435–440.
[42] N. Writing Committee for the Diabetic Retinopathy Clinical Research, J.G. Gross, A.R. Glassman, L.M. Jampol, S. Inusah, L.P. Aiello, A.N. Antoszyk, C.W. Baker, B.B. Berger, N.M. Bressler, D. Browning, M.J. Elman, F.L. Ferris 3rd, S.M. Friedman, D.M. Marcus, M. Melia, C.R. Stockdale, J.K. Sun, R.W. Beck, Panretinal photocoagulation vs intravitreous ranibizumab for proliferative Diabetic retinopathy: a randomized clinical trial, JAMA 314 (2015), 2015, pp. 2137–2146.
[43] M.C. Chan, J.P. Holt-Martyn, C.J. Schofield, P.J. Ratcliffe, Pharmacological targeting of the HIF hydroxylases–A new field in medicine development, Mol. Asp. Med. 47–48 (2016) 54–75.
[44] C. Wigerup, S. Pahlman, D. Bexell, Therapeutic targeting of hypoxia and hypoxia-inducible factors in cancer, Pharm. Ther. 164 (2016) 152–169.

7.4 HeLa cell identification testing

HeLa cells were trypsinised and centrifuged and gDNA extracted using a QIAamp DNA Blood Mini kit (Qiagen) by the candidate. The sample was submitted to CellBank Australia for human cell line authentication testing by Emily Button (Laboratory of Professor Murray Whitelaw, University of Adelaide, Adelaide, SA, Australia). Certificate of analysis is presented below.

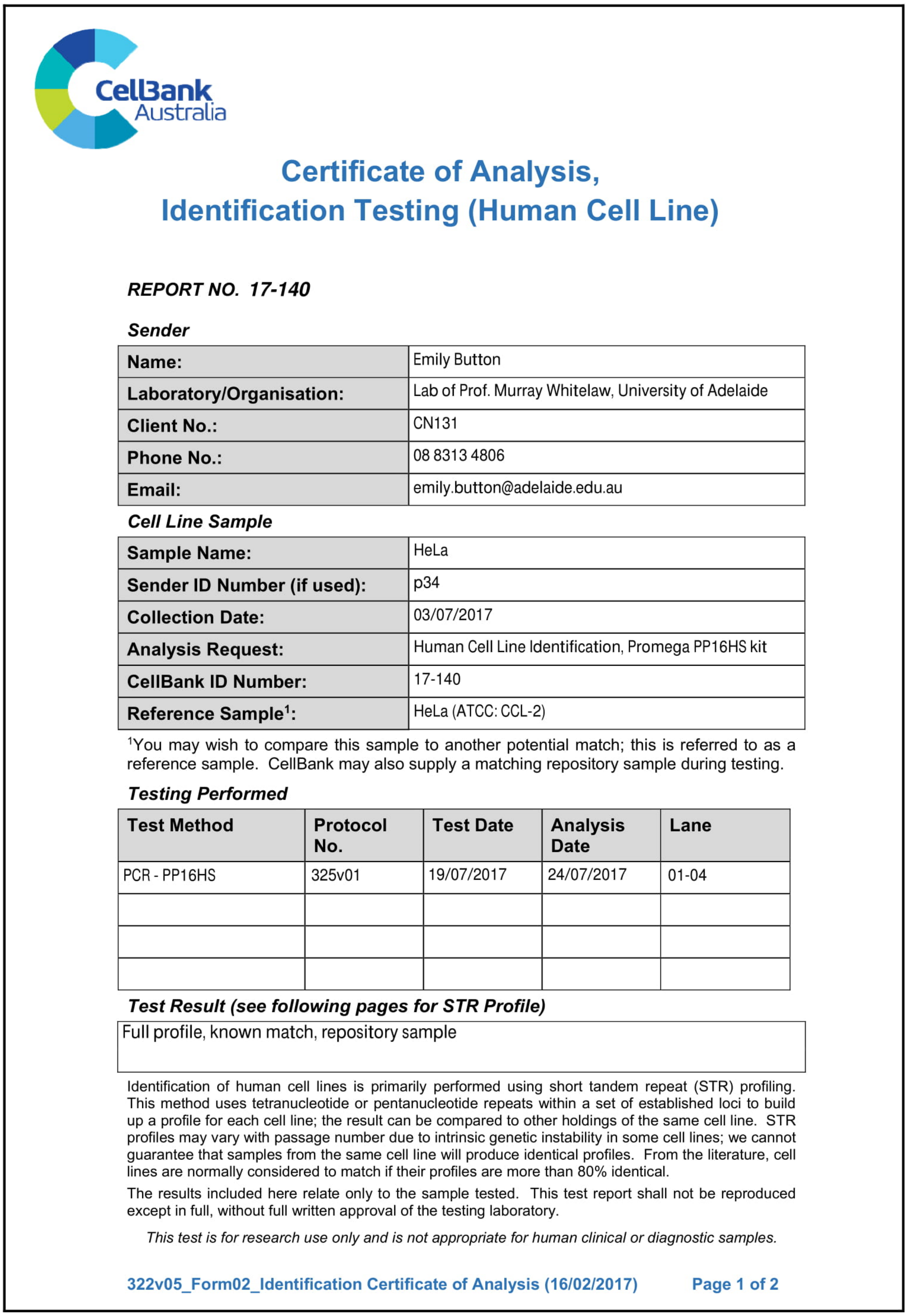

Certificate of Analysis,
Identification Testing (Human Cell Line)

REPORT NO. 17-140

Sender

Name:	Emily Button
Laboratory/Organisation:	Lab of Prof. Murray Whitelaw, University of Adelaide
Client No.:	CN131
Phone No.:	08 8313 4806
Email:	emily.button@adelaide.edu.au

Cell Line Sample

Sample Name:	HeLa
Sender ID Number (if used):	p34
Collection Date:	03/07/2017
Analysis Request:	Human Cell Line Identification, Promega PP16HS kit
CellBank ID Number:	17-140
Reference Sample[1]:	HeLa (ATCC: CCL-2)

[1]You may wish to compare this sample to another potential match; this is referred to as a reference sample. CellBank may also supply a matching repository sample during testing.

Testing Performed

Test Method	Protocol No.	Test Date	Analysis Date	Lane
PCR - PP16HS	325v01	19/07/2017	24/07/2017	01-04

Test Result (see following pages for STR Profile)

Full profile, known match, repository sample

Identification of human cell lines is primarily performed using short tandem repeat (STR) profiling. This method uses tetranucleotide or pentanucleotide repeats within a set of established loci to build up a profile for each cell line; the result can be compared to other holdings of the same cell line. STR profiles may vary with passage number due to intrinsic genetic instability in some cell lines; we cannot guarantee that samples from the same cell line will produce identical profiles. From the literature, cell lines are normally considered to match if their profiles are more than 80% identical.

The results included here relate only to the sample tested. This test report shall not be reproduced except in full, without full written approval of the testing laboratory.

This test is for research use only and is not appropriate for human clinical or diagnostic samples.

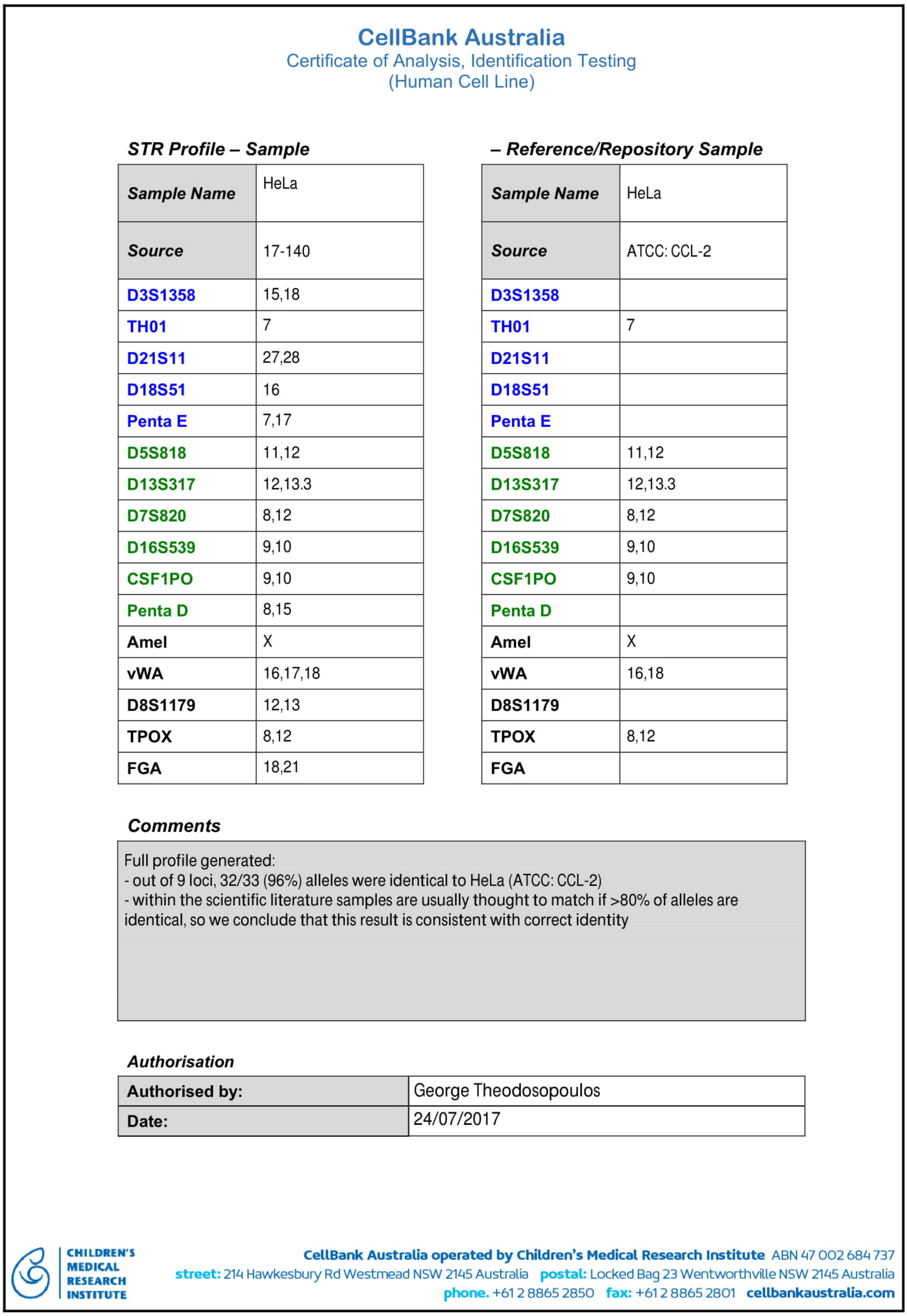

CellBank Australia

Certificate of Analysis, Identification Testing
(Human Cell Line)

STR Profile – Sample

Sample Name	HeLa
Source	17-140
D3S1358	15,18
TH01	7
D21S11	27,28
D18S51	16
Penta E	7,17
D5S818	11,12
D13S317	12,13.3
D7S820	8,12
D16S539	9,10
CSF1PO	9,10
Penta D	8,15
Amel	X
vWA	16,17,18
D8S1179	12,13
TPOX	8,12
FGA	18,21

– Reference/Repository Sample

Sample Name	HeLa
Source	ATCC: CCL-2
D3S1358	
TH01	7
D21S11	
D18S51	
Penta E	
D5S818	11,12
D13S317	12,13.3
D7S820	8,12
D16S539	9,10
CSF1PO	9,10
Penta D	
Amel	X
vWA	16,18
D8S1179	
TPOX	8,12
FGA	

Comments

Full profile generated:
- out of 9 loci, 32/33 (96%) alleles were identical to HeLa (ATCC: CCL-2)
- within the scientific literature samples are usually thought to match if >80% of alleles are identical, so we conclude that this result is consistent with correct identity

Authorisation

Authorised by:	George Theodosopoulos
Date:	24/07/2017

CHILDREN'S MEDICAL RESEARCH INSTITUTE

CellBank Australia operated by Children's Medical Research Institute ABN 47 002 684 737
street: 214 Hawkesbury Rd Westmead NSW 2145 Australia **postal:** Locked Bag 23 Wentworthville NSW 2145 Australia
phone. +61 2 8865 2850 **fax:** +61 2 8865 2801 **cellbankaustralia.com**

7.5 Paper 4: Supplementary table S1

Supplementary table S1. Differentially expressed genes (DEGs) in SIRMu-1 cells and/or rMC-1 cells relative to primary (1^{o}) MCs. Reproduced from (Kittipassorn et al., 2019a), the main article of which can be found in section 3.3.1 in Chapter 3.

(A) DEGs in both the SIRMu-1 and the rMC-1 cell lines relative to 1^{o} MCs.

Gene symbol	**Gene ENTREZID**	**Gene name**	**DEGs compared to 1° MC**	
			SIRMu-1	**rMC-1**
Rab6b	363123	RAB6B, member RAS oncogene family	1	1
Meis2	311311	Meis homeobox 2	1	1
Kif26a	314473	kinesin family member 26A	-1	1
Serpina3n	24795	serine (or cysteine) peptidase inhibitor, clade A, member 3N	-1	1
Olr59	170816	olfactory receptor 59	1	-1
Grem1	50566	gremlin 1, DAN family BMP antagonist	-1	-1
Glb1l	301525	galactosidase, beta 1-like	-1	-1
Serpine2	29366	serpin family E member 2	-1	-1
Ccnd2	64033	cyclin D2	-1	-1
Apoe	25728	apolipoprotein E	-1	-1
Sod3	25352	superoxide dismutase 3, extracellular	-1	-1
Ctsk	29175	cathepsin K	-1	-1
C1qtnf5	315598	C1q and tumor necrosis factor related protein 5	-1	-1
Pvrl1	NA	NA	-1	-1
38231	287606	septin 4	-1	-1
Scn1b	29686	sodium voltage-gated channel beta subunit 1	-1	-1
Fndc1	308099	fibronectin type III domain containing 1	-1	-1
Acvrl1	25237	activin A receptor like type 1	-1	-1
Ly6e	362934	lymphocyte antigen 6 complex, locus E	-1	-1
Scamp5	65171	secretory carrier membrane protein 5	-1	-1
Cpxm1	296156	carboxypeptidase X (M14 family), member 1	-1	-1
Ociad2	100361733	OCIA domain containing 2	-1	-1
Rarres1	310486	retinoic acid receptor responder 1	-1	-1
Fgfr1	79114	Fibroblast growth factor receptor 1	-1	-1
Olfm1	93667	olfactomedin 1	-1	-1
Smpdl3a	294422	sphingomyelin phosphodiesterase, acid-like 3A	-1	-1
Thy1	24832	Thy-1 cell surface antigen	-1	-1
Mgp	25333	matrix Gla protein	-1	-1
Ttc9	500689	tetratricopeptide repeat domain 9	-1	-1
Tspan12	362326	tetraspanin 12	-1	-1
Gng2	80850	G protein subunit gamma 2	-1	-1
Stk26	317589	serine/threonine protein kinase 26	-1	-1
Cpeb1	293056	cytoplasmic polyadenylation element binding protein 1	-1	-1

Map3k9	500690	mitogen-activated protein kinase kinase kinase 9	-1	-1
Zbtb7c	679155	zinc finger and BTB domain containing 7C	-1	-1
Lrp3	89787	LDL receptor related protein 3	-1	-1
Ccdc125	499518	coiled-coil domain containing 125	-1	-1
Lrfn3	308495	leucine rich repeat and fibronectin type III domain containing 3	-1	-1
Dchs1	308912	dachsous cadherin-related 1	-1	-1
Pamr1	311252	peptidase domain containing associated with muscle regeneration 1	-1	-1
Slc16a3	80878	solute carrier family 16 member 3	-1	-1
Rbpjl	362268	recombination signal binding protein for immunoglobulin kappa J region-like	-1	-1
Acp5	25732	acid phosphatase 5, tartrate resistant	-1	-1
St3gal6	304023	ST3 beta-galactoside alpha-2,3-sialyltransferase 6	-1	-1
Ttbk1	316229	tau tubulin kinase 1	-1	-1
Rai2	501555	retinoic acid induced 2	-1	-1
Fbxo44	500587	F-box protein 44	-1	-1
Lpl	24539	lipoprotein lipase	-1	-1
RGD1563349	502727	similar to RIKEN cDNA 9330182L06	-1	-1
Zfp641	300197	zinc finger protein 641	-1	-1
Cpz	83575	carboxypeptidase Z	-1	-1
Car3	54232	carbonic anhydrase 3	-1	-1
Colec12	361289	collectin sub-family member 12	-1	-1
Sat2	360547	spermidine/spermine N1-acetyltransferase family member 2	-1	-1
Layn	500996	layilin	-1	-1
Gfpt2	360518	glutamine-fructose-6-phosphate transaminase 2	-1	-1
Gpc3	25236	glypican 3	-1	-1
Pde2a	81743	phosphodiesterase 2A	-1	-1
Ndn	308690	necdin, MAGE family member	-1	-1
Kirrel3	315546	kin of IRRE like 3 (Drosophila)	-1	-1
Egflam	365691	EGF-like, fibronectin type III and laminin G domains	-1	-1
Nefm	24588	neurofilament, medium polypeptide	-1	-1
Pla2g7	301265	phospholipase A2 group VII	-1	-1
Erc2	259269	ELKS/RAB6-interacting/CAST family member 2	-1	-1
Ric3	687147	RIC3 acetylcholine receptor chaperone	-1	-1
Eya2	156826	EYA transcriptional coactivator and phosphatase 2	-1	-1
Astn1	304900	astrotactin 1	-1	-1
Epb41l4b	500464	erythrocyte membrane protein band 4.1 like 4B	-1	-1
Plcb1	24654	phospholipase C beta 1	-1	-1
Slc22a18	309131	solute carrier family 22, member 18	-1	-1
Ntng2	311836	netrin G2	-1	-1
Plagl1	25157	PLAG1 like zinc finger 1	-1	-1
Reln	24718	reelin	-1	-1
Serpinb2	60325	serpin family B member 2	-1	-1
Unc79	314401	unc-79 homolog (C. elegans)	-1	-1
Map7d3	317614	MAP7 domain containing 3	-1	-1
Prkcz	25522	protein kinase C, zeta	-1	-1

Panx2	362979	pannexin 2	-1	-1
Tmem200a	498987	transmembrane protein 200A	-1	-1
Pik3ap1	294048	phosphoinositide-3-kinase adaptor protein 1	-1	-1
Cnrip1	364208	cannabinoid receptor interacting protein 1	-1	-1
Pcdha13	116742	protocadherin alpha 13	-1	-1
Frem2	310418	Fras1 related extracellular matrix protein 2	-1	-1
Cfh	155012	complement factor H	-1	-1
Tmem117	500921	transmembrane protein 117	-1	-1
Zfp286a	497923	zinc finger protein 286A	-1	-1
Dok6	498898	docking protein 6	-1	-1
Shroom2	317435	shroom family member 2	-1	-1
Actn2	291245	actinin alpha 2	-1	-1
Pcdha11	394223	protocadherin alpha 11	-1	-1
RGD1566401	500717	similar to GTL2, imprinted maternally expressed untranslated	-1	-1
Enpp5	316249	ectonucleotide pyrophosphatase/phosphodiesterase 5	-1	-1
Zfp423	94188	zinc finger protein 423	-1	-1
Tfpi2	286926	tissue factor pathway inhibitor 2	-1	-1
Pde7b	140929	phosphodiesterase 7B	-1	-1
Limch1	305332	LIM and calponin homology domains 1	-1	-1
Lrrc15	246296	leucine rich repeat containing 15	-1	-1
Sfrp1	84402	secreted frizzled-related protein 1	-1	-1
Tyrp1	298182	tyrosinase-related protein 1	-1	-1
Rbm46	310548	RNA binding motif protein 46	-1	-1
Opcml	116597	opioid binding protein/cell adhesion molecule-like	-1	-1
Ina	24503	internexin neuronal intermediate filament protein, alpha	-1	-1
Mal2	362911	mal, T-cell differentiation protein 2	-1	-1
Amtn	689404	amelotin	-1	-1
Chrm2	81645	cholinergic receptor, muscarinic 2	-1	-1
Tmem179	314472	transmembrane protein 179	-1	-1
Bace2	288227	beta-site APP-cleaving enzyme 2	-1	-1
Cpne8	362988	copine 8	-1	-1
Entpd1	64519	ectonucleoside triphosphate diphosphohydrolase 1	-1	-1
Rab38	252916	RAB38, member RAS oncogene family	-1	-1
Dcaf12	313296	DDB1 and CUL4 associated factor 12	-1	-1
Car2	54231	carbonic anhydrase 2	-1	-1
Hoga1	293949	4-hydroxy-2-oxoglutarate aldolase 1	-1	-1
RGD1562726	498060	similar to Putative protein C21orf62 homolog	-1	-1
Rgs6	54295	regulator of G-protein signaling 6	-1	-1
Cyp7b1	25429	cytochrome P450, family 7, subfamily b, polypeptide 1	-1	-1
Rspo3	498997	R-spondin 3	-1	-1
Gucy1a2	66012	guanylate cyclase 1 soluble subunit alpha 2	-1	-1
Lrrn2	289020	leucine rich repeat neuronal 2	-1	-1
Pnmal2	308393	paraneoplastic Ma antigen family-like 2	-1	-1
Ryr2	689560	ryanodine receptor 2	-1	-1
Plcl2	301173	phospholipase C-like 2	-1	-1

Gabra2	289606	gamma-aminobutyric acid type A receptor alpha2 subunit	-1	-1
Sobp	309860	sine oculis binding protein homolog	-1	-1
Mctp2	308742	multiple C2 and transmembrane domain containing 2	-1	-1
Acss1	296259	acyl-CoA synthetase short-chain family member 1	-1	-1

Differentially expressed genes (DEGs) by a fold-change of at least 5, relative to primary MCs, in the SIRMu-1 cells compared to the primary MCs (results shown in the column named “SIRMu-1”), and in the rMC-1 cells compared to the primary MCs (results shown in the column named “rMC-1”). Downregulation is indicated by -1, upregulation by 1.

(B) DEGs only in the SIRMu-1 cell line relative to 1° MCs.

Gene symbol	Gene ENTREZID	Gene name	DEGs in SIRMu-1 compared to 1° MC
Lrp2	29216	LDL receptor related protein 2	1
Flt1	54251	FMS-related tyrosine kinase 1	1
Avil	79253	advillin	1
Ddx3	1E+08	DEAD (Asp-Glu-Ala-Asp) box polypeptide 3	1
Tek	89804	TEK receptor tyrosine kinase	1
Eif2s3y	1E+08	eukaryotic translation initiation factor 2, subunit 3, structural gene Y-linked	1
Dmrt3	293976	doublesex and mab-3 related transcription factor 3	1
Mageb4	317271	melanoma antigen family B, 4	1
Tbx1	360737	T-box 1	1
Adprhl1	290880	ADP-ribosylhydrolase like 1	1
Bpgm	296973	bisphosphoglycerate mutase	-1
Adcy7	84420	adenylate cyclase 7	-1
Sirpa	25528	signal-regulatory protein alpha	-1
Npdc1	296562	neural proliferation, differentiation and control, 1	-1
Prkag2	373545	protein kinase AMP-activated non-catalytic subunit gamma 2	-1
Shroom3	305230	shroom family member 3	-1
Prkar1b	25521	protein kinase cAMP-dependent type 1 regulatory subunit beta	-1
Ephx2	65030	epoxide hydrolase 2	-1
Rnf130	652955	ring finger protein 130	-1
Myh14	308572	myosin heavy chain 14	-1
Cacna1a	25398	calcium voltage-gated channel subunit alpha1 A	-1
Ctsc	25423	cathepsin C	-1
Ppm1h	314897	protein phosphatase, Mg2+/Mn2+ dependent, 1H	-1
Gspt2	501582	G1 to S phase transition 2	-1
Oasl2	304549	2'-5' oligoadenylate synthetase-like 2	-1
Mb21d2	498100	Mab-21 domain containing 2	-1
Fam83h	362937	family with sequence similarity 83, member H	-1
Bcl3	680611	B-cell CLL/lymphoma 3	-1
RGD1309676	361118	similar to RIKEN cDNA 5730469M10	-1
Plce1	114633	phospholipase C, epsilon 1	-1
Tlr3	364594	toll-like receptor 3	-1

Psmb8	24968	proteasome subunit beta 8	-1
Lifr	81680	leukemia inhibitory factor receptor alpha	-1
Mboat2	313997	membrane bound O-acyltransferase domain containing 2	-1
Tnfrsf21	316256	TNF receptor superfamily member 21	-1
Trpv4	66026	transient receptor potential cation channel, subfamily V, member 4	-1
Ptp4a3	362930	protein tyrosine phosphatase type IVA, member 3	-1
Nsg1	25247	neuron specific gene family member 1	-1
Adra1d	29413	adrenoceptor alpha 1D	-1
Cx3cl1	89808	C-X3-C motif chemokine ligand 1	-1
Elmo1	361251	engulfment and cell motility 1	-1
Slc6a17	613226	solute carrier family 6 member 17	-1
Homer2	29547	homer scaffolding protein 2	-1
Irgm	303090	immunity-related GTPase M	-1
Cdh6	25409	cadherin 6	-1
Htr1b	25075	5-hydroxytryptamine receptor 1B	-1
Creg1	289185	cellular repressor of E1A-stimulated genes 1	-1
LOC500956	500956	hypothetical protein LOC500956	-1
Cyp27a1	301517	cytochrome P450, family 27, subfamily a, polypeptide 1	-1
Rtn1	116644	reticulon 1	-1
Jam2	619374	junctional adhesion molecule 2	-1
Hdac11	297453	histone deacetylase 11	-1
Rragd	297960	Ras-related GTP binding D	-1
Nap1l2	317247	nucleosome assembly protein 1-like 2	-1
Phyhipl	309901	phytanoyl-CoA 2-hydroxylase interacting protein-like	-1
Khdrbs3	64015	KH RNA binding domain containing, signal transduction associated 3	-1
Slc7a4	303787	solute carrier family 7, member 4	-1
Sema4d	306790	semaphorin 4D	-1
Stox2	306459	storkhead box 2	-1
Zfhx4	310250	zinc finger homeobox 4	-1
Hand2	64637	heart and neural crest derivatives expressed 2	-1
Begain	79146	brain-enriched guanylate kinase-associated	-1
Svip	499157	small VCP interacting protein	-1
RGD1310110	361032	similar to 3632451O06Rik protein	-1
Mpp7	307035	membrane palmitoylated protein 7	-1
Sorl1	300652	sortilin related receptor 1	-1
Mafb	54264	MAF bZIP transcription factor B	-1
Fam49a	298890	family with sequence similarity 49, member A	-1
Slc35g1	294072	solute carrier family 35, member G1	-1
Kcnc3	117101	potassium voltage-gated channel subfamily C member 3	-1
Grik2	54257	glutamate ionotropic receptor kainate type subunit 2	-1
Elovl7	361895	ELOVL fatty acid elongase 7	-1
Car13	499566	carbonic anhydrase 13	-1
Mmp13	171052	matrix metallopeptidase 13	-1

Differentially expressed genes (DEGs) by a fold-change of at least 5 in the SIRMu-1 cells, relative to primary MCs. Downregulation is indicated by -1, upregulation by 1.

(C) DEGs only in the rMC-1 cell line relative to 1° MCs.

Gene symbol	**Gene ENTREZID**	**Gene name**	**DEGs in SIRMu-1 compared to 1° MC**
Rrm1	685579	ribonucleotide reductase catalytic subunit M1	1
Smc4	295107	structural maintenance of chromosomes 4	1
Tmpo	25359	thymopoietin	1
Psat1	293820	phosphoserine aminotransferase 1	1
Dek	306817	DEK proto-oncogene	1
Smc2	362519	structural maintenance of chromosomes 2	1
Pcna	25737	proliferating cell nuclear antigen	1
Top2a	360243	topoisomerase (DNA) II alpha	1
H2afz	58940	H2A histone family, member Z	1
Mcm2	312538	minichromosome maintenance complex component 2	1
Fam111a	499322	family with sequence similarity 111, member A	1
Hmgn2	114637	high mobility group nucleosomal binding domain 2	1
Mki67	291234	marker of proliferation Ki-67	1
Mcm4	29728	minichromosome maintenance complex component 4	1
Atad2	314993	ATPase family, AAA domain containing 2	1
Nasp	298441	nuclear autoantigenic sperm protein	1
Prc1	308761	protein regulator of cytokinesis 1	1
Cenpf	257649	centromere protein F	1
Cdkn1b	83571	cyclin-dependent kinase inhibitor 1B	1
Prim1	246327	primase, DNA, polypeptide 1	1
Psip1	313323	PC4 and SFRS1 interacting protein 1	1
Aif1l	362107	allograft inflammatory factor 1-like	1
Dnajc9	364240	DnaJ heat shock protein family (Hsp40) member C9	1
Mcm7	288532	minichromosome maintenance complex component 7	1
Usp1	313387	ubiquitin specific peptidase 1	1
Tpx2	311546	TPX2, microtubule nucleation factor	1
Mcm6	29685	minichromosome maintenance complex component 6	1
Kif23	315740	kinesin family member 23	1
Ezh2	312299	enhancer of zeste 2 polycomb repressive complex 2 subunit	1
Incenp	293733	inner centromere protein	1
Kif20a	361308	kinesin family member 20A	1
Cdk1	54237	cyclin-dependent kinase 1	1
Slfn13	303378	schlafen family member 13	1
Kntc1	304477	kinetochore associated 1	1
Stmn1	29332	stathmin 1	1
Kif11	171304	kinesin family member 11	1
Mcm3	316273	minichromosome maintenance complex component 3	1
Nup85	287830	nucleoporin 85	1
Arhgap11a	296060	Rho GTPase activating protein 11A	1
Amer1	501584	APC membrane recruitment protein 1	1
Ect2	361921	epithelial cell transforming 2	1
Lmnb2	299625	lamin B2	1

Bub1	296137	BUB1 mitotic checkpoint serine/threonine kinase	1
Myrf	293736	myelin regulatory factor	1
Timeless	83508	timeless circadian clock	1
Pola1	85241	DNA polymerase alpha 1, catalytic subunit	1
Mcm5	291885	minichromosome maintenance complex component 5	1
Casp2	64314	caspase 2	1
Lmnb1	116685	lamin B1	1
Tk1	24834	thymidine kinase 1	1
Pole	304573	DNA polymerase epsilon, catalytic subunit	1
Iqgap3	310621	IQ motif containing GTPase activating protein 3	1
Kif20b	309523	kinesin family member 20B	1
Ccnb1	25203	cyclin B1	1
Tacc3	360962	transforming, acidic coiled-coil containing protein 3	1
Cdk2	362817	cyclin dependent kinase 2	1
Wdhd1	305827	WD repeat and HMG-box DNA binding protein 1	1
Fen1	84490	flap structure-specific endonuclease 1	1
Hmmr	25460	hyaluronan-mediated motility receptor	1
Dlgap5	289997	DLG associated protein 5	1
Fads2	83512	fatty acid desaturase 2	1
Ccna2	114494	cyclin A2	1
Rrm2	362720	ribonucleotide reductase regulatory subunit M2	1
Plk1	25515	polo-like kinase 1	1
Spag5	252918	sperm associated antigen 5	1
Foxm1	58921	forkhead box M1	1
Mad2l1	297176	MAD2 mitotic arrest deficient-like 1 (yeast)	1
Zfp367	306695	zinc finger protein 367	1
Mdm1	314859	Mdm1 nuclear protein	1
Cdc20	64515	cell division cycle 20	1
Rpa2	59102	replication protein A2	1
Plk4	310344	polo-like kinase 4	1
Fancd2	312641	Fanconi anemia, complementation group D2	1
Rfc3	288414	replication factor C subunit 3	1
Uhrf1	316129	ubiquitin-like with PHD and ring finger domains 1	1
Siva1	362791	SIVA1, apoptosis-inducing factor	1
Bub1b	171576	BUB1 mitotic checkpoint serine/threonine kinase B	1
Crip2	338401	cysteine-rich protein 2	1
Cdca8	500545	cell division cycle associated 8	1
Mybl2	296344	myeloblastosis oncogene-like 2	1
Brca1	497672	BRCA1, DNA repair associated	1
Brca2	360254	BRCA2, DNA repair associated	1
Kifc1	294286	kinesin family member C1	1
Espl1	315330	extra spindle pole bodies like 1, separase	1
Exosc2	366017	exosome component 2	1
Chek1	140583	checkpoint kinase 1	1
Ccne2	362485	cyclin E2	1
Cks2	498709	CDC28 protein kinase regulatory subunit 2	1

Nusap1	311336	nucleolar and spindle associated protein 1	1
Mms22l	313108	MMS22-like, DNA repair protein	1
Rfc4	288003	replication factor C subunit 4	1
Aurkb	114592	aurora kinase B	1
Orc6	291927	origin recognition complex, subunit 6	1
Hmgb2	29395	high mobility group box 2	1
Rbl1	680111	RB transcriptional corepressor like 1	1
Cdca2	305984	cell division cycle associated 2	1
Nuf2	304951	NUF2, NDC80 kinetochore complex component	1
Ube2c	296368	ubiquitin-conjugating enzyme E2C	1
Racgap1	315298	Rac GTPase-activating protein 1	1
Nup43	683983	nucleoporin 43	1
Tcf19	406195	transcription factor 19	1
Knstrn	311325	kinetochore-localized astrin/SPAG5 binding protein	1
Cdh3	116777	cadherin 3	1
Rfc5	304528	replication factor C subunit 5	1
Kif18b	303575	kinesin family member 18B	1
Pola2	85242	DNA polymerase alpha 2, accessory subunit	1
Rad18	362412	RAD18 E3 ubiquitin protein ligase	1
Mtbp	500870	MDM2 binding protein	1
Ttk	315852	Ttk protein kinase	1
Casc5	NA	NA	1
Kif15	353302	kinesin family member 15	1
Aurka	261730	aurora kinase A	1
Skp2	294790	S-phase kinase-associated protein 2, E3 ubiquitin protein ligase	1
Kif2c	171529	kinesin family member 2C	1
Exosc8	295050	exosome component 8	1
Spc25	295661	SPC25, NDC80 kinetochore complex component	1
Slc38a1	170567	solute carrier family 38, member 1	1
Krt8	25626	keratin 8	1
Ndc80	301701	NDC80 kinetochore complex component	1
Cenpn	361416	centromere protein N	1
Cep55	294074	centrosomal protein 55	1
Cbx2	303730	chromobox 2	1
Hspa4l	294993	heat shock protein 4-like	1
Mcm10	307126	minichromosome maintenance 10 replication initiation factor	1
Cenpi	25448	centromere protein I	1
Fbxo5	292263	F-box protein 5	1
Pmf1	681050	polyamine-modulated factor 1	1
Tube1	361856	tubulin, epsilon 1	1
Melk	362510	maternal embryonic leucine zipper kinase	1
Cdca3	297594	cell division cycle associated 3	1
Rad51ap1	689055	RAD51 associated protein 1	1
Cdkn2c	54238	cyclin-dependent kinase inhibitor 2C	1
Troap	300219	trophinin associated protein	1
Hjurp	316602	Holliday junction recognition protein	1

Depdc1	295538	DEP domain containing 1	1
Pbk	290326	PDZ binding kinase	1
Cdc6	360621	cell division cycle 6	1
Birc5	64041	baculoviral IAP repeat-containing 5	1
Ska3	361047	spindle and kinetochore associated complex subunit 3	1
Gmnn	291137	geminin, DNA replication inhibitor	1
Tprn	499749	taperin	1
Cdc45	287961	cell division cycle 45	1
Cdt1	292071	chromatin licensing and DNA replication factor 1	1
Ddias	499204	DNA damage-induced apoptosis suppressor	1
Kif18a	362186	kinesin family member 18A	1
Mcm8	296178	minichromosome maintenance 8 homologous recombination repair factor	1
Chaf1b	288242	chromatin assembly factor 1 subunit B	1
Xrcc2	499966	X-ray repair cross complementing 2	1
Pkmyt1	287101	protein kinase, membrane associated tyrosine/threonine 1	1
Dhfr	24312	dihydrofolate reductase	1
Recql4	300057	RecQ like helicase 4	1
Mtfr2	1.01E+08	mitochondrial fission regulator 2	1
Cenpk	294712	centromere protein K	1
Asf1b	304648	anti-silencing function 1B histone chaperone	1
LOC498265	498265	similar to hypothetical protein FLJ10706	1
Gins2	292058	GINS complex subunit 2	1
Ns5atp9	300795	NS5A (hepatitis C virus) transactivated protein 9	1
Cenpt	307805	centromere protein T	1
Celsr2	83465	cadherin, EGF LAG seven-pass G-type receptor 2	1
Depdc7	295971	DEP domain containing 7	1
Pttg1	64193	pituitary tumor-transforming 1	1
Fanca	361435	Fanconi anemia, complementation group A	1
Tonsl	366953	tonsoku-like, DNA repair protein	1
Trip13	292206	thyroid hormone receptor interactor 13	1
Gins3	307639	GINS complex subunit 3	1
Dbf4	312046	DBF4 zinc finger	1
Bard1	64557	BRCA1 associated RING domain 1	1
Clspn	298534	claspin	1
Ccnb2	363088	cyclin B2	1
Parpbp	1E+08	PARP1 binding protein	1
Nsl1	498310	NSL1, MIS12 kinetochore complex component	1
Dscc1	299933	DNA replication and sister chromatid cohesion 1	1
Cenpw	689399	centromere protein W	1
Ercc6l	317252	ERCC excision repair 6 like, spindle assembly checkpoint helicase	1
Fam83d	311598	family with sequence similarity 83, member D	1
Stard10	293150	StAR-related lipid transfer domain containing 10	1
Prr11	360591	proline rich 11	1
RGD1306227	310377	similar to 4833420G17Rik protein	1
Scd1	NA	NA	1
Pard6b	362279	par-6 family cell polarity regulator beta	1

Rad51	499870	RAD51 recombinase	1
Ska1	291441	spindle and kinetochore associated complex subunit 1	1
Lhx2	296706	LIM homeobox 2	1
Cenpm	315164	centromere protein M	1
Cdca7	311742	cell division cycle associated 7	1
Cenpq	363198	centromere protein Q	1
Cenpu	306464	centromere protein U	1
Exo1	305000	exonuclease 1	1
Polq	288079	DNA polymerase theta	1
Gins1	499914	GINS complex subunit 1	1
E2f7	314818	E2F transcription factor 7	1
Rad54l	298429	RAD54 like (S. cerevisiae)	1
Sass6	310807	SAS-6 centriolar assembly protein	1
Psrc1	691380	proline and serine rich coiled-coil 1	1
Fancb	501552	Fanconi anemia, complementation group B	1
Nek2	114482	NIMA-related kinase 2	1
Orc1	313479	origin recognition complex, subunit 1	1
Exnef	309036	exonuclease NEF-sp	1
Pole2	299112	DNA polymerase epsilon 2, accessory subunit	1
Traip	367167	TRAF-interacting protein	1
Sapcd2	680531	suppressor APC domain containing 2	1
Ube2t	360847	ubiquitin-conjugating enzyme E2T	1
Rab15	299156	RAB15, member RAS oncogene family	1
Gpr19	312787	G protein-coupled receptor 19	1
Igsf9	304982	immunoglobulin superfamily, member 9	1
Depdc1b	310074	DEP domain containing 1B	1
Cep70	367153	centrosomal protein 70	1
Mxd3	252915	Max dimerization protein 3	1
Cenpa	298850	centromere protein A	1
Msh5	294252	mutS homolog 5	1
Arrb2	25388	arrestin, beta 2	1
Rad54b	313063	RAD54 homolog B (S. cerevisiae)	1
Cdca5	684771	cell division cycle associated 5	1
Tst	25274	thiosulfate sulfurtransferase	1
LOC303566	303566	E2F1-inducible gene	1
Psmb9	24967	proteasome subunit beta 9	1
Dctpp1	192252	dCTP pyrophosphatase 1	1
Atp2c2	171496	ATPase secretory pathway Ca2+ transporting 2	1
Srd5a1	24950	steroid 5 alpha-reductase 1	1
L1cam	50687	L1 cell adhesion molecule	1
Eme1	287634	essential meiotic structure-specific endonuclease 1	1
Nup210	58958	nucleoporin 210	1
Lmo1	245979	LIM domain only 1	1
Gatm	81660	glycine amidinotransferase	1
Ccsap	307926	centriole, cilia and spindle-associated protein	1
Cd24	25145	CD24 molecule	1

Tmem173	498840	transmembrane protein 173	1
Fignl1	289777	fidgetin-like 1	1
Ppl	302934	periplakin	1
Xk	497078	X-linked Kx blood group	1
Neil3	290729	nei-like DNA glycosylase 3	1
Tfcp2l1	304741	transcription factor CP2-like 1	1
Lsr	64355	lipolysis stimulated lipoprotein receptor	1
Rhox5	24631	reproductive homeobox 5	1
Slc29a4	288499	solute carrier family 29 member 4	1
Mecom	294924	MDS1 and EVI1 complex locus	1
Slc16a14	316578	solute carrier family 16, member 14	1
Efna2	84358	ephrin A2	1
Efcab11	500705	EF-hand calcium binding domain 11	1
Mlf1	310483	myeloid leukemia factor 1	1
Padi3	29520	peptidyl arginine deiminase 3	1
Apold1	444983	apolipoprotein L domain containing 1	1
B4galnt4	309105	beta-1,4-N-acetyl-galactosaminyl transferase 4	1
Smpd3	94338	sphingomyelin phosphodiesterase 3	1
Pard6a	307799	par-6 family cell polarity regulator alpha	1
Pde3b	29516	phosphodiesterase 3B	1
Rps6ka6	317203	ribosomal protein S6 kinase A6	1
Mab21l1	688394	mab-21 like 1	1
Asb12	503446	ankyrin repeat and SOCS box-containing 12	1
Them6	300015	thioesterase superfamily member 6	1
Rfx2	301121	regulatory factor X2	1
Gchfr	171128	GTP cyclohydrolase I feedback regulator	1
Lck	313050	LCK proto-oncogene, Src family tyrosine kinase	1
Lrr1	685860	leucine rich repeat protein 1	1
Sptb	314251	spectrin, beta, erythrocytic	1
Ybx2	303250	Y box binding protein 2	1
Cxcl10	245920	C-X-C motif chemokine ligand 10	1
Bst2	378947	bone marrow stromal cell antigen 2	1
Tjp3	314640	tight junction protein 3	1
Sall1	307740	spalt-like transcription factor 1	1
Foxn1	287469	forkhead box N1	1
Mir25	1E+08	microRNA 25	1
RT1-CE6	415073	RT1 class I, locus CE6	1
Hoxc4	24459	homeo box C4	1
Gper1	171104	G protein-coupled estrogen receptor 1	1
Dapp1	362046	dual adaptor of phosphotyrosine and 3-phosphoinositides 1	1
Fcho1	290639	FCH domain only 1	1
Phactr1	306844	phosphatase and actin regulator 1	1
B3gnt5	116740	UDP-GlcNAc:betaGal beta-1,3-N-acetylglucosaminyltransferase 5	1
Cdhr5	171554	cadherin-related family member 5	1
Cdx2	66019	caudal type homeo box 2	1
Krt15	287700	keratin 15	1

Tspan8	171048	tetraspanin 8	1
MAST1	353118	microtubule associated serine/threonine kinase 1	1
Foxa2	25099	forkhead box A2	1
Dennd2d	310772	DENN domain containing 2D	1
Hist3h2ba	303175	histone cluster 3, H2ba	1
Dok7	305448	docking protein 7	1
Runx3	156726	runt-related transcription factor 3	1
Grhl2	299979	grainyhead-like transcription factor 2	1
Hnf1b	25640	HNF1 homeobox B	1
Hoxa2	1.04E+08	homeo box A2	1
Apol3	315108	apolipoprotein L, 3	1
Hpgd	79242	hydroxyprostaglandin dehydrogenase 15 (NAD)	1
Slc17a7	116638	solute carrier family 17 member 7	1
Usp44	314746	ubiquitin specific peptidase 44	1
Hhex	79237	hematopoietically expressed homeobox	1
Oasl	304545	2'-5'-oligoadenylate synthetase-like	1
Defb29	641519	defensin beta 29	1
Gata4	54254	GATA binding protein 4	1
Inhbe	83711	inhibin beta E subunit	1
C5ar2	445269	complement component 5a receptor 2	1
Cecr2	500308	CECR2, histone acetyl-lysine reader	1
Hoxb9	287647	homeo box B9	1
Slc9b1	365946	solute carrier family 9 member B1	1
Hoxc10	315338	homeo box C10	1
Ifit1	56824	interferon-induced protein with tetratricopeptide repeats 1	1
Mpp3	114202	membrane palmitoylated protein 3	1
S1pr5	60399	sphingosine-1-phosphate receptor 5	1
Htr5b	79247	5-hydroxytryptamine (serotonin) receptor 5B	1
Bnc1	365299	basonuclin 1	1
Tal1	313507	TAL bHLH transcription factor 1, erythroid differentiation factor	1
Hoxc9	368178	homeobox C9	1
Hoxb3	303488	homeo box B3	1
Fabp12	499570	fatty acid binding protein 12	1
Hmx3	293537	H6 family homeobox 3	1
Tex101	207113	testis expressed 101	1
Mak	25677	male germ cell-associated kinase	1
R3hdml	366245	R3H domain containing-like	1
Nr0b2	117274	nuclear receptor subfamily 0, group B, member 2	1
Col1a1	29393	collagen type I alpha 1 chain	-1
Fn1	25661	fibronectin 1	-1
Thbs1	445442	thrombospondin 1	-1
Sparc	24791	secreted protein acidic and cysteine rich	-1
Col3a1	84032	collagen type III alpha 1 chain	-1
Bgn	25181	biglycan	-1
Fat1	83720	FAT atypical cadherin 1	-1
Col4a1	290905	collagen type IV alpha 1 chain	-1

Fbn1	83727	fibrillin 1	-1
Tpm2	500450	tropomyosin 2, beta	-1
Ltbp2	59106	latent transforming growth factor beta binding protein 2	-1
Postn	361945	periostin	-1
Pdgfrb	24629	platelet derived growth factor receptor beta	-1
Ccng1	25405	cyclin G1	-1
Lamp1	25328	lysosomal-associated membrane protein 1	-1
Pam	25508	peptidylglycine alpha-amidating monooxygenase	-1
Htra1	65164	HtrA serine peptidase 1	-1
Col8a1	304021	collagen type VIII alpha 1 chain	-1
Adam19	303068	ADAM metallopeptidase domain 19	-1
Itm2c	301575	integral membrane protein 2C	-1
Mmp14	81707	matrix metallopeptidase 14	-1
Map1a	25152	microtubule-associated protein 1A	-1
Flnc	362332	filamin C	-1
Sulf1	171396	sulfatase 1	-1
Npc2	286898	NPC intracellular cholesterol transporter 2	-1
Cpe	25669	carboxypeptidase E	-1
Bc1	29294	brain cytoplasmic RNA 1	-1
Pdlim1	54133	PDZ and LIM domain 1	-1
Cdkn1a	114851	cyclin-dependent kinase inhibitor 1A	-1
Akap12	83425	A-kinase anchoring protein 12	-1
Myl9	296313	myosin light chain 9	-1
Fkbp10	360627	FK506 binding protein 10	-1
Nucb2	59295	nucleobindin 2	-1
Adamts12	294809	ADAM metallopeptidase with thrombospondin type 1 motif, 12	-1
Nid2	302248	nidogen 2	-1
Itga11	315744	integrin subunit alpha 11	-1
Mmp2	81686	matrix metallopeptidase 2	-1
Igfbp7	289560	insulin-like growth factor binding protein 7	-1
Hmox1	24451	heme oxygenase 1	-1
Fam198b	310540	family with sequence similarity 198, member B	-1
Lbh	683626	limb bud and heart development	-1
Fbln5	29158	fibulin 5	-1
Ehbp1l1	309169	EH domain binding protein 1-like 1	-1
Chpf	316533	chondroitin polymerizing factor	-1
Fam129a	63912	family with sequence similarity 129, member A	-1
Tp53inp2	362246	tumor protein p53 inducible nuclear protein 2	-1
Serpinf1	287526	serpin family F member 1	-1
Emilin1	298845	elastin microfibril interfacer 1	-1
Npr3	25339	natriuretic peptide receptor 3	-1
Gpr176	117257	G protein-coupled receptor 176	-1
Gpc4	317322	glypican 4	-1
Wisp2	29576	WNT1 inducible signaling pathway protein 2	-1
P3h3	297595	prolyl 3-hydroxylase 3	-1
Anxa3	25291	annexin A3	-1

Dkk3	171548	dickkopf WNT signaling pathway inhibitor 3	-1
Pdzrn3	312607	PDZ domain containing RING finger 3	-1
Pragmin	306506	pragma of Rnd2	-1
Smim14	364154	small integral membrane protein 14	-1
Hist1h2bh	306945	histone cluster 1, H2bh	-1
Spp1	25353	secreted phosphoprotein 1	-1
Lmcd1	494021	LIM and cysteine-rich domains 1	-1
Scara5	305974	scavenger receptor class A, member 5	-1
Nkd2	308068	naked cuticle homolog 2	-1
Tll1	678743	tolloid-like 1	-1
Aebp1	305494	AE binding protein 1	-1
Sulf2	311642	sulfatase 2	-1
Marveld1	309375	MARVEL domain containing 1	-1
Nexn	246172	nexilin (F actin binding protein)	-1
Jam3	315509	junctional adhesion molecule 3	-1
Tfpi	29436	tissue factor pathway inhibitor	-1
Rin2	311494	Ras and Rab interactor 2	-1
Sat1	302642	spermidine/spermine N1-acetyl transferase 1	-1
Mmp19	304608	matrix metallopeptidase 19	-1
Cdh11	84407	cadherin 11	-1
Wfdc1	171112	WAP four-disulfide core domain 1	-1
Npr2	116564	natriuretic peptide receptor 2	-1
Gpnmb	113955	glycoprotein nmb	-1
Tcn2	64365	transcobalamin 2	-1
Ptprn	116660	protein tyrosine phosphatase, receptor type, N	-1
Wfs1	83725	wolframin ER transmembrane glycoprotein	-1
Grb10	498416	growth factor receptor bound protein 10	-1
Aen	361594	apoptosis enhancing nuclease	-1
Rasl11b	305302	RAS-like family 11 member B	-1
Cd59	25407	CD59 molecule	-1
Itga8	364786	integrin subunit alpha 8	-1
Ddah2	294239	dimethylarginine dimethylaminohydrolase 2	-1
Mrvi1	308899	murine retrovirus integration site 1 homolog	-1
Cnn1	65204	calponin 1	-1
Il1r1	25663	interleukin 1 receptor type 1	-1
Pcsk6	25507	proprotein convertase subtilisin/kexin type 6	-1
Ehd3	192249	EH-domain containing 3	-1
Tgfb1i1	84574	transforming growth factor beta 1 induced transcript 1	-1
Lmod1	304816	leiomodin 1	-1
Nfatc4	305897	nuclear factor of activated T-cells 4	-1
Dsel	297865	dermatan sulfate epimerase-like	-1
Scara3	364405	scavenger receptor class A, member 3	-1
Cdh13	192248	cadherin 13	-1
Nbl1	50594	neuroblastoma 1, DAN family BMP antagonist	-1
Plxdc2	361282	plexin domain containing 2	-1
C1qtnf6	315114	C1q and tumor necrosis factor related protein 6	-1

Zfp36l1	29344	zinc finger protein 36, C3H type-like 1	-1
Grb14	58844	growth factor receptor bound protein 14	-1
Neu1	24591	neuraminidase 1	-1
Tgfa	24827	transforming growth factor alpha	-1
Plekhh2	313866	pleckstrin homology, MyTH4 and FERM domain containing H2	-1
Ckb	24264	creatine kinase B	-1
Cyba	79129	cytochrome b-245 alpha chain	-1
Tmem119	304581	transmembrane protein 119	-1
Flrt2	299236	fibronectin leucine rich transmembrane protein 2	-1
Pla2g16	24913	phospholipase A2, group XVI	-1
Flvcr2	314323	feline leukemia virus subgroup C cellular receptor family, member 2	-1
Fam214b	298201	family with sequence similarity 214, member B	-1
Abca1	313210	ATP binding cassette subfamily A member 1	-1
Prss35	315866	protease, serine, 35	-1
Ptprk	360302	protein tyrosine phosphatase, receptor type, K	-1
Dact3	499088	dishevelled-binding antagonist of beta-catenin 3	-1
Fgfr2	25022	fibroblast growth factor receptor 2	-1
Timp3	25358	TIMP metallopeptidase inhibitor 3	-1
Abcb1b	24646	ATP-binding cassette, subfamily B (MDR/TAP), member 1B	-1
Pcdh7	360942	protocadherin 7	-1
Cobl	305497	cordon-bleu WH2 repeat protein	-1
Rnase4	56759	ribonuclease A family member 4	-1
Ephx1	25315	epoxide hydrolase 1	-1
Nav3	314814	neuron navigator 3	-1
Itga1	25118	integrin subunit alpha 1	-1
Arhgef6	363509	Rac/Cdc42 guanine nucleotide exchange factor 6	-1
Cpt1c	308579	carnitine palmitoyltransferase 1c	-1
Cacna1c	24239	calcium voltage-gated channel subunit alpha1 C	-1
Qsox1	84491	quiescin sulfhydryl oxidase 1	-1
Sdc3	116673	syndecan 3	-1
Pdgfrl	290771	platelet-derived growth factor receptor-like	-1
Tmem150a	245966	transmembrane protein 150A	-1
Slc8a1	29715	solute carrier family 8 member A1	-1
Fam101b	NA	NA	-1
Palmd	310811	palmdelphin	-1
Jph2	296345	junctophilin 2	-1
Stk39	54348	serine threonine kinase 39	-1
Tfap2b	301285	transcription factor AP-2 beta	-1
Igf2bp2	303824	insulin-like growth factor 2 mRNA binding protein 2	-1
Srpx2	317181	sushi-repeat-containing protein, X-linked 2	-1
Aldh1l2	299699	aldehyde dehydrogenase 1 family, member L2	-1
Arnt2	25243	aryl hydrocarbon receptor nuclear translocator 2	-1
Spry2	306141	sprouty RTK signaling antagonist 2	-1
Pla2g4a	24653	phospholipase A2 group IVA	-1
Npl	304860	N-acetylneuraminate pyruvate lyase	-1

Acad11	315973	acyl-CoA dehydrogenase family, member 11	-1
Trim2	361970	tripartite motif-containing 2	-1
Trib2	313974	tribbles pseudokinase 2	-1
Mme	24590	membrane metallo-endopeptidase	-1
Gpx7	298376	glutathione peroxidase 7	-1
Ctsh	25425	cathepsin H	-1
Tmem223	690285	transmembrane protein 223	-1
Arhgap24	305156	Rho GTPase activating protein 24	-1
Dhrs3	313689	dehydrogenase/reductase 3	-1
Prkg1	54286	protein kinase, cGMP-dependent, type 1	-1
Cntn2	25356	contactin 2	-1
Fblim1	362650	filamin binding LIM protein 1	-1
Sema4g	361764	semaphorin 4G	-1
Pappa	313262	pregnancy-associated plasma protein A	-1
Baiap2l1	304282	BAI1-associated protein 2-like 1	-1
Prickle2	312563	prickle planar cell polarity protein 2	-1
Nkain4	296469	Na+/K+ transporting ATPase interacting 4	-1
RGD1311756	362769	similar to hypothetical protein FLJ20950	-1
Shroom4	317391	shroom family member 4	-1
Papss2	294103	3'-phosphoadenosine 5'-phosphosulfate synthase 2	-1
Avpr1a	25107	arginine vasopressin receptor 1A	-1
RGD1562618	501007	similar to RIKEN cDNA 6030419C18 gene	-1
Bend6	363212	BEN domain containing 6	-1
Gria3	29628	glutamate ionotropic receptor AMPA type subunit 3	-1
Nudt18	361068	nudix hydrolase 18	-1
Prrx1	266813	paired related homeobox 1	-1
Lims2	361303	LIM zinc finger domain containing 2	-1
Gpr153	619550	G protein-coupled receptor 153	-1
Nfia	25492	nuclear factor I/A	-1
Uchl1	29545	ubiquitin C-terminal hydrolase L1	-1
Cybrd1	295669	cytochrome b reductase 1	-1
Dlg3	58948	discs large MAGUK scaffold protein 3	-1
Ntm	50864	neurotrimin	-1
Smarca1	317575	SWI/SNF related, matrix associated, actin dependent regulator of chromatin, subfamily a, member 1	-1
Pitx2	54284	paired-like homeodomain 2	-1
Adm	25026	adrenomedullin	-1
Rab27a	50645	RAB27A, member RAS oncogene family	-1
Aff3	363220	AF4/FMR2 family, member 3	-1
Trpv2	29465	transient receptor potential cation channel, subfamily V, member 2	-1
Gnb4	294962	G protein subunit beta 4	-1
Apc2	299611	APC2, WNT signaling pathway regulator	-1
Sdk2	360652	sidekick cell adhesion molecule 2	-1
Ppt2	54398	palmitoyl-protein thioesterase 2	-1
Rftn1	501095	raftlin lipid raft linker 1	-1
Unc13a	64829	unc-13 homolog A	-1
Scn2a	24766	sodium voltage-gated channel alpha subunit 2	-1

C2	24231	complement C2	-1
Ptprv	64576	protein tyrosine phosphatase, receptor type, V	-1
Mgmt	25332	O-6-methylguanine-DNA methyltransferase	-1
Galt	298003	galactose-1-phosphate uridylyltransferase	-1
Ptgs1	24693	prostaglandin-endoperoxide synthase 1	-1
Scube3	294297	signal peptide, CUB domain and EGF like domain containing 3	-1
Itpr2	81678	inositol 1,4,5-trisphosphate receptor, type 2	-1
Il1rl2	171106	interleukin 1 receptor-like 2	-1
Itpkb	54260	inositol-trisphosphate 3-kinase B	-1
Galnt13	311039	polypeptide N-acetylgalactosaminyltransferase 13	-1
Dhtkd1	361272	dehydrogenase E1 and transketolase domain containing 1	-1
Sox9	140586	SRY box 9	-1
Clmp	286939	CXADR-like membrane protein	-1
Peg3	1.04E+08	paternally expressed 3	-1
Cd48	245962	Cd48 molecule	-1
Ctsz	252929	cathepsin Z	-1
Efs	290212	embryonal Fyn-associated substrate	-1
Cyp4f6	266689	cytochrome P450, family 4, subfamily f, polypeptide 6	-1
Armcx6	363496	armadillo repeat containing, X-linked 6	-1
Cdc42ep5	361505	CDC42 effector protein 5	-1
Mapkapk3	315994	mitogen-activated protein kinase-activated protein kinase 3	-1
C1qtnf2	497886	C1q and tumor necrosis factor related protein 2	-1
Ror2	306782	receptor tyrosine kinase-like orphan receptor 2	-1
Slc2a10	366251	solute carrier family 2 member 10	-1
Triqk	500413	triple QxxK/R motif containing	-1
Manba	310864	mannosidase beta	-1
Rhoj	299145	ras homolog family member J	-1
Slc2a13	171147	solute carrier family 2 member 13	-1
Trim16	303214	tripartite motif-containing 16	-1
Dmd	24907	dystrophin	-1
Gatsl3	360969	GATS protein-like 3	-1
Rorb	309288	RAR-related orphan receptor B	-1
Usp13	310306	ubiquitin specific peptidase 13	-1
Def6	309642	DEF6 guanine nucleotide exchange factor	-1
Dcn	29139	decorin	-1
Zfp521	307579	zinc finger protein 521	-1
Asah2	114104	N-acylsphingosine amidohydrolase 2	-1
Mks1	287612	Meckel syndrome, type 1	-1
Fbxl7	361907	F-box and leucine-rich repeat protein 7	-1
Paqr7	313615	progestin and adipoQ receptor family member 7	-1
Prickle3	317380	prickle planar cell polarity protein 3	-1
Shc2	314612	SHC adaptor protein 2	-1
Pde10a	63885	phosphodiesterase 10A	-1
Wnt5a	64566	wingless-type MMTV integration site family, member 5A	-1
Tnfrsf10b	364420	tumor necrosis factor receptor superfamily, member 10b	-1
Rbpms	498642	RNA binding protein with multiple splicing	-1

Col15a1	298069	collagen type XV alpha 1 chain	-1
Phactr2	308291	phosphatase and actin regulator 2	-1
Nr2f1	81808	nuclear receptor subfamily 2, group F, member 1	-1
Pparg	25664	peroxisome proliferator-activated receptor gamma	-1
Zmym6	362602	zinc finger MYM-type containing 6	-1
Epb41l3	116724	erythrocyte membrane protein band 4.1-like 3	-1
Slc9a9	363115	solute carrier family 9 member A9	-1
Ghr	25235	growth hormone receptor	-1
Smim1	500595	small integral membrane protein 1	-1
Mycbpap	494192	Mycbp associated protein	-1
Adcy5	64532	adenylate cyclase 5	-1
Dync2li1	298767	dynein cytoplasmic 2 light intermediate chain 1	-1
Tmem204	287129	transmembrane protein 204	-1
Csgalnact1	306375	chondroitin sulfate N-acetylgalactosaminyltransferase 1	-1
Plag1	297804	PLAG1 zinc finger	-1
Cyp4v3	266761	cytochrome P450, family 4, subfamily v, polypeptide 3	-1
Procr	362248	protein C receptor	-1
Plac9	361105	placenta-specific 9	-1
Tox	362481	thymocyte selection-associated high mobility group box	-1
Enpep	64017	glutamyl aminopeptidase	-1
Efhc1	301295	EF-hand domain containing 1	-1
Hecw2	316395	HECT, C2 and WW domain containing E3 ubiquitin protein ligase 2	-1
Nap1l3	170914	nucleosome assembly protein 1-like 3	-1
Ppfia4	140592	PTPRF interacting protein alpha 4	-1
Fam46a	300870	family with sequence similarity 46, member A	-1
Tmsbl1	286978	thymosin beta-like protein 1	-1
Abtb2	171440	ankyrin repeat and BTB domain containing 2	-1
Ebpl	361054	emopamil binding protein-like	-1
LOC100909539	1.01E+08	uncharacterized LOC100909539	-1
Htr2a	29595	5-hydroxytryptamine receptor 2A	-1
Rgs7bp	294715	regulator of G-protein signaling 7 binding protein	-1
Figf	NA	NA	-1
Il17rd	498576	interleukin 17 receptor D	-1
Nudt22	293703	nudix hydrolase 22	-1
Rps6ka2	117269	ribosomal protein S6 kinase polypeptide 2	-1
Rgs16	360857	regulator of G-protein signaling 16	-1
Mageh1	367767	MAGE family member H1	-1
Cd80	25408	Cd80 molecule	-1
Mansc1	690606	MANSC domain containing 1	-1
Pak3	29433	p21 (RAC1) activated kinase 3	-1
Rasl10b	303382	RAS-like, family 10, member B	-1
Cys1	690489	cystin 1	-1
Irx2	306657	iroquois homeobox 2	-1
Nudt7	361413	nudix hydrolase 7	-1
Nlrp3	287362	NLR family, pyrin domain containing 3	-1
Emx2	499380	empty spiracles homeobox 2	-1

Kcnd3	65195	potassium voltage-gated channel subfamily D member 3	-1
Thsd7a	500032	thrombospondin type 1 domain containing 7A	-1
Rims1	84556	regulating synaptic membrane exocytosis 1	-1
Nipal2	362899	NIPA-like domain containing 2	-1
Stc1	81801	stanniocalcin 1	-1
S1pr1	29733	sphingosine-1-phosphate receptor 1	-1
LOC690276	690276	hypothetical protein LOC690276	-1
Pde3a	50678	phosphodiesterase 3A	-1
Fam173a	287150	family with sequence similarity 173, member A	-1
Pcdha4	116741	protocadherin alpha 4	-1
Rcan2	140666	regulator of calcineurin 2	-1
Gnai1	25686	G protein subunit alpha i1	-1
Ly96	448830	lymphocyte antigen 96	-1
Tram1l1	310846	translocation associated membrane protein 1-like 1	-1
Camk2n1	287005	calcium/calmodulin-dependent protein kinase II inhibitor 1	-1
Tspyl4	309828	TSPY-like 4	-1
Zrsr1	498425	zinc finger (CCCH type), RNA binding motif and serine/arginine rich 1	-1
Ache	83817	acetylcholinesterase	-1
Nalcn	266760	sodium leak channel, non-selective	-1
Pth1r	56813	parathyroid hormone 1 receptor	-1
Pln	64672	phospholamban	-1
B3gnt7	316583	UDP-GlcNAc:betaGal beta-1,3-N-acetylglucosaminyltransferase 7	-1
Inpp4b	116699	inositol polyphosphate-4-phosphatase type II B	-1
Ogdhl	290566	oxoglutarate dehydrogenase-like	-1
Pde4a	25638	phosphodiesterase 4A	-1
Tmem246	362518	transmembrane protein 246	-1
Eda	302424	ectodysplasin-A	-1
Hspb7	50565	heat shock protein family B (small) member 7	-1
Tmem30b	314224	transmembrane protein 30B	-1
Peg12	308692	paternally expressed 12	-1
Lyn	81515	LYN proto-oncogene, Src family tyrosine kinase	-1
Fndc5	260327	fibronectin type III domain containing 5	-1
Alx4	296511	ALX homeobox 4	-1
Fam58b	303321	family with sequence similarity 58, member B	-1
Cdo1	81718	cysteine dioxygenase type 1	-1
Ptafr	58949	platelet-activating factor receptor	-1
Apobec3b	315137	apolipoprotein B mRNA editing enzyme catalytic subunit 3B	-1
Fut4	60670	fucosyltransferase 4	-1
Itgb3	29302	integrin subunit beta 3	-1
Tbx3	353305	T-box 3	-1
Adam23	301460	ADAM metallopeptidase domain 23	-1
Gda	83585	guanine deaminase	-1
Ophn1	312108	oligophrenin 1	-1
Ppp1r3d	689995	protein phosphatase 1, regulatory subunit 3D	-1
Ttc12	300696	tetratricopeptide repeat domain 12	-1

Tmem220	287405	transmembrane protein 220	-1
Dock11	313438	dedicator of cytokinesis 11	-1
Dcxr	171408	dicarbonyl and L-xylulose reductase	-1
Celf4	307540	CUGBP, Elav-like family member 4	-1
Ppapdc3	NA	NA	-1
Rgs8	54297	regulator of G-protein signaling 8	-1
Ndst3	295430	N-deacetylase and N-sulfotransferase 3	-1
Gal3st4	498166	galactose-3-O-sulfotransferase 4	-1
Stxbp6	362734	syntaxin binding protein 6	-1
Adora2b	29316	adenosine A2B receptor	-1
Hic1	303310	hypermethylated in cancer 1	-1
Lpcat2	1E+08	lysophosphatidylcholine acyltransferase 2	-1
Mbp	24547	myelin basic protein	-1
Magi2	113970	membrane associated guanylate kinase, WW and PDZ domain containing 2	-1
Pcdhga2	498846	protocadherin gamma subfamily A, 2	-1
Six2	366542	SIX homeobox 2	-1
Smoc2	292401	SPARC related modular calcium binding 2	-1
Clec2g	362447	C-type lectin domain family 2, member G	-1
Tmem14a	363206	transmembrane protein 14A	-1
Gpc2	171517	glypican 2	-1
Cln3	293485	ceroid-lipofuscinosis, neuronal 3	-1
Vstm4	361112	V-set and transmembrane domain containing 4	-1
Tbx15	295315	T-box 15	-1
Nova1	298992	NOVA alternative splicing regulator 1	-1
Calcrl	25029	calcitonin receptor-like	-1
Tmod2	58814	tropomodulin 2	-1
Klhl31	315833	kelch-like family member 31	-1
Fgf10	25443	fibroblast growth factor 10	-1
Tbx2	303398	T-box 2	-1
Acyp2	364224	acylphosphatase 2	-1
Vsnl1	24877	visinin-like 1	-1
Kcng1	296395	potassium voltage-gated channel modifier subfamily G member 1	-1
Zfp385d	305691	zinc finger protein 385D	-1
Lpar4	302378	lysophosphatidic acid receptor 4	-1
Zfp37	115768	zinc finger protein 37	-1
Plscr1	117540	phospholipid scramblase 1	-1
Scube1	315174	signal peptide, CUB domain and EGF like domain containing 1	-1
Epm2a	114005	epilepsy, progressive myoclonus type 2A	-1
Nipal4	303070	NIPA-like domain containing 4	-1
Tmem86a	308602	transmembrane protein 86A	-1
Ica1	81024	islet cell autoantigen 1	-1
Cdyl2	292044	chromodomain Y-like 2	-1
Nr3c2	25672	nuclear receptor subfamily 3, group C, member 2	-1
St6galnac3	29758	ST6 N-acetylgalactosaminide alpha-2,6-sialyltransferase 3	-1
Cd302	295629	CD302 molecule	-1

Hdac9	687001	histone deacetylase 9	-1
LOC501110	501110	similar to Glutathione S-transferase A1 (GTH1) (HA subunit 1) (GST-epsilon) (GSTA1-1) (GST class-alpha)	-1
Hrasls5	293711	HRAS-like suppressor family, member 5	-1
Cacnb2	116600	calcium voltage-gated channel auxiliary subunit beta 2	-1
Rab27b	84590	RAB27B, member RAS oncogene family	-1
Matn4	296358	matrilin 4	-1
Atp6v1c2	362802	ATPase H+ transporting V1 subunit C2	-1
Rnf180	685384	ring finger protein 180	-1
Amz1	304317	archaelysin family metallopeptidase 1	-1
Fez1	81730	fasciculation and elongation protein zeta 1	-1
Cds1	81925	CDP-diacylglycerol synthase 1	-1
Negr1	59318	neuronal growth regulator 1	-1
Cap2	116653	CAP, adenylate cyclase-associated protein, 2 (yeast)	-1
Aard	246323	alanine and arginine rich domain containing protein	-1
Slc25a27	85262	solute carrier family 25, member 27	-1
Pcdhb3	291656	protocadherin beta 3	-1
Nme4	685679	NME/NM23 nucleoside diphosphate kinase 4	-1
Nostrin	311111	nitric oxide synthase trafficking	-1
Drp2	66027	dystrophin related protein 2	-1
Dusp15	362238	dual specificity phosphatase 15	-1
Apbb1ip	307171	amyloid beta precursor protein binding family B member 1 interacting protein	-1
Prrt1	406167	proline-rich transmembrane protein 1	-1
Grip1	84016	glutamate receptor interacting protein 1	-1
Syndig1	362235	synapse differentiation inducing 1	-1
Trpc4	84494	transient receptor potential cation channel, subfamily C, member 4	-1
Grm8	60590	glutamate metabotropic receptor 8	-1
Thnsl2	297332	threonine synthase-like 2	-1
Nox1	114243	NADPH oxidase 1	-1
Sema6d	311384	semaphorin 6D	-1
Fbxo41	312504	F-box protein 41	-1
Sdsl	360816	serine dehydratase-like	-1
Pcdhb2	498843	protocadherin beta 2	-1
Rarres2	297073	retinoic acid receptor responder 2	-1
Brinp1	140610	BMP/retinoic acid inducible neural specific 1	-1
Exo5	313563	exonuclease 5	-1
Ptpru	116680	protein tyrosine phosphatase, receptor type, U	-1
Slc16a4	295356	solute carrier family 16, member 4	-1
Adcy8	29241	adenylate cyclase 8	-1
Fmo5	246248	flavin containing monooxygenase 5	-1
Pycard	282817	PYD and CARD domain containing	-1
Fam217b	311692	family with sequence similarity 217, member B	-1
Mdfi	501097	MyoD family inhibitor	-1
Tmem35	308134	transmembrane protein 35	-1
Hs6st3	364476	heparan sulfate 6-O-sulfotransferase 3	-1
Erbb4	59323	erb-b2 receptor tyrosine kinase 4	-1

Zfp583	499068	zinc finger protein 583	-1
Pclo	56768	piccolo (presynaptic cytomatrix protein)	-1
Col1a2	84352	collagen type I alpha 2 chain	-1
Epha3	29210	Eph receptor A3	-1
Ccdc19	NA	NA	-1
Msx2	25483	msh homeobox 2	-1
Sgcd	497892	sarcoglycan, delta	-1
Mir214	1E+08	microRNA 214	-1
Glrb	25456	glycine receptor, beta	-1
Gramd1b	300644	GRAM domain containing 1B	-1
Cmklr1	60669	chemerin chemokine-like receptor 1	-1
Mrgpre	404660	MAS related GPR family member E	-1
Dgkg	25666	diacylglycerol kinase, gamma	-1
Susd2	294335	sushi domain containing 2	-1
Hspa12a	307997	heat shock protein family A (Hsp70) member 12A	-1
Heyl	313575	hes-related family bHLH transcription factor with YRPW motif-like	-1
Spa17	85244	sperm autoantigenic protein 17	-1
Hsd11b1	25116	hydroxysteroid 11-beta dehydrogenase 1	-1
Plcd4	140693	phospholipase C, delta 4	-1
Atp8b1	291555	ATPase phospholipid transporting 8B1	-1
Slc35f1	502421	solute carrier family 35, member F1	-1
Tmem202	691306	transmembrane protein 202	-1
Rem1	366232	RRAD and GEM like GTPase 1	-1
Cnksr2	59322	connector enhancer of kinase suppressor of Ras 2	-1
Lrrtm3	294380	leucine rich repeat transmembrane neuronal 3	-1
Adcy10	59320	adenylate cyclase 10 (soluble)	-1
Plcl1	84587	phospholipase C-like 1	-1
Gsap	311984	gamma-secretase activating protein	-1
Agmo	362732	alkylglycerol monooxygenase	-1
Cacna1d	29716	calcium voltage-gated channel subunit alpha1 D	-1
Tmem45a	680866	transmembrane protein 45A	-1
Prr16	361327	proline rich 16	-1
B3galt1	366064	Beta-1,3-galactosyltransferase 1	-1
Park2	56816	parkin RBR E3 ubiquitin protein ligase	-1
Nkd1	364952	naked cuticle homolog 1	-1
Mgat4a	367252	mannosyl (alpha-1,3-)-glycoprotein beta-1,4-N-acetylglucosaminyltransferase, isozyme A	-1
Clcnkb	79430	chloride voltage-gated channel Kb	-1
Zfp3	497944	zinc finger protein 3	-1
Sema5b	303901	semaphorin 5B	-1
Myrip	360034	myosin VIIA and Rab interacting protein	-1
Ptgir	292661	prostaglandin I2 (prostacyclin) receptor (IP)	-1
Hrasls	288025	HRAS-like suppressor	-1
Cntn3	54279	contactin 3	-1
Nrcam	497815	neuronal cell adhesion molecule	-1
Pcdhac2	393092	protocadherin alpha subfamily C, 2	-1
Thegl	498350	theg spermatid protein-like	-1

Map7	293016	microtubule-associated protein 7	-1
Gpr85	64020	G protein-coupled receptor 85	-1
Rarb	24706	retinoic acid receptor, beta	-1
Rxfp1	295144	relaxin/insulin-like family peptide receptor 1	-1
Mir143	1E+08	microRNA 143	-1
Pde1b	29691	phosphodiesterase 1B	-1
Astn2	1E+08	astrotactin 2	-1
Svop	171442	SV2 related protein	-1
Shisa2	498528	shisa family member 2	-1
Cacng7	140728	calcium voltage-gated channel auxiliary subunit gamma 7	-1
Cdnf	361276	cerebral dopamine neurotrophic factor	-1
Sult2a2	361510	sulfotransferase family 2A, dehydroepiandrosterone (DHEA)-preferring, member 2	-1
Ddit4l2	140582	DNA-damage-inducible transcript 4-like 2	-1
Pak7	311450	p21 (RAC1) activated kinase 7	-1
Fli1	315532	Fli-1 proto-oncogene, ETS transcription factor	-1
Slc2a9	501925	solute carrier family 2 member 9	-1
Mmp9	81687	matrix metallopeptidase 9	-1
Slc6a7	117100	solute carrier family 6 member 7	-1
Cd93	84398	CD93 molecule	-1
Ednrb	50672	endothelin receptor type B	-1
Abcb4	24891	ATP binding cassette subfamily B member 4	-1
Gfra1	25454	GDNF family receptor alpha 1	-1
Ehhadh	171142	enoyl-CoA hydratase and 3-hydroxyacyl CoA dehydrogenase	-1
Htr1f	60448	5-hydroxytryptamine receptor 1F	-1
MGC109340	317409	similar to Microsomal signal peptidase 23 kDa subunit (SPase 22 kDa subunit) (SPC22/23)	-1
Slitrk6	290467	SLIT and NTRK-like family, member 6	-1
Hcn1	84390	hyperpolarization-activated cyclic nucleotide-gated potassium channel 1	-1
Slc16a2	259248	solute carrier family 16 member 2	-1
Ctnna2	297357	catenin alpha 2	-1
LOC100125362	1E+08	hypothetical protein LOC100125362	-1
Il13ra2	171060	interleukin 13 receptor subunit alpha 2	-1
Pcdha3	116780	protocadherin alpha 3	-1

Differentially expressed genes (DEGs) by a fold-change of at least 5 in the rMC-1 cells, relative to primary MCs. Downregulation is indicated by -1, upregulation by 1.

7.6 Seahorse XF Cell Mito Stress Tests of cultured primary and immortalised Müller cells in normoxia

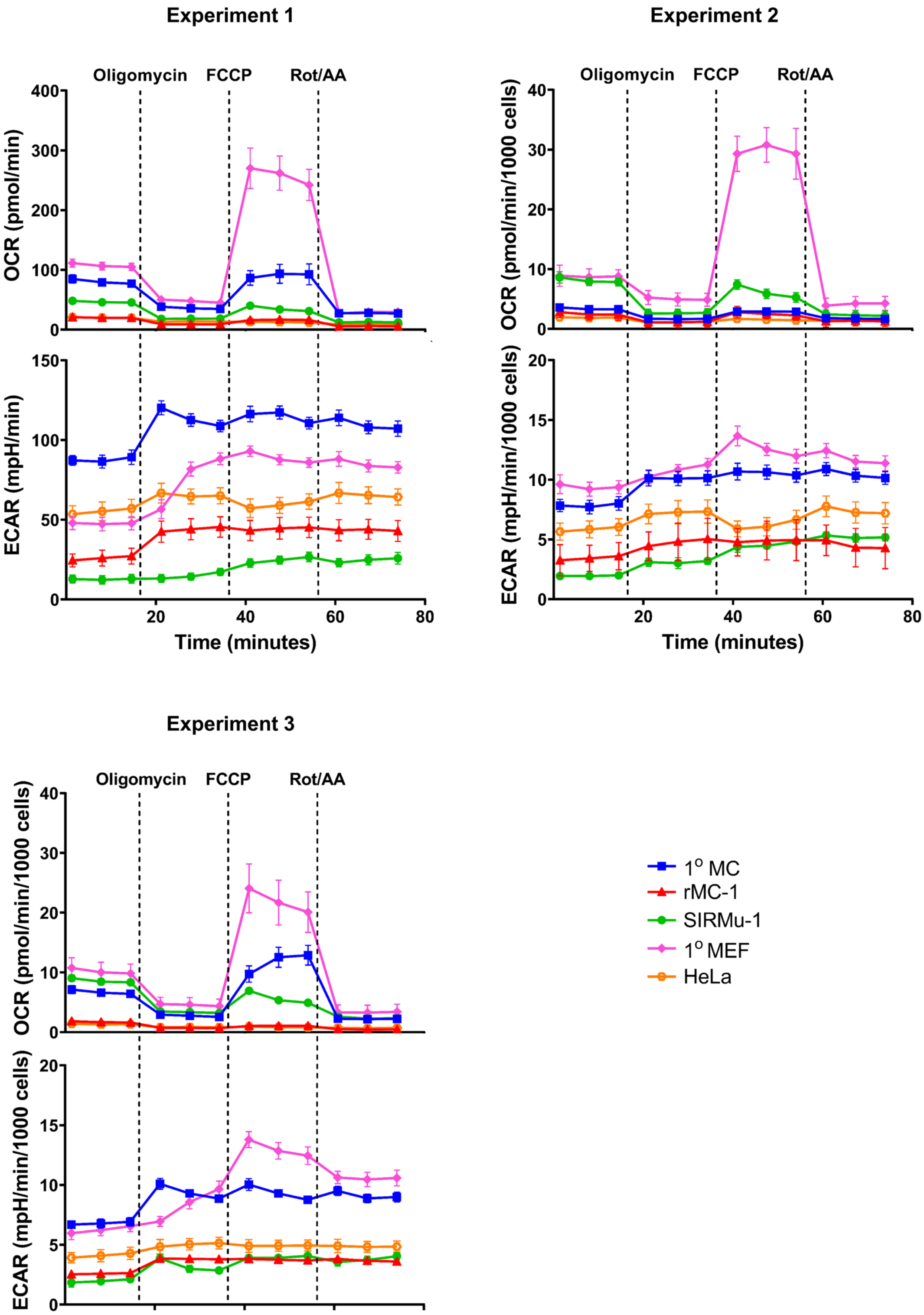

Appendix 7.6. Seahorse XF Cell Mito Stress Tests of cultured primary and immortalised Müller cells in normoxia (associated with Fig 4.3.). Kinetic graphs of oxygen consumption rates (OCRs) and extracellular acidification rates (ECARs) from three independent experiments discussed in Figure 4.3 are shown. Primary (1°) MC (15,000 cells/well), rMC-1 (15,000 cells/well), SIRMu-1 (10,000 cells/well), 1° MEF (15,000 cells/well), and HeLa (10,000 cells/well) cells were seeded in a Seahorse 96-well cell culture. On the following day, cells were washed and incubated in fresh assay medium (XF base medium with 10 mM glucose) for an hour before the medium of each well was collected to use as samples for lactate assays. Cells were then subjected to an XF Cell Mito Stress test where OCRs and ECARs in the presence of glucose (10 mM) were measured by the Seahorse XFe96 extracellular flux analyser at a basal state and after the addition of oligomycin (2 μM), FCCP (0.5 μM), and rotenone/antimycin A (Rot/AA, 0.5 μM). OCRs and ECARs were measured three times during each of the four conditions. Three independent experiments (each with a minimum of six replicate wells per group) were performed, and presented as mean ± SD of each measurement point. In Experiment 1 (labelled in the figure), cell numbers not determined. For Experiment 2 and Experiment 3 (labelled in the figure), cell numbers were determined after the Cell Mito Stress tests by fluorescence microscopy after Hoechst 33342 nuclear staining.

7.7 FCCP concentration testing in a Seahorse XF Cell Mito Stress Test in SIRMu-1 cells

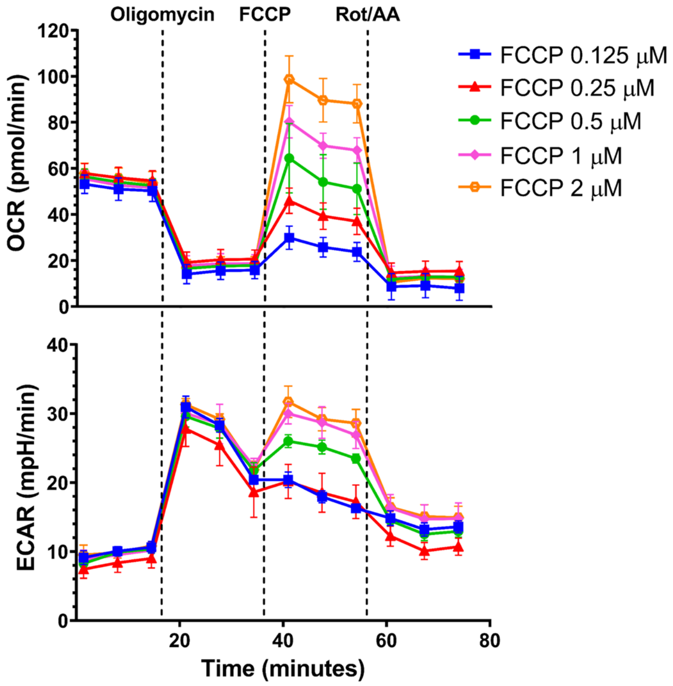

Appendix 7.7. FCCP concentration testing in a Seahorse XF Cell Mito Stress Test in SIRMu-1 cells. Cells were seeded in a Seahorse 96-well cell culture plate at 10,000 cells per well. On the following day, an XF Cell Mito Stress test was performed where oxygen consumption rates (OCRs) and extracellular acidification rates (ECARs) in the presence of glucose (10 mM), glutamine (2 mM) and sodium pyruvate (1 mM) were measured simultaneously by the Seahorse XFe96 extracellular flux analyser at a basal state and after the addition of oligomycin (2 μM), FCCP (various concentrations as indicated), and rotenone/antimycin A (Rot/AA, 0.5 μM). OCRs and ECARs were measured three times during each of the four conditions. Data from one experiment, presented as mean ± SD of each measurement point from four replicate wells per group.

7.8 Seahorse XF Cell Mito Stress Tests of PKM2 knockdown rMC-1 cells

Experiment 1

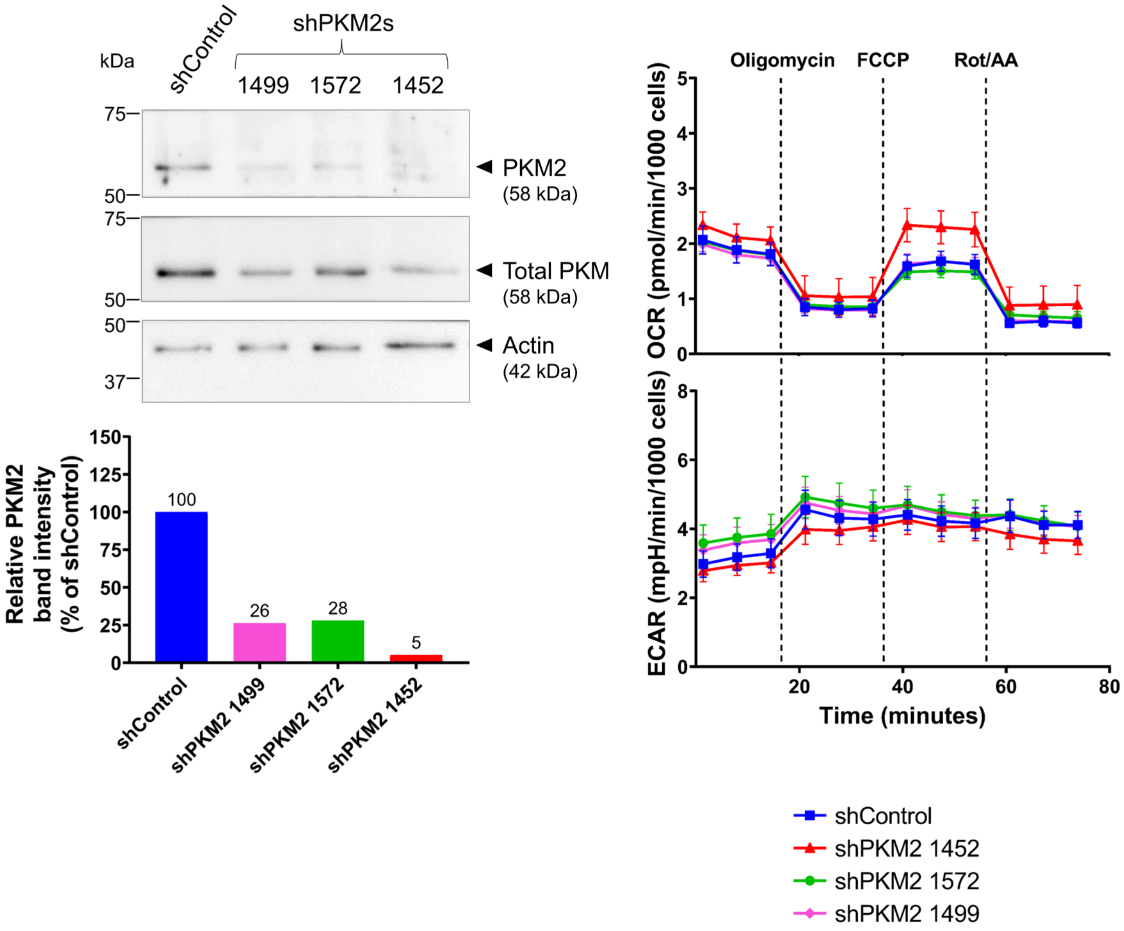

Experiment 2

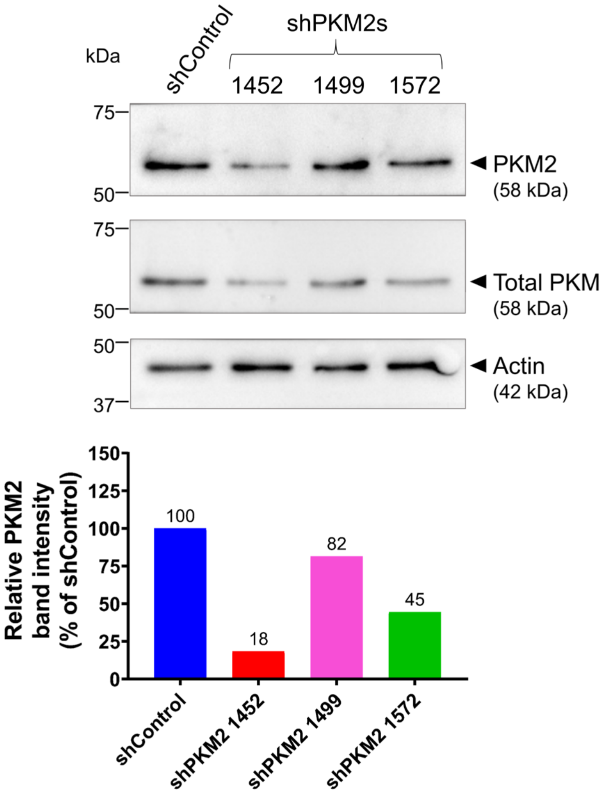

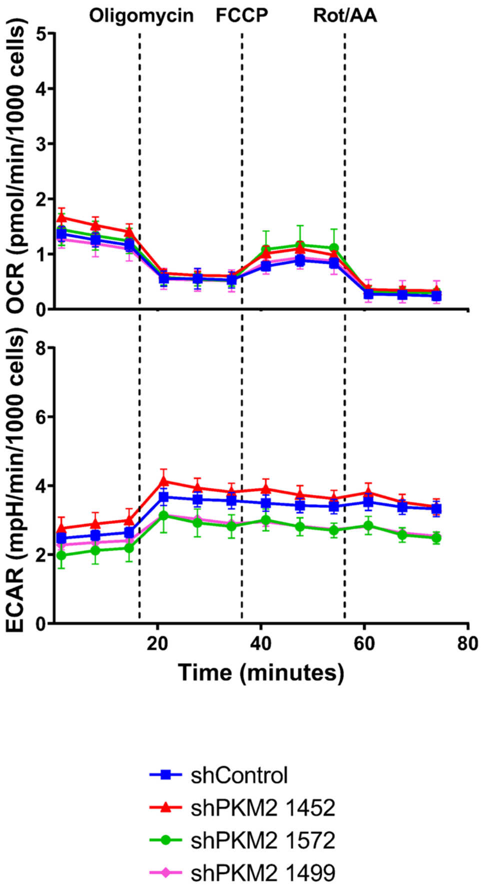

Experiment 3

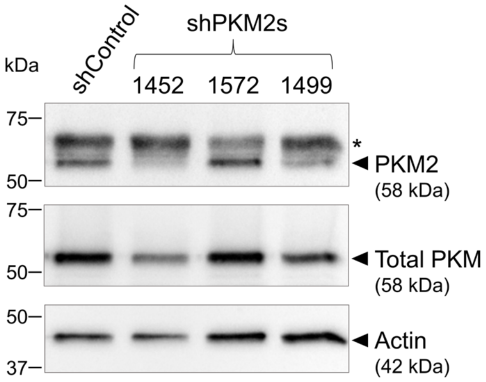

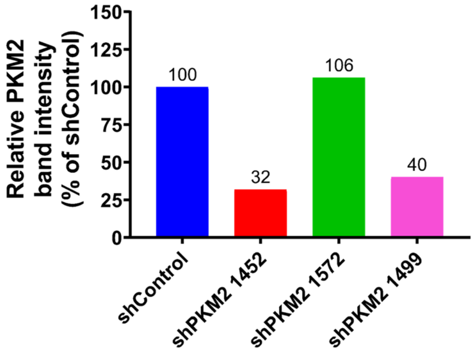

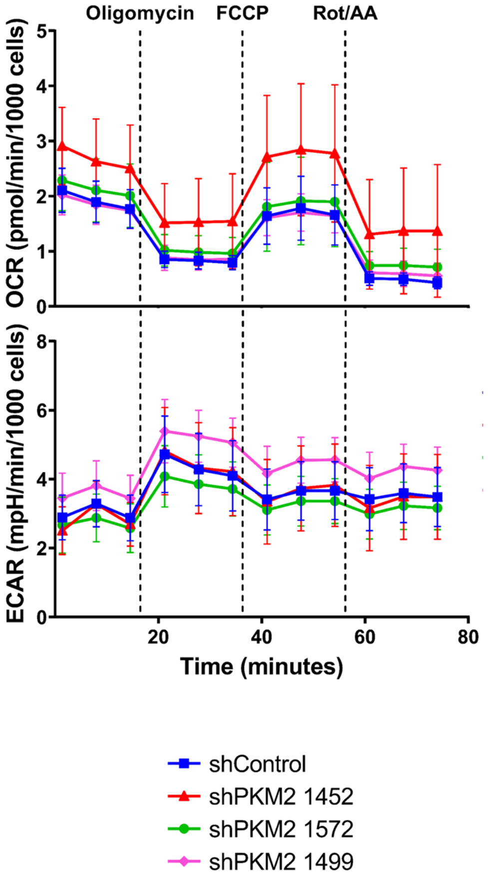

Appendix 7.8. Seahorse XF Cell Mito Stress Tests of PKM2 knockdown rMC-1 cells (associated with Fig 5.8). Western blots probed for PKM2 and total PKM, PKM2 band intensity normalised to actin (value of the shControl is set to 100%), and kinetic graphs of oxygen consumption rates (OCRs) and extracellular acidification rates (ECARs) from three independent experiments discussed in Figure 5.8 are shown. rMC-1 (3750 cells/well) were seeded in a Seahorse 96-well cell culture plate and transduced with lentivirus encoding either a non-targeting shRNA (shControl) or one of three shRNAs targeting PKM2 (shPKM2s 1452, 1572, 1499). Three days after transduction, cells were washed and incubated in fresh assay medium (XF base medium with 10 mM glucose) for an hour before the medium of each well was collected to use as samples for lactate assays. Cells were then subjected to a XF Cell Mito Stress Test where OCRs and ECARs in the presence of glucose (10 mM) were measured simultaneously by the Seahorse XFe96 extracellular flux analyser at a basal state and after the addition of oligomycin (2 μM), FCCP (0.5 μM), and rotenone/antimycin A (Rot/AA, 0.5 μM). OCRs and ECARs were measured three times during each of the four conditions. Three independent experiments (each with a minimum of six replicate wells per group) were performed, and presented as mean ± SD of each measurement point. In Experiment 1 and Experiment 2 (labelled in the figure), cell numbers were determined in representative wells by fluorescence microscopy after Hoechst 33342 nuclear staining. In Experiment 3, cell numbers were determined by the ArrayScan after Hoechst 33342 nuclear staining.

7.9 Seahorse XF Cell Mito Stress Tests of PKM2 knockout rMC-1 cell lines

A.

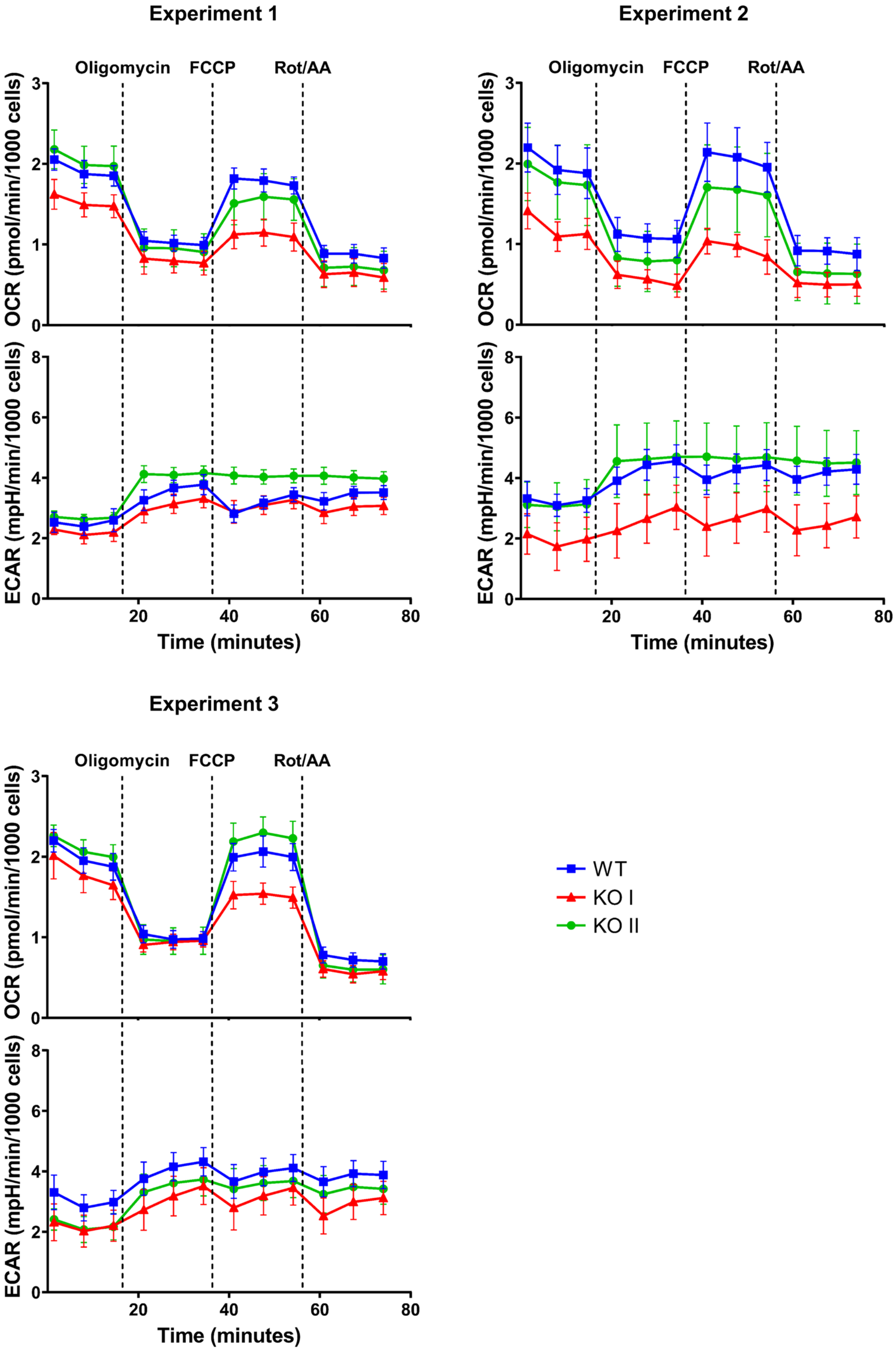

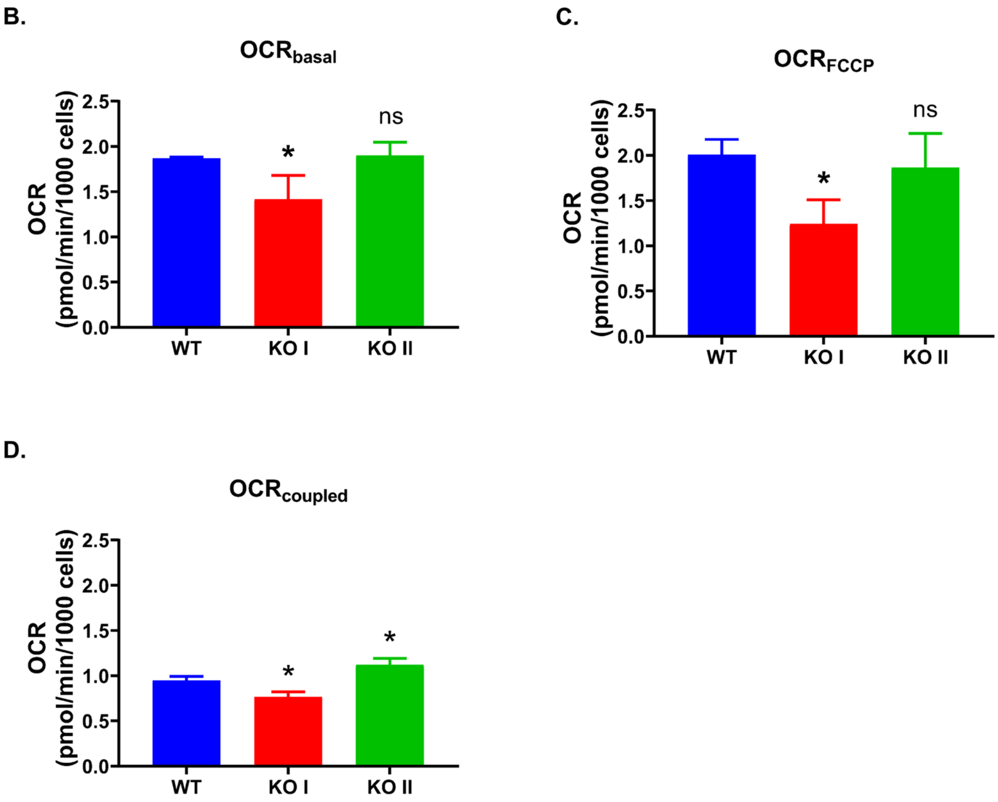

Appendix 7.9. Seahorse XF Cell Mito Stress Tests of PKM2 knockout (KO) rMC-1 cell lines (associated with Fig 5.10). Experiments were performed on three rMC-1 monoclonal cell lines: WT (the empty vector EV1 line isolated from wildtype control cells generated using a Cas9 nuclease plasmid without gRNA), PKM2 KO I (the KO I line 12 isolated from PKM2 KO cells generated using a Cas9 plasmid with gRNAs A1 and B1) and PKM2 KO II (the KO II line 1 isolated from PKM2 KO cells generated using a Cas9 plasmid with gRNAs A2 and B2). The WT, the PKM2 KO I and the PKM2 KO II rMC-1 cell lines were seeded at 15,000 cells/well in a Seahorse 96-well cell culture plate. On the following day, cells were washed and incubated in fresh assay medium (XF base medium with 10 mM glucose) for an hour before the medium of each well was collected to use as samples for lactate assays. Cells were then subjected to a XF Cell Mito Stress Test where oxygen consumption rates (OCRs) and extracellular acidification rates (ECARs) in the presence of glucose (10 mM) were measured simultaneously by the Seahorse XFe96 extracellular flux analyser at a basal state and after the addition of oligomycin (2 µM), FCCP (0.5 µM), and rotenone/antimycin A (Rot/AA, 0.5 µM). OCRs and ECARs were measured three times during each of the four conditions. Three independent experiments (each with a minimum of eight replicate wells per group) were performed, and presented as mean ± SD of each measurement point. Cell numbers from all three experiments were determined by the ArrayScan after Hoechst 33342 nuclear staining. **(A)** Kinetic graphs of OCRs and ECARs from each of the three independent experiments discussed in Figure 5.11. **(B)** basal OCR (OCR$_{basal}$), **(C)** FCCP-induced OCR (OCR$_{FCCP}$) and **(D)** OCR coupled to ATP production (OCR$_{coupled}$) are presented as mean ± SD from the three independent experiments. Statistical significance comparing to WT was determined by one-way ANOVA followed by Dunnett's multiple comparison test. *p<0.05; ns, not significant.

Chapter 8

REFERENCES

CHAPTER 8: References

Abdel-Haleem, A.M., Lewis, N.E., Jamshidi, N., Mineta, K., Gao, X., and Gojobori, T. (2017). The Emerging Facets of Non-Cancerous Warburg Effect. Front Endocrinol (Lausanne) *8*, 279.

Adikusuma, F., Pfitzner, C., and Thomas, P.Q. (2017). Versatile single-step-assembly CRISPR/Cas9 vectors for dual gRNA expression. PloS one *12*, e0187236.

Affourtit, C., and Brand, M.D. (2009). Measuring mitochondrial bioenergetics in INS-1E insulinoma cells. Methods in enzymology *457*, 405-424.

Ahn, C.S., and Metallo, C.M. (2015). Mitochondria as biosynthetic factories for cancer proliferation. Cancer Metab *3*, 1.

Ames, A., 3rd, Li, Y.Y., Heher, E.C., and Kimble, C.R. (1992). Energy metabolism of rabbit retina as related to function: high cost of Na+ transport. The Journal of neuroscience : the official journal of the Society for Neuroscience *12*, 840-853.

Anastasiou, D., Poulogiannis, G., Asara, J.M., Boxer, M.B., Jiang, J.K., Shen, M., Bellinger, G., Sasaki, A.T., Locasale, J.W., Auld, D.S.*, et al.* (2011). Inhibition of pyruvate kinase M2 by reactive oxygen species contributes to cellular antioxidant responses. Science *334*, 1278-1283.

Arif, W., Datar, G., and Kalsotra, A. (2017). Intersections of post-transcriptional gene regulatory mechanisms with intermediary metabolism. Biochim Biophys Acta Gene Regul Mech *1860*, 349-362.

Ashizawa, K., Willingham, M.C., Liang, C.M., and Cheng, S.Y. (1991). In vivo regulation of monomer-tetramer conversion of pyruvate kinase subtype M2 by glucose is mediated via fructose 1,6-bisphosphate. The Journal of biological chemistry *266*, 16842-16846.

Atsuzawa, K., Nakazawa, A., Mizutani, K., Fukasawa, M., Yamamoto, N., Hashimoto, T., and Usuda, N. (2010). Immunohistochemical localization of mitochondrial fatty acid beta-oxidation enzymes in Muller cells of the retina. Histochem Cell Biol *134*, 565-579.

Bailey, E., Stirpe, F., and Taylor, C.B. (1968). Regulation of rat liver pyruvate kinase. The effect of preincubation, pH, copper ions, fructose 1,6-diphosphate and dietary changes on enzyme activity. The Biochemical journal *108*, 427-436.

Barben, M., Ail, D., Storti, F., Klee, K., Schori, C., Samardzija, M., Michalakis, S., Biel, M., Meneau, I., Blaser, F.*, et al.* (2018). Hif1a inactivation rescues photoreceptor degeneration induced by a chronic hypoxia-like stress. Cell death and differentiation *25*, 2071-2085.

Barrett, K.E., Barman, S.M., Boitano, S., and Brooks, H.L. (2012). Vision. In Ganong's Review of Medical Physiology, K.E. Barrett, S.M. Barman, S. Boitano, and H.L. Brooks, eds. (New York: McGraw-Hill).

Bersten, D.C., Sullivan, A.E., Li, D., Bhakti, V., Bent, S.J., and Whitelaw, M.L. (2015). Inducible and reversible lentiviral and Recombination Mediated Cassette Exchange (RMCE) systems for controlling gene expression. PloS one *10*, e0116373.

Bibliowicz, J., Tittle, R.K., and Gross, J.M. (2011). Toward a better understanding of human eye disease insights from the zebrafish, Danio rerio. Prog Mol Biol Transl Sci *100*, 287-330.

Bluemlein, K., Gruning, N.M., Feichtinger, R.G., Lehrach, H., Kofler, B., and Ralser, M. (2011). No evidence for a shift in pyruvate kinase PKM1 to PKM2 expression during tumorigenesis. Oncotarget *2*, 393-400.

Boehning, A.L., Essien, S.A., Underwood, E.L., Dash, P.K., and Boehning, D. (2018). Cell type-dependent effects of ellagic acid on cellular metabolism. Biomed Pharmacother *106*, 411-418.

Bonner, J.A., Harari, P.M., Giralt, J., Azarnia, N., Shin, D.M., Cohen, R.B., Jones, C.U., Sur, R., Raben, D., Jassem, J*., et al.* (2006). Radiotherapy plus cetuximab for squamous-cell carcinoma of the head and neck. The New England journal of medicine *354*, 567-578.

Brand, M.D. (2005). The efficiency and plasticity of mitochondrial energy transduction. Biochem Soc Trans *33*, 897-904.

Bringmann, A., Pannicke, T., Grosche, J., Francke, M., Wiedemann, P., Skatchkov, S.N., Osborne, N.N., and Reichenbach, A. (2006). Muller cells in the healthy and diseased retina. Progress in retinal and eye research *25*, 397-424.

Bryant, J.D., Sweeney, S.R., Sentandreu, E., Shin, M., Ipas, H., Xhemalce, B., Momb, J., Tiziani, S., and Appling, D.R. (2018). Deletion of the neural tube defect-associated gene Mthfd1l disrupts one-carbon and central energy metabolism in mouse embryos. The Journal of biological chemistry *293*, 5821-5833.

Cao, Y., Rathmell, J.C., and Macintyre, A.N. (2014). Metabolic reprogramming towards aerobic glycolysis correlates with greater proliferative ability and resistance to metabolic inhibition in CD8 versus CD4 T cells. PloS one *9*, e104104.

Casson, R.J., Chidlow, G., Han, G., and Wood, J.P. (2012). An explanation for the Warburg effect in the adult mammalian retina. Clinical & experimental ophthalmology.

Casson, R.J., Wood, J.P., Han, G., Kittipassorn, T., Peet, D.J., and Chidlow, G. (2016). M-Type Pyruvate Kinase Isoforms and Lactate Dehydrogenase A in the Mammalian Retina: Metabolic Implications. Investigative ophthalmology & visual science *57*, 66-80.

Chaneton, B., and Gottlieb, E. (2012). Rocking cell metabolism: revised functions of the key glycolytic regulator PKM2 in cancer. Trends in biochemical sciences *37*, 309-316.

Chaneton, B., Hillmann, P., Zheng, L., Martin, A.C.L., Maddocks, O.D.K., Chokkathukalam, A., Coyle, J.E., Jankevics, A., Holding, F.P., Vousden, K.H*., et al.* (2012). Serine is a natural ligand and allosteric activator of pyruvate kinase M2. Nature *491*, 458-462.

Chen, M., David, C.J., and Manley, J.L. (2012). Concentration-dependent control of pyruvate kinase M mutually exclusive splicing by hnRNP proteins. Nat Struct Mol Biol *19*, 346-354.

Chidlow, G., Wood, J.P., Graham, M., and Osborne, N.N. (2005). Expression of monocarboxylate transporters in rat ocular tissues. American journal of physiology Cell physiology *288*, C416-428.

Chilov, D., Camenisch, G., Kvietikova, I., Ziegler, U., Gassmann, M., and Wenger, R.H. (1999). Induction and nuclear translocation of hypoxia-inducible factor-1 (HIF-1): heterodimerization with ARNT is not necessary for nuclear accumulation of HIF-1alpha. Journal of cell science *112 (Pt 8)*, 1203-1212.

Chinchore, Y., Begaj, T., Wu, D., Drokhlyansky, E., and Cepko, C.L. (2017). Glycolytic reliance promotes anabolism in photoreceptors. Elife *6*.

Christofk, H.R., Vander Heiden, M.G., Harris, M.H., Ramanathan, A., Gerszten, R.E., Wei, R., Fleming, M.D., Schreiber, S.L., and Cantley, L.C. (2008a). The M2 splice isoform of pyruvate kinase is important for cancer metabolism and tumour growth. Nature *452*, 230-U274.

Christofk, H.R., Vander Heiden, M.G., Wu, N., Asara, J.M., and Cantley, L.C. (2008b). Pyruvate kinase M2 is a phosphotyrosine-binding protein. Nature *452*, 181-U127.

Clower, C.V., Chatterjee, D., Wang, Z., Cantley, L.C., Vander Heiden, M.G., and Krainer, A.R. (2010). The alternative splicing repressors hnRNP A1/A2 and PTB influence pyruvate kinase isoform expression and cell metabolism. Proceedings of the National Academy of Sciences of the United States of America *107*, 1894-1899.

Cohen, L.H., and Noell, W.K. (1960). Glucose catabolism of rabbit retina before and after development of visual function. Journal of neurochemistry *5*, 253-276.

Cunningham, D., Humblet, Y., Siena, S., Khayat, D., Bleiberg, H., Santoro, A., Bets, D., Mueser, M., Harstrick, A., Verslype, C.*, et al.* (2004). Cetuximab monotherapy and cetuximab plus irinotecan in irinotecan-refractory metastatic colorectal cancer. The New England journal of medicine *351*, 337-345.

Dayton, T.L., Gocheva, V., Miller, K.M., Israelsen, W.J., Bhutkar, A., Clish, C.B., Davidson, S.M., Luengo, A., Bronson, R.T., Jacks, T.*, et al.* (2016a). Germline loss of PKM2 promotes metabolic distress and hepatocellular carcinoma. Genes & development *30*, 1020-1033.

Dayton, T.L., Jacks, T., and Vander Heiden, M.G. (2016b). PKM2, cancer metabolism, and the road ahead. EMBO reports *17*, 1721-1730.

Dejure, F.R., and Eilers, M. (2017). MYC and tumor metabolism: chicken and egg. The EMBO journal *36*, 3409-3420.

Divakaruni, A.S., Paradyse, A., Ferrick, D.A., Murphy, A.N., and Jastroch, M. (2014). Analysis and interpretation of microplate-based oxygen consumption and pH data. Methods in enzymology *547*, 309-354.

Dombrauckas, J.D., Santarsiero, B.D., and Mesecar, A.D. (2005). Structural basis for tumor pyruvate kinase M2 allosteric regulation and catalysis. Biochemistry *44*, 9417-9429.

Dow, L.E., Premsrirut, P.K., Zuber, J., Fellmann, C., McJunkin, K., Miething, C., Park, Y., Dickins, R.A., Hannon, G.J., and Lowe, S.W. (2012). A pipeline for the generation of shRNA transgenic mice. Nat Protoc *7*, 374-393.

Dubois-Dauphin, M., Poitry-Yamate, C., de Bilbao, F., Julliard, A.K., Jourdan, F., and Donati, G. (2000). Early postnatal Muller cell death leads to retinal but not optic nerve degeneration in NSE-Hu-Bcl-2 transgenic mice. Neuroscience *95*, 9-21.

Edgar, R., Domrachev, M., and Lash, A.E. (2002). Gene Expression Omnibus: NCBI gene expression and hybridization array data repository. Nucleic Acids Res *30*, 207-210.

Eide, L., and McMurray, C.T. (2005). Culture of adult mouse neurons. Biotechniques *38*, 99-104.

Epstein, A.C., Gleadle, J.M., McNeill, L.A., Hewitson, K.S., O'Rourke, J., Mole, D.R., Mukherji, M., Metzen, E., Wilson, M.I., Dhanda, A.*, et al.* (2001). C. elegans EGL-9 and mammalian homologs define a family of dioxygenases that regulate HIF by prolyl hydroxylation. Cell *107*, 43-54.

Esumi, N., Oshima, Y., Li, Y., Campochiaro, P.A., and Zack, D.J. (2004). Analysis of the VMD2 promoter and implication of E-box binding factors in its regulation. The Journal of biological chemistry *279*, 19064-19073.

Faccenda, D., Nakamura, J., Gorini, G., Dhoot, G.K., Piacentini, M., Yoshida, M., and Campanella, M. (2017). Control of Mitochondrial Remodeling by the ATPase Inhibitory Factor 1 Unveils a Pro-survival Relay via OPA1. Cell Rep *18*, 1869-1883.

Favre, C., Zhdanov, A., Leahy, M., Papkovsky, D., and O'Connor, R. (2010). Mitochondrial pyrimidine nucleotide carrier (PNC1) regulates mitochondrial biogenesis and the invasive phenotype of cancer cells. Oncogene *29*, 3964-3976.

Gao, X., Wang, H., Yang, J.J., Liu, X., and Liu, Z.R. (2012). Pyruvate kinase M2 regulates gene transcription by acting as a protein kinase. Molecular cell *45*, 598-609.

Garrett, R., and Grisham, C.M. (2010). Biochemistry, 4th edn (Belmont, CA: Brooks/Cole, Cengage Learning).

Gasteiger, E., Hoogland, C., Gattiker, A., Duvaud, S., Wilkins, M.R., Appel, R.D., and Bairoch, A. (2005). Protein Identification and Analysis Tools on the ExPASy Server. In The Proteomics Protocols Handbook, J.M. Walker, ed. (Humana Press), pp. 571-607.

Giang, A.H., Raymond, T., Brookes, P., de Mesy Bentley, K., Schwarz, E., O'Keefe, R., and Eliseev, R. (2013). Mitochondrial dysfunction and permeability transition in osteosarcoma cells showing the Warburg effect. The Journal of biological chemistry *288*, 33303-33311.

Gibson, D.G., Young, L., Chuang, R.Y., Venter, J.C., Hutchison, C.A., 3rd, and Smith, H.O. (2009). Enzymatic assembly of DNA molecules up to several hundred kilobases. Nat Methods *6*, 343-345.

Goda, N., and Kanai, M. (2012). Hypoxia-inducible factors and their roles in energy metabolism. International journal of hematology *95*, 457-463.

Goldberg, M.S., and Sharp, P.A. (2012). Pyruvate kinase M2-specific siRNA induces apoptosis and tumor regression. The Journal of experimental medicine *209*, 217-224.

Hartong, D.T., Dange, M., McGee, T.L., Berson, E.L., Dryja, T.P., and Colman, R.F. (2008). Insights from retinitis pigmentosa into the roles of isocitrate dehydrogenases in the Krebs cycle. Nature genetics *40*, 1230-1234.

Hauck, S.M., Suppmann, S., and Ueffing, M. (2003). Proteomic profiling of primary retinal Muller glia cells reveals a shift in expression patterns upon adaptation to in vitro conditions. Glia *44*, 251-263.

Hitosugi, T., Kang, S., Vander Heiden, M.G., Chung, T.W., Elf, S., Lythgoe, K., Dong, S., Lonial, S., Wang, X., Chen, G.Z.*, et al.* (2009). Tyrosine phosphorylation inhibits PKM2 to promote the Warburg effect and tumor growth. Science signaling *2*, ra73.

Hosios, A.M., Hecht, V.C., Danai, L.V., Johnson, M.O., Rathmell, J.C., Steinhauser, M.L., Manalis, S.R., and Vander Heiden, M.G. (2016). Amino Acids Rather than Glucose Account for the Majority of Cell Mass in Proliferating Mammalian Cells. Dev Cell *36*, 540-549.

Hsu, P.P., and Sabatini, D.M. (2008). Cancer cell metabolism: Warburg and beyond. Cell *134*, 703-707.

Hu, C.J., Wang, L.Y., Chodosh, L.A., Keith, B., and Simon, M.C. (2003). Differential roles of hypoxia-inducible factor 1alpha (HIF-1alpha) and HIF-2alpha in hypoxic gene regulation. Molecular and cellular biology *23*, 9361-9374.

Hughes, J.M., Groot, A.J., van der Groep, P., Sersansie, R., Vooijs, M., van Diest, P.J., Van Noorden, C.J., Schlingemann, R.O., and Klaassen, I. (2010). Active HIF-1 in the normal human retina. The journal of histochemistry and cytochemistry : official journal of the Histochemistry Society *58*, 247-254.

Hynes, J., Nadanaciva, S., Swiss, R., Carey, C., Kirwan, S., and Will, Y. (2013). A high-throughput dual parameter assay for assessing drug-induced mitochondrial dysfunction provides additional predictivity over two established mitochondrial toxicity assays. Toxicol In Vitro *27*, 560-569.

Imamura, K., and Tanaka, T. (1972). Multimolecular forms of pyruvate kinase from rat and other mammalian tissues. I. Electrophoretic studies. Journal of biochemistry *71*, 1043-1051.

Imamura, K., Tanaka, T., Nishina, T., Nakashima, K., and Miwa, S. (1973). Studies on pyruvate kinase (PK) deficiency. II. Electrophoretic, kinetic and immunological studies on pyruvate kinase of erythrocytes and other tissues. Journal of biochemistry *74*, 1165-1175.

Israelsen, W.J., Dayton, T.L., Davidson, S.M., Fiske, B.P., Hosios, A.M., Bellinger, G., Li, J., Yu, Y., Sasaki, M., Horner, J.W.*, et al.* (2013). PKM2 Isoform-Specific Deletion Reveals a Differential Requirement for Pyruvate Kinase in Tumor Cells. Cell *155*, 397-409.

Jeon, C.J., Strettoi, E., and Masland, R.H. (1998). The major cell populations of the mouse retina. The Journal of neuroscience : the official journal of the Society for Neuroscience *18*, 8936-8946.

Kast, B., Schori, C., and Grimm, C. (2016). Hypoxic preconditioning protects photoreceptors against light damage independently of hypoxia inducible transcription factors in rods. Experimental eye research *146*, 60-71.

Ke, Q., and Costa, M. (2006). Hypoxia-inducible factor-1 (HIF-1). Molecular pharmacology *70*, 1469-1480.

Keller, K.E., Tan, I.S., and Lee, Y.S. (2012). SAICAR stimulates pyruvate kinase isoform M2 and promotes cancer cell survival in glucose-limited conditions. Science *338*, 1069-1072.

Kittipassorn, T. (2013). Investigating the role of hypoxia-inducible factor-1alpha and pyruvate kinase M2 in the Warburg effect in the mammalian retina. In Discipline of Biochemistry (Adelaide: University of Adelaide).

Kittipassorn, T., Haydinger, C.D., Wood, J.P.M., Mammone, T., Casson, R.J., and Peet, D.J. (2019a). Characterization of the novel spontaneously immortalized rat Muller cell line SIRMu-1. Experimental eye research *181*, 127-135.

Kittipassorn, T., Haydinger, C.D., Wood, J.P.M., Mammone, T., Casson, R.J., and Peet, D.J. (2019b). RNA sequencing data of cultured primary rat Müller cells, the spontaneously immortalized rat Müller cell line, SIRMu-1, and the SV40-transformed rat Müller cell line, rMC-1. Data Brief *23*, 103721.

Kolb, H. (1995a). Photoreceptors. In Webvision: The Organization of the Retina and Visual System, H. Kolb, E. Fernandez, and R. Nelson, eds. (Salt Lake City (UT)).

Kolb, H. (1995b). Simple Anatomy of the Retina. In Webvision: The Organization of the Retina and Visual System, H. Kolb, E. Fernandez, and R. Nelson, eds. (Salt Lake City (UT)).

Koppenol, W.H., Bounds, P.L., and Dang, C.V. (2011). Otto Warburg's contributions to current concepts of cancer metabolism. Nature reviews Cancer *11*, 325-337.

Lando, D., Peet, D.J., Gorman, J.J., Whelan, D.A., Whitelaw, M.L., and Bruick, R.K. (2002a). FIH-1 is an asparaginyl hydroxylase enzyme that regulates the transcriptional activity of hypoxia-inducible factor. Genes & development *16*, 1466-1471.

Lando, D., Peet, D.J., Whelan, D.A., Gorman, J.J., and Whitelaw, M.L. (2002b). Asparagine hydroxylation of the HIF transactivation domain a hypoxic switch. Science *295*, 858-861.

LaVail, M.M. (1980). Circadian nature of rod outer segment disc shedding in the rat. Investigative ophthalmology & visual science *19*, 407-411.

Li, Z., and Graham, B.H. (2012). Measurement of mitochondrial oxygen consumption using a Clark electrode. Methods Mol Biol *837*, 63-72.

Liberti, M.V., and Locasale, J.W. (2016). The Warburg Effect: How Does it Benefit Cancer Cells? Trends in biochemical sciences *41*, 211-218.

Limb, G.A., Salt, T.E., Munro, P.M., Moss, S.E., and Khaw, P.T. (2002). In vitro characterization of a spontaneously immortalized human Muller cell line (MIO-M1). Investigative ophthalmology & visual science *43*, 864-869.

Lin, M., Chen, Y., Jin, J., Hu, Y., Zhou, K.K., Zhu, M., Le, Y.Z., Ge, J., Johnson, R.S., and Ma, J.X. (2011). Ischaemia-induced retinal neovascularisation and diabetic retinopathy in mice with conditional knockout of hypoxia-inducible factor-1 in retinal Muller cells. Diabetologia *54*, 1554-1566.

Lindsay, K.J., Du, J., Sloat, S.R., Contreras, L., Linton, J.D., Turner, S.J., Sadilek, M., Satrustegui, J., and Hurley, J.B. (2014). Pyruvate kinase and aspartate-glutamate carrier distributions reveal key metabolic links between neurons and glia in retina. Proceedings of the National Academy of Sciences of the United States of America.

Lu, H., Li, X., Luo, Z., Liu, J., and Fan, Z. (2013). Cetuximab reverses the Warburg effect by inhibiting HIF-1-regulated LDH-A. Molecular cancer therapeutics *12*, 2187-2199.

Lundholt, B.K., Scudder, K.M., and Pagliaro, L. (2003). A simple technique for reducing edge effect in cell-based assays. J Biomol Screen *8*, 566-570.

Luo, W., Hu, H., Chang, R., Zhong, J., Knabel, M., O'Meally, R., Cole, R.N., Pandey, A., and Semenza, G.L. (2011). Pyruvate kinase M2 is a PHD3-stimulated coactivator for hypoxia-inducible factor 1. Cell *145*, 732-744.

Luo, W., and Semenza, G.L. (2012). Emerging roles of PKM2 in cell metabolism and cancer progression. Trends Endocrinol Metab *23*, 560-566.

Luwor, R.B., Lu, Y., Li, X., Mendelsohn, J., and Fan, Z. (2005). The antiepidermal growth factor receptor monoclonal antibody cetuximab/C225 reduces hypoxia-inducible factor-1 alpha, leading to transcriptional inhibition of vascular endothelial growth factor expression. Oncogene *24*, 4433-4441.

Lv, L., Li, D., Zhao, D., Lin, R., Chu, Y., Zhang, H., Zha, Z., Liu, Y., Li, Z., Xu, Y.*, et al.* (2011). Acetylation targets the M2 isoform of pyruvate kinase for degradation through chaperone-mediated autophagy and promotes tumor growth. Molecular cell *42*, 719-730.

Macosko, E.Z., Basu, A., Satija, R., Nemesh, J., Shekhar, K., Goldman, M., Tirosh, I., Bialas, A.R., Kamitaki, N., Martersteck, E.M.*, et al.* (2015). Highly Parallel Genome-wide Expression Profiling of Individual Cells Using Nanoliter Droplets. Cell *161*, 1202-1214.

Makinoshima, H., Takita, M., Saruwatari, K., Umemura, S., Obata, Y., Ishii, G., Matsumoto, S., Sugiyama, E., Ochiai, A., Abe, R.*, et al.* (2015). Signaling through the Phosphatidylinositol 3-Kinase (PI3K)/Mammalian Target of Rapamycin (mTOR) Axis Is Responsible for Aerobic Glycolysis mediated by Glucose Transporter in Epidermal Growth Factor Receptor (EGFR)-mutated Lung Adenocarcinoma. The Journal of biological chemistry *290*, 17495-17504.

Maxwell, P.H., Wiesener, M.S., Chang, G.W., Clifford, S.C., Vaux, E.C., Cockman, M.E., Wykoff, C.C., Pugh, C.W., Maher, E.R., and Ratcliffe, P.J. (1999). The tumour suppressor protein VHL targets hypoxia-inducible factors for oxygen-dependent proteolysis. Nature *399*, 271-275.

Mazurek, S. (2011). Pyruvate kinase type M2: a key regulator of the metabolic budget system in tumor cells. The international journal of biochemistry & cell biology *43*, 969-980.

Mescher, A.L. (2010). The Eye and Ear: Special Sense Organs. In Junqueira's Basic Histology: Text & Atlas, A.L. Mescher, ed. (New York: McGraw-Hill).

Mookerjee, S.A., Gerencser, A.A., Nicholls, D.G., and Brand, M.D. (2017). Quantifying intracellular rates of glycolytic and oxidative ATP production and consumption using extracellular flux measurements. The Journal of biological chemistry *292*, 7189-7207.

Mookerjee, S.A., Gerencser, A.A., Nicholls, D.G., and Brand, M.D. (2018). Quantifying intracellular rates of glycolytic and oxidative ATP production and consumption using extracellular flux measurements (additions and corrections). The Journal of biological chemistry *293*, 12649-12652.

Mookerjee, S.A., Goncalves, R.L.S., Gerencser, A.A., Nicholls, D.G., and Brand, M.D. (2015). The contributions of respiration and glycolysis to extracellular acid production. Biochimica et biophysica acta *1847*, 171-181.

Moreno-Sanchez, R., Rodriguez-Enriquez, S., Marin-Hernandez, A., and Saavedra, E. (2007). Energy metabolism in tumor cells. The FEBS journal *274*, 1393-1418.

Morgan, H.P., O'Reilly, F.J., Wear, M.A., O'Neill, J.R., Fothergill-Gilmore, L.A., Hupp, T., and Walkinshaw, M.D. (2013). M2 pyruvate kinase provides a mechanism for nutrient sensing and regulation of cell proliferation. Proceedings of the National Academy of Sciences of the United States of America *110*, 5881-5886.

Morohoshi, K., Ohbayashi, M., Patel, N., Chong, V., Bird, A.C., and Ono, S.J. (2012). Identification of anti-retinal antibodies in patients with age-related macular degeneration. Experimental and molecular pathology *93*, 193-199.

Mucaj, V., Shay, J.E., and Simon, M.C. (2012). Effects of hypoxia and HIFs on cancer metabolism. International journal of hematology *95*, 464-470.

Ng, S.K., Wood, J.P., Chidlow, G., Han, G., Kittipassorn, T., Peet, D.J., and Casson, R.J. (2015). Cancer-like metabolism of the mammalian retina. Clin Exp Ophthalmol *43*, 367-376.

Nicholas, D., Proctor, E.A., Raval, F.M., Ip, B.C., Habib, C., Ritou, E., Grammatopoulos, T.N., Steenkamp, D., Dooms, H., Apovian, C.M.*, et al.* (2017). Advances in the quantification of mitochondrial function in primary human immune cells through extracellular flux analysis. PloS one *12*, e0170975.

Noguchi, T., Inoue, H., and Tanaka, T. (1986). The M1- and M2-type isozymes of rat pyruvate kinase are produced from the same gene by alternative RNA splicing. The Journal of biological chemistry *261*, 13807-13812.

Noguchi, T., Yamada, K., Inoue, H., Matsuda, T., and Tanaka, T. (1987). The L- and R-type isozymes of rat pyruvate kinase are produced from a single gene by use of different promoters. The Journal of biological chemistry *262*, 14366-14371.

Okawa, H., Sampath, A.P., Laughlin, S.B., and Fain, G.L. (2008). ATP consumption by mammalian rod photoreceptors in darkness and in light. Curr Biol *18*, 1917-1921.

Oliveira, P.F., Martins, A.D., Moreira, A.C., Cheng, C.Y., and Alves, M.G. (2015). The Warburg effect revisited--lesson from the Sertoli cell. Med Res Rev *35*, 126-151.

Osborne, N.N. (1990). Stimulatory and inhibitory actions of excitatory amino acids on inositol phospholipid metabolism in rabbit retina. Evidence for a specific quisqualate receptor subtype associated with neurones. Experimental eye research *50*, 397-405.

Palsson-McDermott, E.M., Curtis, A.M., Goel, G., Lauterbach, M.A., Sheedy, F.J., Gleeson, L.E., van den Bosch, M.W., Quinn, S.R., Domingo-Fernandez, R., Johnston, D.G., *et al.* (2015). Pyruvate kinase M2 regulates Hif-1alpha activity and IL-1beta induction and is a critical determinant of the warburg effect in LPS-activated macrophages. Cell metabolism *21*, 65-80.

Palsson-McDermott, E.M., and O'Neill, L.A. (2013). The Warburg effect then and now: from cancer to inflammatory diseases. Bioessays *35*, 965-973.

Papkovsky, D.B., and Zhdanov, A.V. (2015). Cell energy budget platform for assessment of cell metabolism. Methods Mol Biol *1265*, 333-348.

Peet, D.J., Kittipassorn, T., Wood, J.P., Chidlow, G., and Casson, R.J. (2017). HIF signalling: The eyes have it. Exp Cell Res *356*, 136-140.

Petit, L., Ma, S., Cipi, J., Cheng, S.Y., Zieger, M., Hay, N., and Punzo, C. (2018). Aerobic Glycolysis Is Essential for Normal Rod Function and Controls Secondary Cone Death in Retinitis Pigmentosa. Cell Rep *23*, 2629-2642.

Poitry-Yamate, C.L., Poitry, S., and Tsacopoulos, M. (1995). Lactate released by Muller glial cells is metabolized by photoreceptors from mammalian retina. The Journal of neuroscience : the official journal of the Society for Neuroscience *15*, 5179-5191.

Potter, M., Newport, E., and Morten, K.J. (2016). The Warburg effect: 80 years on. Biochem Soc Trans *44*, 1499-1505.

Raini, G., Sharet, R., Herrero, M., Atzmon, A., Shenoy, A., Geiger, T., and Elroy-Stein, O. (2017). Mutant eIF2B leads to impaired mitochondrial oxidative phosphorylation in vanishing white matter disease. Journal of neurochemistry *141*, 694-707.

Rajala, A., Wang, Y., Brush, R.S., Tsantilas, K., Jankowski, C.S.R., Lindsay, K.J., Linton, J.D., Hurley, J.B., Anderson, R.E., and Rajala, R.V.S. (2018a). Pyruvate kinase M2 regulates photoreceptor structure, function, and viability. Cell Death Dis *9*, 240.

Rajala, A., Wang, Y., Soni, K., and Rajala, R.V.S. (2018b). Pyruvate kinase M2 isoform deletion in cone photoreceptors results in age-related cone degeneration. Cell Death Dis *9*, 737.

Rajala, R.V., Rajala, A., Kooker, C., Wang, Y., and Anderson, R.E. (2016). The Warburg Effect Mediator Pyruvate Kinase M2 Expression and Regulation in the Retina. Sci Rep *6*, 37727.

Ramamurthy, V., Niemi, G.A., Reh, T.A., and Hurley, J.B. (2004). Leber congenital amaurosis linked to AIPL1: a mouse model reveals destabilization of cGMP phosphodiesterase. Proceedings of the National Academy of Sciences of the United States of America *101*, 13897-13902.

Reidel, B., Thompson, J.W., Farsiu, S., Moseley, M.A., Skiba, N.P., and Arshavsky, V.Y. (2011). Proteomic profiling of a layered tissue reveals unique glycolytic specializations of photoreceptor cells. Mol Cell Proteomics *10*, M110 002469.

Reitzer, L.J., Wice, B.M., and Kennell, D. (1979). Evidence that glutamine, not sugar, is the major energy source for cultured HeLa cells. The Journal of biological chemistry *254*, 2669-2676.
Rodriguez-Prados, J.C., Traves, P.G., Cuenca, J., Rico, D., Aragones, J., Martin-Sanz, P., Cascante,

M., and Bosca, L. (2010). Substrate fate in activated macrophages: a comparison between innate, classic, and alternative activation. J Immunol *185*, 605-614.

Roesch, K., Jadhav, A.P., Trimarchi, J.M., Stadler, M.B., Roska, B., Sun, B.B., and Cepko, C.L. (2008). The transcriptome of retinal Muller glial cells. The Journal of comparative neurology *509*, 225-238.

Rueda, E.M., Johnson, J.E., Jr., Giddabasappa, A., Swaroop, A., Brooks, M.J., Sigel, I., Chaney, S.Y., and Fox, D.A. (2016). The cellular and compartmental profile of mouse retinal glycolysis, tricarboxylic acid cycle, oxidative phosphorylation, and ~P transferring kinases. Molecular vision *22*, 847-885.

Sarthy, P.V. (1985). Establishment of Muller cell cultures from adult rat retina. Brain research *337*, 138-141.

Sarthy, V.P., Brodjian, S.J., Dutt, K., Kennedy, B.N., French, R.P., and Crabb, J.W. (1998). Establishment and characterization of a retinal Muller cell line. Investigative ophthalmology & visual science *39*, 212-216.

Savage, F.J., Day, J.E., Hogg, P., and Grierson, I. (1988). Tissue culture of retinal glial cells. Eye *2 Suppl*, S164-179.

Scaife, R.M., and Langdon, W.Y. (2000). c-Cbl localizes to actin lamellae and regulates lamellipodia formation and cell morphology. Journal of cell science *113 Pt 2*, 215-226.

Schindelin, J., Arganda-Carreras, I., Frise, E., Kaynig, V., Longair, M., Pietzsch, T., Preibisch, S., Rueden, C., Saalfeld, S., Schmid, B.*, et al.* (2012). Fiji: an open-source platform for biological-image analysis. Nat Methods *9*, 676-682.

Semenza, G.L. (2012). Hypoxia-inducible factors: mediators of cancer progression and targets for cancer therapy. Trends in pharmacological sciences *33*, 207-214.

Semenza, G.L., Roth, P.H., Fang, H.M., and Wang, G.L. (1994). Transcriptional regulation of genes encoding glycolytic enzymes by hypoxia-inducible factor 1. The Journal of biological chemistry *269*, 23757-23763.

Semenza, G.L., and Wang, G.L. (1992). A nuclear factor induced by hypoxia via de novo protein synthesis binds to the human erythropoietin gene enhancer at a site required for transcriptional activation. Molecular and cellular biology *12*, 5447-5454.

Shen, W., Fruttiger, M., Zhu, L., Chung, S.H., Barnett, N.L., Kirk, J.K., Lee, S., Coorey, N.J., Killingsworth, M., Sherman, L.S.*, et al.* (2012). Conditional Mullercell ablation causes independent neuronal and vascular pathologies in a novel transgenic model. The Journal of neuroscience : the official journal of the Society for Neuroscience *32*, 15715-15727.

Siddiqui, F.A., Prakasam, G., Chattopadhyay, S., Rehman, A.U., Padder, R.A., Ansari, M.A., Irshad, R., Mangalhara, K., Bamezai, R.N.K., Husain, M.*, et al.* (2018). Curcumin decreases Warburg effect in cancer cells by down-regulating pyruvate kinase M2 via mTOR-HIF1alpha inhibition. Sci Rep *8*, 8323.

Stanisz, J., Wice, B.M., and Kennell, D.E. (1983). Comparative energy metabolism in cultured heart muscle and HeLa cells. Journal of cellular physiology *115*, 320-330.

Stincone, A., Prigione, A., Cramer, T., Wamelink, M.M., Campbell, K., Cheung, E., Olin-Sandoval, V., Gruning, N.M., Kruger, A., Tauqeer Alam, M.*, et al.* (2015). The return of metabolism: biochemistry and physiology of the pentose phosphate pathway. Biol Rev Camb Philos Soc *90*, 927-963.

Stone, J., van Driel, D., Valter, K., Rees, S., and Provis, J. (2008). The locations of mitochondria in mammalian photoreceptors: relation to retinal vasculature. Brain research *1189*, 58-69.

Tennant, D.A., Duran, R.V., and Gottlieb, E. (2010). Targeting metabolic transformation for cancer therapy. Nature reviews Cancer *10*, 267-277.

Tien, T., Zhang, J., Muto, T., Kim, D., Sarthy, V.P., and Roy, S. (2017). High Glucose Induces Mitochondrial Dysfunction in Retinal Muller Cells: Implications for Diabetic Retinopathy. Investigative ophthalmology & visual science *58*, 2915-2921.

Tornquist, P., and Alm, A. (1979). Retinal and choroidal contribution to retinal metabolism in vivo. A study in pigs. Acta physiologica Scandinavica *106*, 351-357.

Tsutsumi, H., Tani, K., Fujii, H., and Miwa, S. (1988). Expression of L- and M-type pyruvate kinase in human tissues. Genomics *2*, 86-89.

Ueki, Y., Ash, J.D., Zhu, M., Zheng, L., and Le, Y.Z. (2009). Expression of Cre recombinase in retinal Muller cells. Vision Res *49*, 615-621.

Upadhyay, M., Samal, J., Kandpal, M., Singh, O.V., and Vivekanandan, P. (2013). The Warburg effect: Insights from the past decade. Pharmacology & therapeutics *137*, 318-330.

Vander Heiden, M.G., Cantley, L.C., and Thompson, C.B. (2009). Understanding the Warburg effect: the metabolic requirements of cell proliferation. Science *324*, 1029-1033.

Vander Heiden, M.G., Christofk, H.R., Schuman, E., Subtelny, A.O., Sharfi, H., Harlow, E.E., Xian, J., and Cantley, L.C. (2010a). Identification of small molecule inhibitors of pyruvate kinase M2. Biochemical pharmacology *79*, 1118-1124.

Vander Heiden, M.G., Locasale, J.W., Swanson, K.D., Sharfi, H., Heffron, G.J., Amador-Noguez, D., Christofk, H.R., Wagner, G., Rabinowitz, J.D., Asara, J.M.*, et al.* (2010b). Evidence for an alternative glycolytic pathway in rapidly proliferating cells. Science *329*, 1492-1499.

Vecino, E., Rodriguez, F.D., Ruzafa, N., Pereiro, X., and Sharma, S.C. (2016). Glia-neuron interactions in the mammalian retina. Progress in retinal and eye research *51*, 1-40.

Wang, G.L., Jiang, B.H., Rue, E.A., and Semenza, G.L. (1995). Hypoxia-inducible factor 1 is a basic-helix-loop-helix-PAS heterodimer regulated by cellular O2 tension. Proceedings of the National Academy of Sciences of the United States of America *92*, 5510-5514.

Wang, H.J., Hsieh, Y.J., Cheng, W.C., Lin, C.P., Lin, Y.S., Yang, S.F., Chen, C.C., Izumiya, Y., Yu, J.S., Kung, H.J., *et al.* (2014). JMJD5 regulates PKM2 nuclear translocation and reprograms HIF-1alpha-mediated glucose metabolism. Proceedings of the National Academy of Sciences of the United States of America *111*, 279-284.

Wang, L., Tornquist, P., and Bill, A. (1997a). Glucose metabolism in pig outer retina in light and darkness. Acta physiologica Scandinavica *160*, 75-81.

Wang, L., Tornquist, P., and Bill, A. (1997b). Glucose metabolism of the inner retina in pigs in darkness and light. Acta physiologica Scandinavica *160*, 71-74.

Warburg, O. (1925). The metabolism of carcinoma cells 1. The Journal of Cancer Research *9*, 148-163.

Warburg, O. (1956). On the origin of cancer cells. Science *123*, 309-314.

Warburg, O., Posener, K., and Negelein, E. (1924). On the metabolism of carcinoma cells. Biochem Z *152*, 309-344.

Warburg, O., Wind, F., and Negelein, E. (1927). The Metabolism of Tumors in the Body. The Journal of general physiology *8*, 519-530.

Warburg, O.H., Dickens, F., and Kaiser-Wilhelm-Institut für, B. (1930). The metabolism of tumours; investigations from the Kaiser Wilhelm institute for biology, Berlin-Dahlem (London: Constable & Co. Ltd.).

Ward, P.S., and Thompson, C.B. (2012). Metabolic reprogramming: a cancer hallmark even warburg did not anticipate. Cancer cell *21*, 297-308.

Wilkinson-Berka, J.L. (2004). Diabetes and retinal vascular disorders: role of the renin-angiotensin system. Expert reviews in molecular medicine *6*, 1-18.

Winkler, B.S. (1981). Glycolytic and oxidative metabolism in relation to retinal function. The Journal of general physiology *77*, 667-692.

Winkler, B.S. (1995). A quantitative assessment of glucose metabolism in the isolated rat retina. Sem Ophtalm *6*, 78-96.

Winkler, B.S., Arnold, M.J., Brassell, M.A., and Puro, D.G. (2000). Energy metabolism in human retinal Muller cells. Investigative ophthalmology & visual science *41*, 3183-3190.

Winkler, B.S., Sauer, M.W., and Starnes, C.A. (2003). Modulation of the Pasteur effect in retinal cells: implications for understanding compensatory metabolic mechanisms. Experimental eye research *76*, 715-723.

Winkler, B.S., Starnes, C.A., Sauer, M.W., Firouzgan, Z., and Chen, S.C. (2004). Cultured retinal neuronal cells and Muller cells both show net production of lactate. Neurochem Int *45*, 311-320.

Wood, J.P., Chidlow, G., Graham, M., and Osborne, N.N. (2005). Energy substrate requirements for survival of rat retinal cells in culture: the importance of glucose and monocarboxylates. Journal of neurochemistry *93*, 686-697.

Wood, J.P., Schmidt, K.G., Melena, J., Chidlow, G., Allmeier, H., and Osborne, N.N. (2003). The beta-adrenoceptor antagonists metipranolol and timolol are retinal neuroprotectants: comparison with betaxolol. Experimental eye research *76*, 505-516.

Wu, J.J., Quijano, C., Chen, E., Liu, H., Cao, L., Fergusson, M.M., Rovira, II, Gutkind, S., Daniels, M.P., Komatsu, M*., et al.* (2009). Mitochondrial dysfunction and oxidative stress mediate the physiological impairment induced by the disruption of autophagy. Aging (Albany NY) *1*, 425-437.

Yang, W., Xia, Y., Hawke, D., Li, X., Liang, J., Xing, D., Aldape, K., Hunter, T., Alfred Yung, W.K., and Lu, Z. (2012). PKM2 phosphorylates histone H3 and promotes gene transcription and tumorigenesis. Cell *150*, 685-696.

Yang, W., Xia, Y., Ji, H., Zheng, Y., Liang, J., Huang, W., Gao, X., Aldape, K., and Lu, Z. (2011). Nuclear PKM2 regulates beta-catenin transactivation upon EGFR activation. Nature *480*, 118-122.

Young, J.D. (2013). Metabolic flux rewiring in mammalian cell cultures. Curr Opin Biotechnol *24*, 1108-1115.

Young, R.W. (1967). The renewal of photoreceptor cell outer segments. The Journal of cell biology *33*, 61-72.

Yu, L., Chen, X., Wang, L., and Chen, S. (2016). The sweet trap in tumors: aerobic glycolysis and potential targets for therapy. Oncotarget *7*, 38908-38926.

Zhang, J., Nuebel, E., Wisidagama, D.R., Setoguchi, K., Hong, J.S., Van Horn, C.M., Imam, S.S., Vergnes, L., Malone, C.S., Koehler, C.M*., et al.* (2012). Measuring energy metabolism in cultured cells, including human pluripotent stem cells and differentiated cells. Nat Protoc *7*, 1068-1085.

Zhdanov, A.V., Favre, C., O'Flaherty, L., Adam, J., O'Connor, R., Pollard, P.J., and Papkovsky, D.B. (2011). Comparative bioenergetic assessment of transformed cells using a cell energy budget platform. Integr Biol (Camb) *3*, 1135-1142.

Zhong, H., De Marzo, A.M., Laughner, E., Lim, M., Hilton, D.A., Zagzag, D., Buechler, P., Isaacs, W.B., Semenza, G.L., and Simons, J.W. (1999). Overexpression of hypoxia-inducible factor 1alpha in common human cancers and their metastases. Cancer research *59*, 5830-5835.